Energy, Mines and
Resources Canada

Énergie, Mines et
Ressources Canada

CANMET

Canada Centre for
Mineral and Energy
Technology

Centre canadien de la
technologie des
minéraux et de l'énergie

**Mining
Research
Laboratories**

**Laboratoires
de recherche
minière**

Canada

91-07101/

THE POST-FAILURE BEHAVIOUR OF THE LAC DU BONNET GREY GRANITE

J.S.O. L u and B. Gorski July 1991

Mining Research Laboratories
Divisional Report MRL 91-079(TR)

This document is an unedited interim report prepared primarily for discussion and internal reference purposes. It does not represent a final expression of the opinion of the Canada Centre for Mineral and Energy Technology (CANMET)

Ce document est un rapport provisoire non-revisé et rédigé principalement pour fin de discussion et de documentation interne. Il ne représente nullement l'expression définitive de l'opinion du Centre canadien de la technologie des minéraux et de l'énergie (CANMET)

146 pp

THE POST-FAILURE BEHAVIOUR OF THE LAC DU BONNET GREY GRANITE

by

J.S.O. Lau[1] and B. Gorski[2]

ABSTRACT

A laboratory testing program was carried out to study the post-failure behaviour of the Lac du Bonnet grey granite obtained from the 420 Level of the URL. The rock was found to exhibit class II behaviour. The development of cracks in the specimens appeared to start at stress levels in the range of 35 - 40% of the peak strength under uniaxial compression, and 35 - 45% of the peak strength under triaxial compression. The peak strength increased with confining pressure. The residual strength appeared to be somewhere between 20 and 40 MPa.

Crack closure caused the tangent Young's modulus to increase as the confining pressure was increased from 0 to 8 MPa. Poisson's ratio was similarly affected in the 0 to 2 MPa confining pressure range. The predicted uniaxial compressive strength, σ_c, and the material constant, m, in the Hoek and Brown failure criterion for the grey granite were found to be 157 MPa and 35.28 respectively.

The strength and stiffness of this rock were lower than those of the same type of rock from another borehole located in the same area.

Keywords: post-failure, uniaxial, triaxial, peak strength, residual strength, stress-strain, tangent Young's modulus, Poisson's ratio, failure criterion

---

[1] Geotechnical Engineer, AECL Research, on attachment to Canadian Mine Technology Laboratory, Mining Research Laboratories, CANMET, Energy, Mines and Resources Canada, Ottawa, Ontario.

[2] Physical Scientist, Canadian Mine Technology Laboratory, Mining Research Laboratories, CANMET, Energy, Mines and Resources Canada, Ottawa, Ontario.

COMPORTEMENT POSTRUPTURE DU GRANITE GRIS DE LAC DU BONNET

par

J.S.O. Lau[1] et B. Gorski[2]

RÉSUMÉ

Un programme d'essais en laboratorie a été mené dans le but d'étudier le comportement postrupture du granite gris de lac du Bonnet prélevé au niveau 420 du Laboratorie de recherches souterraines. On a observé que la roche présentait un comportement de classe II. Les fissures sont apparues dans les échantillons à des niveaux de contrainte de l'ordre de 35 - 40% de la résistance maximale dans le cas d'une compression uniaxiale et de l'ordre de 35 - 45% de la résistance maximale dans le cas d'une compression triaxiale. La résistance maximale augmentait avec la pression de confinement. La résistance résiduelle semblait se situer entre 20 et 40 MPa.

La fermeture des fissures a entraîné une augmentation du module de Young tangent lorsque la pression de confinement passait de 0 à 8 MPa. On a observé le même phénomène pour le rapport de Poisson lorsque la pression de confinement passait de 0 à 2 MPa. La résistance à la compression uniaxiale prédite, σ_c, et la constante du matériau, m, dans le critère de rupture de Hoek et Brown pour le granite gris étaient respectivement égales à 157 MPa et 35.28.

La résistance et la rigidité de cette roche étaient inférieures à celles d'un même type de roche provenant d'un autre trou de sonde situé dans la même zone.

Mots clés: postrupture, uniaxiale, triaxiale, résistance maximale, résistance résiduelle, contrainte-déformation, module de Young tangent, rapport de Poisson, critère de rupture

---

[1] Ingénieur en géotechnique, EACL Recherche, affecté au Laboratoire canadien de technologie minière, Laboratories de recherche minière, CANMET, Énergie, Mines et Ressources Canada, Ottawa, Ontario.

[2] Chercheur en sciences physique, Laboratoire canadien de technologie minière, Laboratoires de recherche minière, CANMET, Énergie, Mines et Ressources Canada, Ottawa, Ontario.

CONTENTS

Page

ABSTRACT i
RÉSUMÉ iii
INTRODUCTION 1
ROCK TYPE AND SPECIMEN PREPARATION 2
TEST APPARATUS AND PROCEDURE 2
TEST PROGRAM AND RESULTS 4
DISCUSSION 5
Stress-Strain Observations 5
  Uniaxial Compression 5
  Triaxial Compression 6
Peak Strength 7
Residual Strength 7
Failure Mode 7
Tangent Young's Modulus 8
Poisson's Ratio 8
Failure Criterion 9
CONCLUSIONS 9
RECOMMENDATIONS 11
ACKNOWLEDGEMENTS 11
REFERENCES 12
APPENDIX A 66

TABLES

No.

1. Dimensions, densities and p-wave velocities of rock specimens. 14
2. Results of post-failure uniaxial and triaxial compression tests. 15
3. Failure characteristics of rock specimens. 18

FIGURES

1. Stress-strain curves for specimen 401-S12-MB1-21.065 ($\sigma_3 = 0$). 19
2. Stress-strain curves for specimen 401-S12-MB1-24.366 ($\sigma_3 = 0$). 20
3. Stress-strain curves for specimen 401-S12-MB1-29.645 ($\sigma_3 = 0$). 21
4. Stress-strain curves for specimen 401-S12-MB1-21.227 ($\sigma_3 = 0$). 22
5. Stress-strain curves for specimen 401-S12-MB1-27.547 ($\sigma_3 = 0$). 23
6. Stress-strain curves for specimen 401-S12-MB1-40.053 ($\sigma_3 = 0$). 24
7. Stress-strain curves for specimen 401-S12-MB1-23.526 ($\sigma_3 = 2$ MPa). . . 25
8. Stress-strain curves for specimen 401-S12-MB1-24.205 ($\sigma_3 = 2$ MPa). . . 26
9. Stress-strain curves for specimen 401-S12-MB1-24.690 ($\sigma_3 = 2$ MPa). . . 27
10. Stress-strain curves for specimen 401-S12-MB1-40.215 ($\sigma_3 = 2$ MPa). . . 28
11. Stress-strain curves for specimen 401-S12-MB1-21.553 ($\sigma_3 = 4$ MPa). . . 29
12. Stress-strain curves for specimen 401-S12-MB1-25.055 ($\sigma_3 = 4$ MPa). . . 30
13. Stress-strain curves for specimen 401-S12-MB1-41.178 ($\sigma_3 = 4$ MPa). . 31
14. Stress-strain curves for specimen 401-S12-MB1-21.717 ($\sigma_3 = 6$ MPa). . 32
15. Stress-strain curves for specimen 401-S12-MB1-25.216 ($\sigma_3 = 6$ MPa). . . 33
16. Stress-strain curves for specimen 401-S12-MB1-52.263 ($\sigma_3 = 6$ MPa). . . 34
17. Stress-strain curves for specimen 401-S12-MB1-22.060 ($\sigma_3 = 8$ MPa). . . 35
18. Stress-strain curves for specimen 401-S12-MB1-24.041 ($\sigma_3 = 8$ MPa). . . 36
19. Stress-strain curves for specimen 401-S12-MB1-52.539 ($\sigma_3 = 8$ MPa). . . 37
20. Stress-strain curves for specimen 401-S12-MB1-22.220 ($\sigma_3 = 10$ MPa). . 38
21. Stress-strain curves for specimen 401-S12-MB1-25.538 ($\sigma_3 = 10$ MPa . 39
22. Stress-strain curves for specimen 401-S12-MB1-52.700 ($\sigma_3 = 10$ MPa). . 40
23. Stress-strain curves for specimen 401-S12-MB1-22.382 ($\sigma_3 = 15$ MPa). . 41
24. Stress-strain curves for specimen 401-S12-MB1-25.702 ($\sigma_3 = 15$ MPa). . 42
25. Stress-strain curves for specimen 401-S12-MB1-52.865 ($\sigma_3 = 15$ MPa). . 43
26. Stress-strain curves for specimen 401-S12-MB1-22.547 ($\sigma_3 = 20$ MPa). . 44
27. Stress-strain curves for specimen 401-S12-MB1-25.864 ($\sigma_3 = 20$ MPa). . 45
28. Stress-strain curves for specimen 401-S12-MB1-60.069 ($\sigma_3 = 20$ MPa). . 46
29. Stress-strain curves for specimen 401-S12-MB1-23.045 ($\sigma_3 = 30$ MPa). . 47
30. Stress-strain curves for specimen 401-S12-MB1-27.065 ($\sigma_3 = 30$ MPa). . 48
31. Stress-strain curves for specimen 401-S12-MB1-60.227 ($\sigma_3 = 30$ MPa). . 49
32. Stress-strain curves for specimen 401-S12-MB1-23.205 ($\sigma_3 = 40$ MPa). . 50
33. Stress-strain curves for specimen 401-S12-MB1-27.225 ($\sigma_3 = 40$ MPa). . 51
34. Stress-strain curves for specimen 401-S12-MB1-60.622 ($\sigma_3 = 40$ MPa). . 52
35. Stress-strain curves for specimen 401-S12-MB1-23.364 ($\sigma_3 = 60$ MPa). . 53
36. Stress-strain curves for specimen 401-S12-MB1-27.387 ($\sigma_3 = 60$ MPa). . 54

37. Stress-strain curves for specimen 401-S12-MB1-62.050 ($\sigma_3 = 60$ MPa). . 55
38. Stress versus axial strain curves (Group 1) of grey granite in uniaxial and triaxial compression. 56
39. Stress versus axial strain curves (Group 2) of grey granite in uniaxial and triaxial compression. 57
40. Stress versus axial strain curves (Group 3) of grey granite in uniaxial and triaxial compression. 58
41. Volumetric strain versus axial strain curves (Group 1) of grey granite in uniaxial and triaxial compression. 59
42. Volumetric strain versus axial strain curves (Group 2) of grey granite in uniaxial and triaxial compression. 60
43. Volumetric strain versus axial strain curves (Group 3) of grey granite in uniaxial and triaxial compression. 61
44. Plots of deviator stress at peak strength versus confining pressure. . . . 62
45. Plots of tangent Young's modulus (E) versus confining pressure. 63
46. Plots of Poisson's ratio (ν) versus confining pressure. 64
47. Hoek and Brown failure envelope. 65

INTRODUCTION

The Canadian Nuclear Fuel Waste Management Program (CNFWMP) is concerned with the assessment of the feasibility and safety of the long-term disposal of high level nuclear wastes in vaults located at depth in plutonic rocks. As part of the CNFWMP, AECL Research has constructed the Underground Research Laboratory (URL) in the Lac du Bonnet batholith located in the southeastern part of Manitoba for large-scale geotechnical and hydrogeological investigations. In support of these activities, over the past decade, the Canada Centre for Mineral and Energy Technology (CANMET), in conjunction with AECL Research, has conducted laboratory-scale studies on the mechanical properties of rock samples from the URL and the surrounding rocks (Annor and Jackson, 1987; Jackson et al., 1989; Lau et al., 1991).

Most of the tests carried out previously were standard uniaxial and triaxial compression tests which never reached the post-failure stage. In those tests, rock specimens failed rapidly and often violently when the applied stresses became equal to their compressive strengths. Does this truly represent the mechanical behaviour of the rock surrounding a vault? The hard rock usually retains some strength beyond its peak strength and the rapid failure is due to the rapid release of strain energy from the testing machine. However, by increasing the stiffness of the testing machine and utilizing computer-controlled servo-hydraulics, it is possible to control the brittle rock failure of a rock specimen and examine the region of deformation beyond its peak strength (Rummel and Fairhurst, 1970; Wawersik and Fairhurst, 1970).

On its acquisition of a MTS 815 Rock Test System, laboratory procedures had been developed in CANMET's Canadian Mine Technology Laboratory to conduct post-failure uniaxial and triaxial compression tests (Gorski, 1987). These procedures were used to carry out a study on the post-failure behaviour of the Lac du Bonnet grey granite. The objectives of this study are twofold. Firstly, it is necessary to understand the behaviour of the grey granite beyond its peak strength because faults and macroscopic fractures appear to form in this region, not prior to reaching the peak strength (Wawersik and Fairhurst, 1970; Wawersik and Brace, 1971). Secondly, post-failure tests performed in this study, using cycles of loading and unloading, would provide data for the development of an elastic-brittle-ductile constitutive model for the grey granite, being carried out by the University of Toronto (Ofoegbu and Curran, 1991).

Six post-failure uniaxial compression tests and thirty-one post-failure triaxial compression tests were conducted on core samples of grey granite obtained from borehole 401-S12-MB1 at the 420 Level of the URL. This report presents and discusses the test results, and makes comparisons of these results with those obtained from standard uniaxial and triaxial compression tests.

ROCK TYPE AND SPECIMEN PREPARATION

Samples used in these tests were HQ rock cores obtained from borehole 401-S12-MB1 at the 420 Level of the URL. The rock is a grey, medium- to coarse-grained granite, composed of approximately 30% K-feldspar, 30% plagioclase, 30% or slightly less quartz and 10% or slightly more mafic minerals, mainly biotite.

Specimens were prepared in accordance with the procedure described in the Pit Slope Manual Supplement 3-5 (Gyenge and Ladanyi, 1977) and the method suggested by the International Society for Rock Mechanics (Brown, 1981). The end surfaces of each of the specimens were ground flat to 0.025 mm to ensure that they were parallel to each other and perpendicular to the axis of the specimen.

The lengths, diameters and bulk densities of the specimens are listed in Table 1. It should be noted that in Table 1, the last number in the specimen identification represents the downhole depth of the specimen in metres. The mean bulk density of all the specimens was found to be 2.64 Mg/m^3. Specimen lengths varied from 150.96 to 155.75 mm and diameters varied from 60.60 to 60.95 mm, with length to diameter ratios ranging from 2.49 to 2.56. Table 1 also shows the p-wave velocities measured on the specimens prior to testing. The mean p-wave velocity (3.594 km/s) of these specimens was comparable to that (3.486 km/s) of specimens from borehole 401-009-HF1, also located at the 420 Level of the URL, indicating the presence of microcracks in these specimens (Lau and Gorski, 1990).

TEST APPARATUS AND PROCEDURE

The post-failure uniaxial and triaxial compression tests were conducted using the MTS 815 Rock Mechanics Test System, a computer-controlled, servo-hydraulic compression machine, consisting of a 2.22 MN rated load cell, load frame, hydraulic power supply, triaxial cell, confining pressure subsystem, test controller, test processor and DEC micro PDP 11/73 computer. The triaxial cell is equipped with three linear variable differential transducers (LVDTs) for the measurement of axial strain and an extensometer with a circumferential kit for the measurement of circumferential strain. For a detailed description of the MTS system and its operation, the reader is referred to the

MTS Operation Manual (MTS Systems Corp., 1986) and CANMET Division Report MRL 87-33(INT) (Gorski, 1987).

The procedures to conduct the post-failure uniaxial and triaxial compression tests were similar, except that in the triaxial test, the confining pressure and the axial stress were first increased from zero, at the same rate of 0.75 MPa/s, until the desired value of confining pressure (equilibrium pressure) was attained. The test (uniaxial or triaxial) began under the load control mode. The axial stress was increased at a rate of 0.75 MPa/s until the axial load was 60 kN greater than the equilibrium load. The control mode was then switched over to the axial strain control. The test continued under the axial strain control mode at a rate approximating an axial stress rate of 0.75 MPa/s. Analog signals from the load cell, LVDTs, extensometer and confining pressure subsystem were scanned every 3 seconds and the data were stored on hard disk in the PDP 11/73 computer. A real time plot of load versus axial displacement was obtained using a Kipp & Zonen pen recorder wired to the test controller. Unloading-reloading cycles were performed at 40 MPa increments of axial stress. Each unloading sequence consisted of reducing the axial stress to a value slightly above the confining pressure. After the axial stress had reached approximately 75% of the estimated peak strength, unloading was performed at 0.063 mm increments of circumferential deformation.

As the peak strength of the specimen was approached, special care was taken to prevent rapid failure in order to continue the test into the post-failure region. The MTS system was programmed in such a way that whenever it detected a drop in axial load (initial failure occurred), the system would immediately unload to a point where the axial strain was reduced by 20%. The system then started to reload again until another drop in axial load was detected. It should be noted that at this stage of the test, unloading-reloading cycles were also performed at 0.063 mm increments of circumferential deformation. The process was repeated until the residual strength of the specimen was attained or the uncontrolled failure of the specimen occurred.

After the test had been terminated, the data were transferred to the VAX 750 computer for data storage and analysis. Plots of axial stress versus axial strain and axial stress versus circumferential strain were obtained from a DEC LVP16 pen plotter connected to the PDP 11/73 computer.

TEST PROGRAM AND RESULTS

Testing for this study took place from November, 1990 to February, 1991 at Canadian Mine Technology Laboratory, Mining Research Laboratories, CANMET, Energy, Mines and Resources Canada in Ottawa. The program consisted of eleven sets of tests conducted under the unconfined condition and at the confining pressures of 2, 4, 6, 8, 10, 15, 20, 30, 40 and 60 MPa. Thirty-seven specimens were tested: 6 specimens in uniaxial and 31 specimens in triaxial compression. At least three specimens were tested at each confining pressure.

Tests were conducted using cycles of loading and unloading. The loading and unloading curves for each test are presented in Appendix A. These plots were obtained directly from the DEC LVP16 pen plotter. The envelopes to the loading and unloading curves for each test, illustrated in Figures 1 to 37, were plotted using DATAPLOT curve fitting computer software. A cubic spline fit was used for this analysis which employed a third degree equation model of the form:

$$\sigma = a_0 + a_1\varepsilon + a_2\varepsilon^2 + a_3\varepsilon^3 \tag{1}$$

where σ = stress
ε = strain
and a_0, a_1, a_2 and a_3 are coefficients

These envelopes will be referred to as stress-strain curves in this report. Plots of stress versus volumetric strain are also shown in those figures. Volumetric strain was computed by using the following equation:

$$\varepsilon_v = \varepsilon_a + 2\varepsilon_c \tag{2}$$

where ε_v = volumetric strain
ε_a = axial strain
ε_r = circumferential strain

For each specimen, the deviator stress ($(\sigma_1 - \sigma_3)_p$), axial strain (ε_{ap}) and volumetric strain (ε_{vp}) at the point of peak strength were measured from the stress-strain curves (Figs. 1 to 37). The deviator stress ($(\sigma_1-\sigma_3)_u$), axial strain (ε_{au}) and volumetric strain (ε_{vu}) at the termination of the test were also measured. The tangent Young's modulus (E) and Poisson's ratio (ν) were determined from the stress-strain curves. The unloading stiffness (E_p) and Poisson's ratio (ν_p) of the specimen immediately after the peak strength was attained were determined from the corresponding unloading curves (Appendix A). These values are given in Table 2.

DISCUSSION

STRESS-STRAIN OBSERVATIONS

Uniaxial Compression

Figures 1 to 6 show the stress-strain characteristics for the grey granite under uniaxial compression. In general, the stress-strain curve (axial strain) from zero deviator stress to peak strength may be divided into three regions. The first one is characterized by a steadily increasing slope, indicating the closure of microcracks in the specimen. The second (middle) region is nearly linear, typical for the brittle rock. In the third region, the slope decreases and reaches zero at peak strength, signalling crack growth and sliding on existing crack interfaces. The post-failure behaviour is marked by regions of abrupt drop in stress and regions of more gentle drop, indicating the formation of small fractures and spalling. The axial strains recorded at the termination of the uniaxial tests were very close to those measured at peak strength (see Table 2). The Lac du Bonnet grey granite exhibited class II rock behaviour. Failure for class II rock behaviour is self-sustaining (Wawersik and Fairhurst, 1970). The elastic strain energy stored in the specimen when the applied stress is equal to the compressive strength is sufficient to maintain fracture propagation until the specimen has lost its load-carrying ability.

The stress-strain curve for the circumferential strain is nearly linear from zero deviator stress to a stress level equivalent to 35 - 40% of the peak strength. The slope of the curve then starts to decrease, suggesting the development of axial cracks in the specimen and possibly the onset of dilation. The slope reaches zero at peak strength. In the post-failure region, the circumferential strain increased rapidly due to the formation of small axial fractures and spalling in the specimen.

Failure development and the eventual disintegration of the specimen can be illustrated using the plot of stress versus volumetric strain. The slope of the curve increases at an increasing rate from zero deviator stress to a stress level equal to 65 - 85% of the peak strength where it reaches its maximum value (infinity). Then, the slope becomes negative, indicating that the specimen was dilating. The slope decreases at an increasing rate and reaches zero at peak strength. This means the maximum rate of cracking occurred at peak strength. At the same time, it can be seen from Table 2 that the Poisson's ratio (ν_p) at peak strength is considerably greater than that (ν) at 50% of the peak strength. In the post-failure region, the volumetric strain increased rapidly as the strength of the specimen decreased, signalling the disintegration of the specimen.

Triaxial Compression

The stress-strain curves, including axial strain, circumferential strain and volumetric strain, for tests performed under triaxial compression are illustrated in Figures 7 to 37. Although there are strong similarities between these curves and those for uniaxial tests, two differences are distinguishable. Progressive increases in post-failure axial strain and decreases in post-failure circumferential and volumetric strains can be observed with increasing confining pressure. The stress-strain (axial strain) curves are divided into three groups and plotted in Figures 38 to 40 respectively to illustrate the effect of the confining pressure on the stress-strain curves. From these plots, it can be seen that there is a progressive slight flattening of the stress-strain curves with increasing confining pressure.

Figures 7 to 37 show that for confined compression tests, the stress-strain (circumferential) curves start to deviate from linear elasticity at stress levels equivalent to 35 - 45% of the peak strengths, just slightly higher than those for unaxial compression tests. This is not surprising because the growth of cracks in the specimen was suppressed by the confining pressure. Whereas, the slopes of the stress-strain (volumetric) curves reach their maximum values and become negative at stress levels equal to 60 - 75% of the peak strengths, slightly lower than those for uniaxial compression tests.

The sequence of events which governed the failure development at low confining pressures was similar to that observed in the uniaxial tests, with localized fractures forming more or less parallel to the core axis. However, as the confining presure increased, the size of these fractures became smaller and local shear failure developed. For the three groups of tests presented in Figures 38 to 40, the corresponding volumetric strains are plotted against the axial strains in Figures 41 to 43 respectively. The change of failure mechanisms is evident in those plots where reductions in dilation were observed with increasing confining pressure (also see Table 2).

PEAK STRENGTH

The peak strengths of these specimens are defined as the maximum compressive strengths attained in the tests. The deviator stresses at peak strength are plotted against the confining pressures in Figure 44. The solid line joins the mean deviator stresses and shows that the deviator stress at peak strength increased with confining pressure. Results from a previous study on the same rock from borehole 401-009-HF1 (Lau and Gorski, 1990), located at the vicinity of borehole 401-S12-MB1, are also plotted in Figure 44. The dashed line represents the mean values from that borehole. It can be seen that specimens from borehole 401-009-HF1 were consistently stronger than those from borehole 401-S12-MB1. Whether this is the result of using different testing methods (standard uniaxial and triaxial tests versus post-failure uniaxial and triaxial tests) or rock anisotropy (401-009-HF1 is vertical whereas 401-S12-MB1 is horizontal) or the effect of size (45-mm versus 61-mm-diameter) is not clear. Further research is needed.

RESIDUAL STRENGTH

These tests were programmed to continue into the post-failure region until the residual strengths were attained. However, uncontrolled failure occurred in most tests before the residual strengths were reached. Residual strengths appeared to be attained in only a few tests (see Figs. 38-41 and Table 2) and their values were somewhere between 20 and 40 MPa.

FAILURE MODE

The failure angle θ (angle between the failure plane and the core axis) and failure characteristics of the specimens are shown in Table 3. Under uniaxial compression, axial cracks developed in the specimens. Slabbing by buckling also occurred in three specimens. Under confined compression, shear fractures developed, sometimes with splays and cracks, and sometimes in the form of conjugate fractures. The failure angles appeared to be slightly greater for specimens tested at confining pressures ranging from 2 to 20 MPa than those tested between 30 and 60 MPa confining pressure. It should be noted that for specimen 401-S12-MB1-62.050, the test was abruptly ended when the disk in the PDP 11/73 computer became full, and therefore no failure occurred in the specimen.

TANGENT YOUNG'S MODULUS

The tangent Young's modulus (E) for each of the specimens was computed from the stress-strain curve at the stress level equal to $0.5(\sigma_1 - \sigma_3)_p$, and is presented in Table 2. The tangent modulus was determined by substituting the axial strain value at $0.5(\sigma_1 - \sigma_3)_p$ into the derivative of the best-fit equation (Eq. 1) representing the stress-strain curve.

Figure 45 reveals the effect of confining pressure on the tangent modulus. The modulus increased as the confining pressure increased from 0 to 8 MPa, suggesting that some stress relaxation had occurred in these specimens, resulting in higher crack porosities, larger deformations and lower modulus values at low confining pressures. This agrees with the results from previous studies (Lau et al., 1991). The modulus dropped slightly when the confining pressure was raised from 8 to 15 MPa and then rose again, and remained fairly constant above the confining pressure of 30 MPa. Modulus values obtained from borehole 401-009-HF1 are also plotted in Figure 45, and can be seen to be higher than those from borehole 401-S12-MB1 under the unconfined condition and at confining pressures above 15 MPa. Again, further research is required to explain the discrepancy.

The unloading stiffness (E_p) immediately after the peak strength had been attained was also determined for each specimen (see Table 2). The values of E_p were found to be lower than those of E under triaxial compression. The reduction in stiffness at peak strength was a result of crack growth in the specimens. However, it is somewhat surprising to see the values of E_p higher than those of E under uniaxial compression.

POISSON'S RATIO

Poisson's ratio was determined from the ratio of the circumferential to the axial tangent moduli at the stress level equivalent to $0.5(\sigma_1 - \sigma_3)_p$. The Poisson's ratios ($\nu$) are presented in Table 2 and are plotted with their mean values (solid line) against the confining pressure in Figure 46. The plot shows that there was a sharp rise in Poisson's ratio when the confining pressure was increased from 0 to 2 MPa, indicating the presence of microcracks in these specimens. Above that, the Poisson's ratio decreased slightly with increasing confining pressure. Poisson's ratios from borehole 401-009-HF1 and their mean values (dash line) are also plotted in Figure 46. The same discrepancy seen in Figure 45 is evident here.

For each specimen, Poisson's ratio was also determined from the unloading curve after the peak strength had been attained. These values (ν_p) were found to be significantly higher than the values of ν, suggesting that the rate of cracking at peak strength was much higher than that at $0.5(\sigma_1 - \sigma_3)_p$.

FAILURE CRITERION

The strength properties of intact rock can be expressed in terms of the Hoek and Brown failure criterion. The empirical relationship developed by Hoek and Brown (1980) between the principal stresses associated with the failure of a rock is given as follows:

$$\sigma_1 = \sigma_3 + \sqrt{m\sigma_c\sigma_3 + s\sigma_c^2} \qquad (3)$$

where σ_1 = major principal stress at failure
σ_3 = minor principal stress applied to the rock sample
σ_c = uniaxial compressive strength of the intact rock material in the specimen
m and s are constants and for these intact rock specimens, $s = 1$

In order to use this failure criterion, failure is assumed to occur at peak strength in these tests. By using the equations suggested by Hoek and Brown (1980), the predicted uniaxial compressive strength of the intact rock material, σ_c, and the material constant, m, for the grey granite were found to be 157 MPa and 35.28 respectively. The failure envelope developed by using these values of σ_c and m is illustrated in Figure 47. These values are considerably lower than those obtained from borehole 401-009-HF1 ($\sigma_c = 178$ MPa, $m = 42.60$). Again, further research is needed to investigate this discrepancy.

CONCLUSIONS

The results of these tests have provided some stress and strain data from zero deviator stress to peak strengths and continuing into the post-failure regions for the development of an elastic-brittle-ductile constitutive model for the Lac du Bonnet grey granite. They have also provided some insight into the behaviour of the grey granite in the post-failure region. The rock exhibited class II behaviour. This implies that in situ fracturing in the grey granite could proceed unstably with the release of considerable amount of strain energy and violent failure might occur, should the peak strength be exceeded. From the results, the following conclusions can be made.

For the uniaxial compression tests, the stress-strain (axial) curves from zero load to peak strength are marked progressively by regions of increasing slope, linear elasticity and decreasing slope. The post-failure regions are characterized by a series of abrupt and gentle drops in stress. The development of axial cracks in the specimens appeared to start at the stress level equivalent to 35 - 40% of the peak strength, suggesting the onset of dilation. The maximum rate of cracking occurred at peak strength. In the post-failure regions, the specimens dilated rapidly, accompanied by slabbing, indicating the disintegration of the specimens.

For the confined compression tests, the stress-strain curves show similar patterns. However, progressive increases in the post-failure axial strain and decreases in the post-failure circumferential and volumetric strains could be observed with increasing confining pressure. The development of cracks in the specimens appeared to start at a stress level equal to 35 - 45% of the peak strength. Growth of cracks was also indicated by the reduction in stiffness at peak strength. Shear fractures developed in the specimens. The angle between the failure plane and the core axis appeared to be slightly greater at higher confining pressure.

Residual strengths appeared to be attained in only a few tests and their values were somewhere between 20 and 40 MPa.

The effects of confining pressure on the mechanical properties of the rock were similar to those observed in standard uniaxial and triaxial compression tests. The deviator stress at peak strength was found to increase with confining pressure. The tangent Young's modulus increased with increasing confining pressure from 0 to 8 MPa, indicating the presence of microcracks in these specimens. Above 8 MPa, the confining pressure appeared to have little effect on the modulus. Poisson's ratio increased only when the confining pressure was raised from 0 to 2 MPa. Above that, Poisson's ratio decreased slightly with increasing confining pressure. It should be noted that all these values are lower than those obtained from standard uniaxial and triaxial tests on core samples of the same rock from borehole 401-009-HF1, located at the vicinity of borehole 401-S12-MB1.

A failure envelope was developed by using the Hoek and Brown failure criterion. The predicted uniaxial compressive strength, σ_c and the material constant, m, were found to be 157 MPa and 35.28 respectively.

RECOMMENDATIONS

One of the main rock mechanics issues related to the construction and operation of the URL is experimentally identifying the post-failure strength and deformation characteristics of the host rock. This post-failure uniaxial and triaxial compression testing program has addressed this issue and is recommended for the URL characterization program during the operating phase of the URL and for any future site selection program if the disposal concept is deemed acceptable.

Although results obtained from this testing program have shed some light on the post-failure behaviour of the Lac du Bonnet grey granite, very few data on the residual strength of the rock were obtained from the tests due to uncontrolled failure of the specimens before the residual strength was reached. Further research on experimental technique is required to prevent premature failure before the residual strength is reached.

The strength and stiffness of the grey granite from borehole 401-S12-MB1 (horizontal) were found to be consistently lower than those from borehole 401-009-HF1 (vertical) located in the same area at the URL. Is this the result of using different testing methods, or rock anisotropy, or specimen size effect or the combination of them? Further research is needed to address these questions.

ACKNOWLEDGEMENTS

The authors wish to express their thanks to R. Jackson of CANMET for reviewing this report and making several helpful suggestions. Gratitude is expressed to J. Folta of CANMET for the preparation of specimens and for carrying out the compression wave velocity measurements on the specimens.

REFERENCES

Annor, A. and Jackson, R. (1987), "Mechanical, thermomechanical and joint properties of rock samples from the Lac du Bonnet Batholith, Manitoba" in Geotechnical studies at Whiteshell Research Area (RA-3) (edited by Katsube, T.J. and Hume, J.P.), Divisional Report MRL 87-52(TR), CANMET, Energy, Mines and Resources Canada, p. 49-110.

Brown, E.T. (1981), "Rock characterization testing and monitoring, ISRM suggested methods", International Society for Rock Mechanics, the Commission on Testing Methods, Pergamon, 211 p.

Gorski, B. (1987), "Post-failure uniaxial strength determinations using a servo-hydraulic test system", Division Report MRL 87-33(INT), CANMET, Energy, Mines and Resources Canada, 77 p.

Gyenge, M. and Ladanyi, B. (1977), "Pit slope manual supplement 3-5 - sampling and specimen preparation", CANMET, Report 77-29, 30 p.

Hoek, E. and Brown, E.T. (1980), "Underground excavations in rock", The Institution of Mining and Metallurgy, London, 527 p.

Jackson, R., Lau, J.S.O. and Annor, A. (1989), "Mechanical, thermo-mechanical and joint properties of rock samples from the site of AECL's Underground Research Laboratory, Lac du Bonnet, Manitoba", in Proceedings of the 42nd Canadian Geotechnical Conference, Winnipeg, Manitoba, October 23-25, 1989, p. 41-49.

Lau, J.S.O. and Gorski, B. (1990), "High temperature uniaxial and triaxial compression tests on URL rock samples from borehole 401-009-HF1", Divisional Report MRL 90-5(TR), CANMET, Energy, Mines and Resources Canada, 91 p.

Lau, J.S.O., Jackson, R. and Gorski, B. (1991), "The effects of temperature and pressure on the mechanical properties of Lac du Bonnet grey granite", in Proceedings of the 32nd U.S. Symposium on Rock Mechanics, Norman, Oklahoma, July 10-12, 1991, p. 313-323.

MTS Systems Corporation (1986), "Operation manual for 815 rock mechanics test systems", MTS Systems Corp., Minneapolis, Minnesota, U.S.A.

Ofoegbu, G.I. and Curran, J.H. (1991), "Development and numerical implementation of an elastic-brittle-ductile constitutive model for intact rock", Department of Civil Engineering, University of Toronto, Publication 91-01, 106 p.

Rummel, F. and Fairhurst, C (1970), "Determination of the post-failure behaviour of brittle rock using a servo-controlled testing machine", Rock Mechanics, Vol. 2, p. 189-204.

Wawersik, W.R. and Fairhurst, C. (1970), "A study of brittle rock fracture in laboratory compression experiments", Int. J. Rock Mech. Min. Sci., Vol. 7, p. 561-575.

Wawersik, W.R. and Brace, W.F. (1971),"Post-failure behaviour of a granite and diabase", Rock Mechanics, Vo. 3, p. 61-85.

Table 1. Dimensions, densities and p-wave velocities of rock specimens.

Specimen *identification*	Length (mm)	Diameter (mm)	Bulk density (Mg/m^3)	P-wave velocity (km/s)
401-S12-MB1-21.065	153.37	60.77	2.64	3.893
401-S12-MB1-21.227	154.26	60.77	2.64	3.895
401-S12-MB1-21.553	153.55	60.70	2.63	3.988
401-S12-MB1-21.717	154.17	60.60	2.63	2.942
401-S12-MB1-22.060	154.09	60.62	2.64	3.251
401-S12-MB1-22.220	152.58	60.66	2.65	3.815
401-S12-MB1-22.382	153.52	60.64	2.65	3.998
401-S12-MB1-22.547	153.15	60.70	2.64	3.681
401-S12-MB1-23.045	154.50	60.67	2.65	4.023
401-S12-MB1-23.205	153.54	60.70	2.65	3.656
401-S12-MB1-23.364	155.02	60.79	2.64	3.691
401-S12-MB1-23.526	154.59	60.75	2.65	3.117
401-S12-MB1-24.041	154.23	60.75	2.65	3.148
401-S12-MB1-24.205	154.23	60.77	2.65	3.254
401-S12-MB1-24.366	153.70	60.80	2.65	2.990
401-S12-MB1-24.690	153.14	60.85	2.64	3.441
401-S12-MB1-25.055	153.19	60.85	2.65	3.404
401-S12-MB1-25.216	154.04	60.88	2.64	2.962
401-S12-MB1-25.538	154.65	60.93	2.64	3.235
401-S12-MB1-25.702	154.54	60.91	2.65	3.260
401-S12-MB1-25.864	154.27	60.87	2.65	3.311
401-S12-MB1-27.065	154.71	60.92	2.66	3.887
401-S12-MB1-27.225	154.22	60.93	2.64	3.338
401-S12-MB1-27.387	154.34	60.95	2.64	3.312
401-S12-MB1-27.547	152.52	60.94	2.63	3.330
401-S12-MB1-29.645	153.69	60.89	2.65	3.730
401-S12-MB1-40.053	154.06	60.80	2.64	4.478
401-S12-MB1-40.215	155.75	60.82	2.64	4.209
401-S12-MB1-41.178	150.96	60.72	2.64	4.193
401-S12-MB1-52.263	154.44	60.82	2.64	3.302
401-S12-MB1-52.539	153.96	60.80	2.64	3.079
401-S12-MB1-52.700	152.63	60.78	2.64	3.797
401-S12-MB1-52.865	154.66	60.78	2.64	3.966
401-S12-MB1-60.069	154.63	60.82	2.64	3.735
401-S12-MB1-60.227	153.63	60.88	2.64	3.675
401-S12-MB1-60.622	154.92	60.87	2.64	4.142
401-S12-MB1-62.050	153.00	60.72	2.62	3.844
Mean			2.64	3.594
Standard deviation			0.08	0.399

Table 2. Results of post-failure uniaxial and triaxial compression tests.

Specimen Identification	σ_3	Deviator Stress		Axial Strain		Volumetric Strain		Young's Modulus		Poisson's Ratio	
		$(\sigma_1 - \sigma_3)_p$	$(\sigma_1 - \sigma_3)_u$	ε_{ap}	ε_{au}	ε_{vp}	ε_{vu}	E	E_p	ν	ν_p
	(MPa)	(MPa)	(MPa)	(10^{-2})	(10^{-2})	(10^{-2})	(10^{-2})	(GPa)	(GPa)		
401-S12-MB1-21.065	0	154	28	0.428	0.400	-0.121	-4.040	50.96	56.53	0.23	0.55
401-S12-MB1-24.366	0	135	42	0.454	0.494	-0.018	-4.594	44.30	52.33	0.31	0.47
401-S12-MB1-29.645	0	142	20	0.404	0.388	-0.011	-3.320	49.38	57.16	0.31	0.49
401-S12-MB1-21.227	0	151	85	0.426	0.417	0.017	-3.820	50.13	56.68	0.22	0.35
401-S12-MB1-27.547	0	137	75	0.425	0.446	-0.001	-4.445	46.39	54.27	0.24	0.32
401-S12-MB1-40.053	0	143	82	0.388	0.389	0.032	-4.908	50.50	56.93	0.24	0.30
401-S12-MB1-23.526	2	171	68	0.456	0.627	-0.711	-4.348	55.13	55.68	0.39	1.53
401-S12-MB1-24.205	2	184	52	0.460	0.595	-0.292	-2.782	56.34	60.29	0.39	0.92
401-S12-MB1-24.690	2	173	86	0.477	0.539	-0.447	-2.282	54.21	57.97	0.36	1.18
401-S12-MB1-40.215	2	185	40	0.405	0.529	-0.299	-2.597	61.22	63.24	0.39	0.97
401-S12-MB1-21.553	4	223	43	0.468	0.600	-0.517	-1.263	63.81	61.53	0.37	1.28
401-S12-MB1-25.055	4	213	62	0.487	0.697	-0.494	-2.352	59.68	59.62	0.38	1.22
401-S12-MB1-41.178	4	214	41	0.460	0.572	-0.612	-1.589	63.96	60.07	0.36	1.43

Table 2 - (Cont'd)

Specimen Identification	σ_3	Deviator Stress		Axial Strain		Volumetric Strain		Young's Modulus		Poisson's Ratio	
	(MPa)	$(\sigma_1 - \sigma_3)_p$ (MPa)	$(\sigma_1 - \sigma_3)_u$ (MPa)	ε_{ap} (10^{-2})	ε_{au} (10^{-2})	ε_{vp} (10^{-2})	ε_{vu} (10^{-2})	E (GPa)	E_p (GPa)	ν	ν_p
401-S12-MB1-21.717	6	245	73	0.499	0.693	-0.493	-1.824	63.74	62.38	0.39	1.13
401-S12-MB1-25.216	6	237	71	0.510	0.597	-0.568	-2.070	62.87	60.13	0.34	1.33
401-S12-MB1-52.263	6	247	68	0.487	0.588	-0.470	-2.091	65.00	62.79	0.40	1.14
401-S12-MB1-22.060	8	275	58	0.541	0.714	-0.638	-1.459	65.97	61.28	0.33	1.34
401-S12-MB1-24.041	8	265	112	0.533	0.738	-0.570	-2.584	64.86	61.73	0.40	1.18
401-S12-MB1-52.539	8	273	103	0.523	0.722	-0.449	-2.469	66.52	63.45	0.38	1.13
401-S12-MB1-22.220	10	280	76	0.552	0.622	-0.673	-1.771	66.06	61.20	0.40	1.31
401-S12-MB1-25.538	10	285	77	0.572	0.767	-0.581	-1.771	64.74	61.31	0.37	1.20
401-S12-MB1-52.700	10	293	88	0.599	0.656	-0.477	-1.393	60.46	56.22	0.35	1.02
401-S12-MB1-22.382	15	329	122	0.685	0.730	-0.506	-1.624	59.49	55.86	0.36	0.97
401-S12-MB1-25.702	15	328	181	0.684	0.736	-0.501	-1.492	59.98	56.20	0.34	0.97
401-S12-MB1-52.865	15	338	66	0.674	0.872	-0.367	-1.161	61.34	57.58	0.33	0.91

Table 2 - (Cont'd)

Specimen Identification	σ_3	Deviator Stress		Axial Strain		Volumetric Strain		Young's Modulus		Poisson's Ratio	
	(MPa)	$(\sigma_1 - \sigma_3)_p$ (MPa)	$(\sigma_1 - \sigma_3)_u$ (MPa)	ε_{ap} (10^{-2})	ε_{au} (10^{-2})	ε_{vp} (10^{-2})	ε_{vu} (10^{-2})	E (GPa)	E_p (GPa)	ν	ν_p
401-S12-MB1-22.547	20	372	119	0.730	0.955	-0.356	-0.715	61.40	57.73	0.36	0.81
401-S12-MB1-25[illegible]	20	371	172	0.747	0.823	-0.485	-1.733	60.98	58.07	0.36	0.86
401-S12-MB1-60.[illegible]	20	[illegible]	149	0.728	0.790	-0.384	-1.264	61.02	57.89	0.37	0.83
401-S12-MB1-23.045	30	438	233	0.810	0.871	-0.261	-1.290	62.66	60.64	0.36	0.70
401-S12-MB1-27.065	30	433	116	0.812	0.721	-0.291	-0.809	62.91	60.60	0.34	0.70
401-S12-MB1-60.227	30	451	332	0.811	0.845	-0.149	-1.111	64.00	61.52	0.33	0.64
401-S12-MB1-23.205	40	489	300	0.904	0.967	-0.258	-1.053	62.78	61.16	0.35	0.64
401-S12-MB1-27.225	40	490	472	0.891	0.912	-0.212	-0.508	63.19	61.69	0.34	0.62
401-S12-MB1-60.622	40	504	390	0.892	0.985	-0.089	-0.981	64.09	62.17	0.31	0.60
401-S12-MB1-23.364	60	587	574	1.079	1.113	-0.209	-0.435	63.71	62.85	0.34	0.56
401-S12-MB1-27.387	60	580	525	1.044	1.018	-0.109	-0.350	63.93	63.97	0.34	0.54
401-S12-MB1-[illegible]	60	[illegible]	570	1.090	1.093	-0.113	-0.377	64.32	63.63	0.34	0.54

Table 3. Failure Characteristics of rock specimens.

Specimen Identification	σ_3 (MPa)	θ (degree)	Failure Characteristics
401-S12-MB1-21.065	0		multiple axial cracks
401-S12-MB1-24.366	0		multiple axial cracks
401-S12-MB1-29.645	0		multiple axial cracks
401-S12-MB1-21.227	0		multiple axial cracks, slabs
401-S12-MB1-27.547	0		multiple axial cracks, slabs
401-S12-MB1-40.053	0		multiple axial cracks, slabs
401-S12-MB1-23.526	2		multiple cracks
401-S12-MB1-24.205	2	20	conjugate fractures
401-S12-MB1-24.690	2	20	conjugate fractures
401-S12-MB1-40.215	2	20	shear fracture
401-S12-MB1-21.553	4	15	shear fracture
401-S12-MB1-25.055	4	20	shear fracture, splays
401-S12-MB1-41.178	4	20	shear fracture
401-S12-MB1-21.717	6	18	conjugate fractures
401-S12-MB1-25.216	6	20	conjugate fractures
401-S12-MB1-52.263	6	18	conjugate fractures
401-S12-MB1-22.060	8	20	shear fracture
401-S12-MB1-24.041	8	25	shear fracture, splays
401-S12-MB1-52.539	8	20	conjugate fractures
401-S12-MB1-22.220	10	17	conjugate fractures, splays
401-S12-MB1-25.538	10	20	shear fracture
401-S12-MB1-52.700	10	23	shear fracture
401-S12-MB1-22.382	15	20	shear fracture, splays
401-S12-MB1-25.702	15	23	shear fracture
401-S12-MB1-52.865	15	23	shear fracture
401-S12-MB1-22.547	20	15	shear fracture, multiple cracks
401-S12-MB1-25.864	20	25	shear fracture, multiple cracks
401-S12-MB1-60.069	20	15	shear fracture, multiple cracks
401-S12-MB1-23.045	30	20	shear fracture, splays
401-S12-MB1-27.065	30	22	shear fracture
401-S12-MB1-60.227	30	20	shear fracture, multiple cracks
401-S12-MB1-23.205	40	27	shear fracture, multiple cracks
401-S12-MB1-27.225	40	25	shear fracture, splays
401-S12-MB1-60.622	40	25	conjugate fractures, cracks
401-S12-MB1-23.364	60	20	shear fracture
401-S12-MB1-27.387	60	30	shear fracture
401-S12-MB1-62.050	60		Failure did not occur.

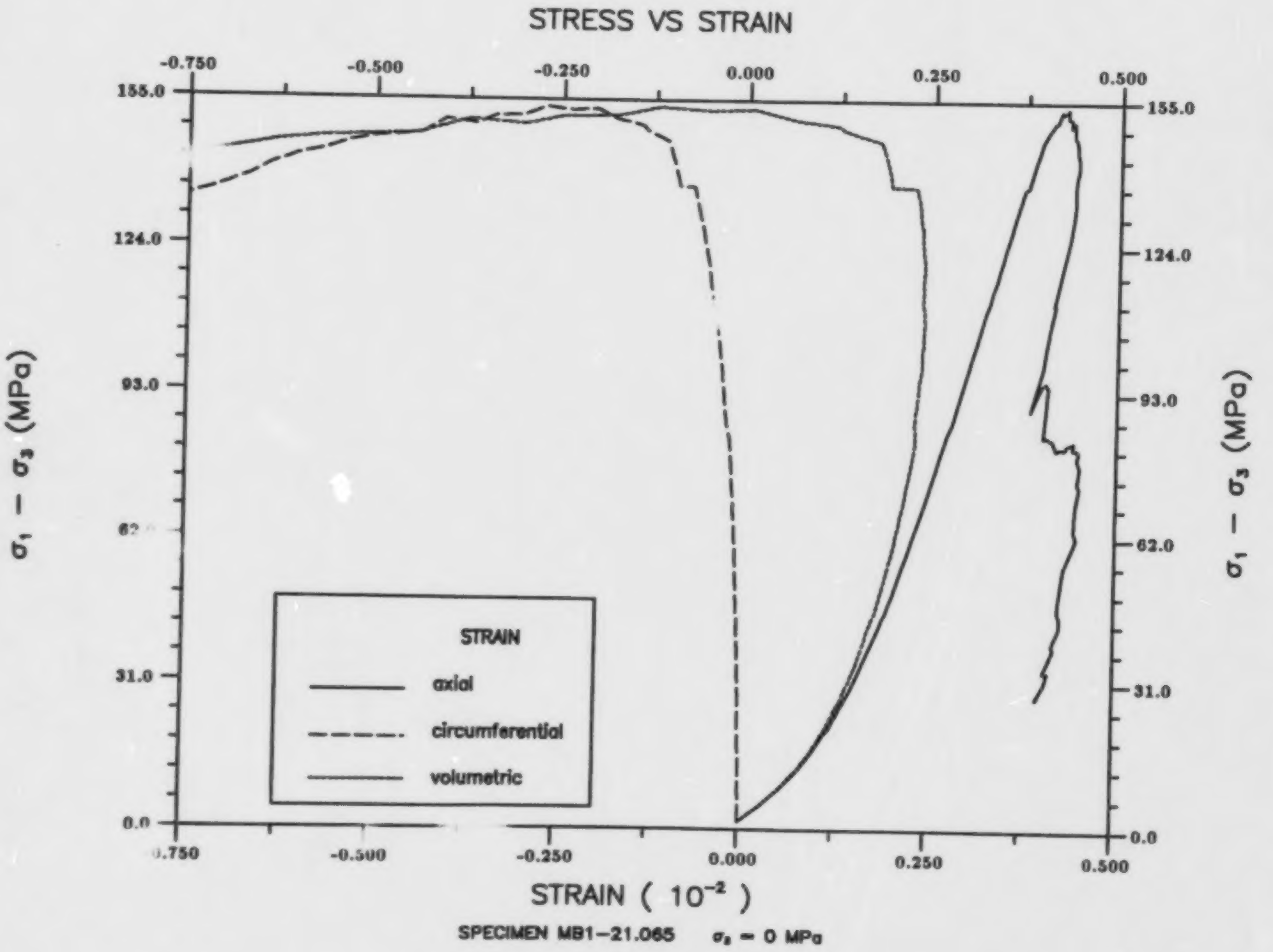

Figure 1. Stress-strain curves for specimen 401-S12-MB1-21.065 ($\sigma_3 = 0$).

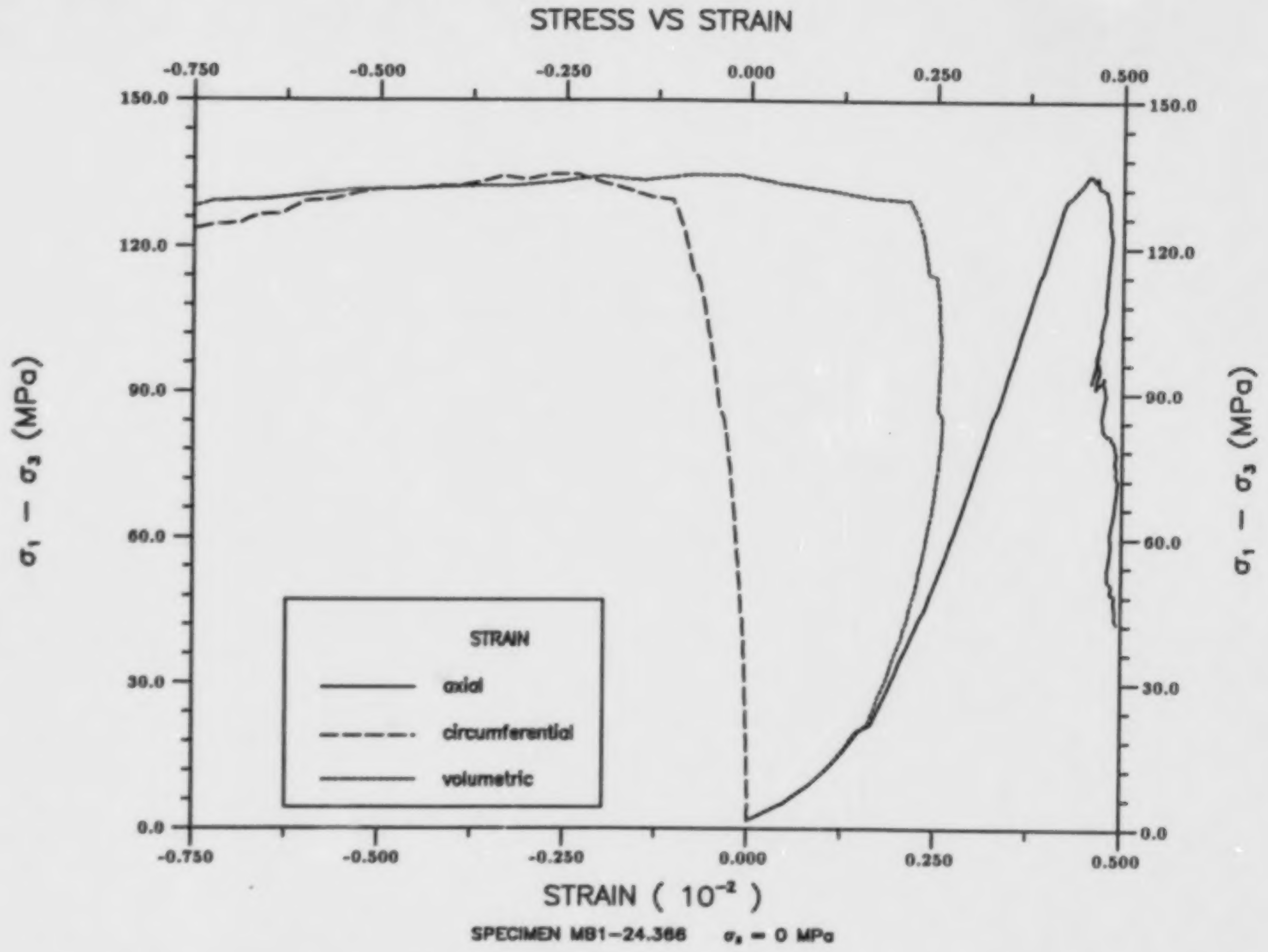

Figure 2. Stress-strain curves for specimen 401-S12-MB1-24.366 ($\sigma_3 = 0$).

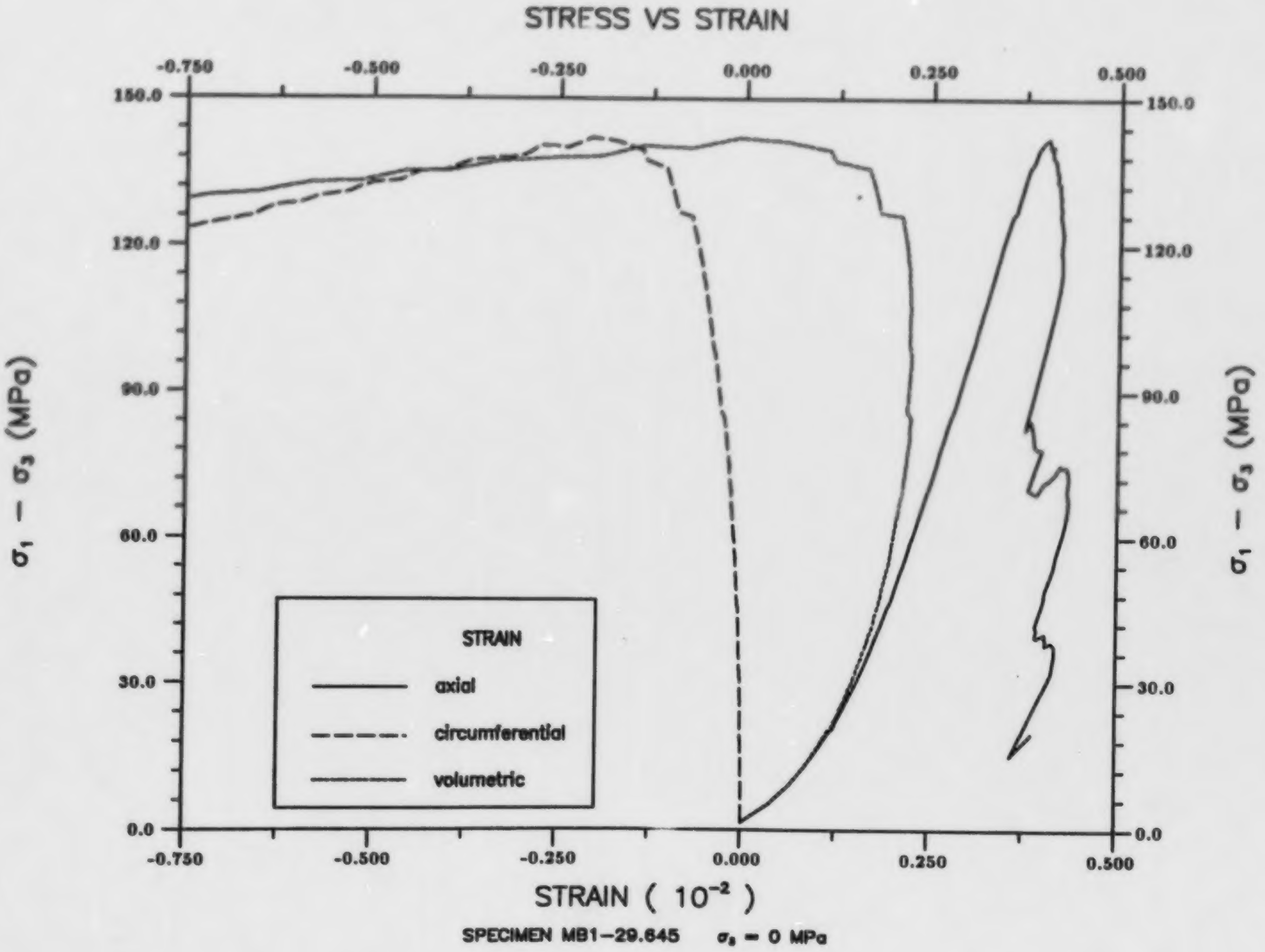

Figure 3. Stress-strain curves for specimen 401-S12-MB1-29.645 ($\sigma_3 = 0$).

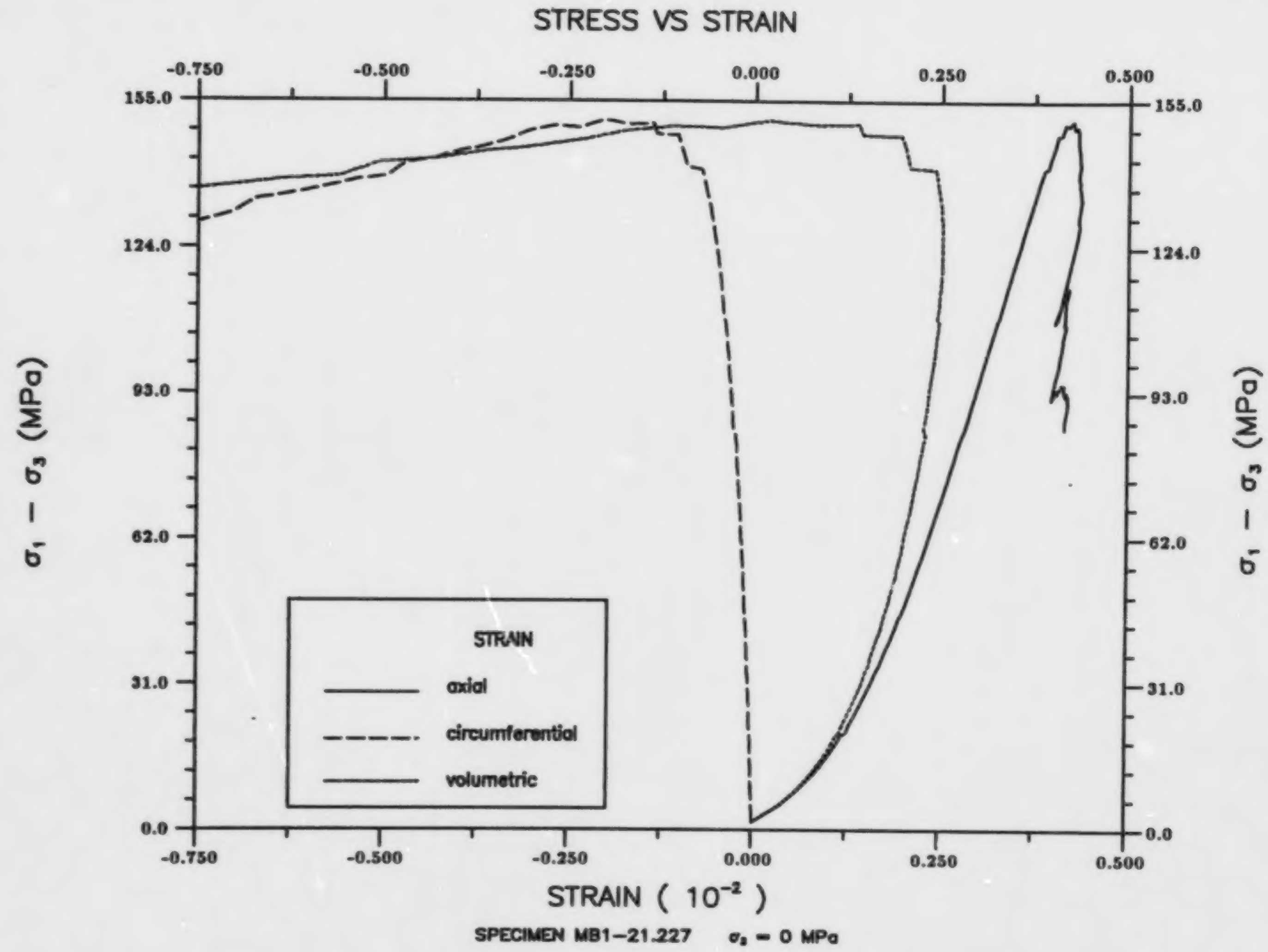

Figure 4. Stress-strain curves for specimen 401-S12-MB1-21.227 ($\sigma_3 = 0$).

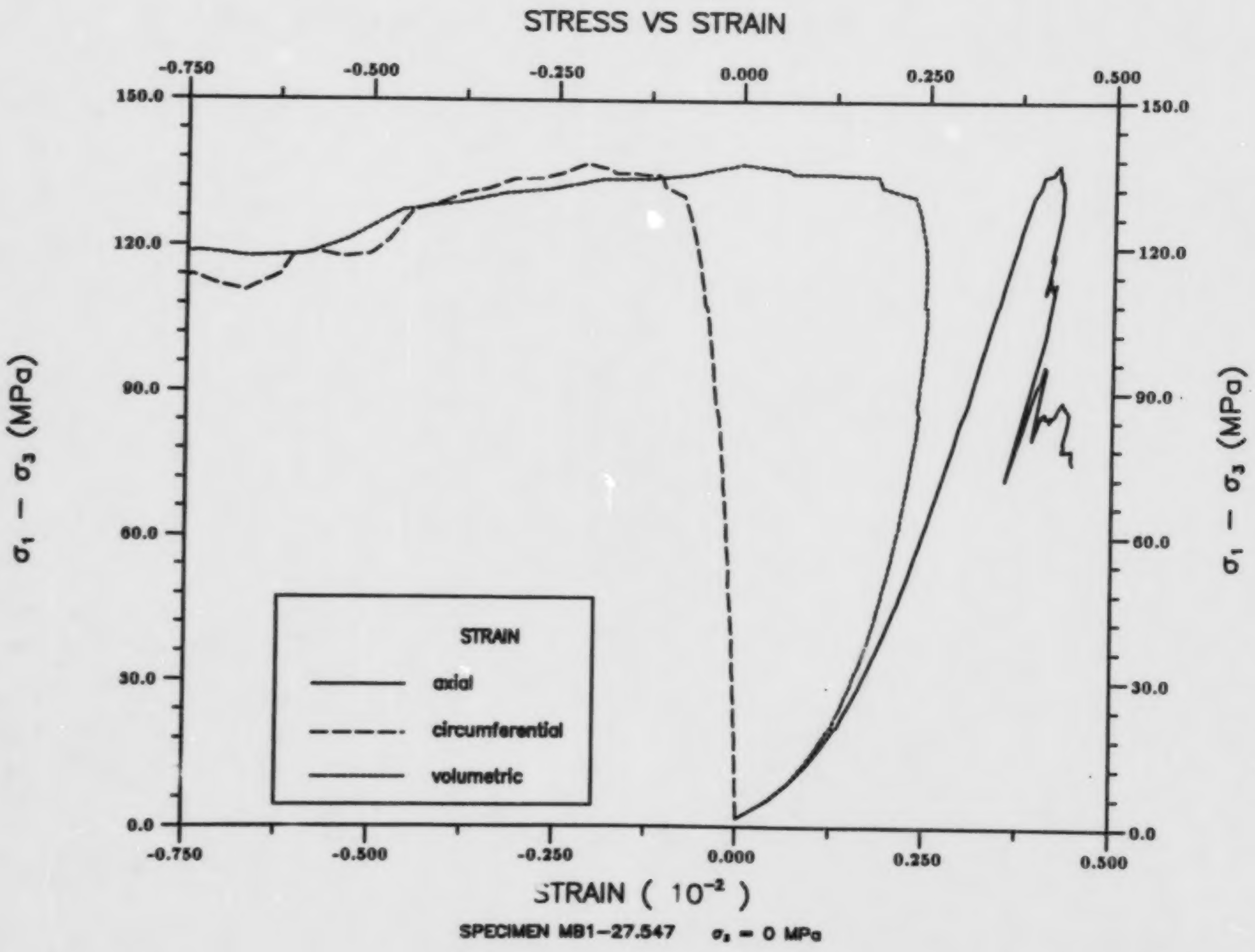

Figure 5. Stress-strain curves for specimen 401-S12-MB1-27.547 ($\sigma_3 = 0$).

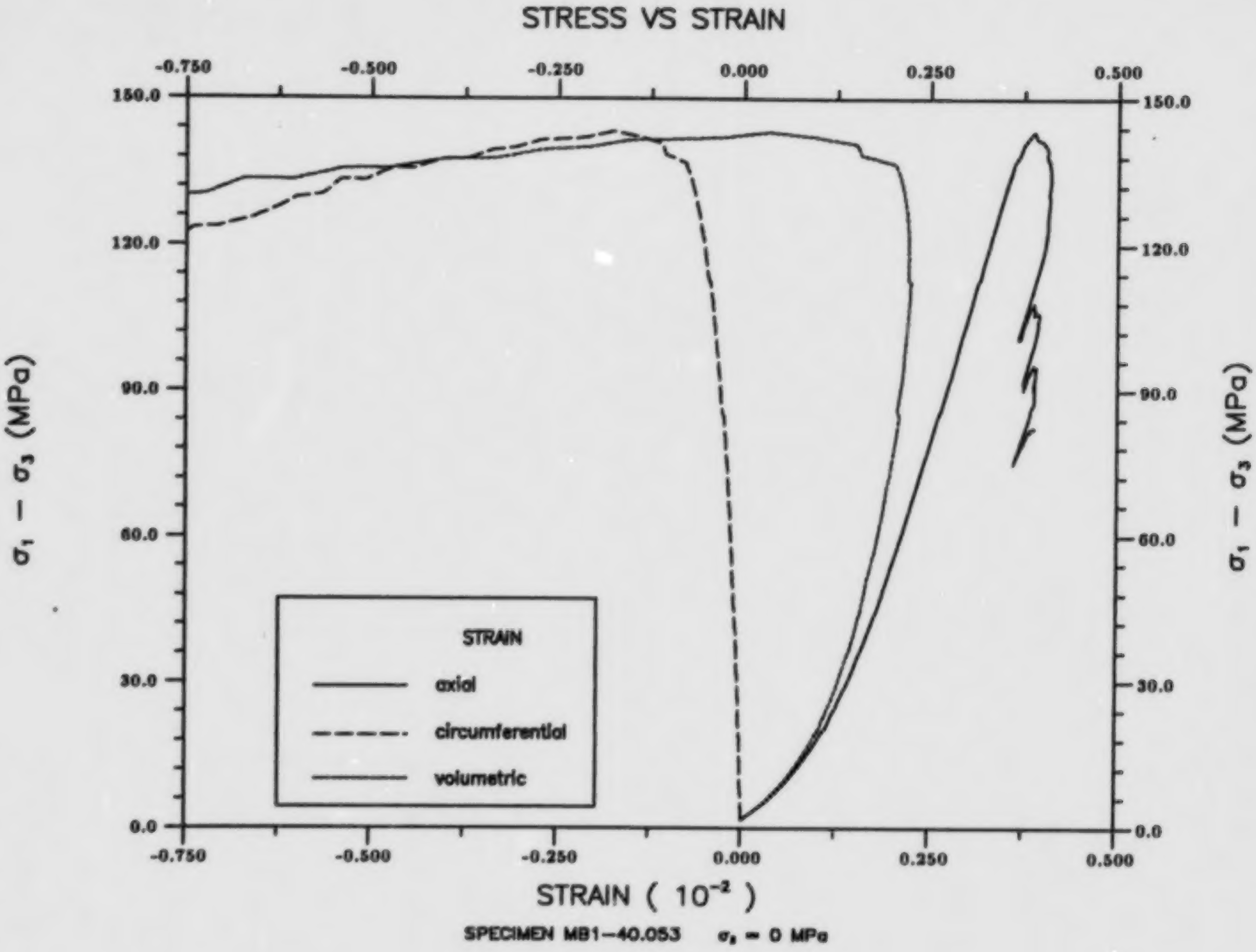

Figure 6. Stress-strain curves for specimen 401-S12-MB1-40.053 ($\sigma_3 = 0$).

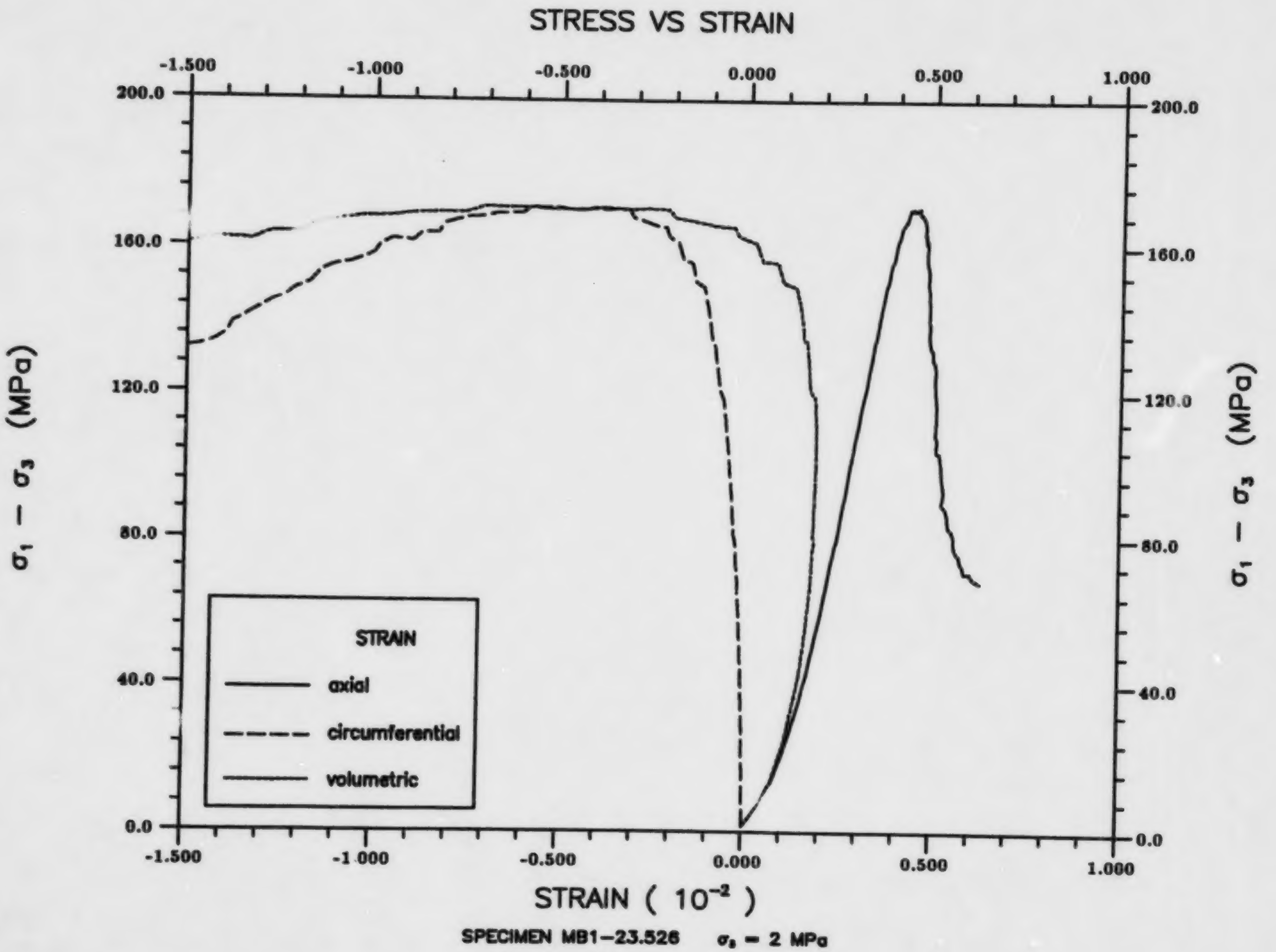

Figure 7. Stress-strain curves for specimen 401-S12-MB1-23.526 ($\sigma_3 = 2$ MPa).

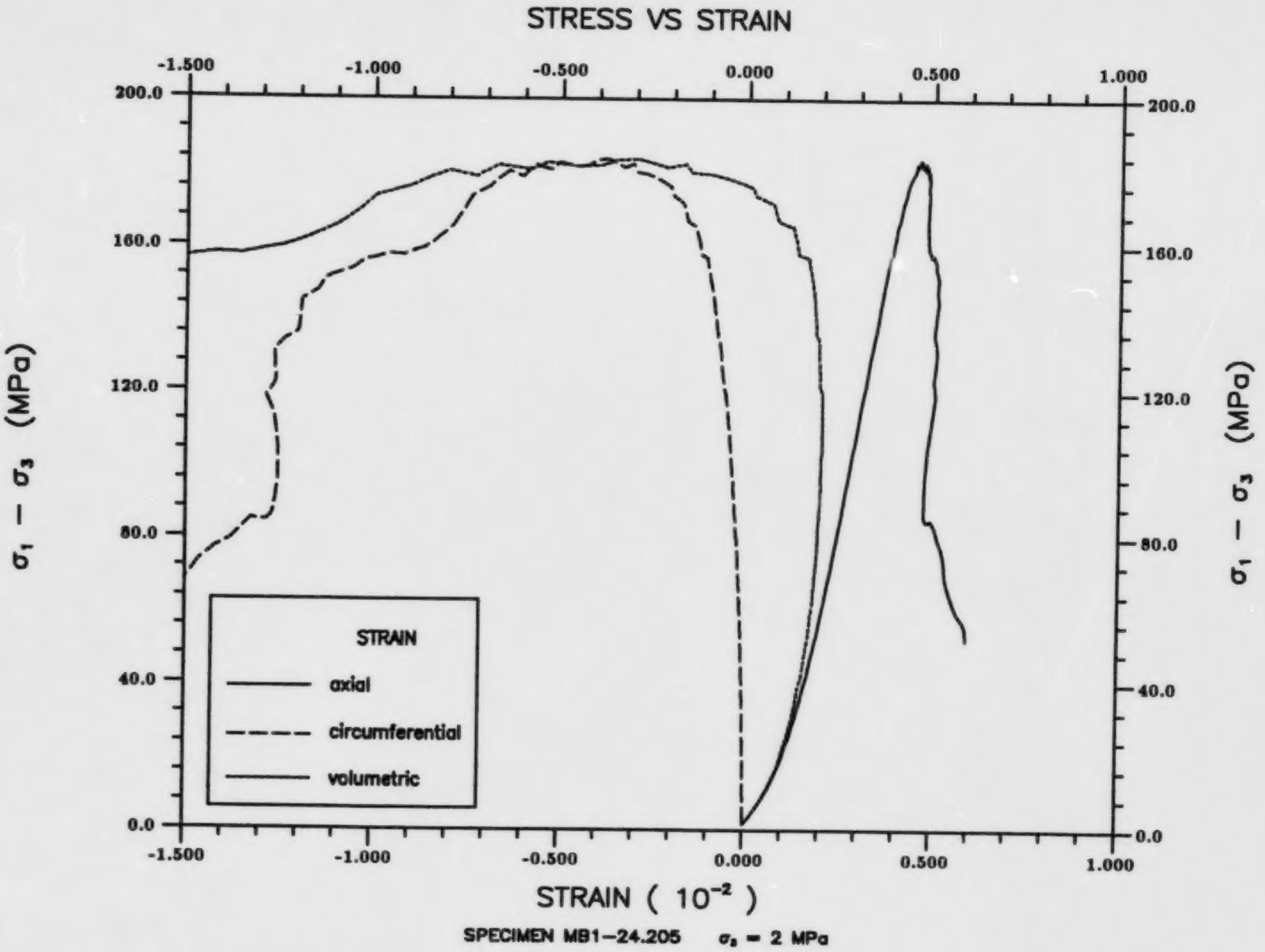

Figure 8. Stress-strain curves for specimen 401-S12-MB1-24.205 ($\sigma_3 = 2$ MPa).

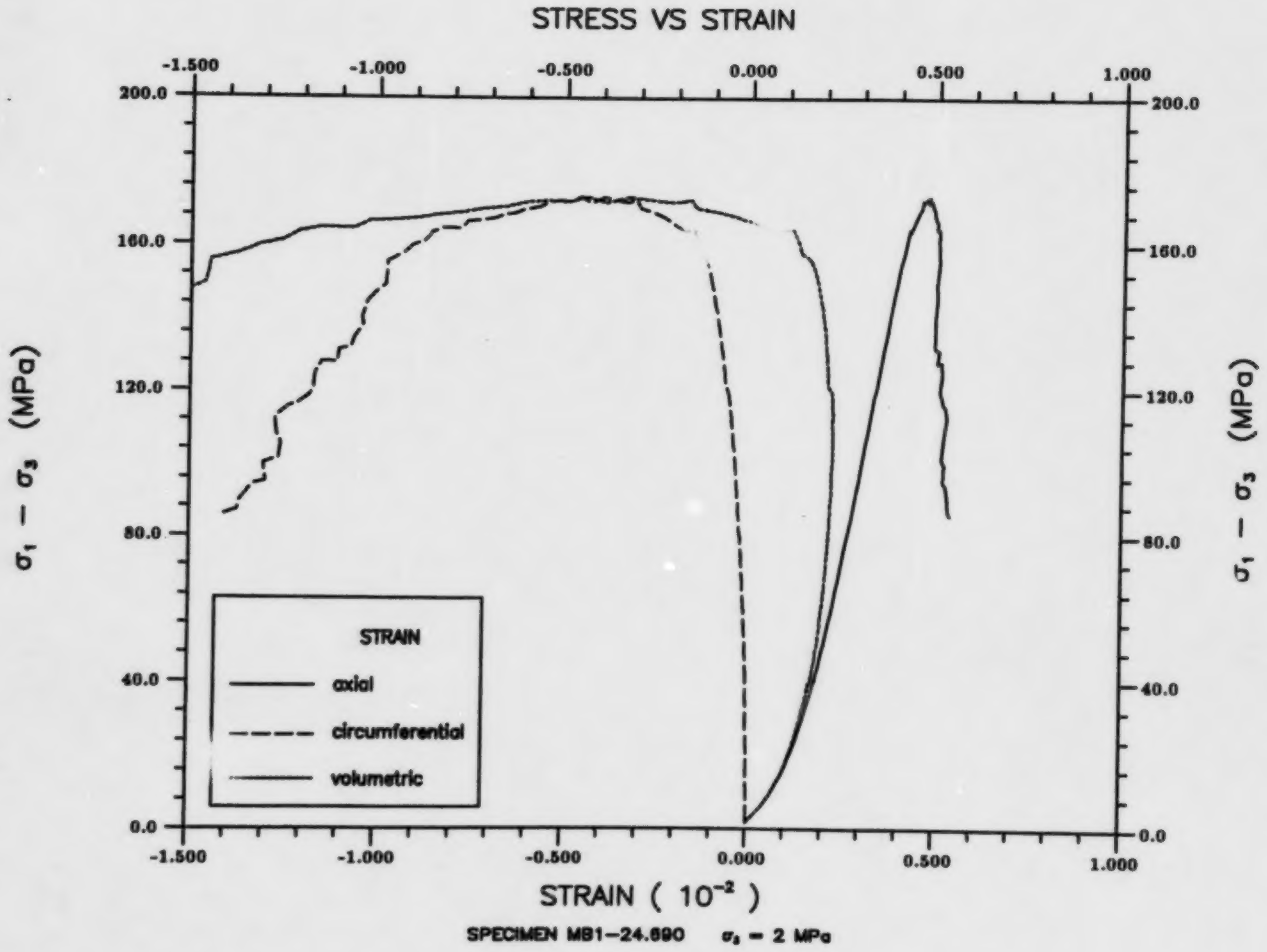

Figure 9. Stress-strain curves for specimen 401-S12-MB1-24.690 ($\sigma_3 = 2$ MPa).

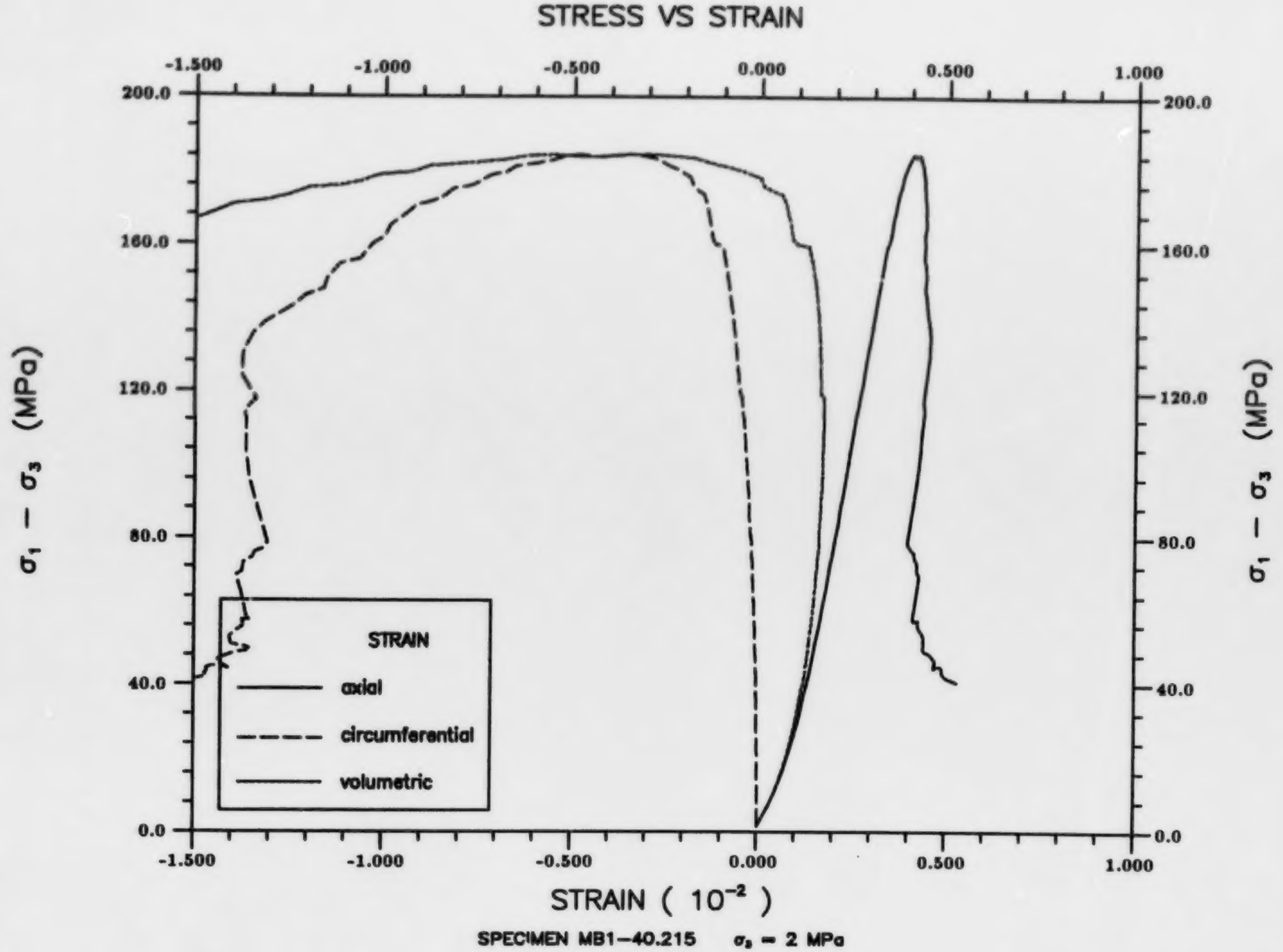

Figure 10. Stress-strain curves for specimen 401-S12-MB1-40.215 ($\sigma_3 = 2$ MPa).

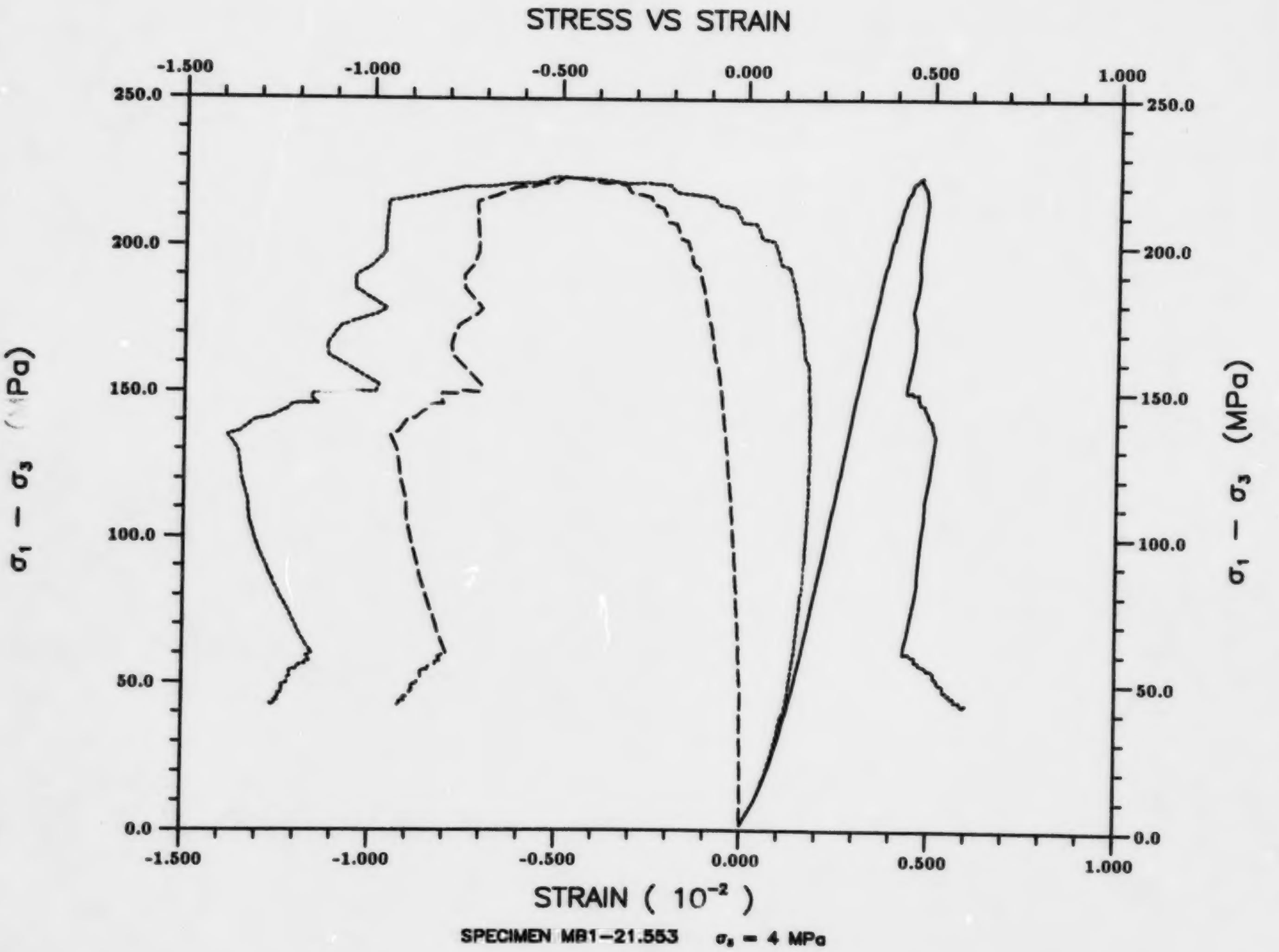

Figure 11. Stress-strain curves for specimen 401-S12-MB1-21.553 ($\sigma_3 = 4$ MPa).

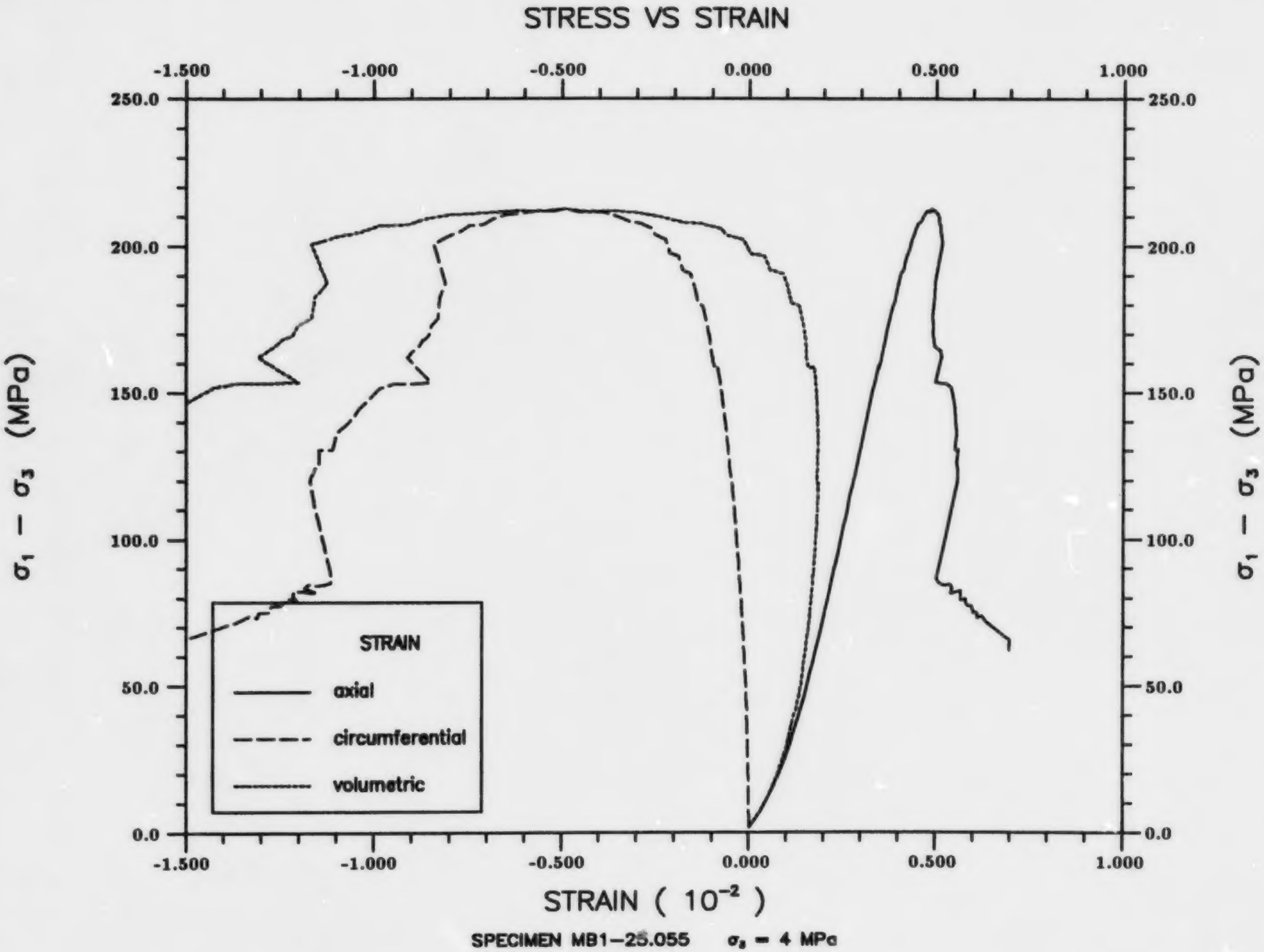

Figure 12. Stress-strain curves for specimen 401-S12-MB1-25.055 ($\sigma_3 = 4$ MPa).

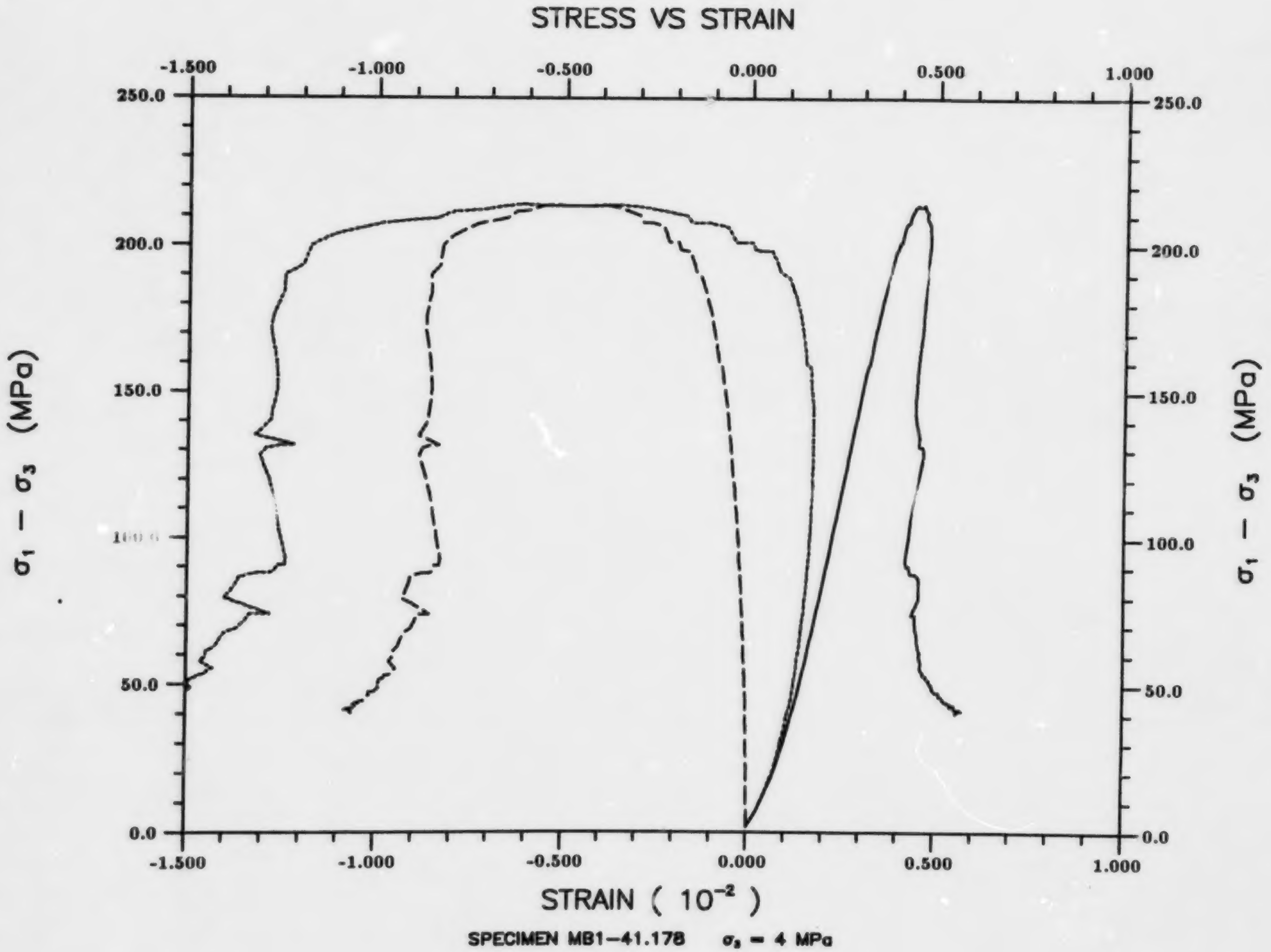

Figure 13. Stress-strain curves for specimen 401-S12-MB1-41.178 ($\sigma_3 = 4$ MPa).

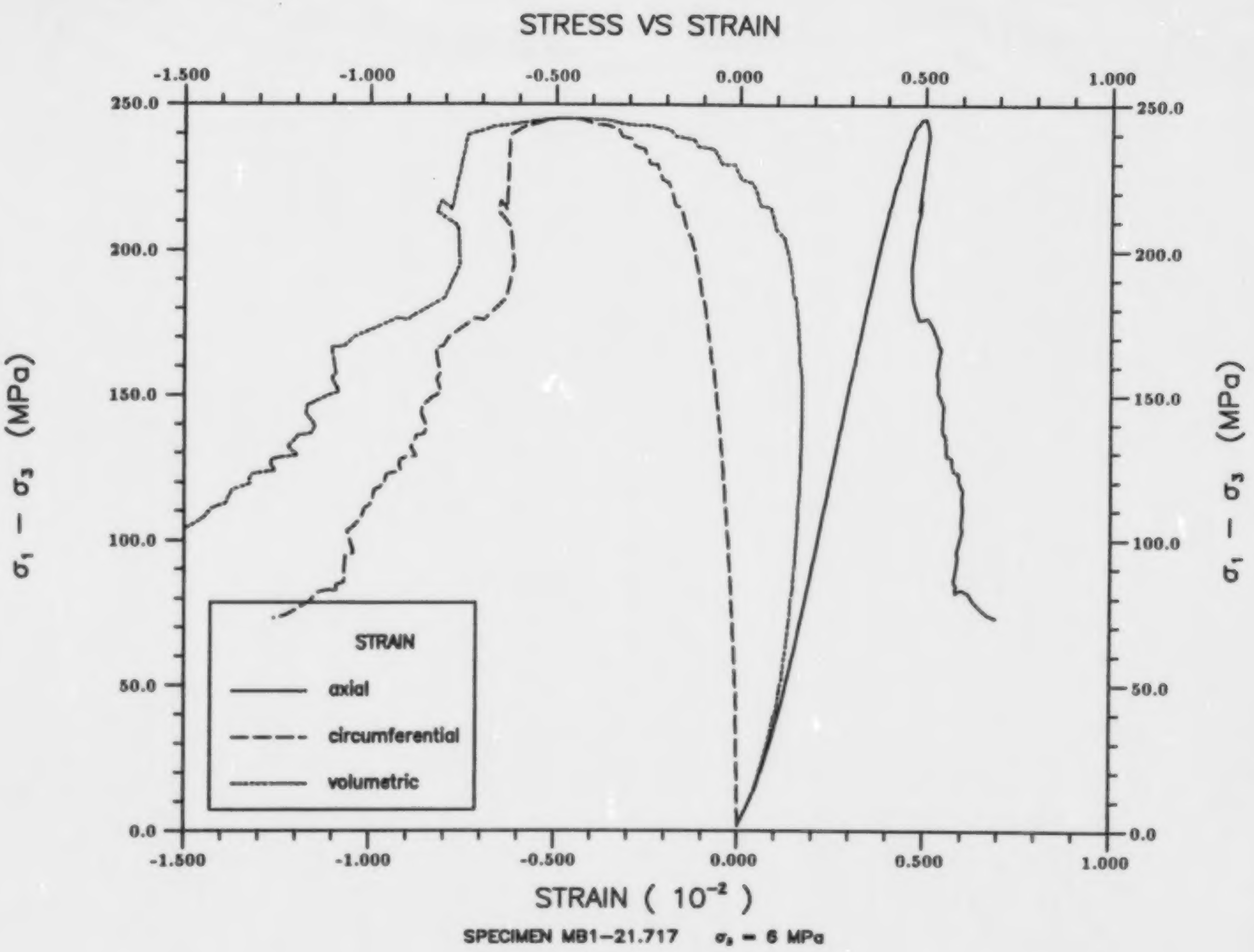

Figure 14. Stress-strain curves for specimen 401-S12-MB1-21.717 ($\sigma_3 = 6$ MPa).

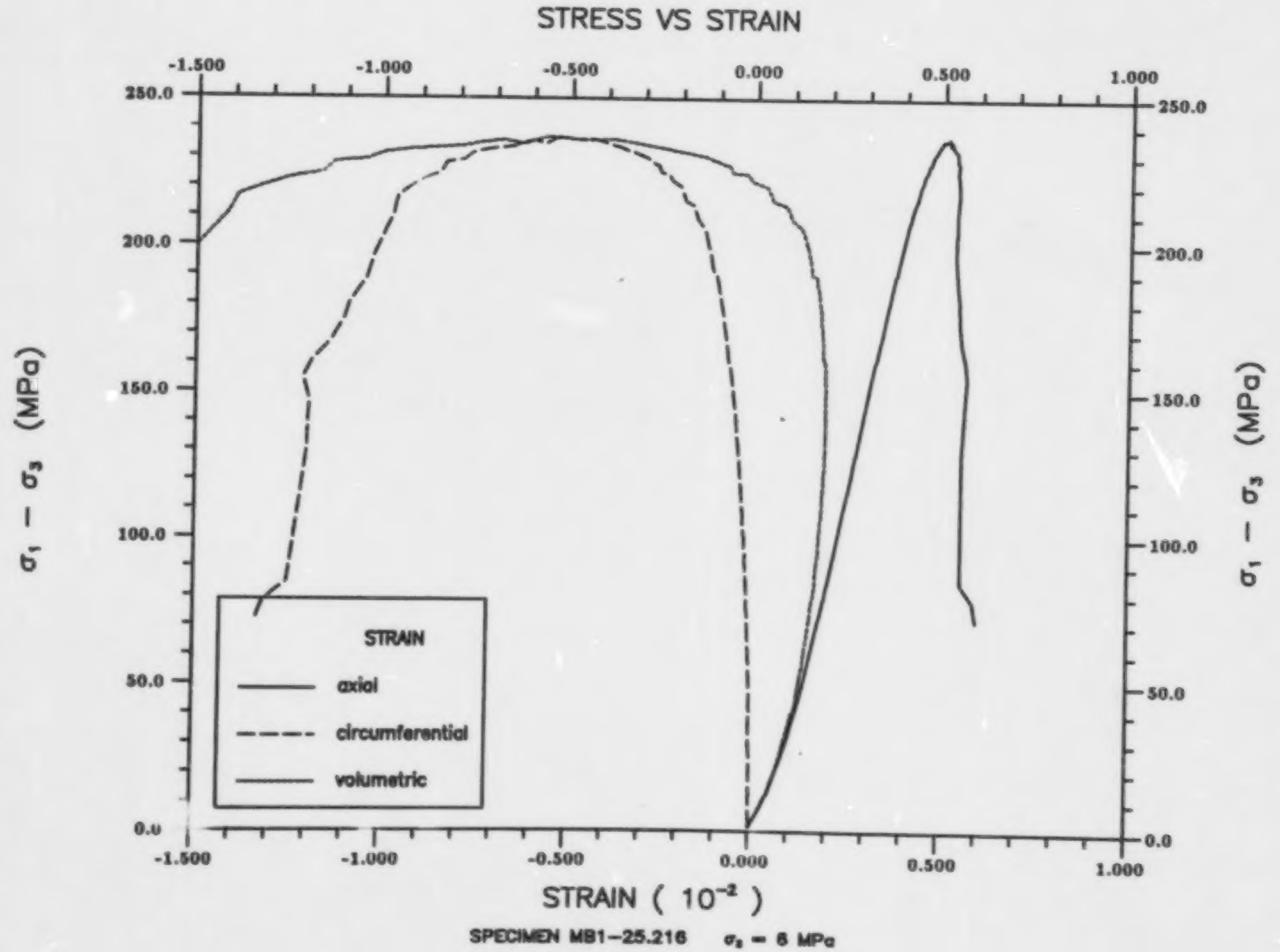

Figure 15. Stress-strain curves for specimen 401-S12-MB1-25.216 ($\sigma_3 = 6$ MPa).

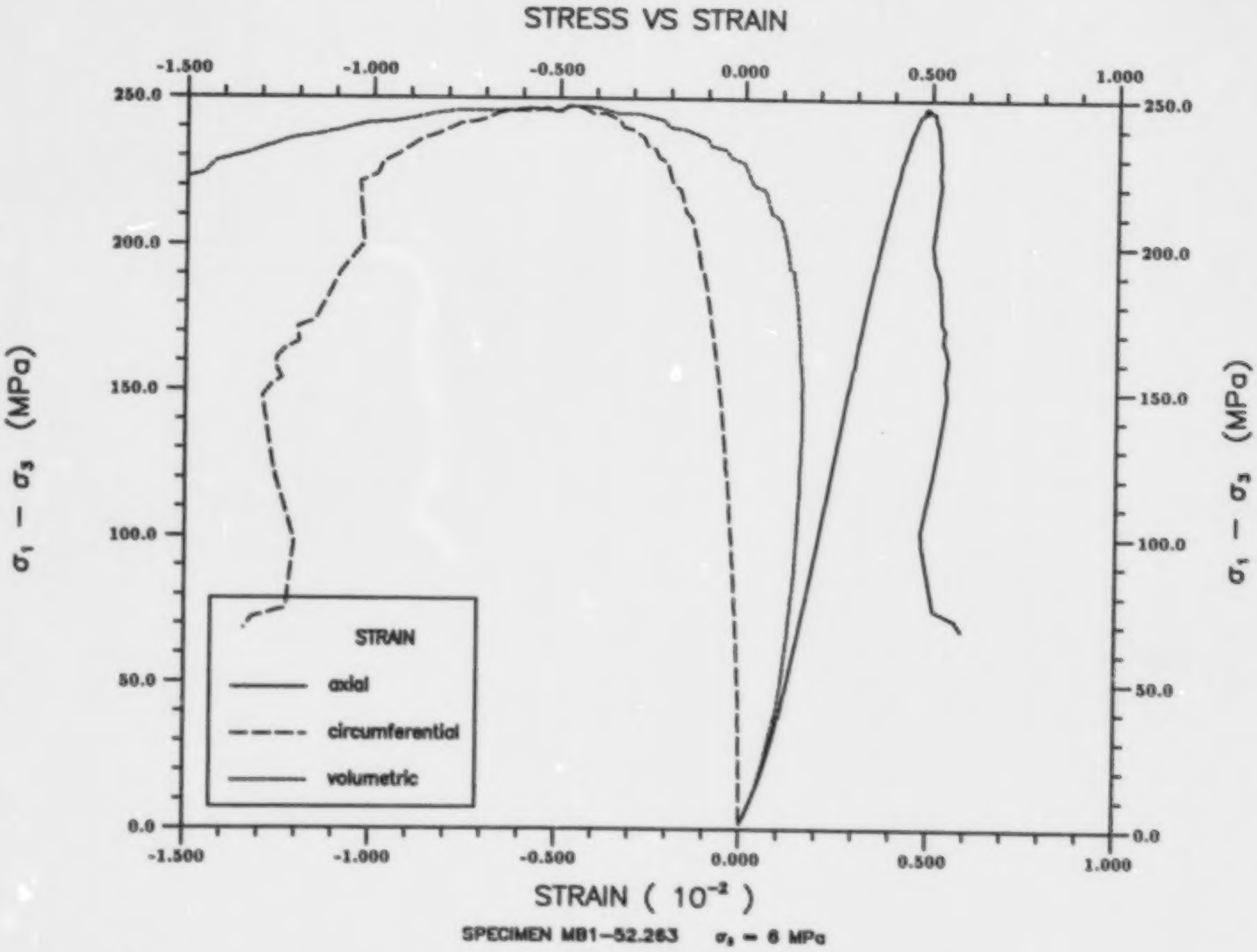

Figure 16. Stress-strain curves for specimen 401-S12-MB1-52.263 ($\sigma_3 = 6$ MPa).

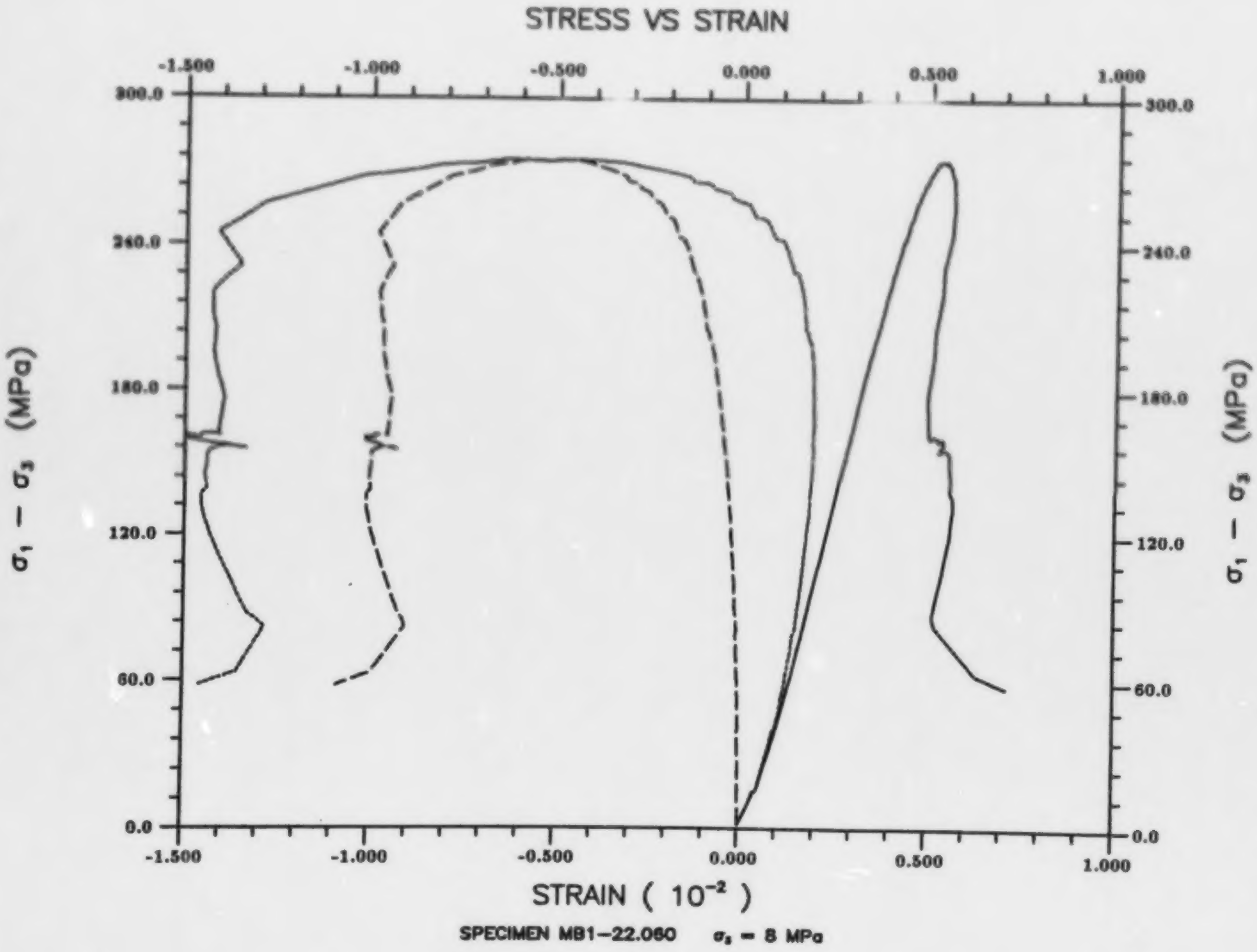

Figure 17. Stress-strain curves for specimen 401-S12-MB1-22.060 ($\sigma_3 = 8$ MPa).

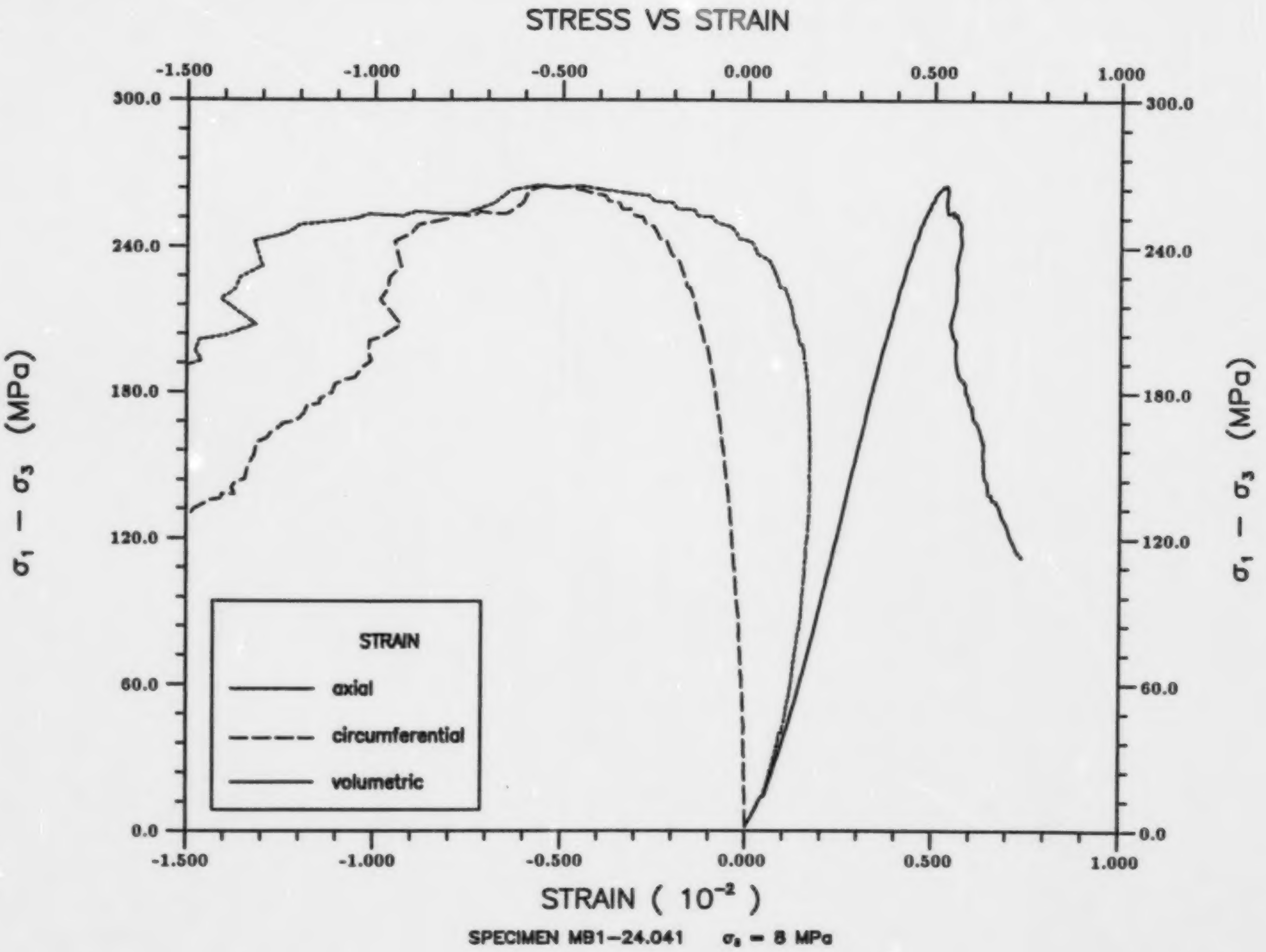

Figure 18. Stress-strain curves for specimen 401-S12-MB1-24.041 ($\sigma_3 = 8$ MPa).

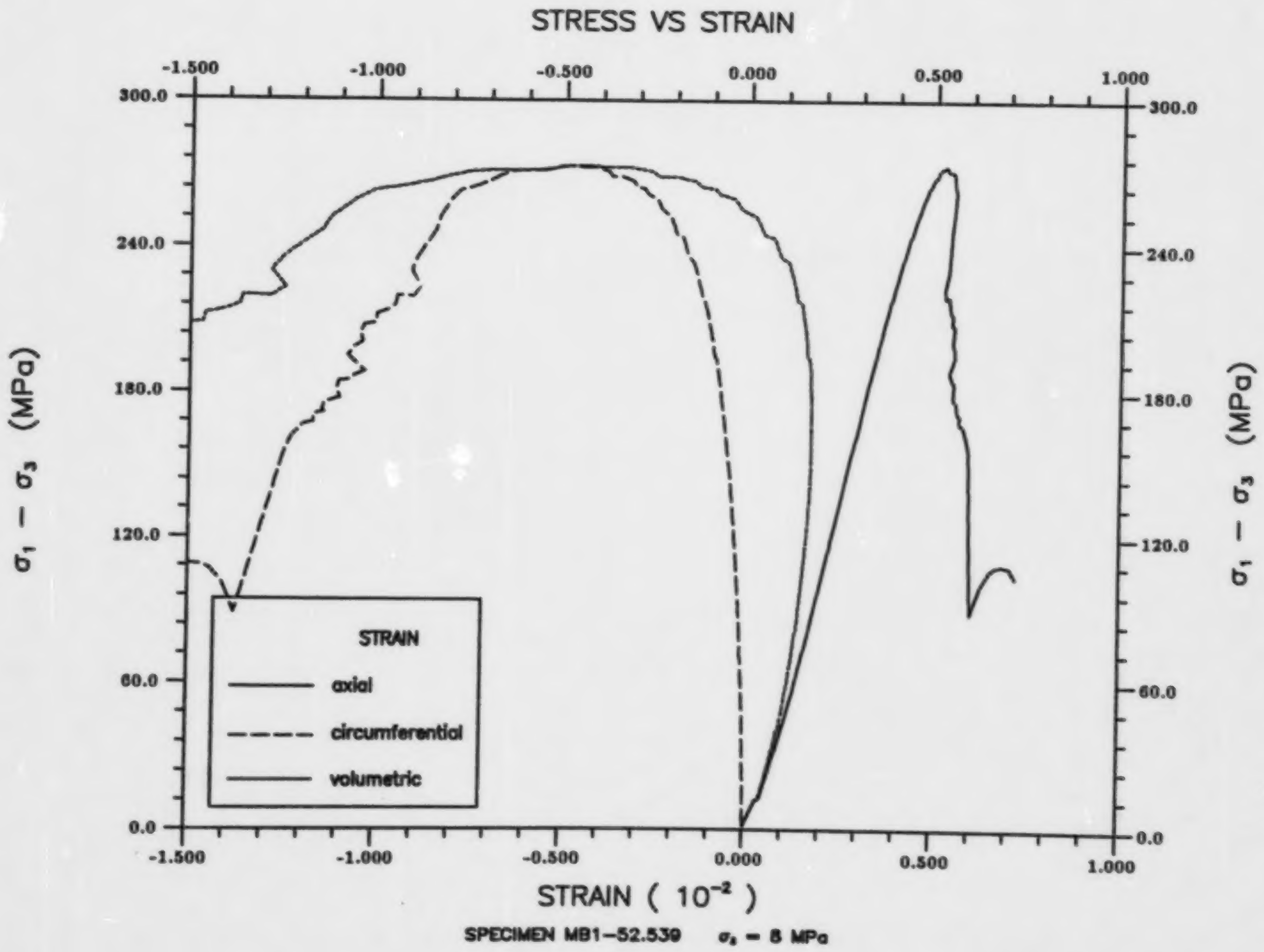

Figure 19. Stress-strain curves for specimen 401-S12-MB1-52.539 ($\sigma_3 = 8$ MPa).

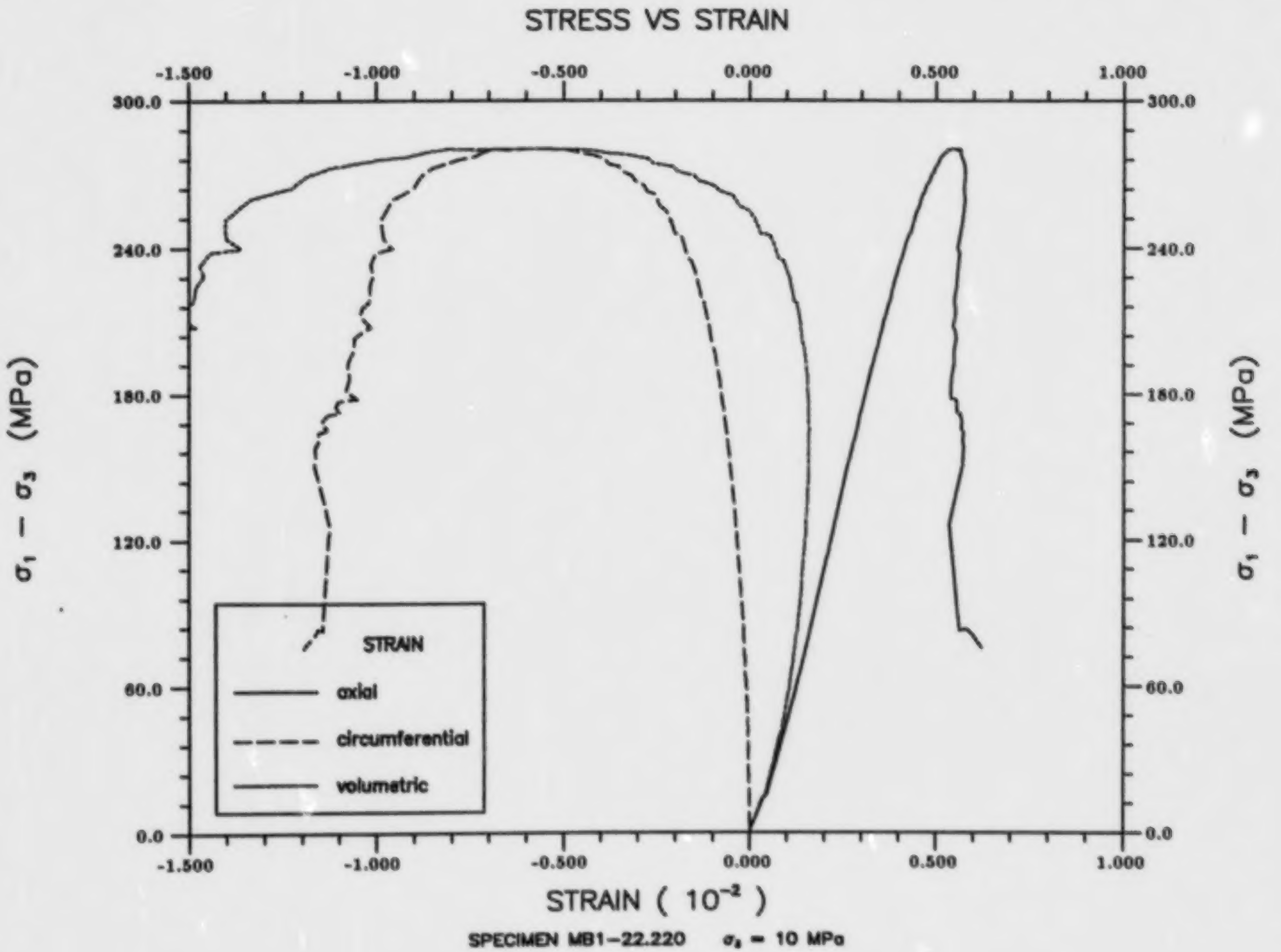

Figure 20. Stress-strain curves for specimen 401-S12-MB1-22.220 ($\sigma_3 = 10$ MPa).

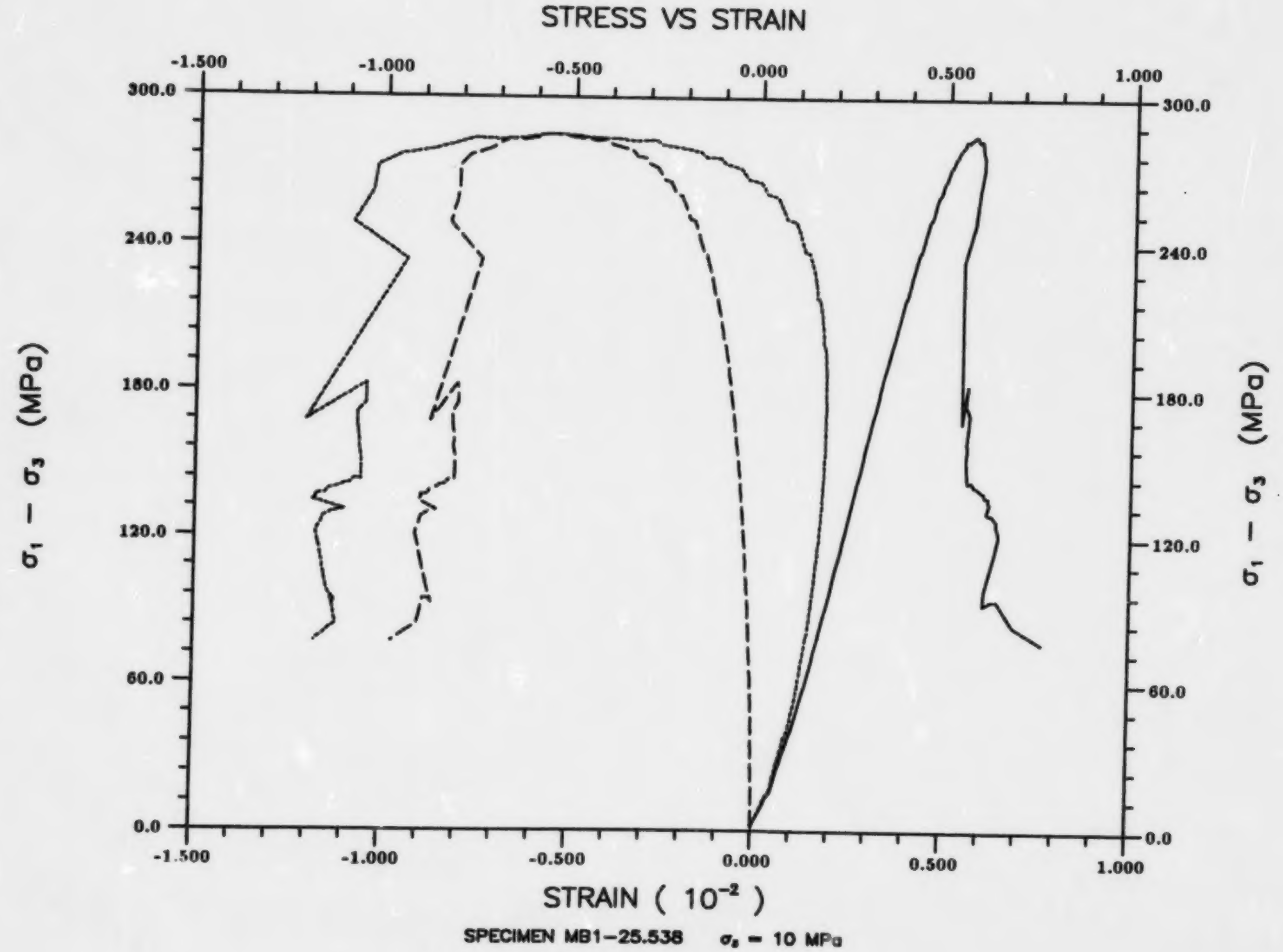

Figure 21. Stress-strain curves for specimen 401-S12-MB1-25.538 ($\sigma_3 = 10$ MPa).

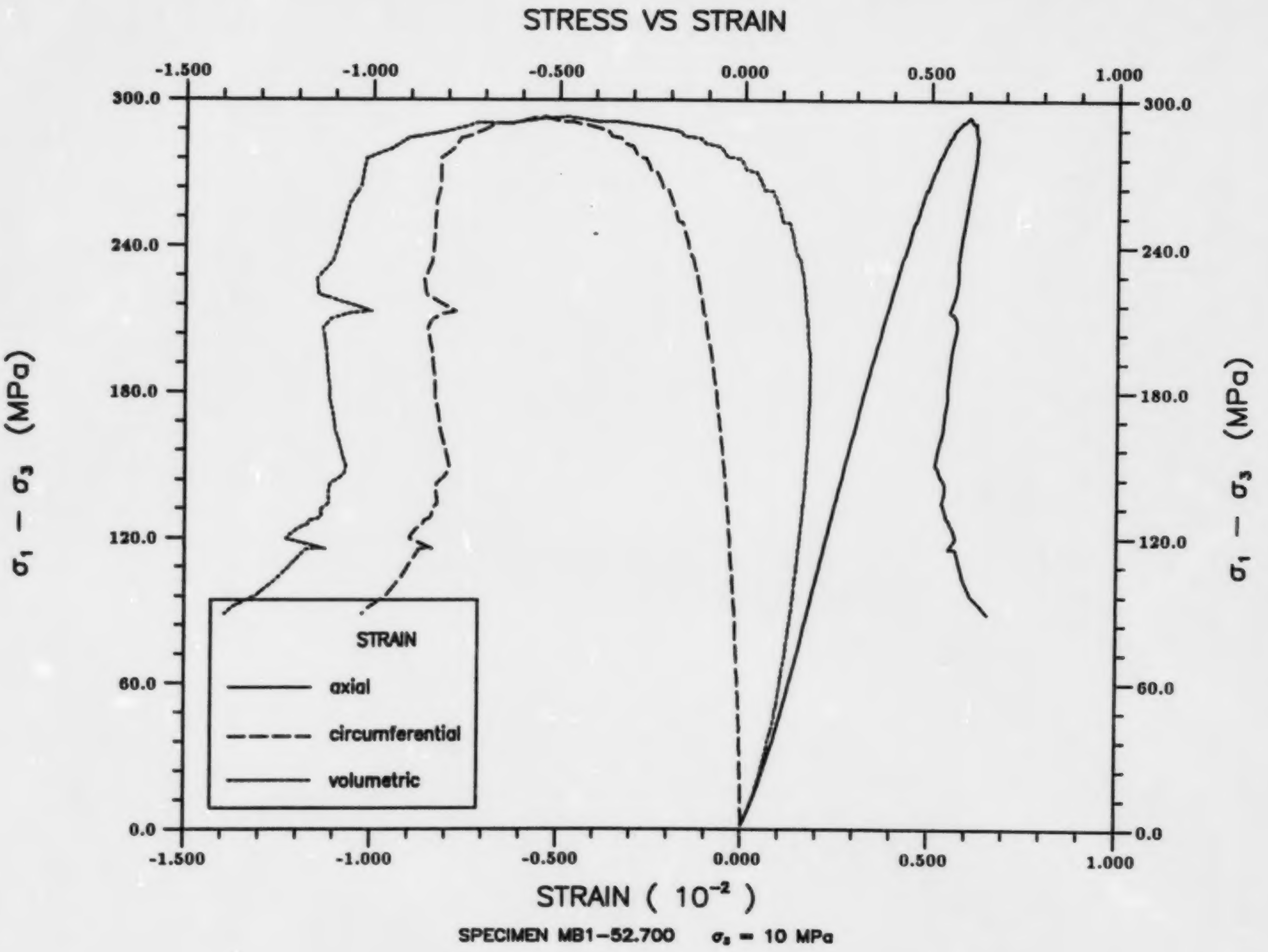

Figure 22. Stress-strain curves for specimen 401-S12-MB1-52.700 ($\sigma_3 = 10$ MPa).

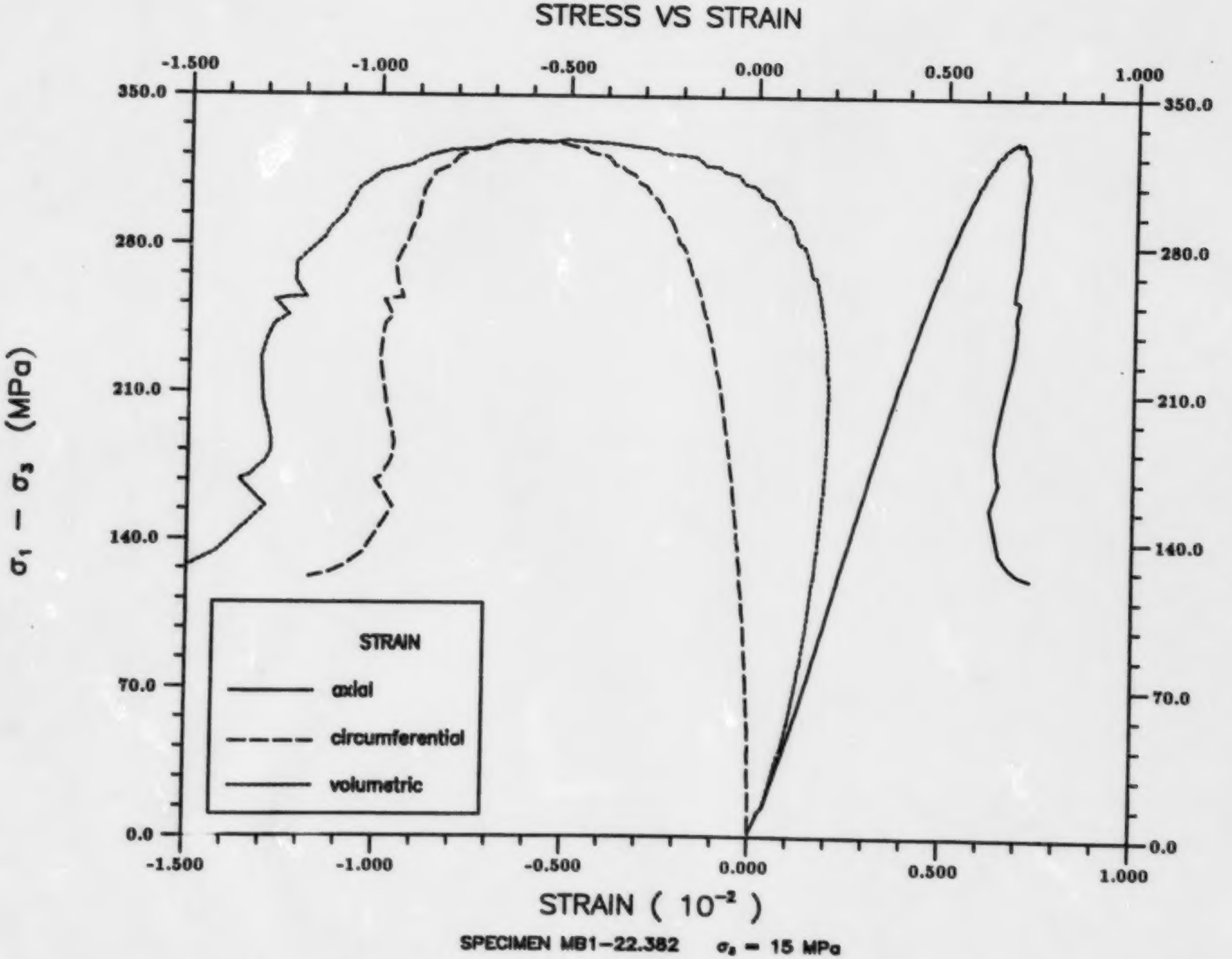

Figure 23. Stress-strain curves for specimen 401-S12-MB1-22.382 ($\sigma_3 = 15$ MPa).

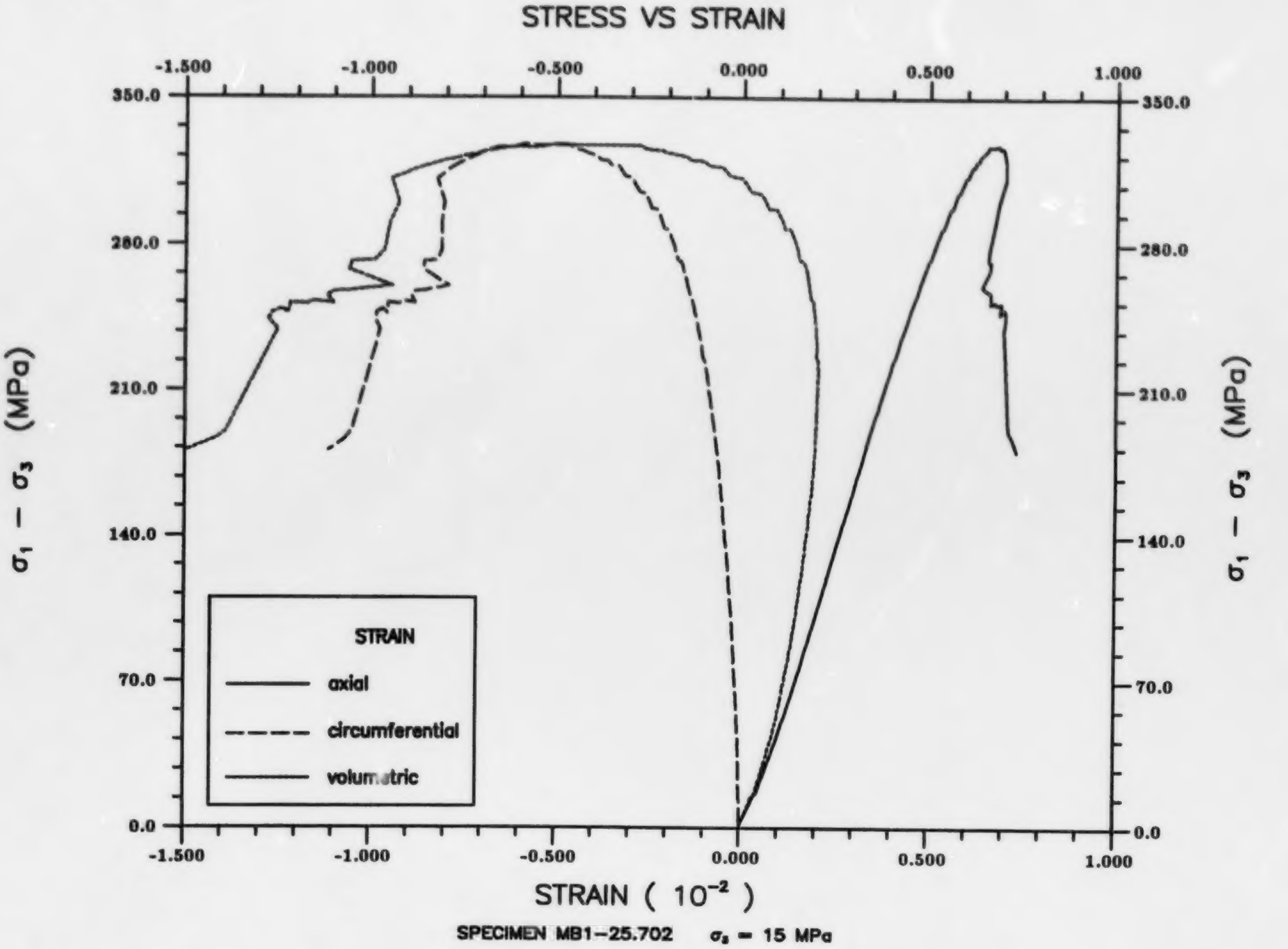

Figure 24. Stress-strain curves for specimen 401-S12-MB1-25.702 ($\sigma_3 = 15$ MPa).

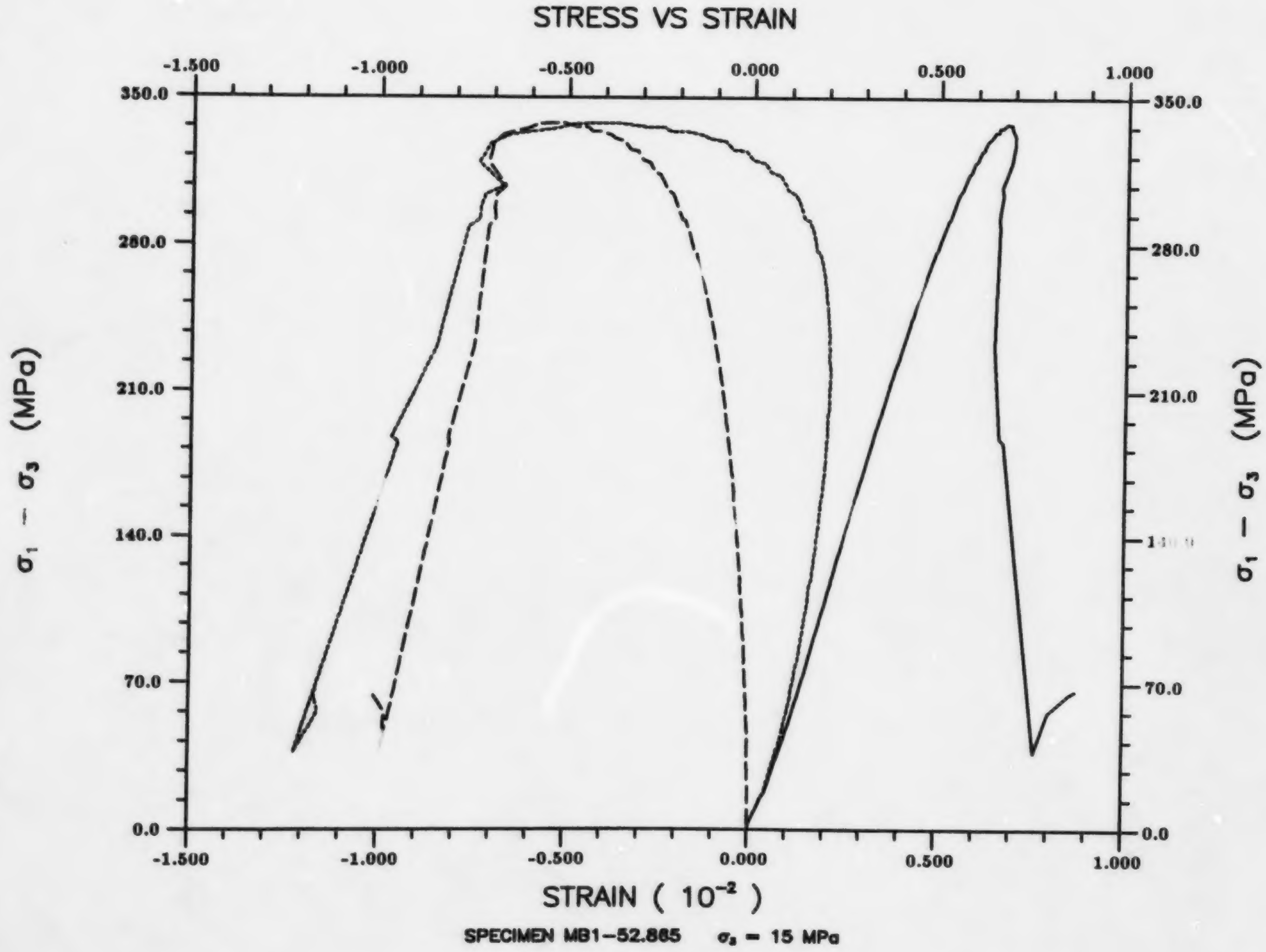

Figure 25. Stress-strain curves for specimen 401-S12-MB1-52.865 ($\sigma_3 = 15$ MPa).

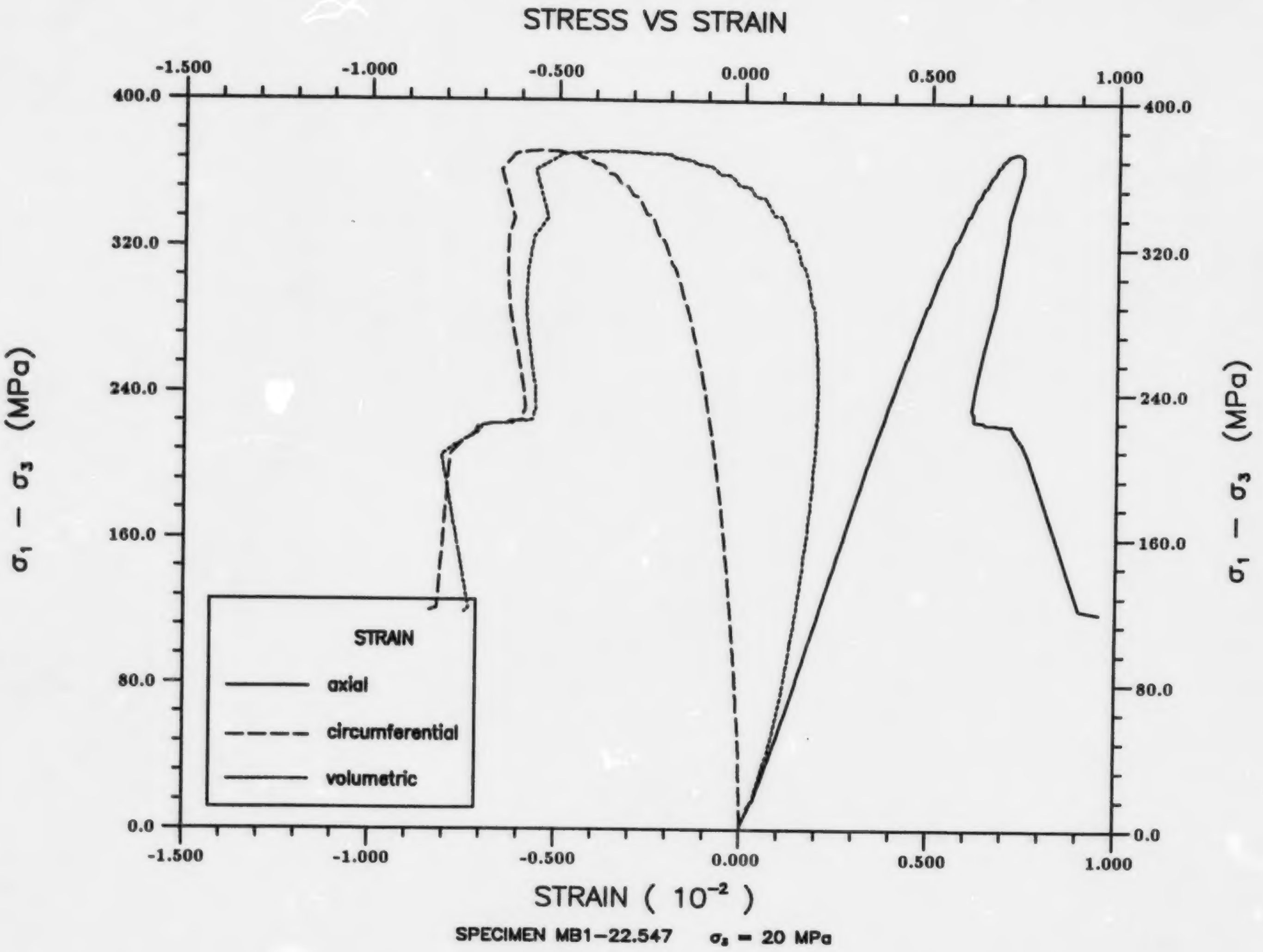

Figure 26. Stress-strain curves for specimen 401-S12-MB1-22.547 ($\sigma_3 = 20$ MPa).

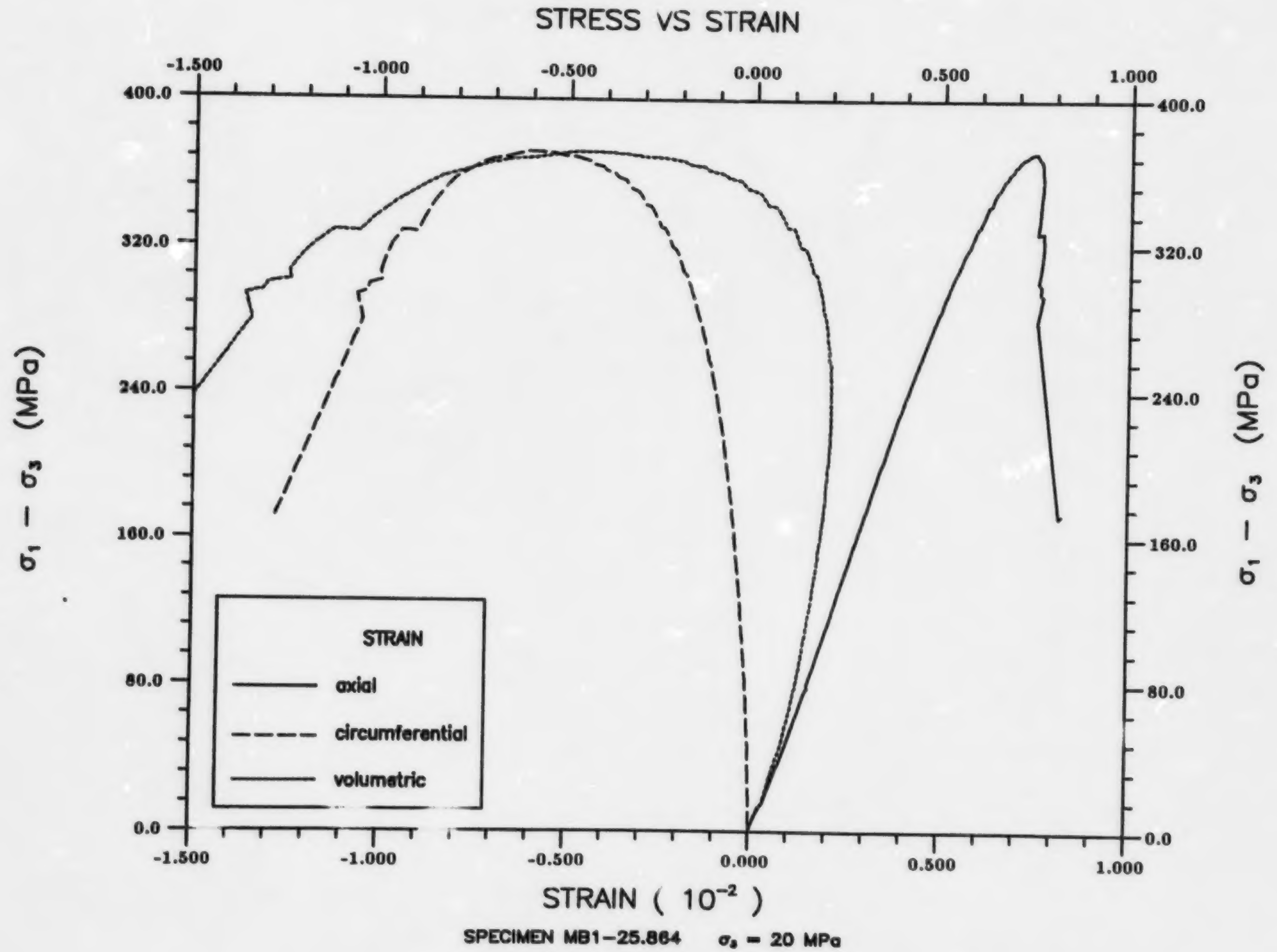

Figure 27. Stress-strain curves for specimen 401-S12-MB1-25.864 ($\sigma_3 = 20$ MPa).

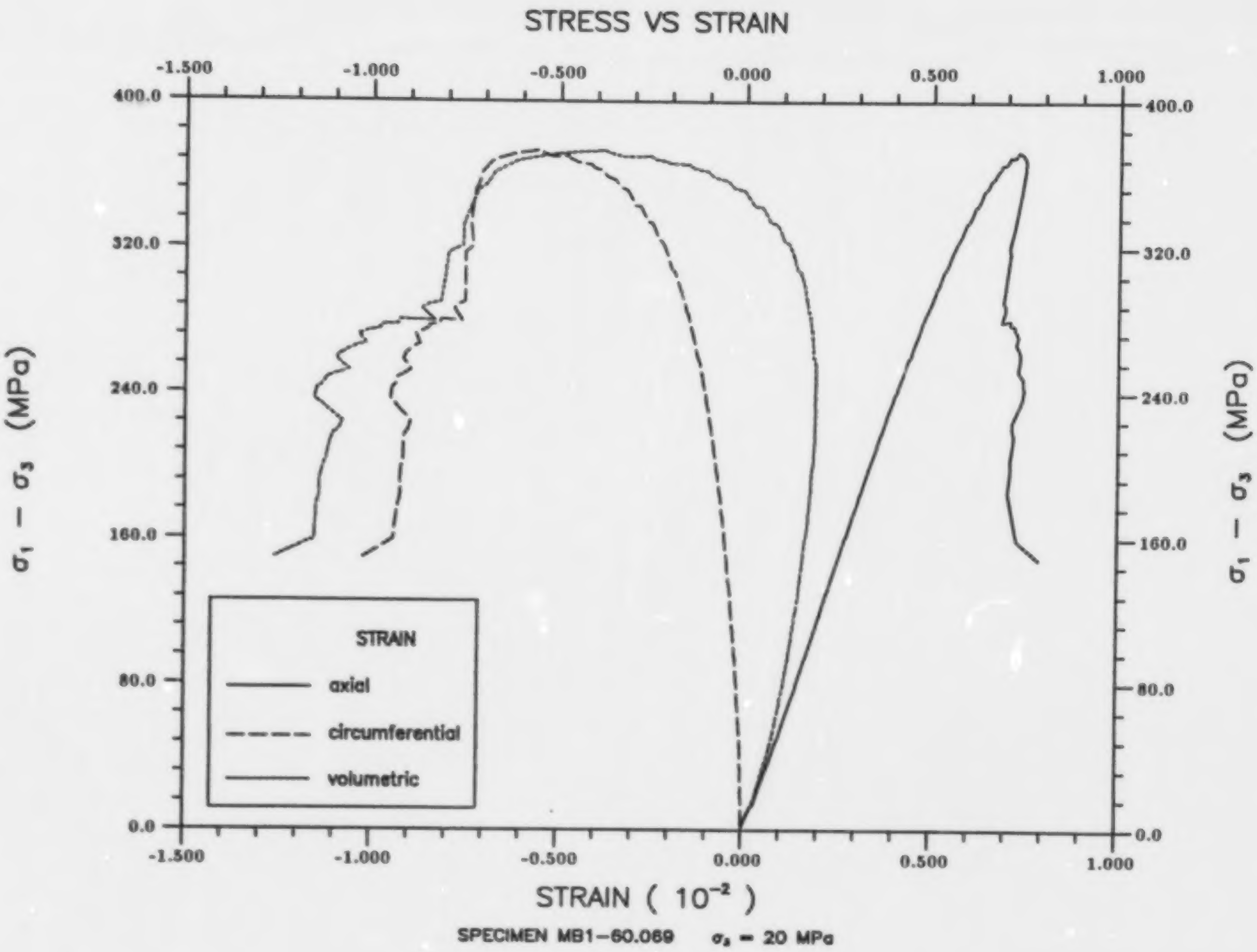

Figure 28. Stress-strain curves for specimen 401-S12-MB1-60.069 ($\sigma_3 = 20$ MPa).

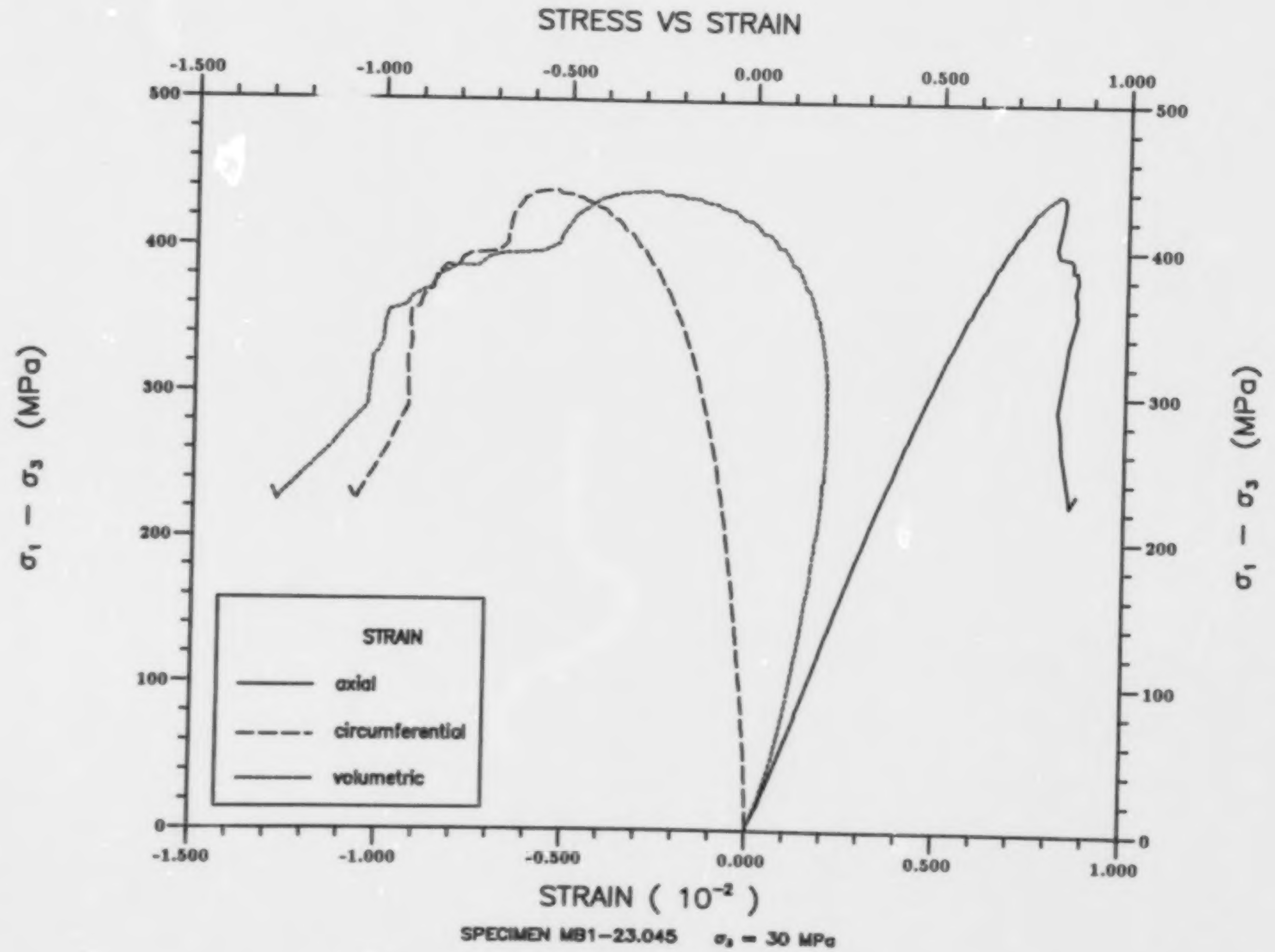

Figure 29. Stress-strain curves for specimen 401-S12-MB1-23.045 ($\sigma_3 = 30$ MPa).

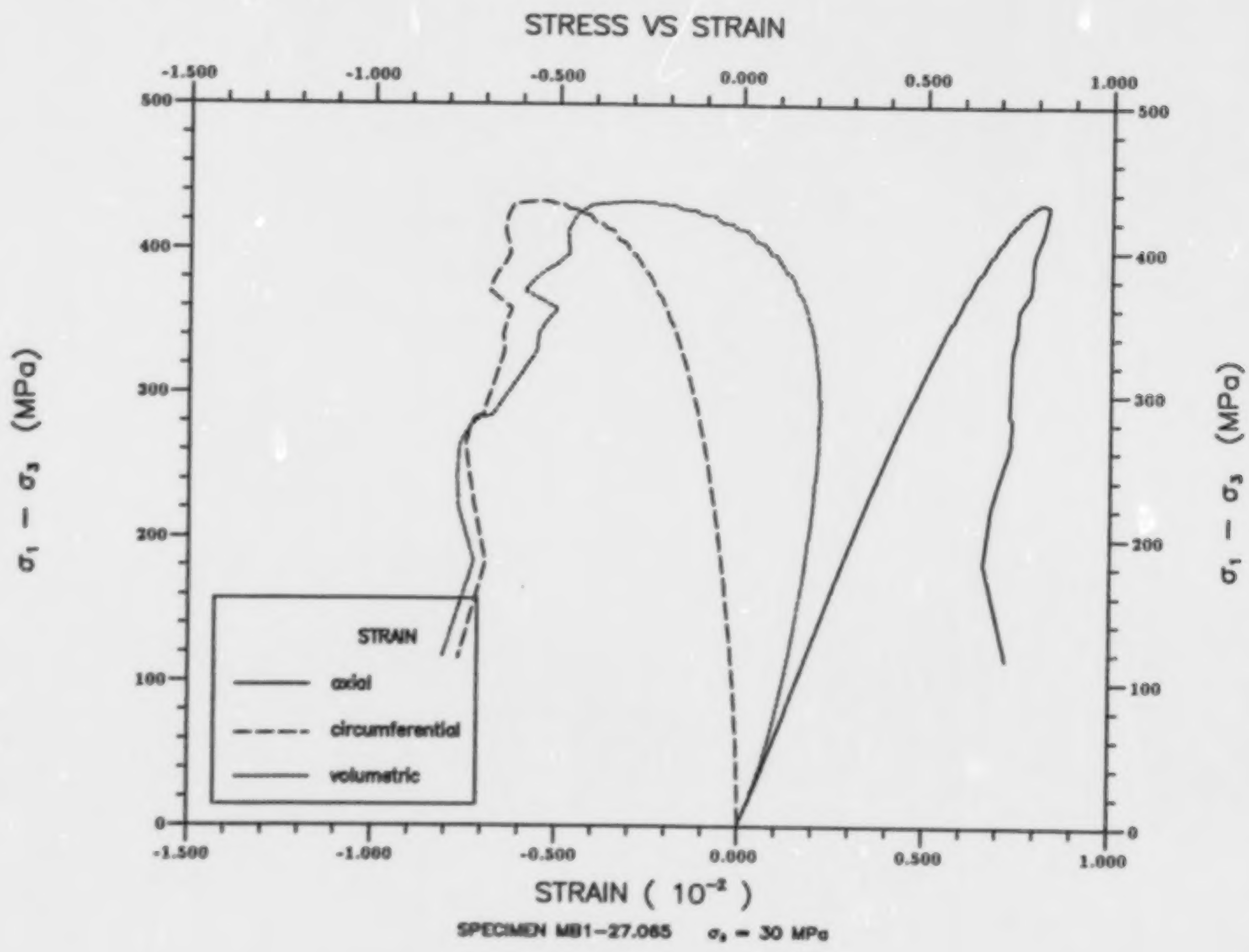

Figure 30. Stress-strain curves for specimen 401-S12-MB1-27.065 ($\sigma_3 = 30$ MPa).

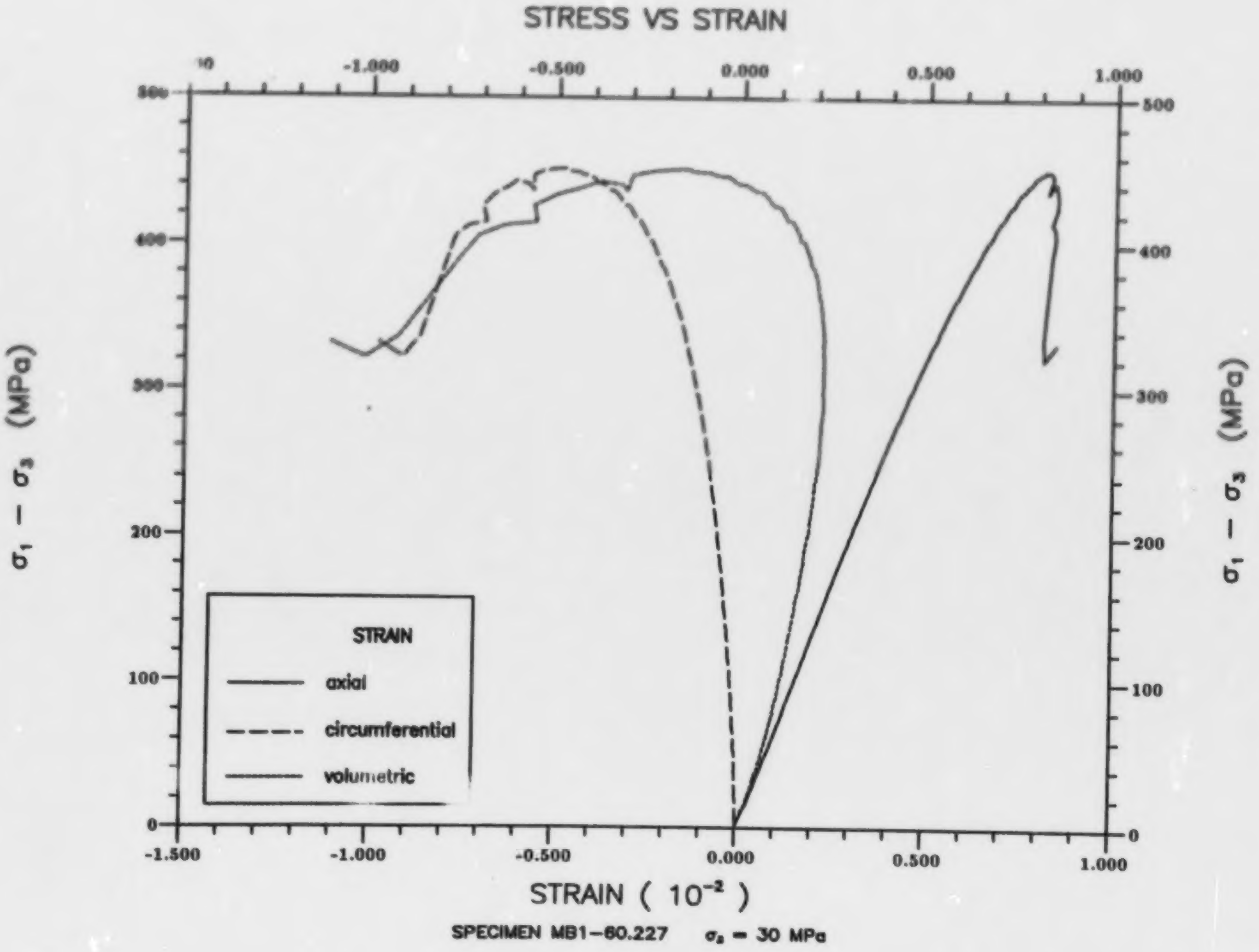

Figure 31. Stress-strain curves for specimen 401-S12-MB1-60.227 ($\sigma_3 = 30$ MPa).

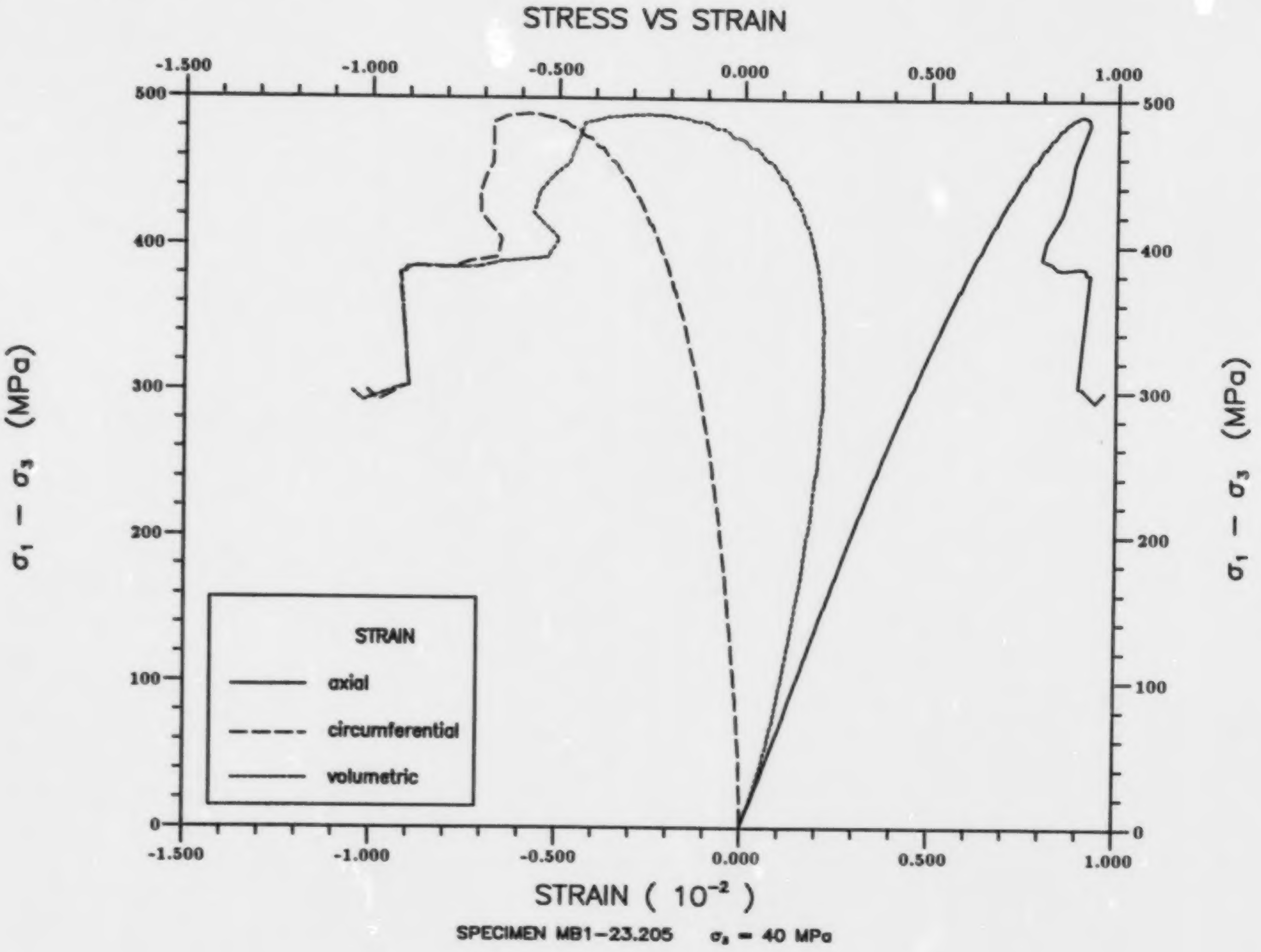

Figure 32. Stress-strain curves for specimen 401-S12-MB1-23.205 ($\sigma_3 = 40$ MPa).

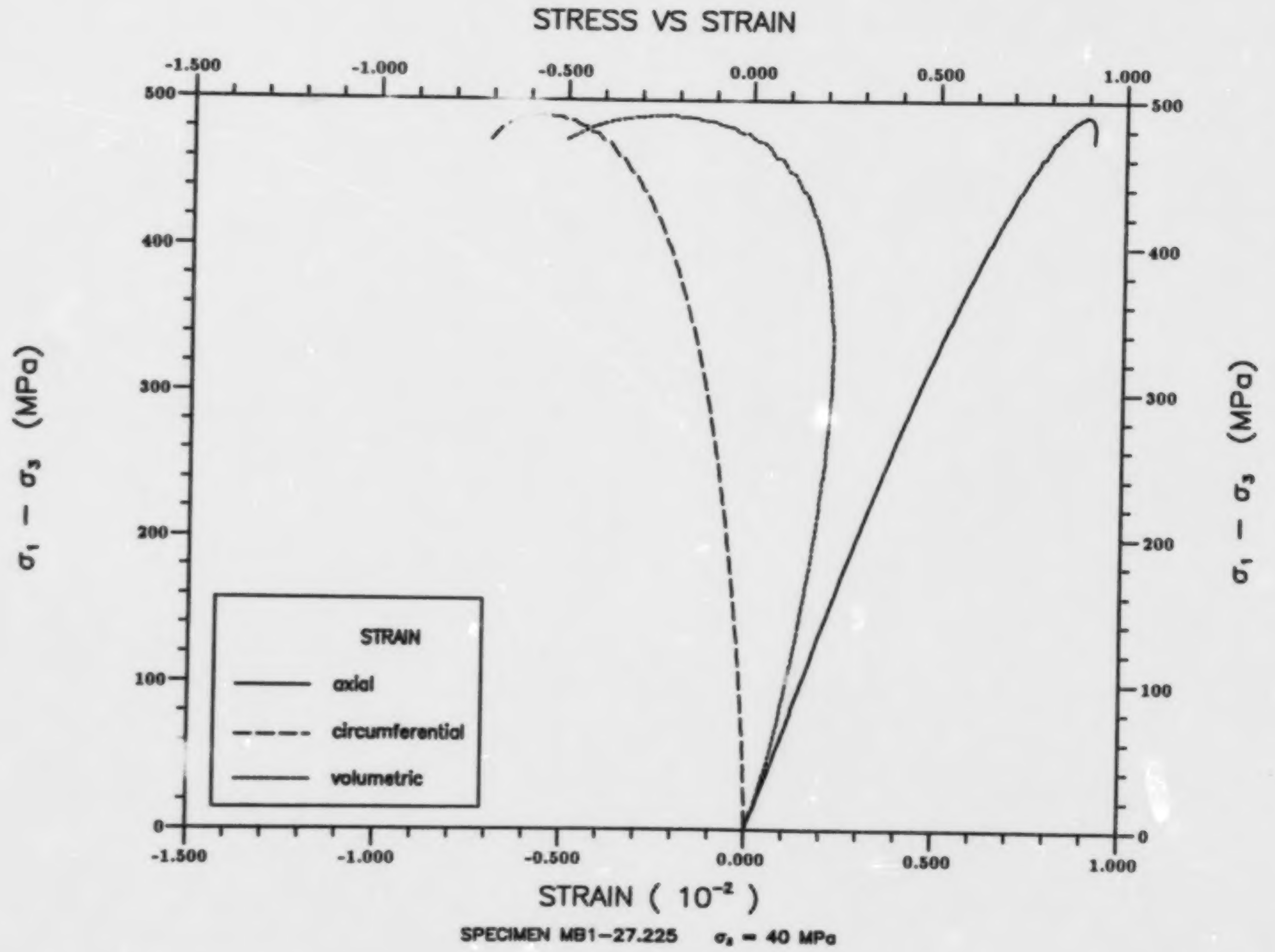

Figure 33. Stress-strain curves for specimen 401-S12-MB1-27.225 ($\sigma_3 = 40$ MPa).

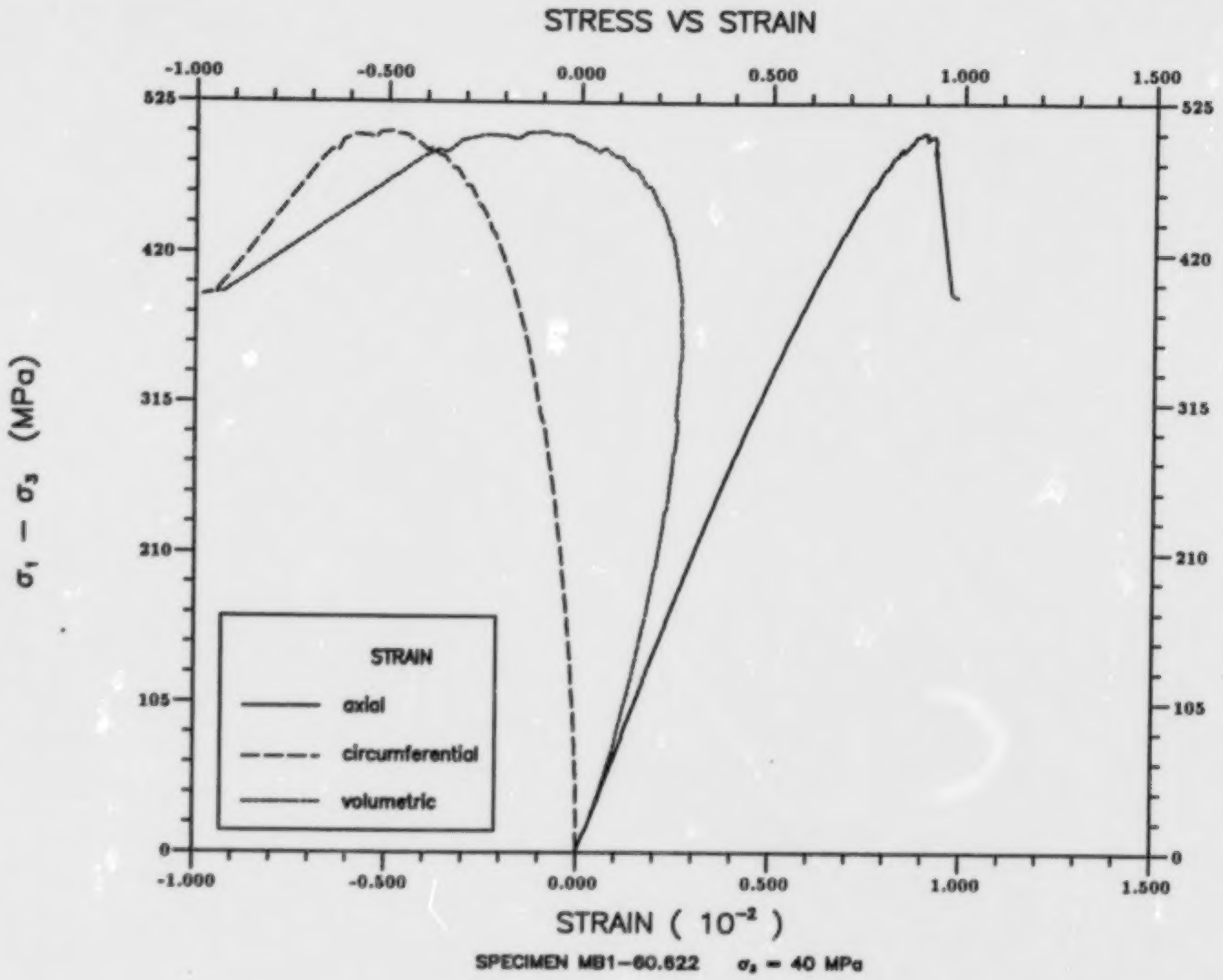

Figure 34. Stress-strain curves for specimen 401-S12-MB1-60.622 ($\sigma_3 = 40$ MPa).

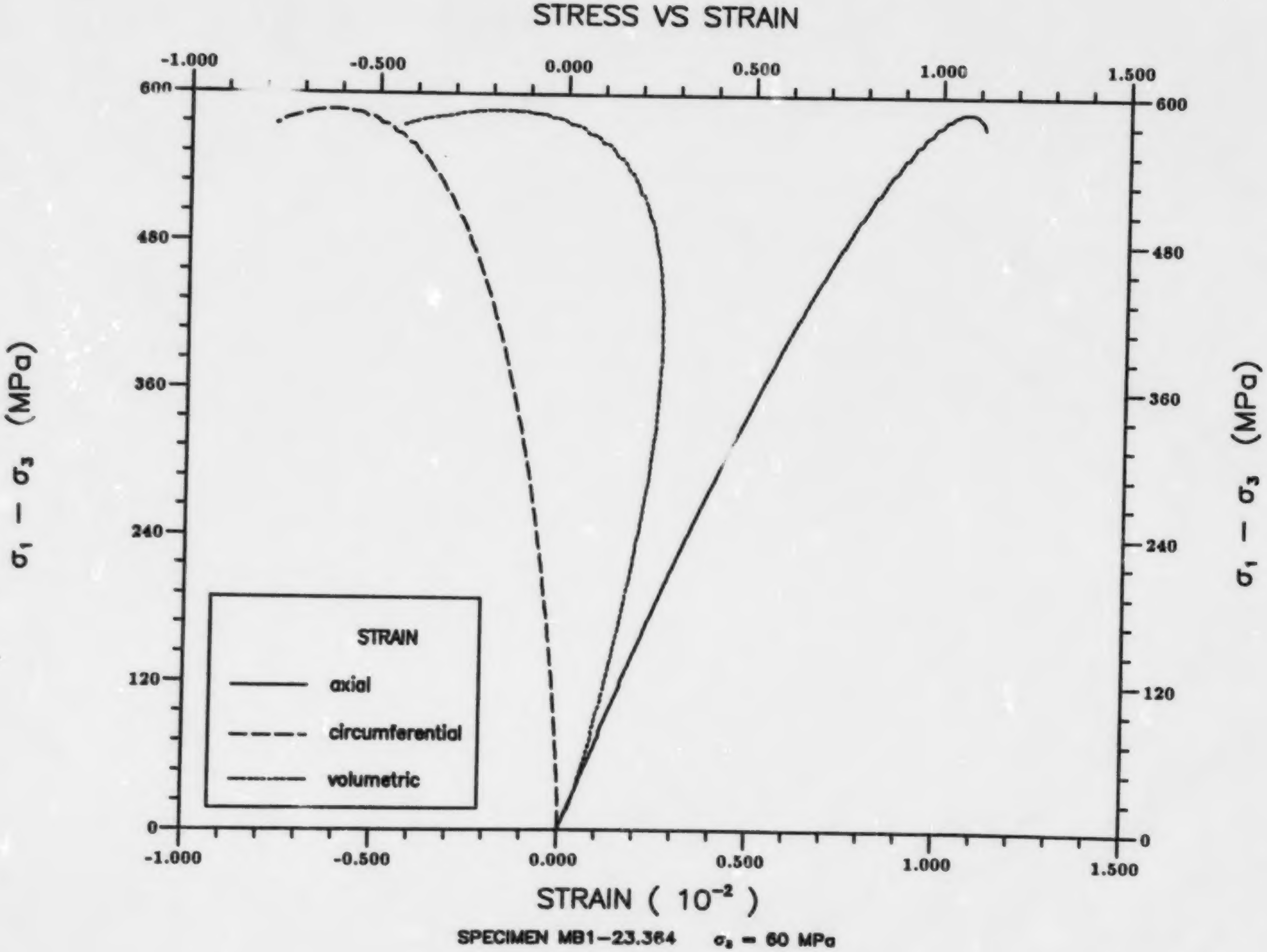

Figure 35. Stress-strain curves for specimen 401-S12-MB1-23.364 ($\sigma_3 = 60$ MPa).

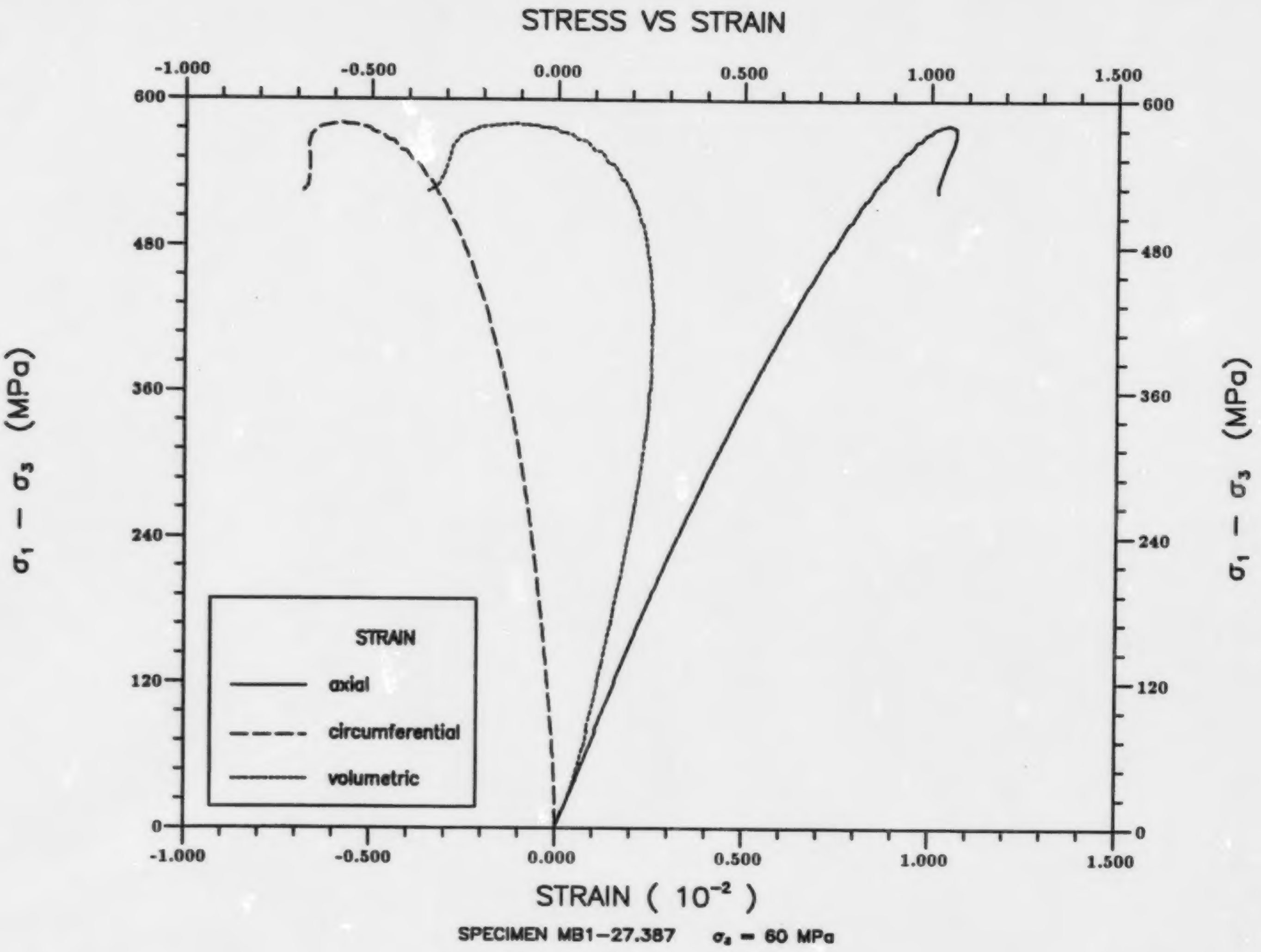

Figure 36. Stress-strain curves for specimen 401-S12-MB1-27.387 ($\sigma_3 = 60$ MPa).

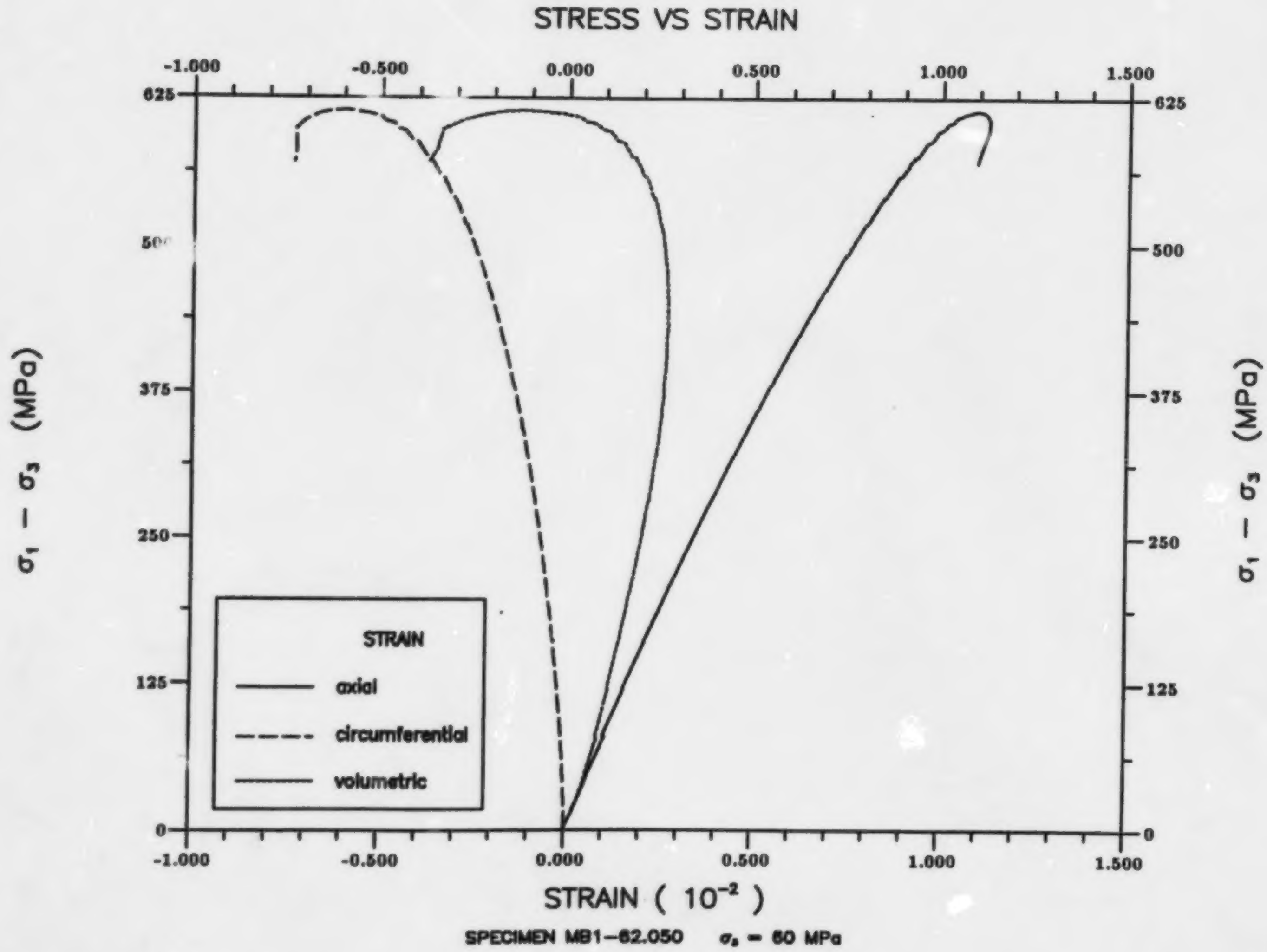

Figure 37. Stress-strain curves for specimen 401-S12-MB1-62.050 ($\sigma_3 = 60$ MPa).

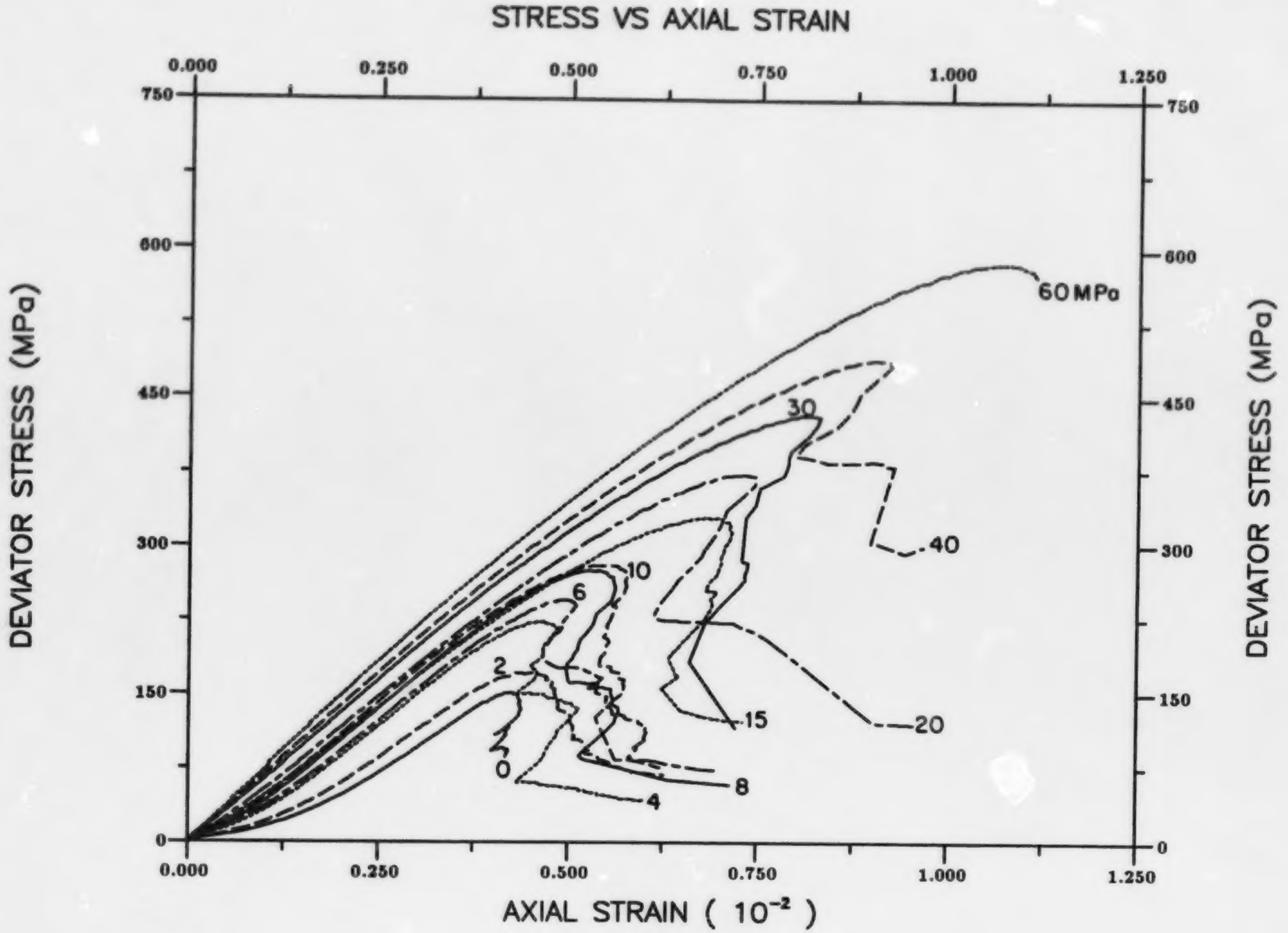

Figure 38. Stress versus axial strain curves (Group 1) of grey granite in uniaxial and triaxial compression.

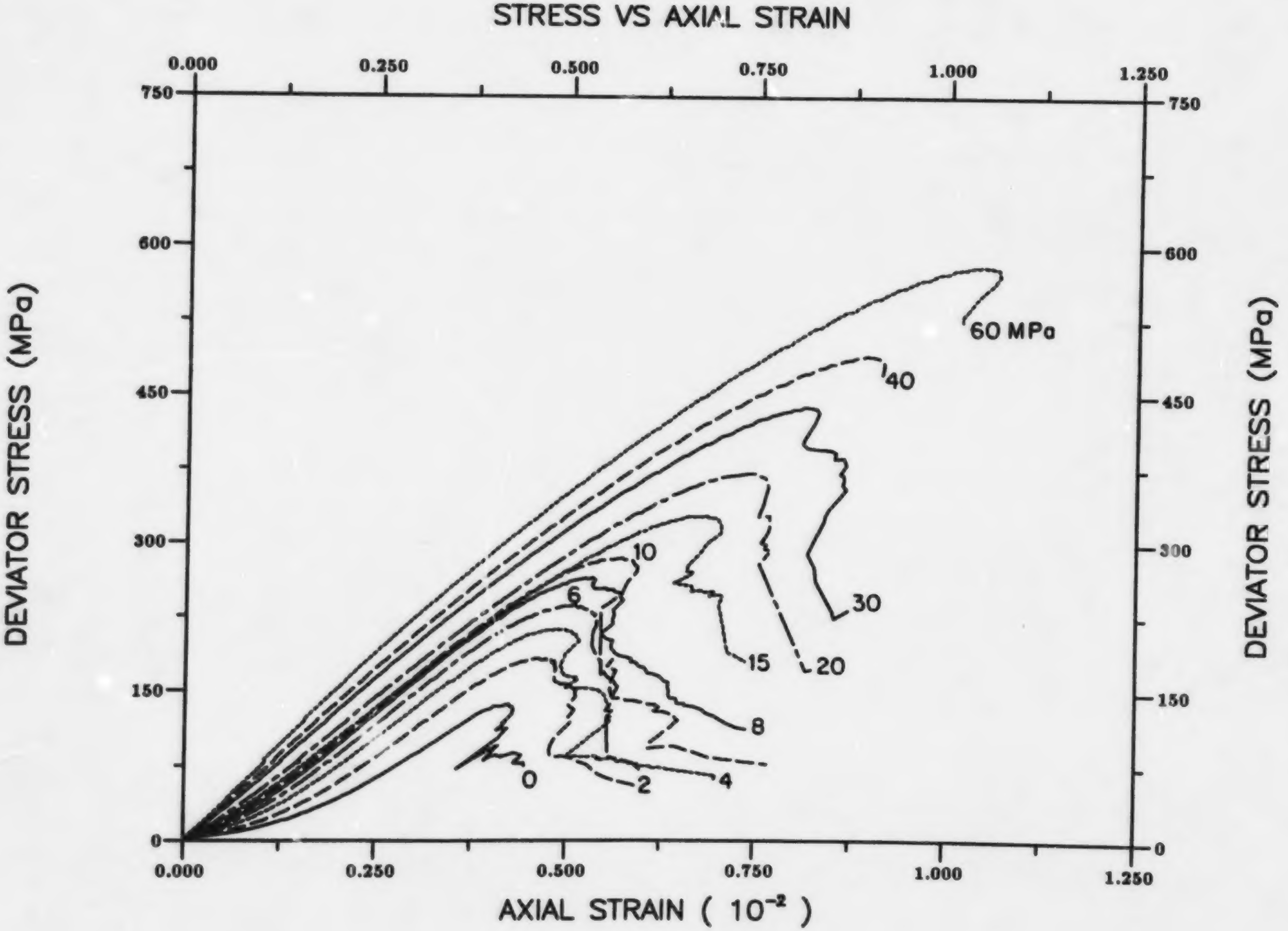

Figure 39. Stress versus axial strain curves (Group 2) of grey granite in uniaxial and triaxial compression.

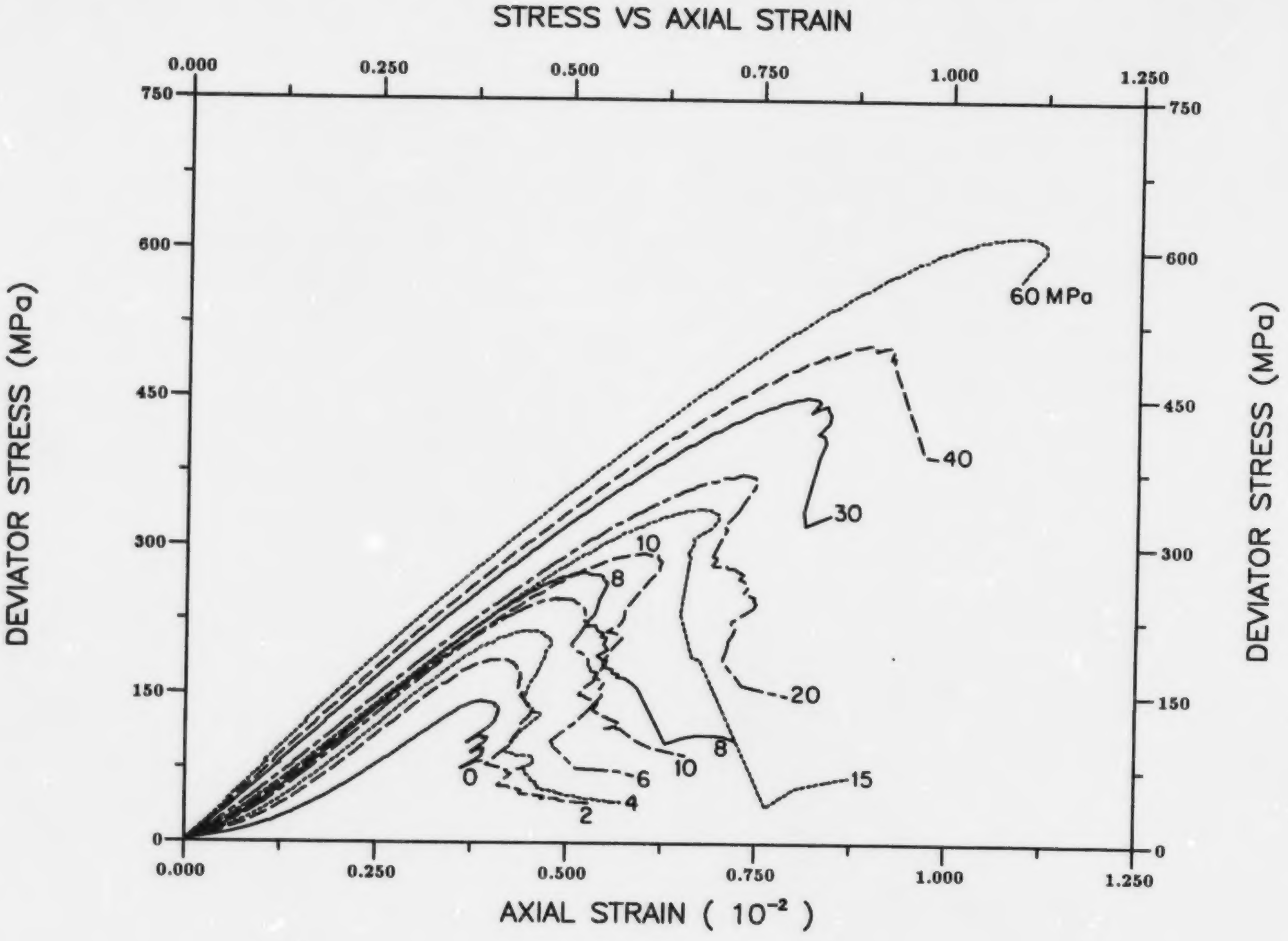

Figure 40. Stress versus axial strain curves (Group 3) of grey granite in uniaxial and triaxial compression.

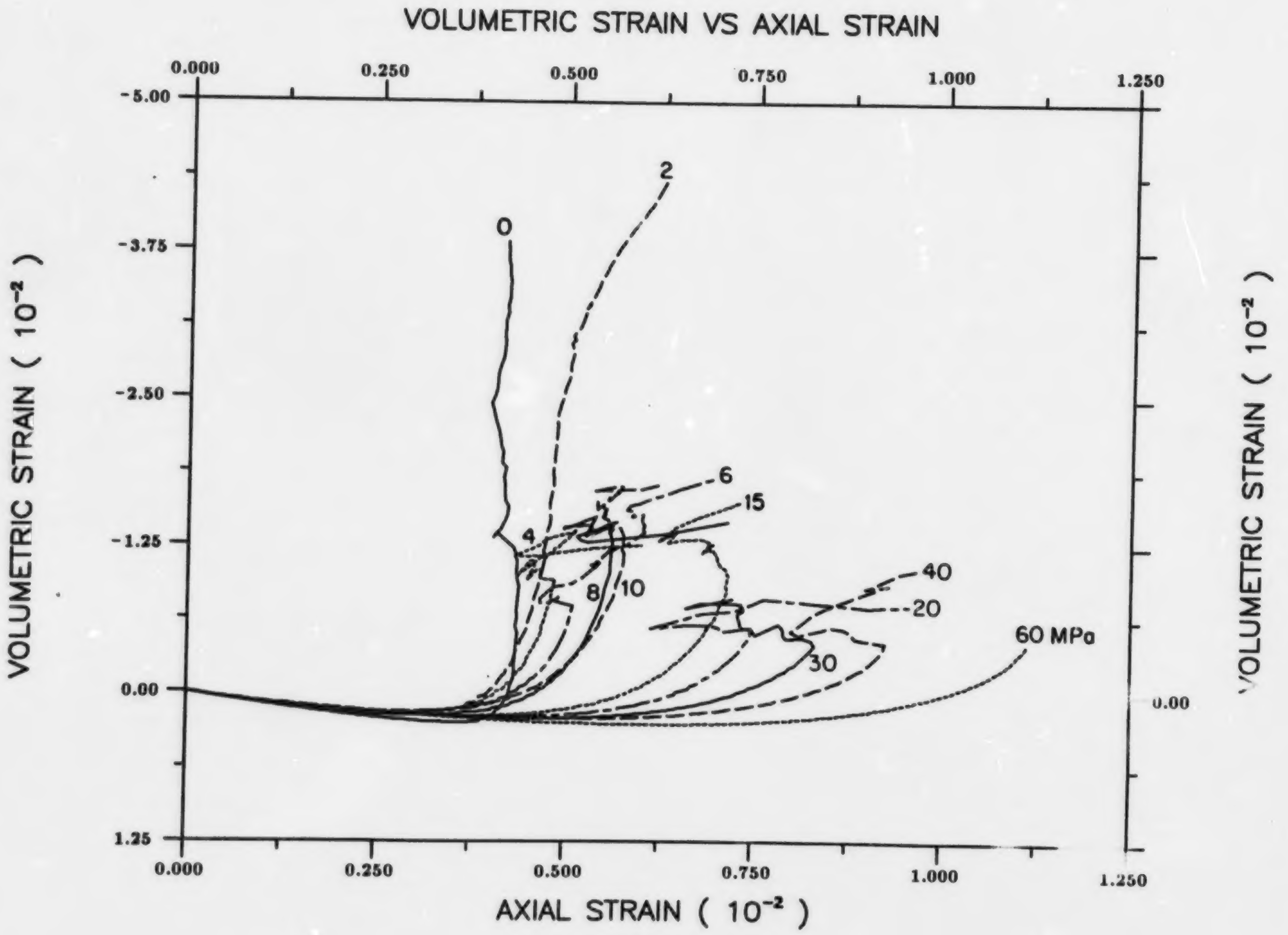

Figure 41. Volumetric strain versus axial strain curves (Group 1) of grey granite in uniaxial and triaxial compression.

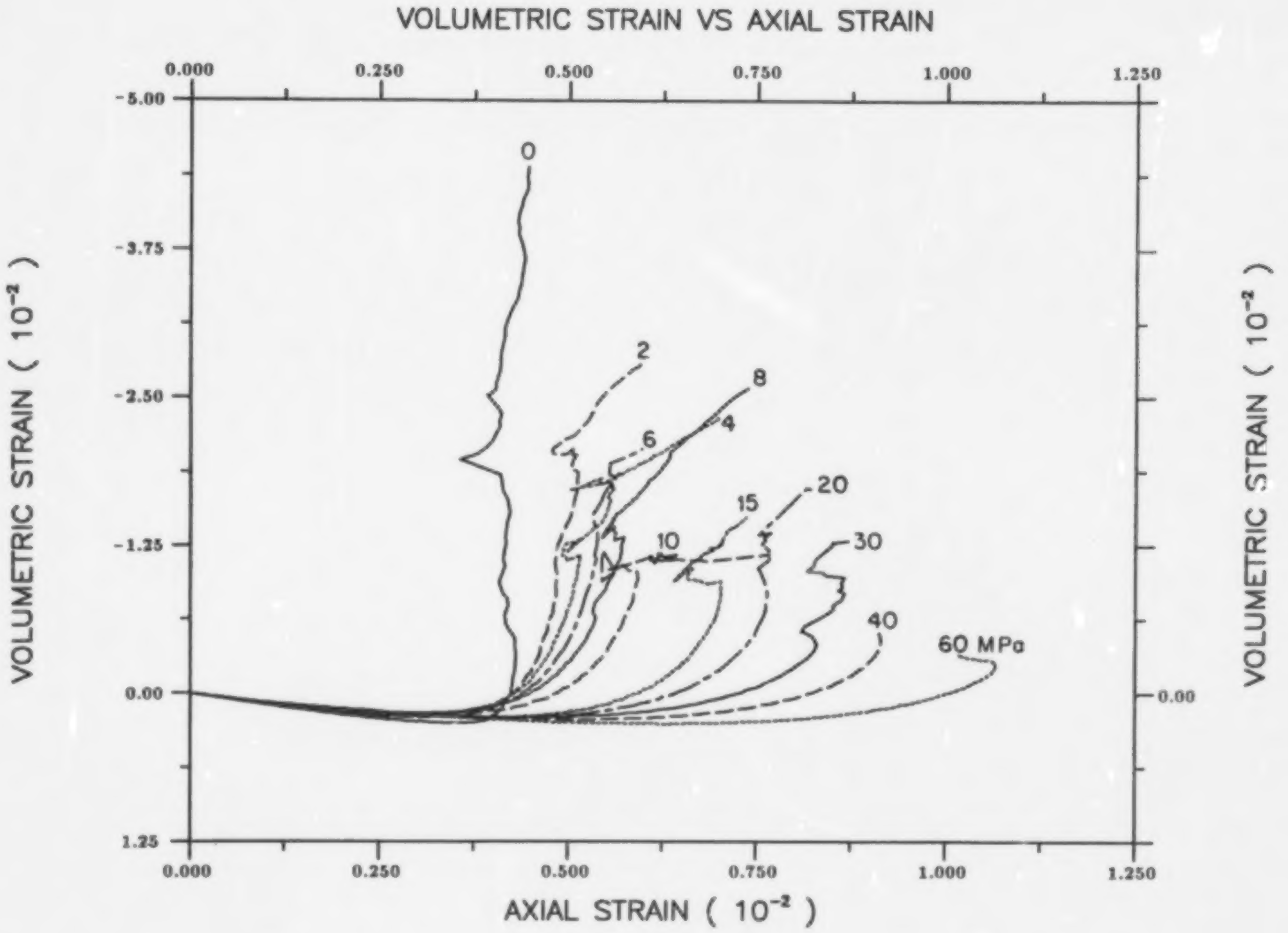

Figure 42. Volumetric strain versus axial strain curves (Group 2) of grey granite in uniaxial and triaxial compression.

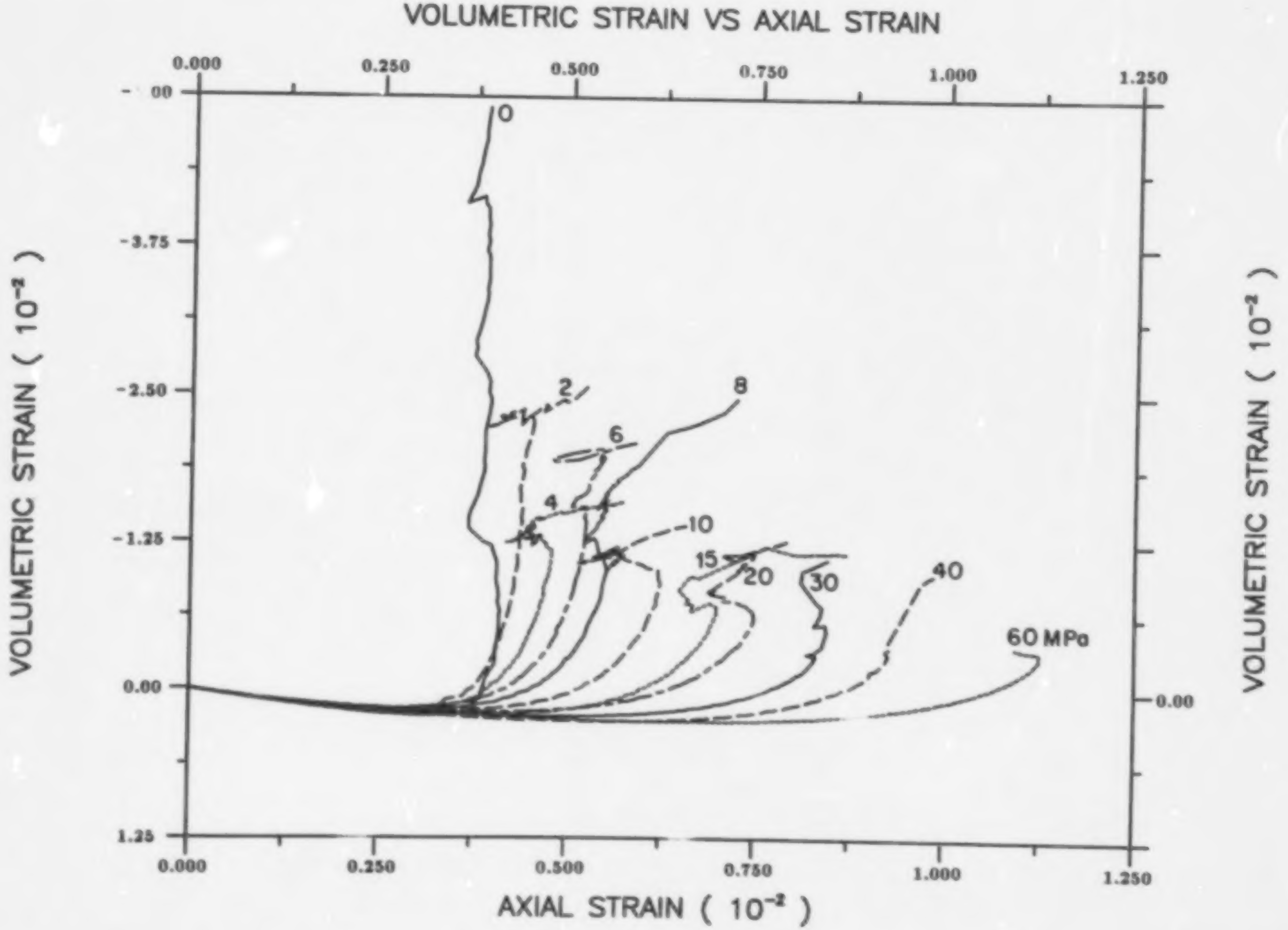

Figure 43. Volumetric strain versus axial strain curves (Group 3) of grey granite in uniaxial and triaxial compression.

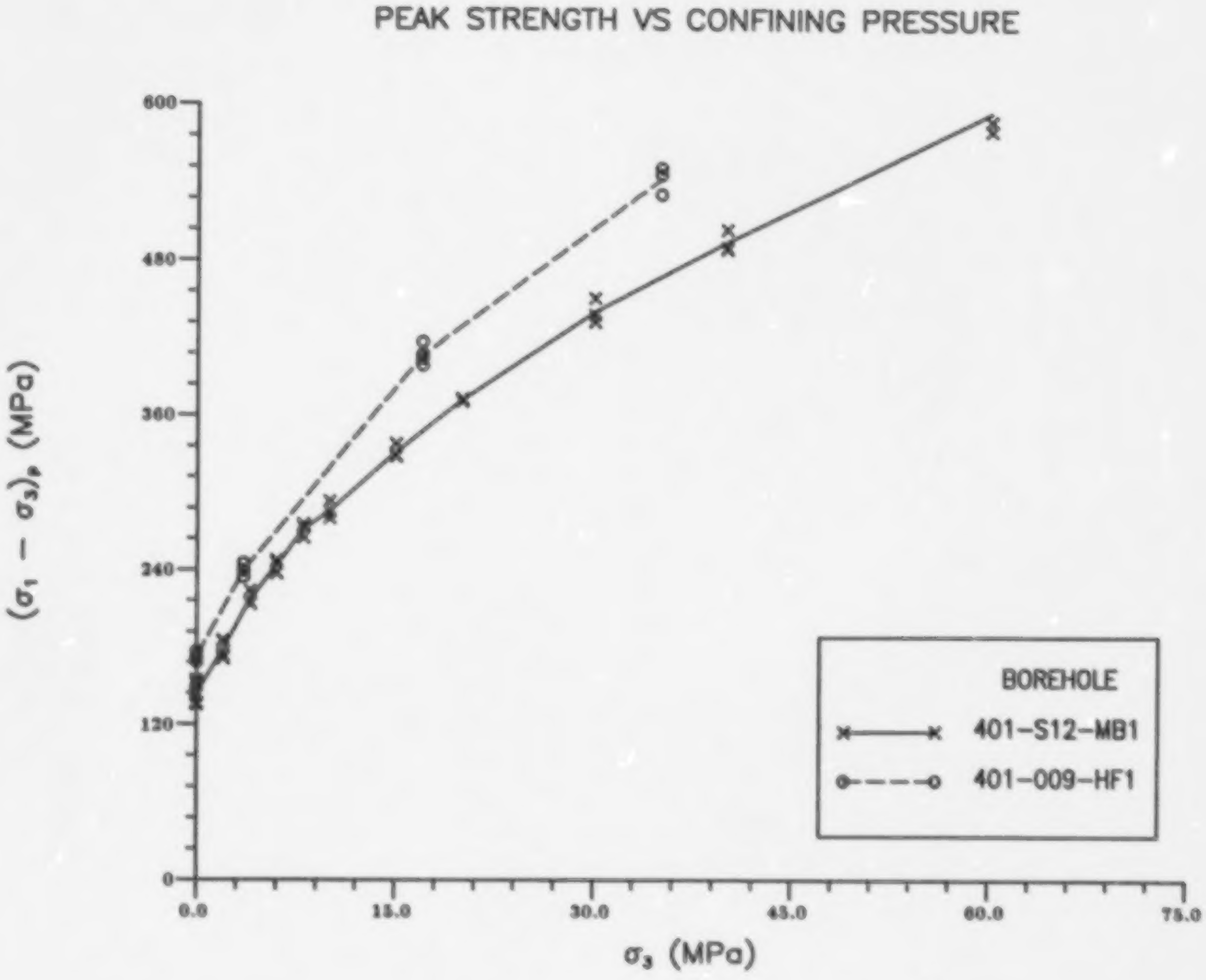

Figure 44. Plots of deviator stress at peak strength versus confining pressure.

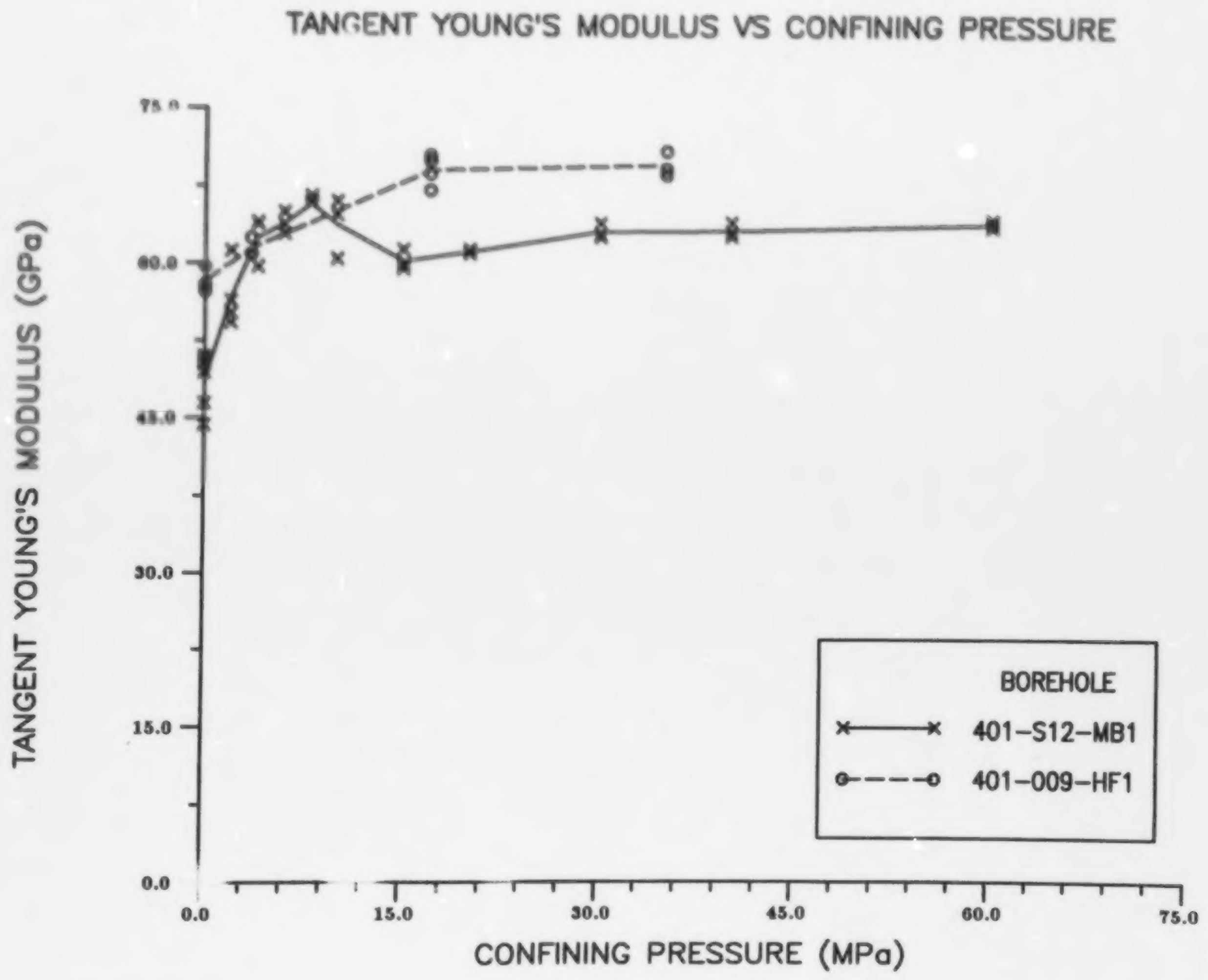

Figure 45. Plots of tangent Young's modulus (E) versus confining pressure.

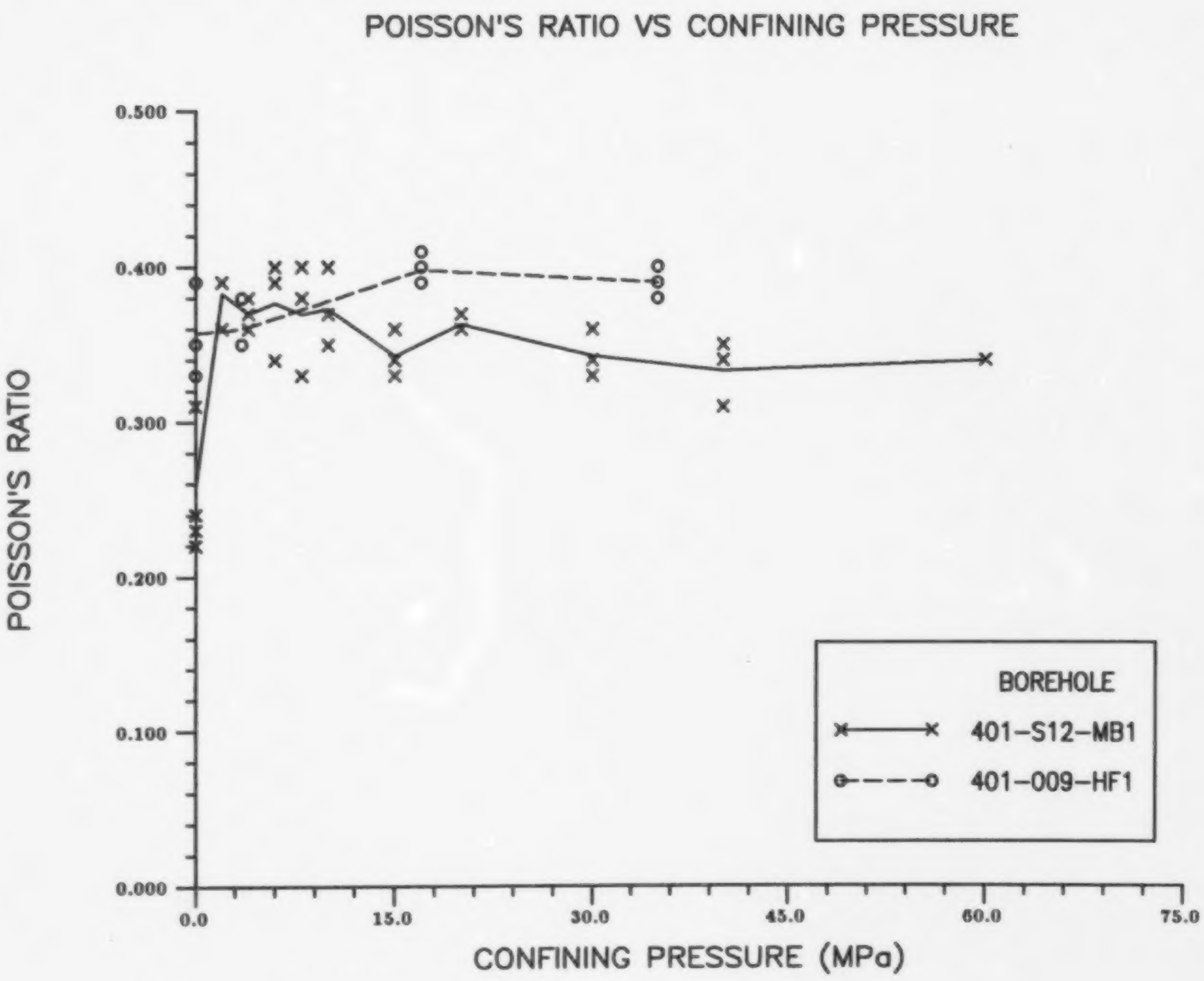

Figure 46. Plots of Poisson's ratio (ν) versus confining pressure.

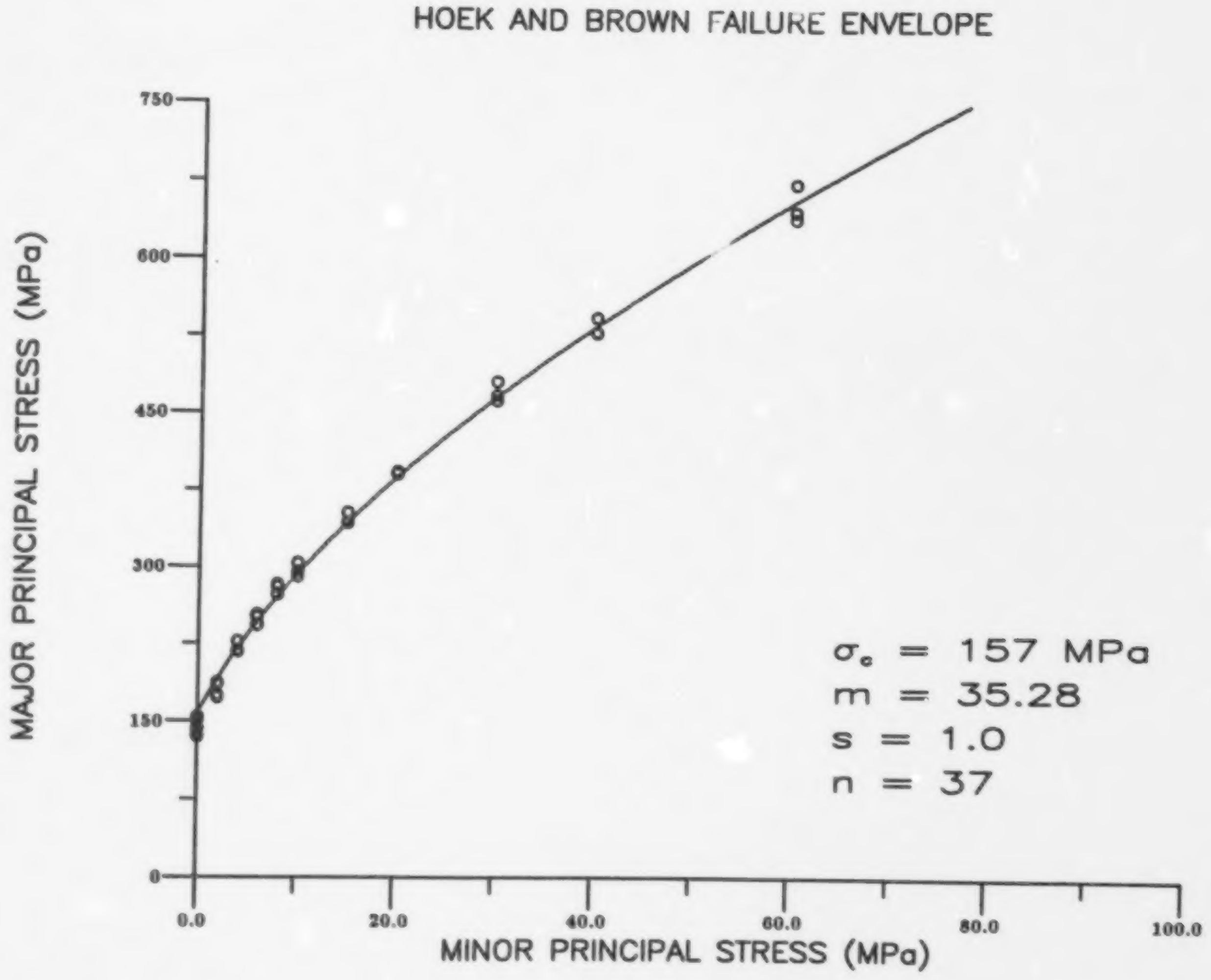

Figure 47. Hoek and Brown failure envelope.

APPENDIX A

Loading-unloading Curves

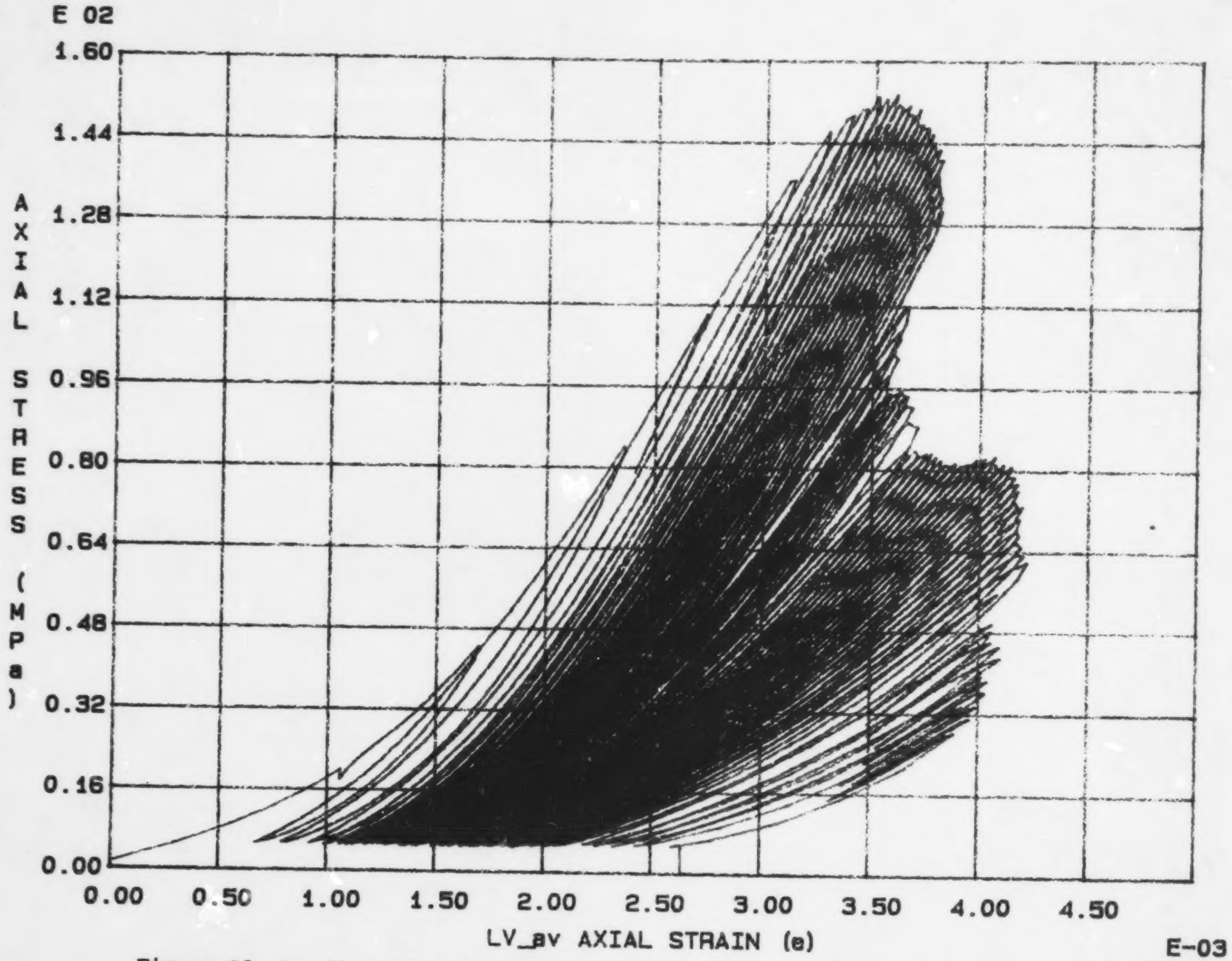

Figure A1. Loading and unloading curves (axial strain) for Specimen MB1-21.065.

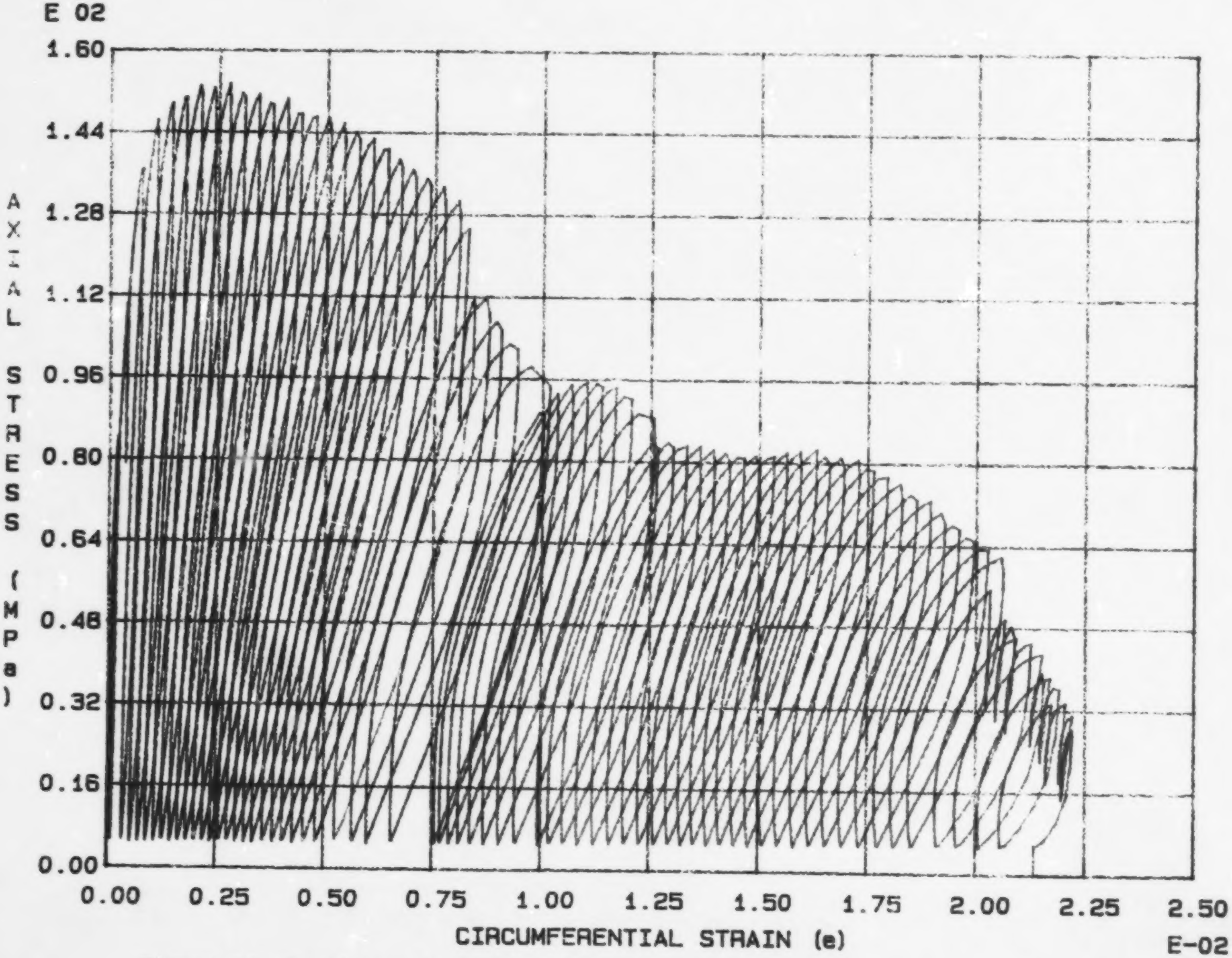

Figure A2. Loading and unloading curves (cir. strain) for Specimen MB1-21.065.

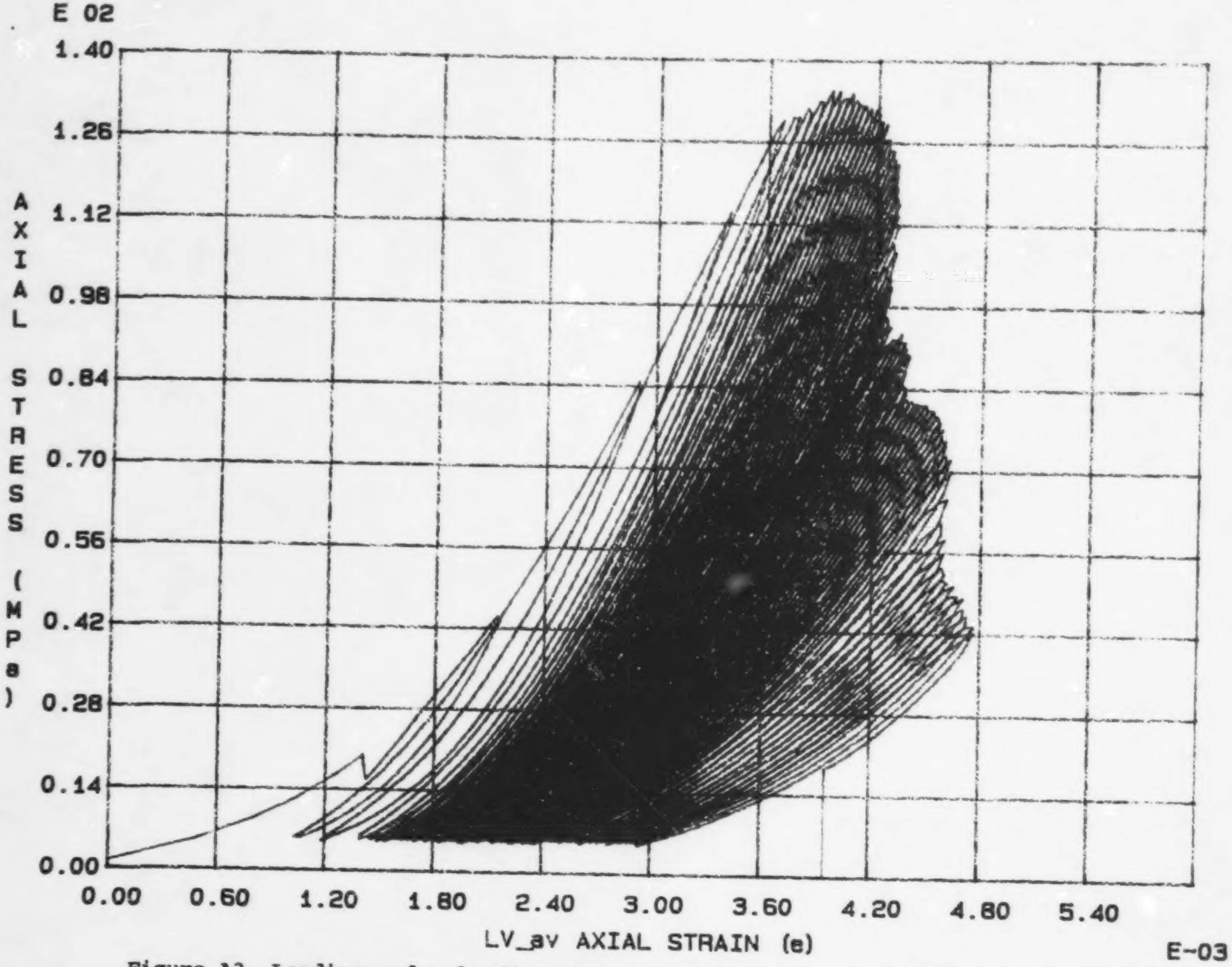

Figure A3. Loading and unloading curves (axial strain) for Specimen MB1-24.366.

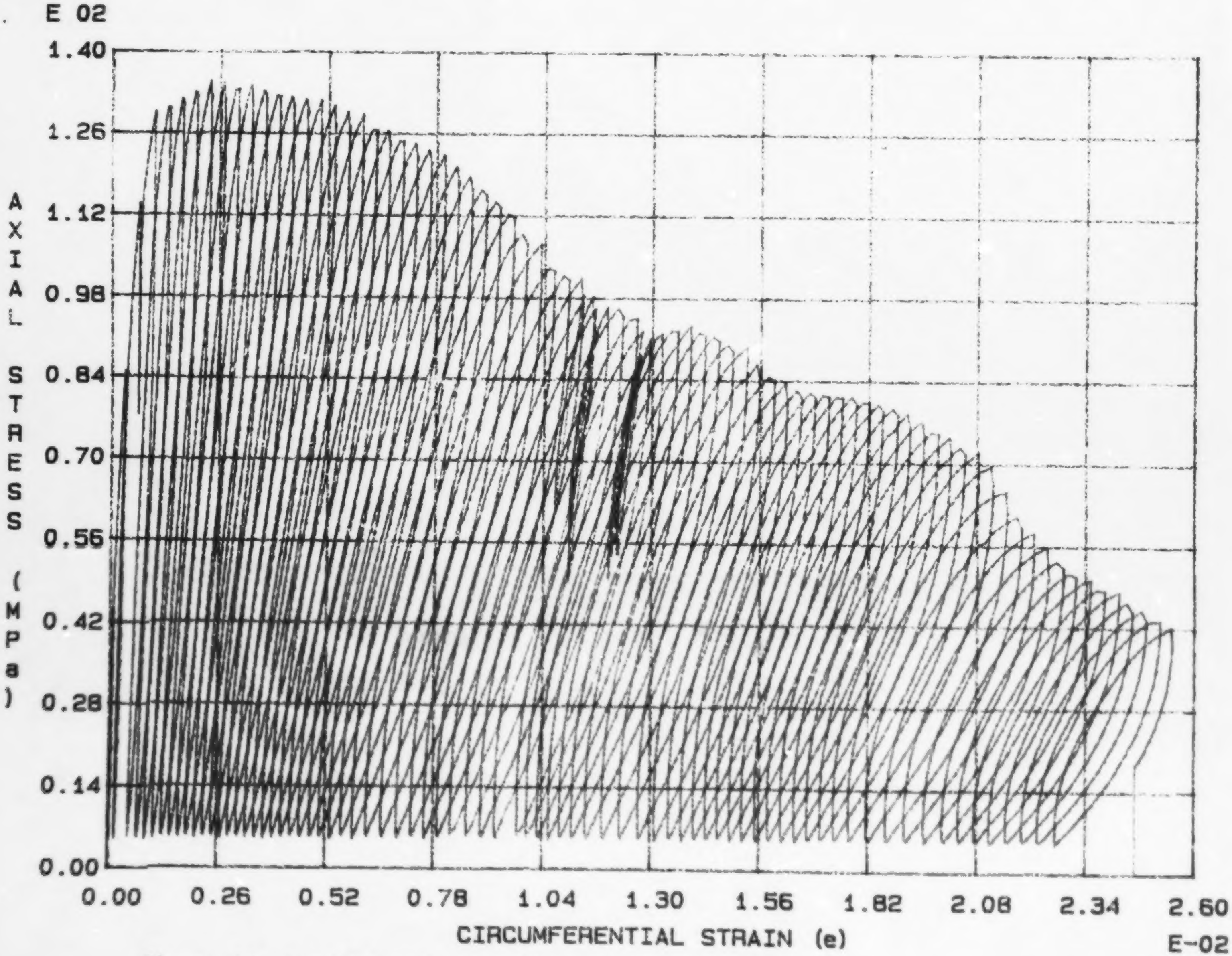

Figure A4. Loading and unloading curves (cir. strain) for Specimen MB1-24.366.

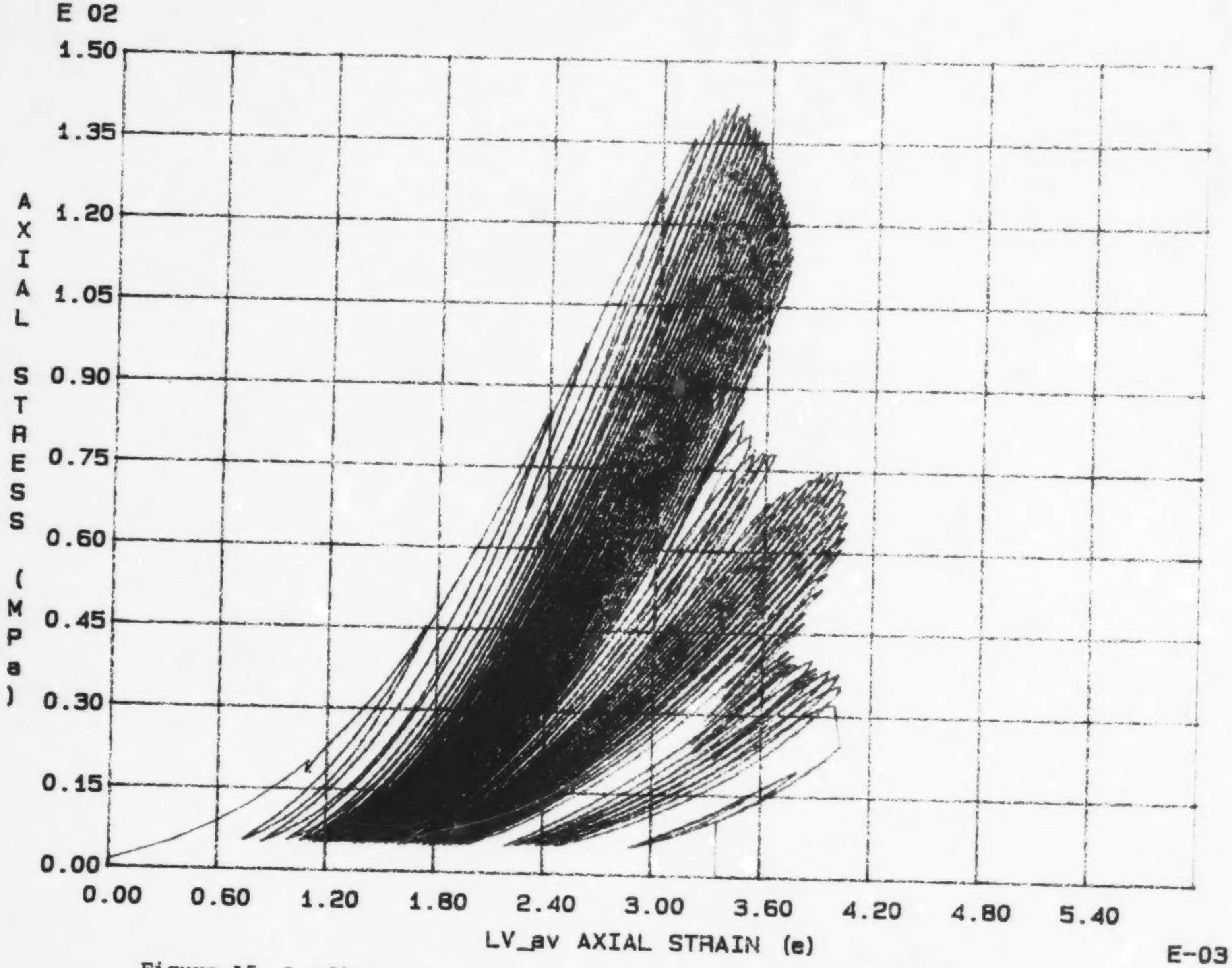

Figure A5. Loading and unloading curves (axial strain) for Specimen MB1-29.645.

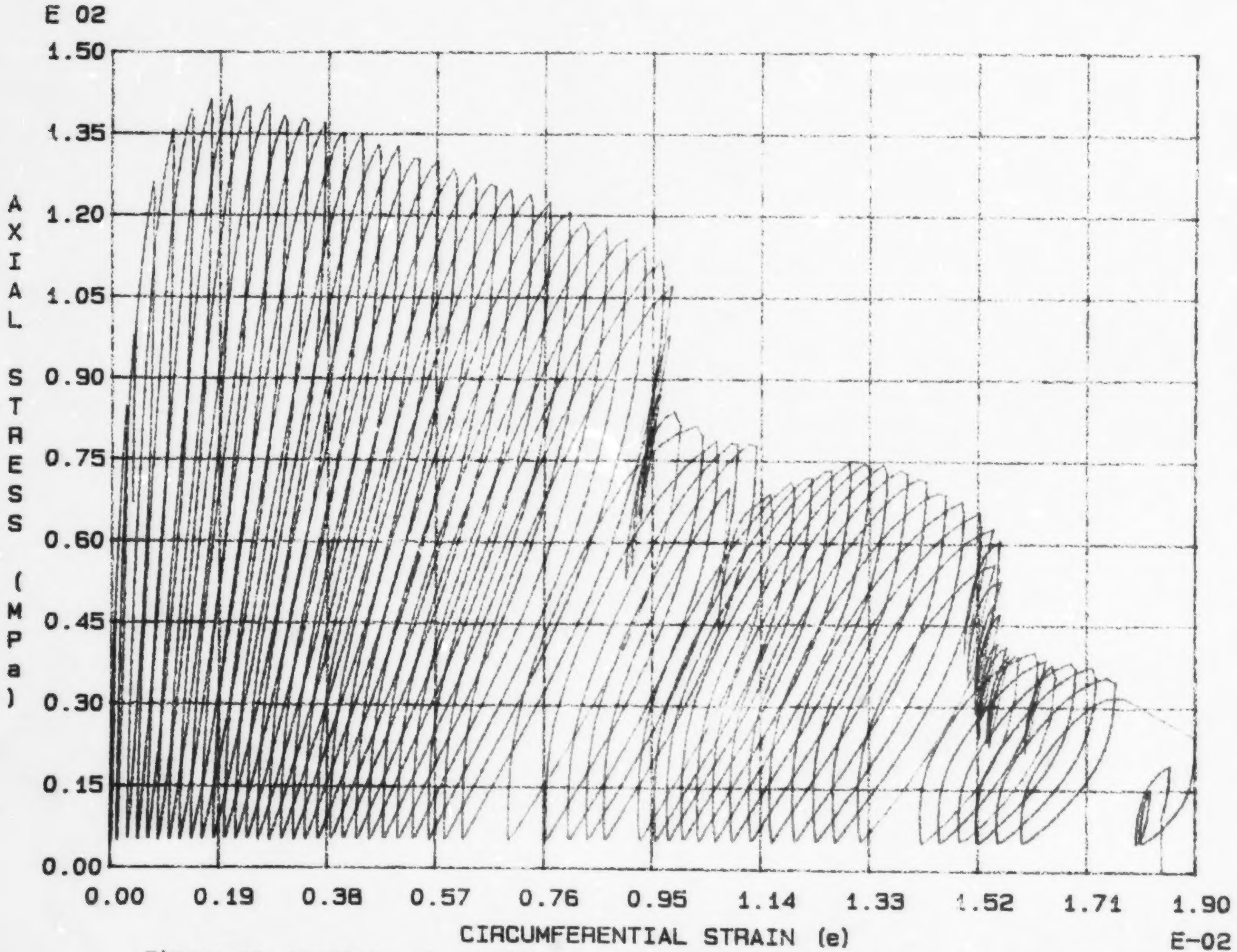

Figure A6. Loading and unloading curves (cir. strain) for Specimen MB1-29.645.

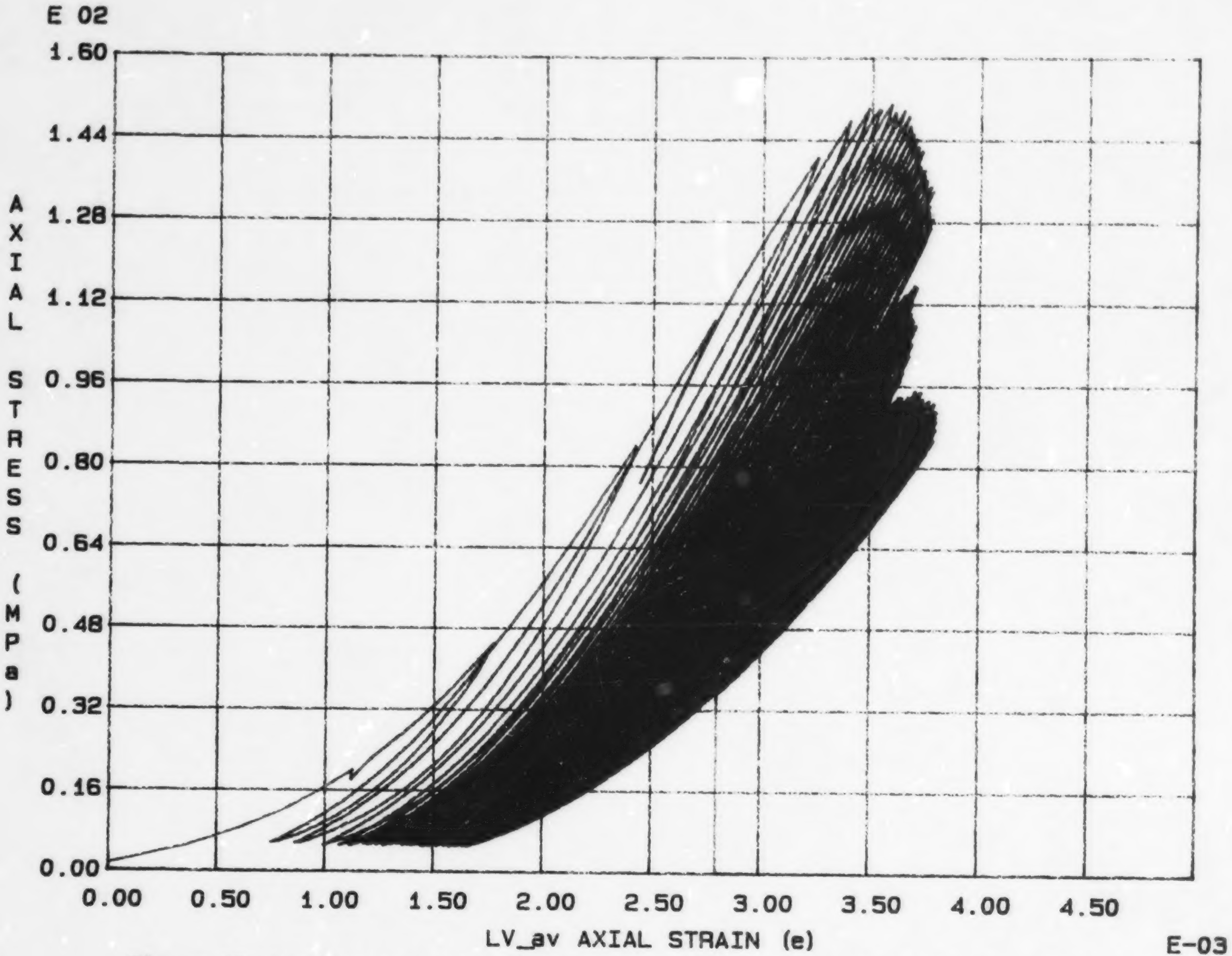

Figure A7. Loading and unloading curves (axial strain) for Specimen MB1-21.227.

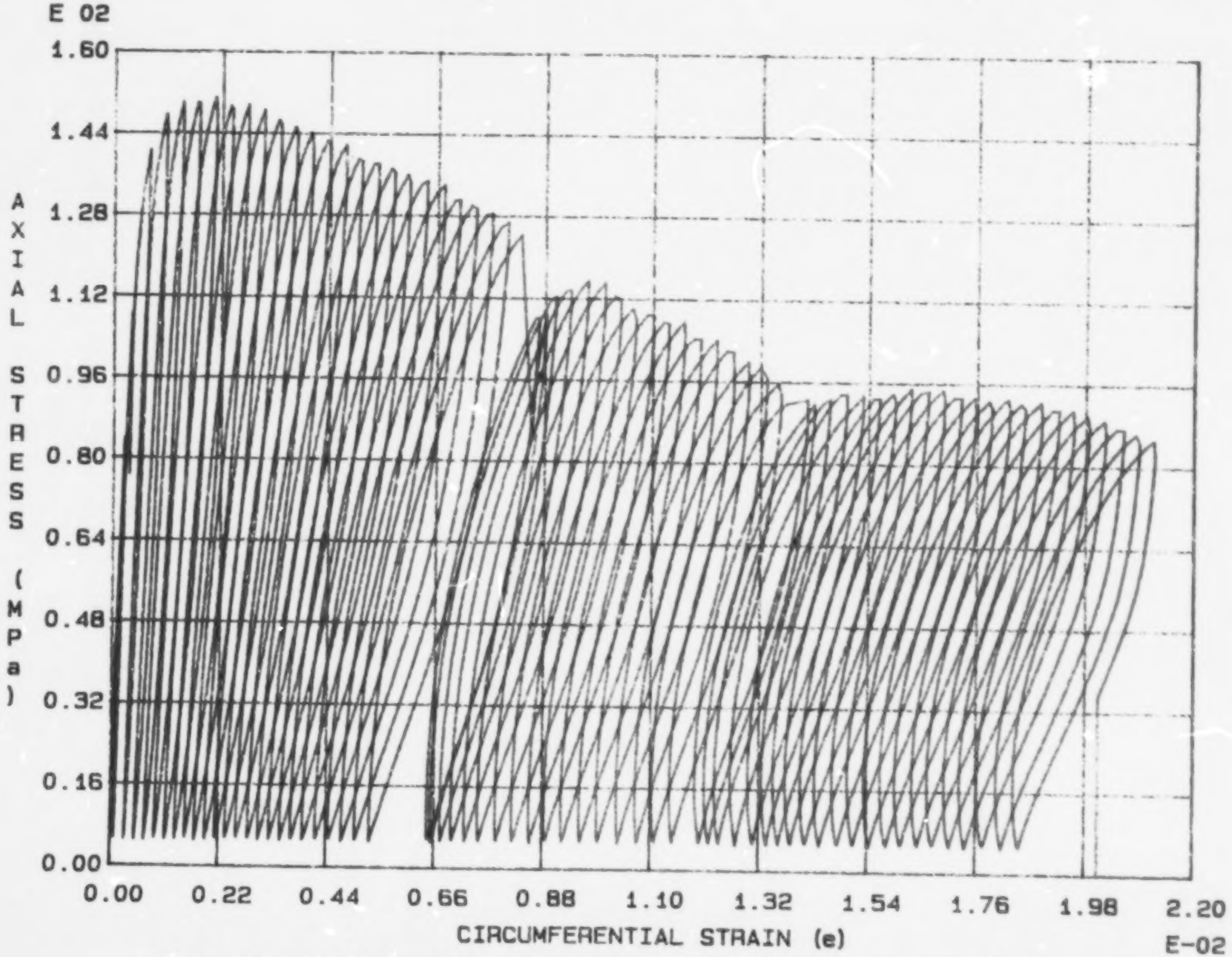

Figure A8. Loading and unloading curves (cir. strain) for Specimen MB1-21.227.

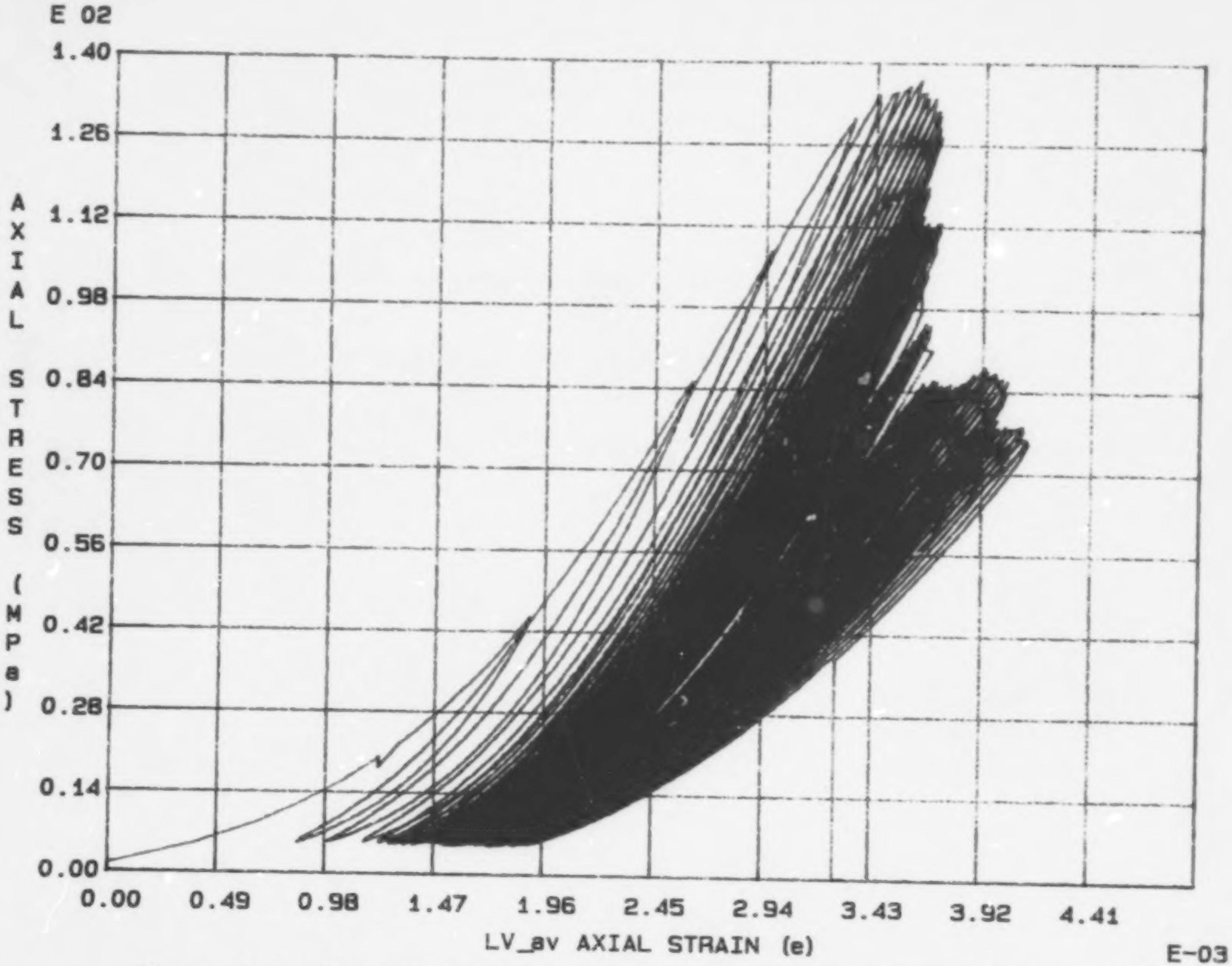

Figure A9. Loading and unloading curves (axial strain) for Specimen MB1-27.547.

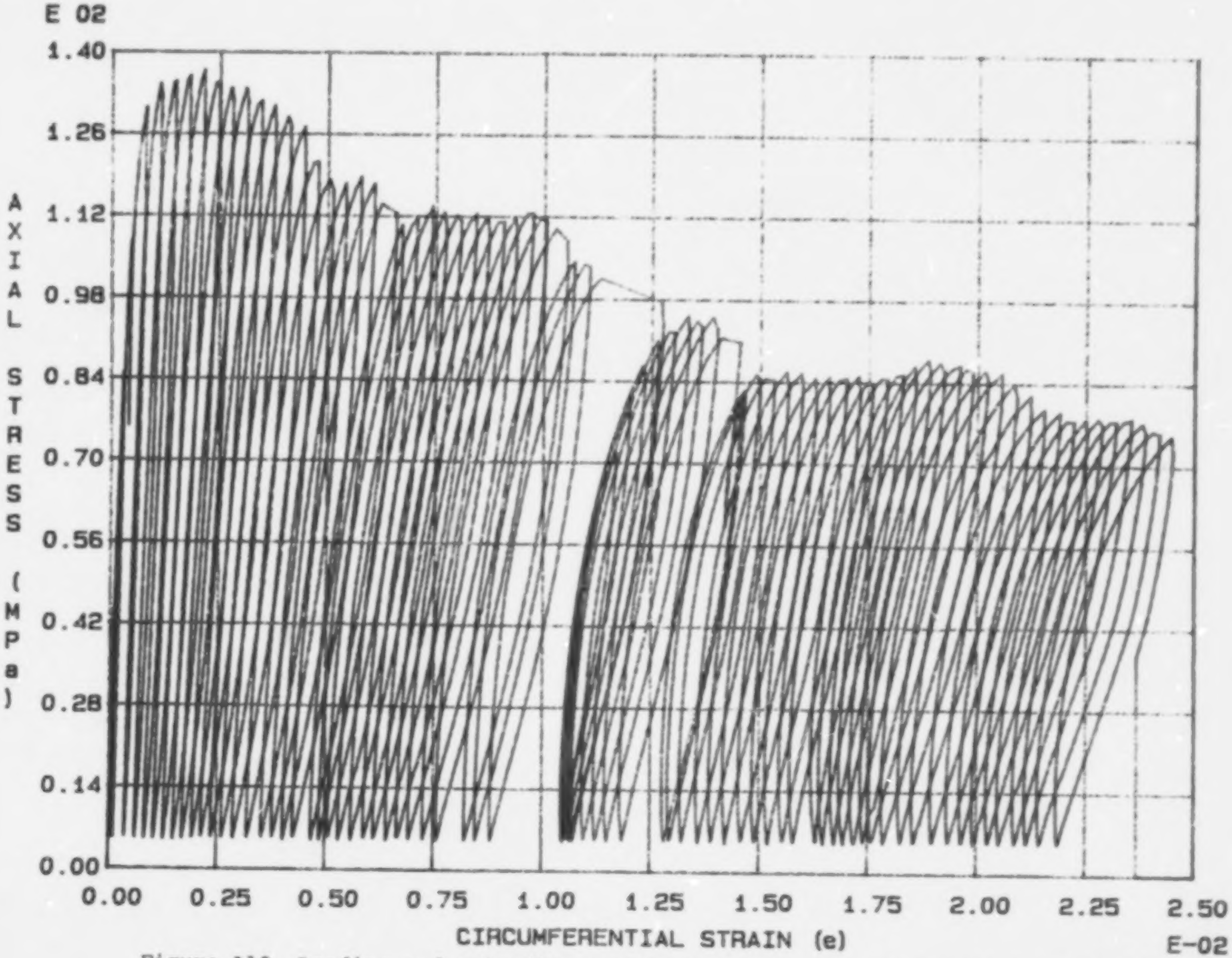

Figure A10. Loading and unloading curves (cir. strain) for Specimen MB1-27.547.

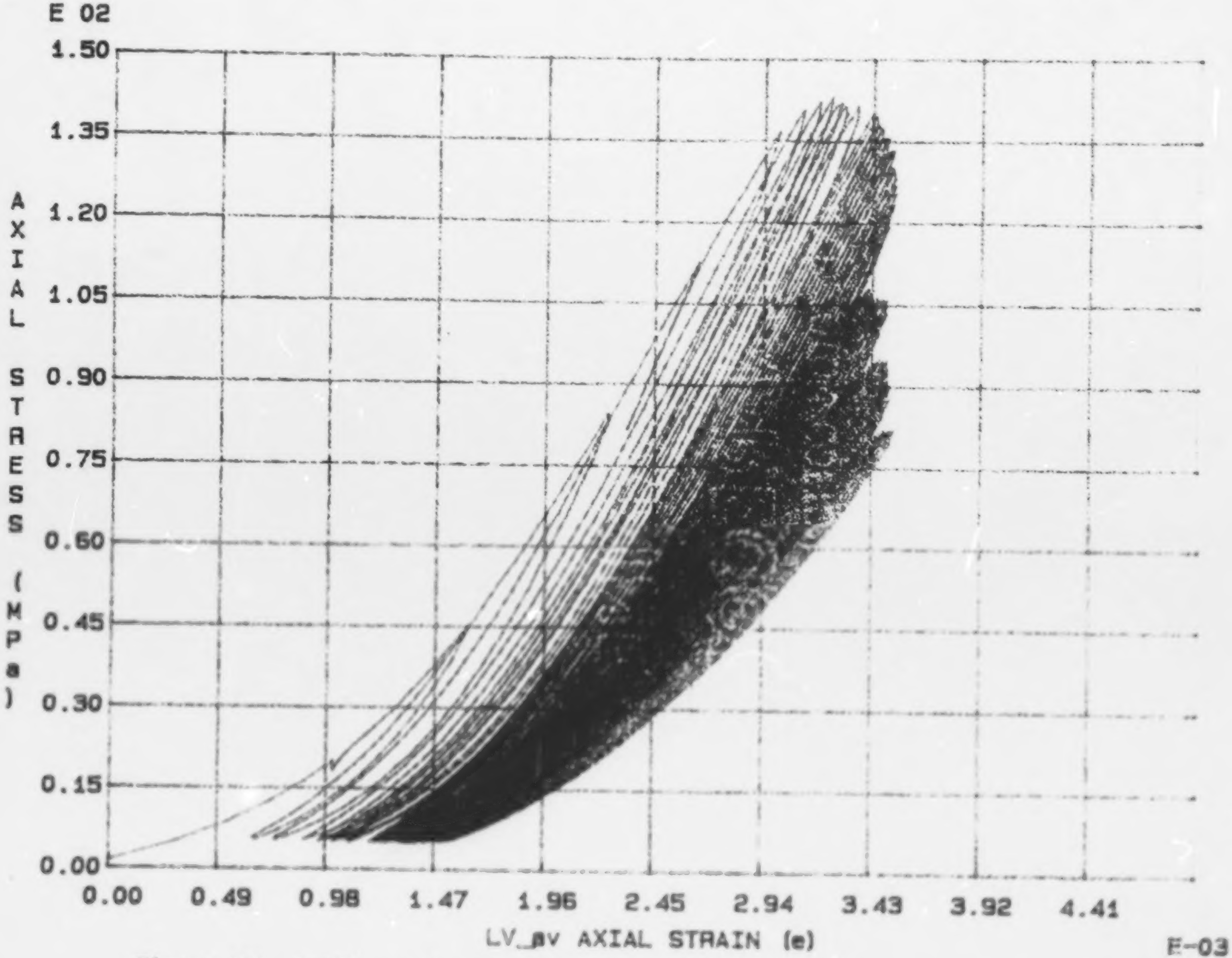

Figure A11. Loading and unloading curves (axial strain) for Specimen MB1-40.053.

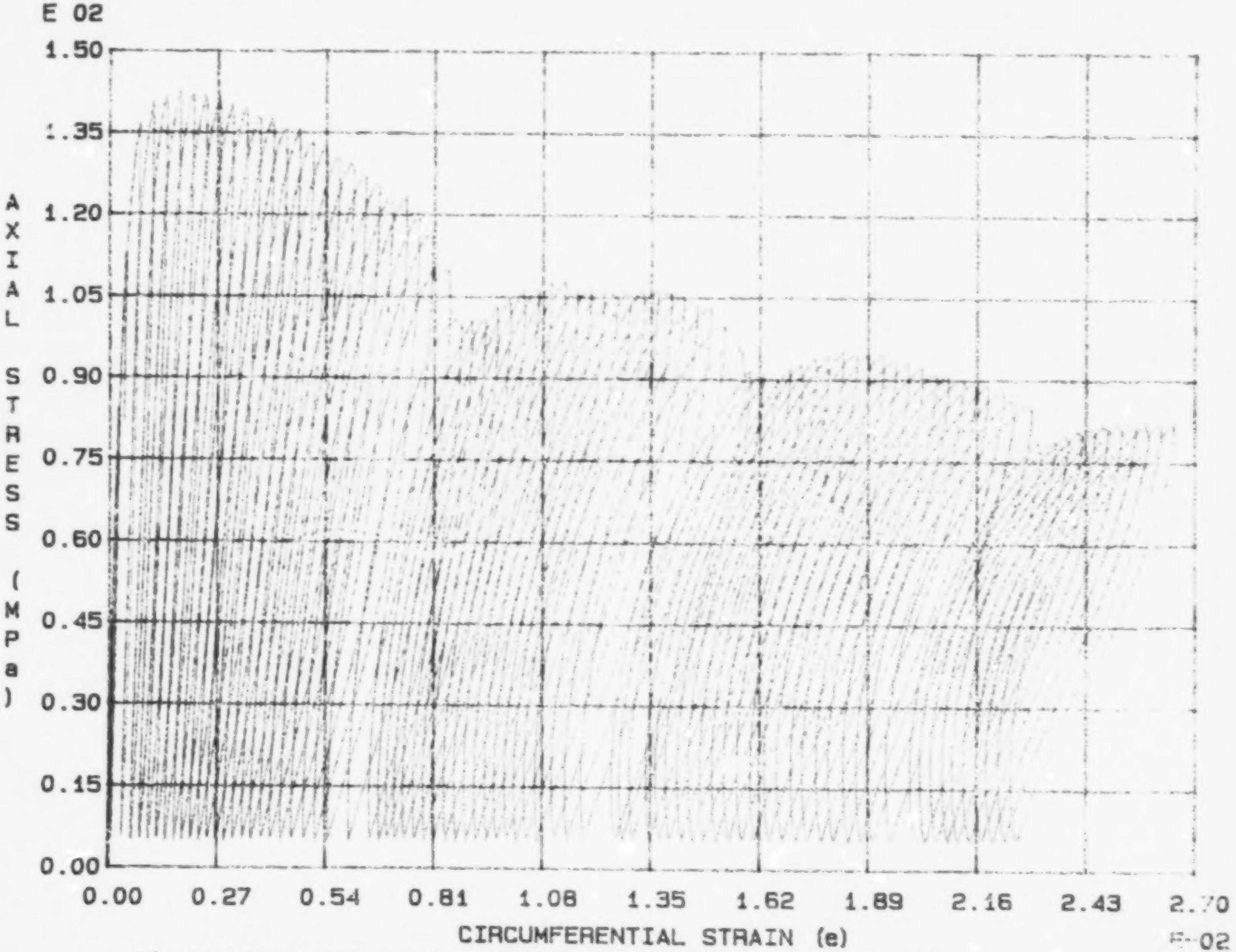

Figure A12. Loading and unloading curves (cir. strain) for Specimen MB1-40.053.

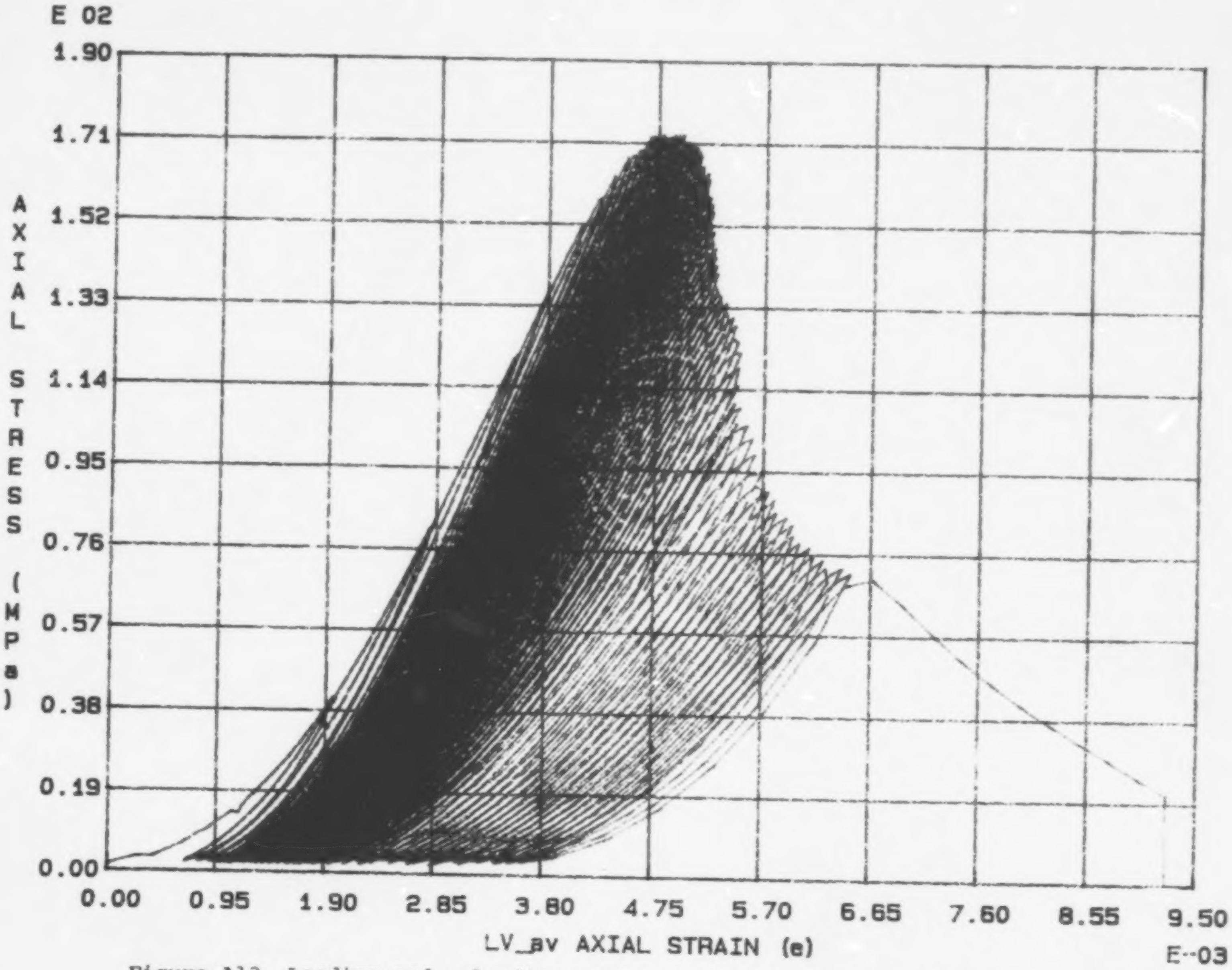

Figure A13. Loading and unloading curves (axial strain) for Specimen MB1-23.526.

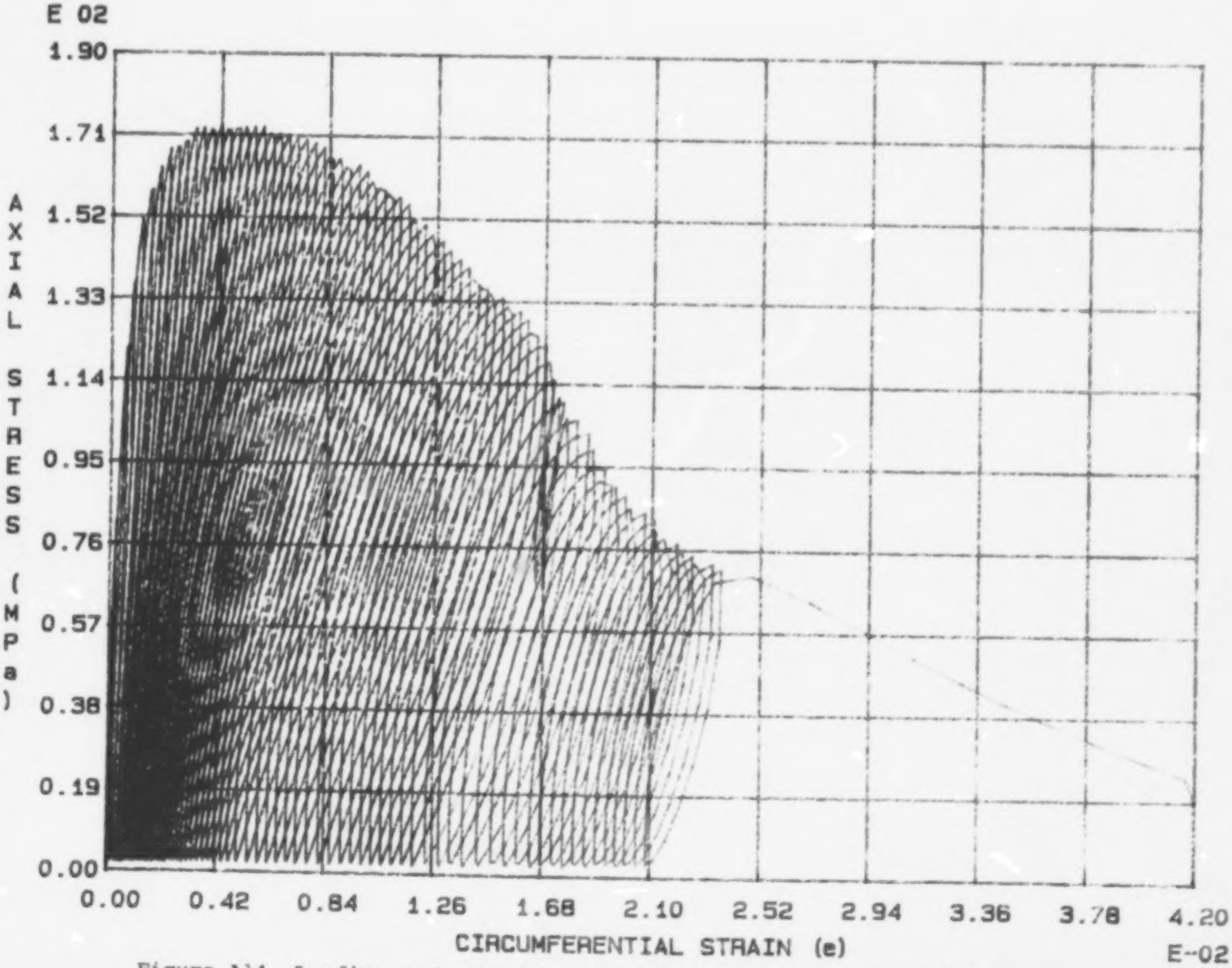

Figure A14. Loading and unloading curves (cir. strain) for Specimen MB1-23.526.

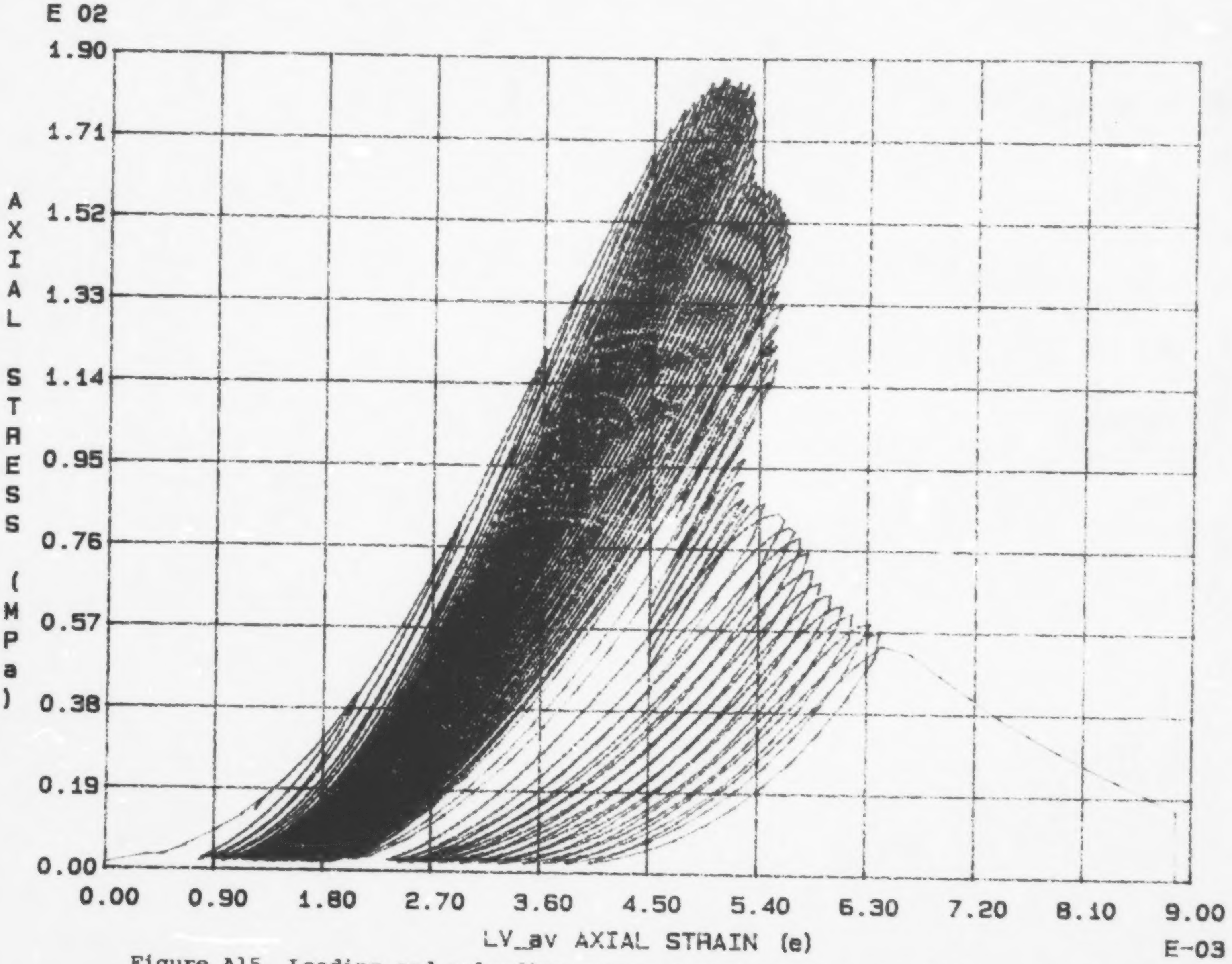

Figure A15. Loading and unloading curves (axial strain) for Specimen MB1-24.205.

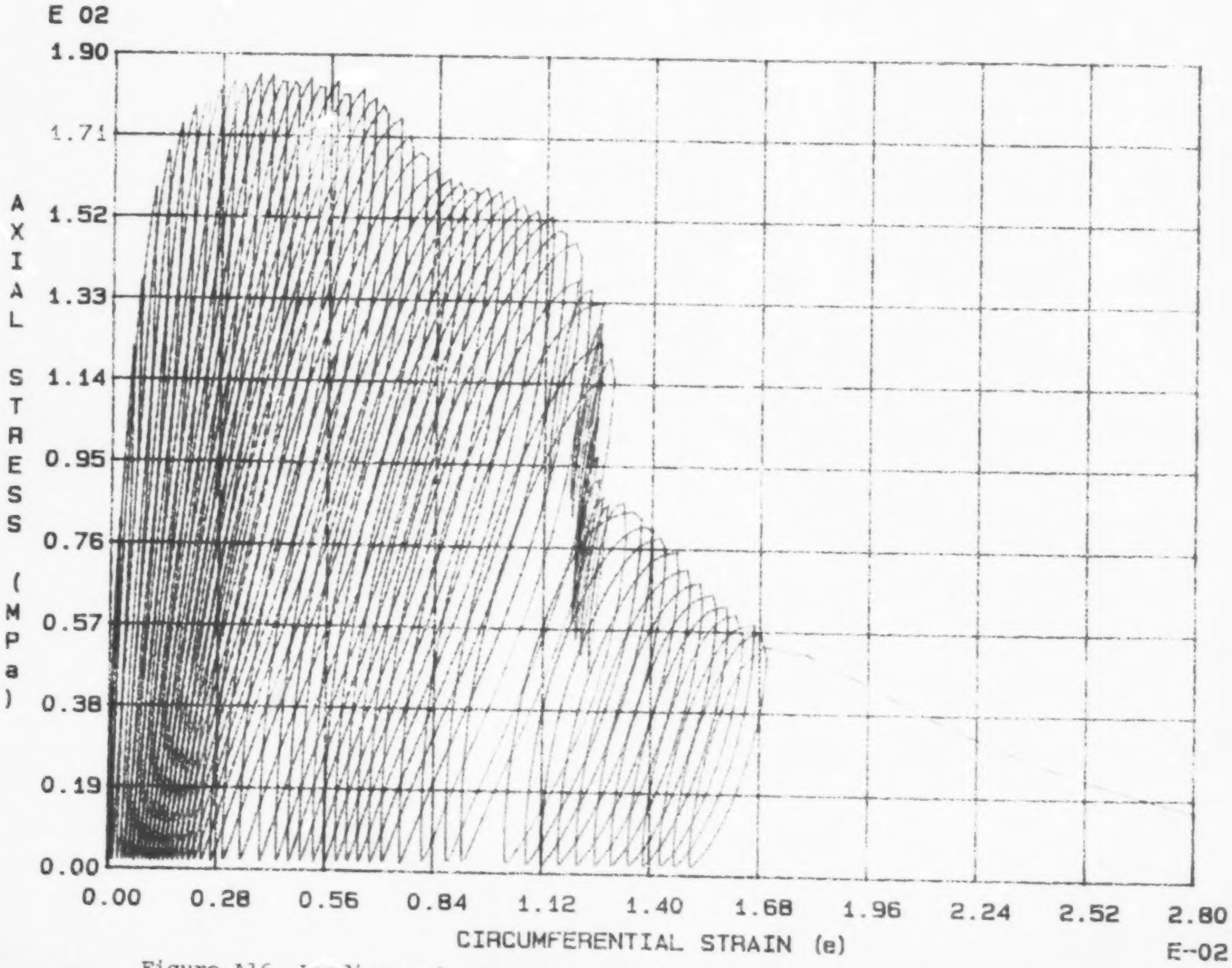

Figure A16. Loading and unloading curves (cir. strain) for Specimen MB1-24.205.

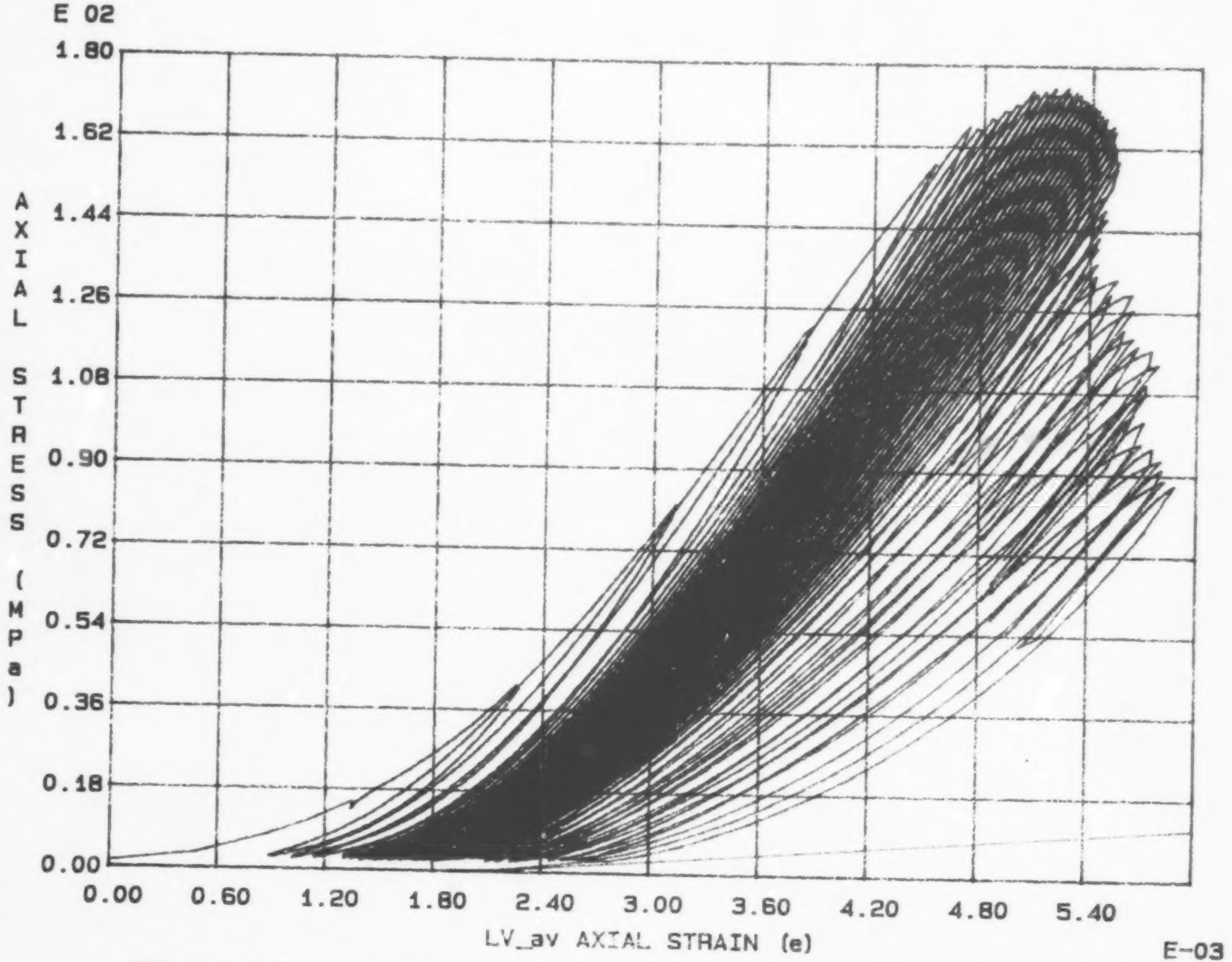

Figure A17. Loading and unloading curves (axial strain) for Specimen MB1-24.690.

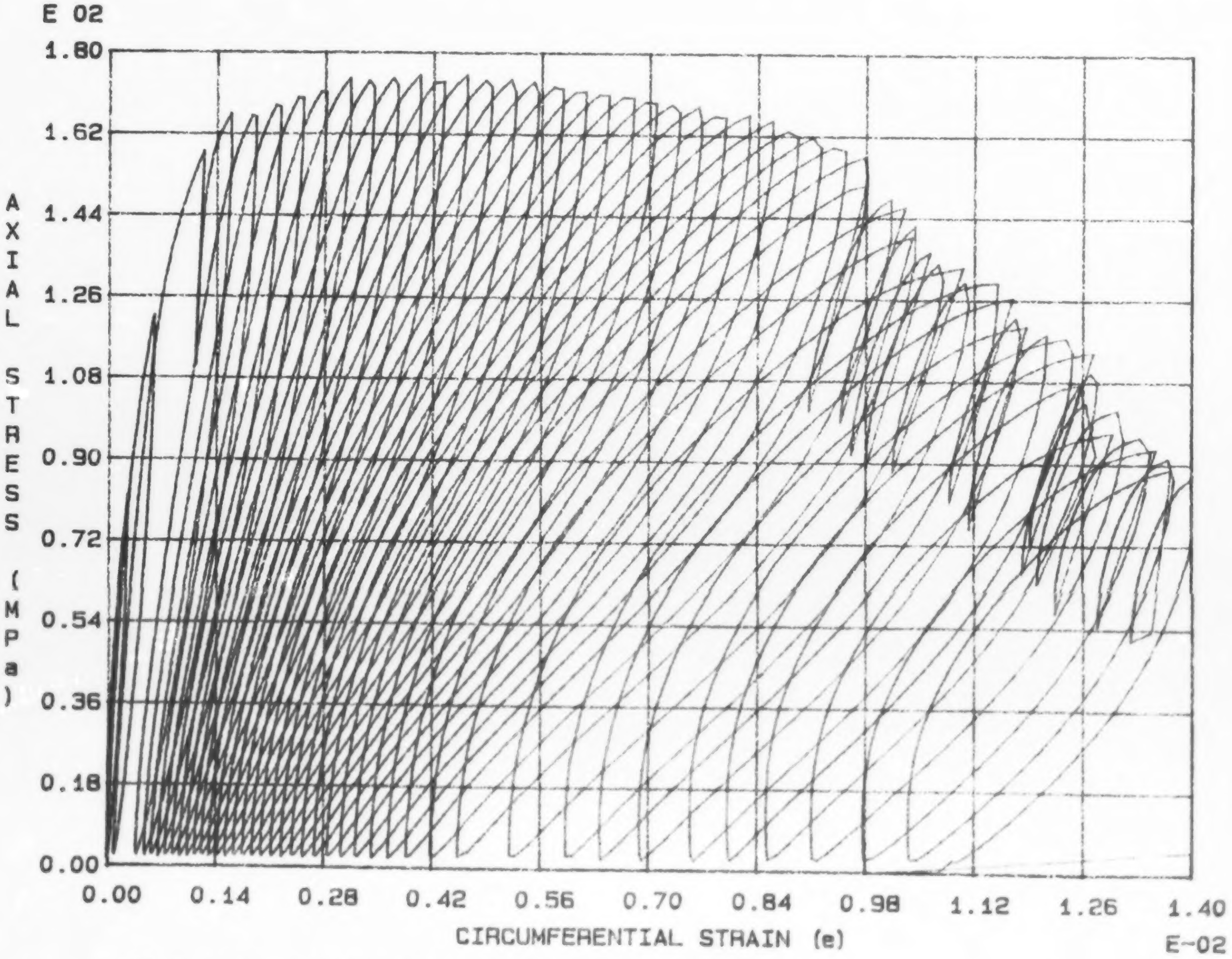

Figure A18. Loading and unloading curves (cir. strain) for Specimen MB1-24.690.

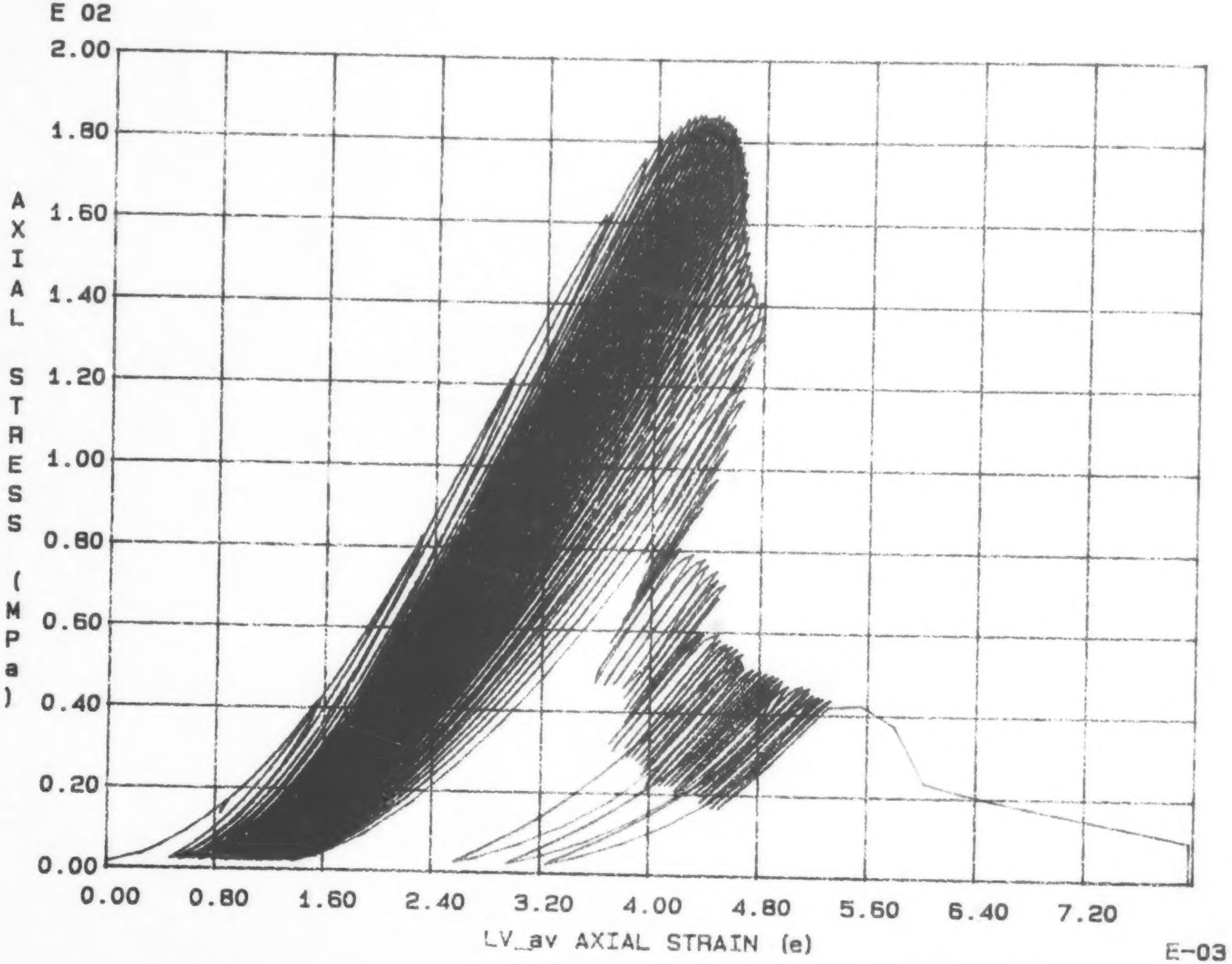

Figure A19. Loading and unloading curves (axial strain) for Specimen MB1-40.215.

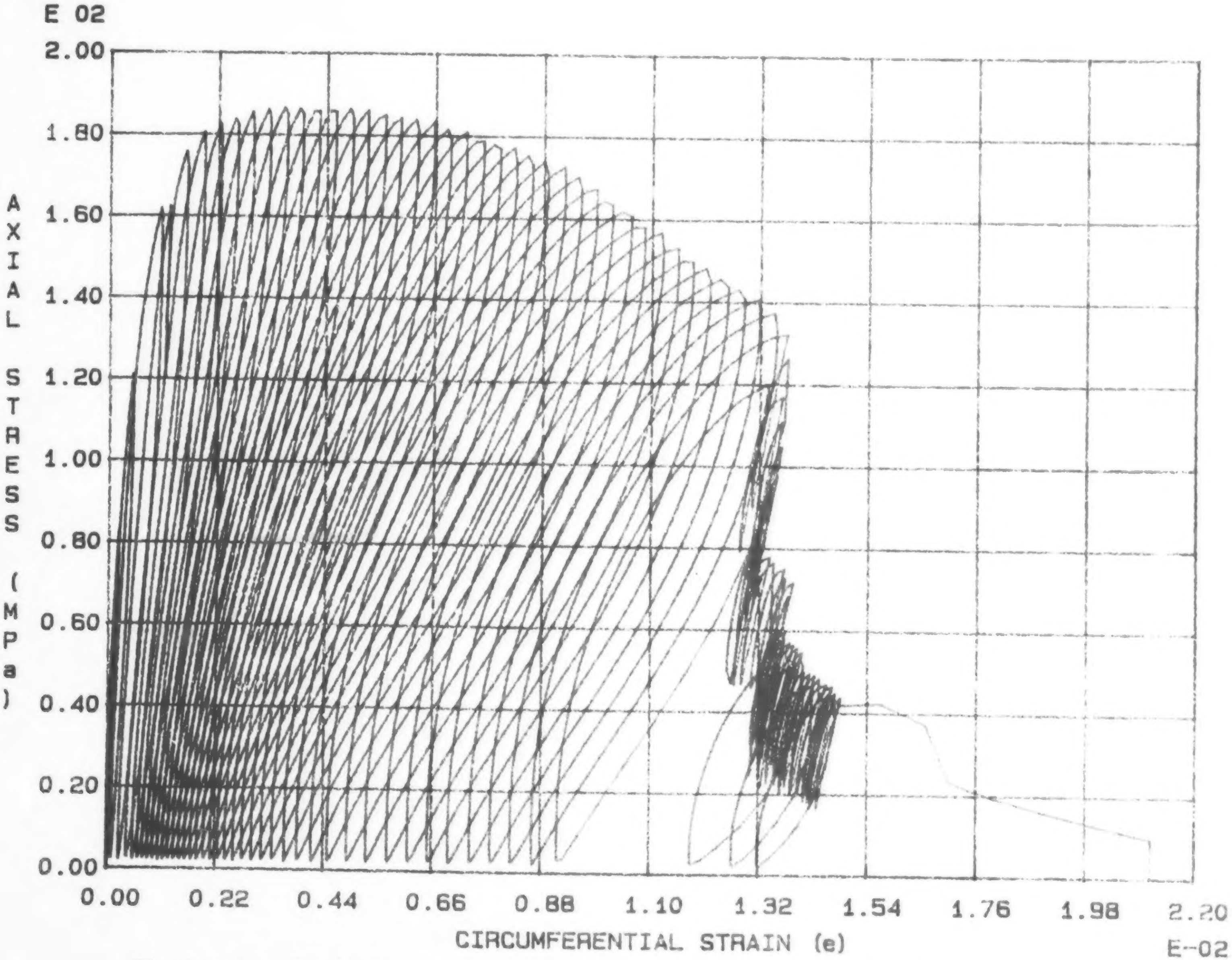

Figure A20. Loading and unloading curves (cir. strain) for Specimen MB1-40.215.

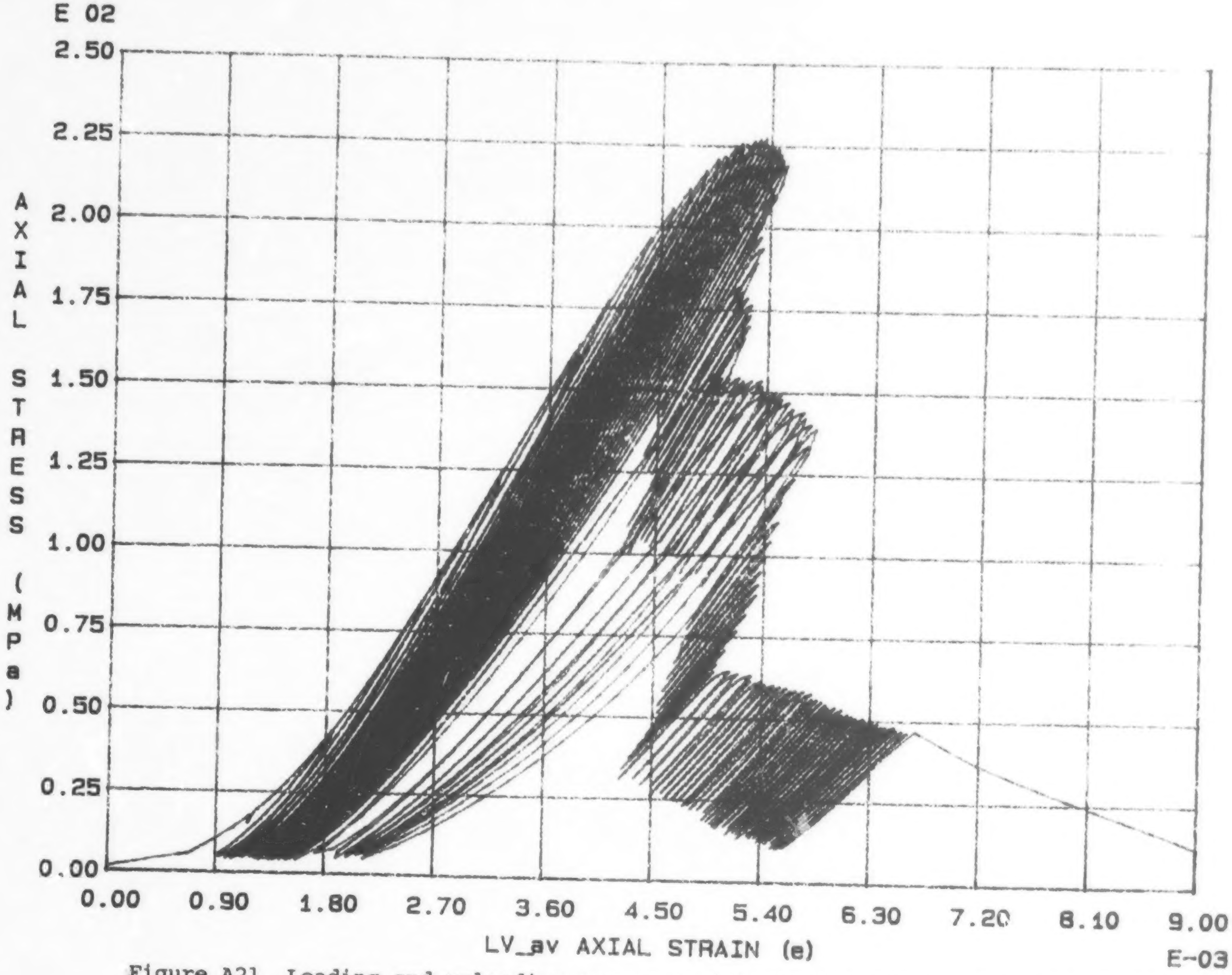

Figure A21. Loading and unloading curves (axial strain) for Specimen MB1-21.553.

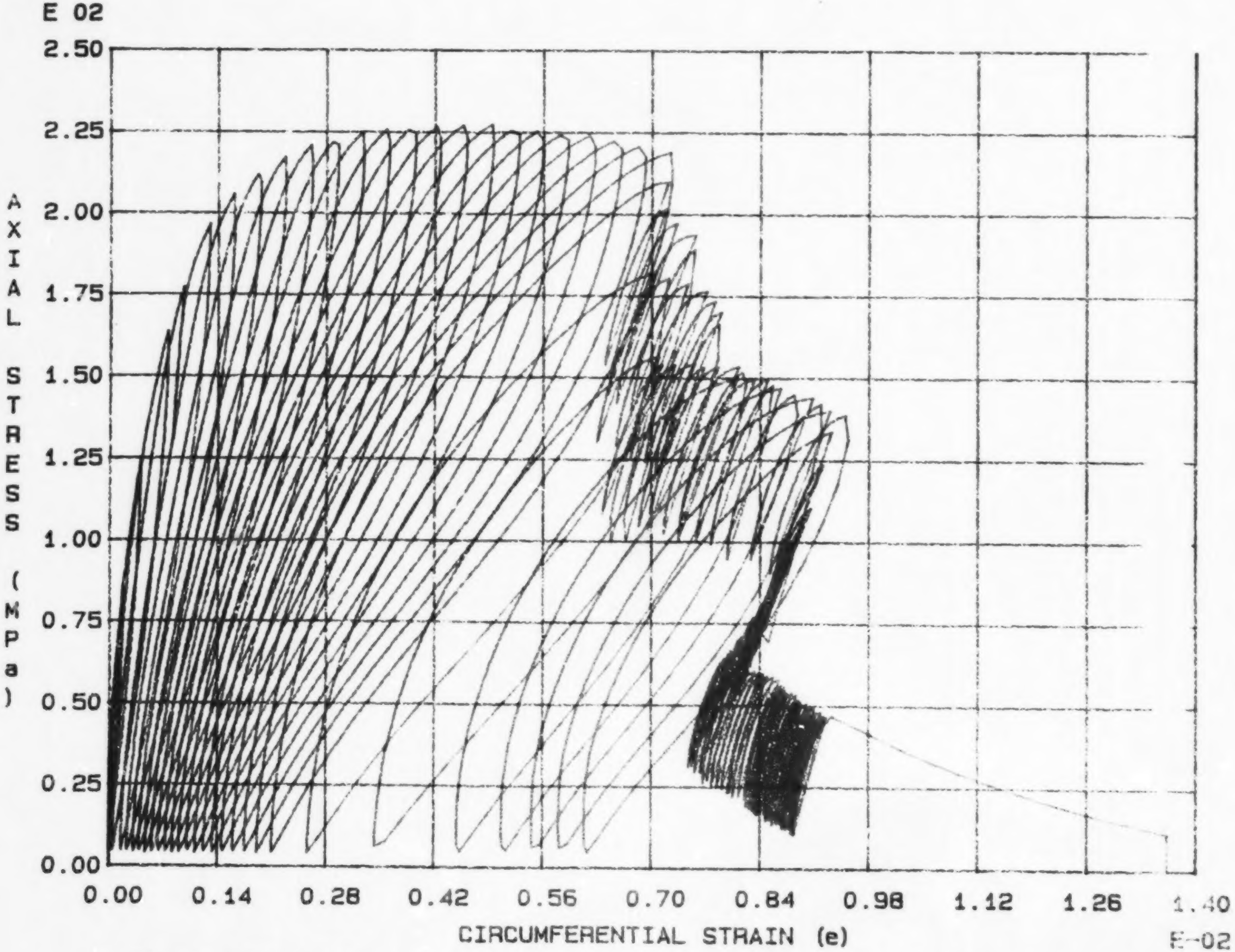

Figure A22. Loading and unloading curves (cir. strain) for Specimen MB1-21.553.

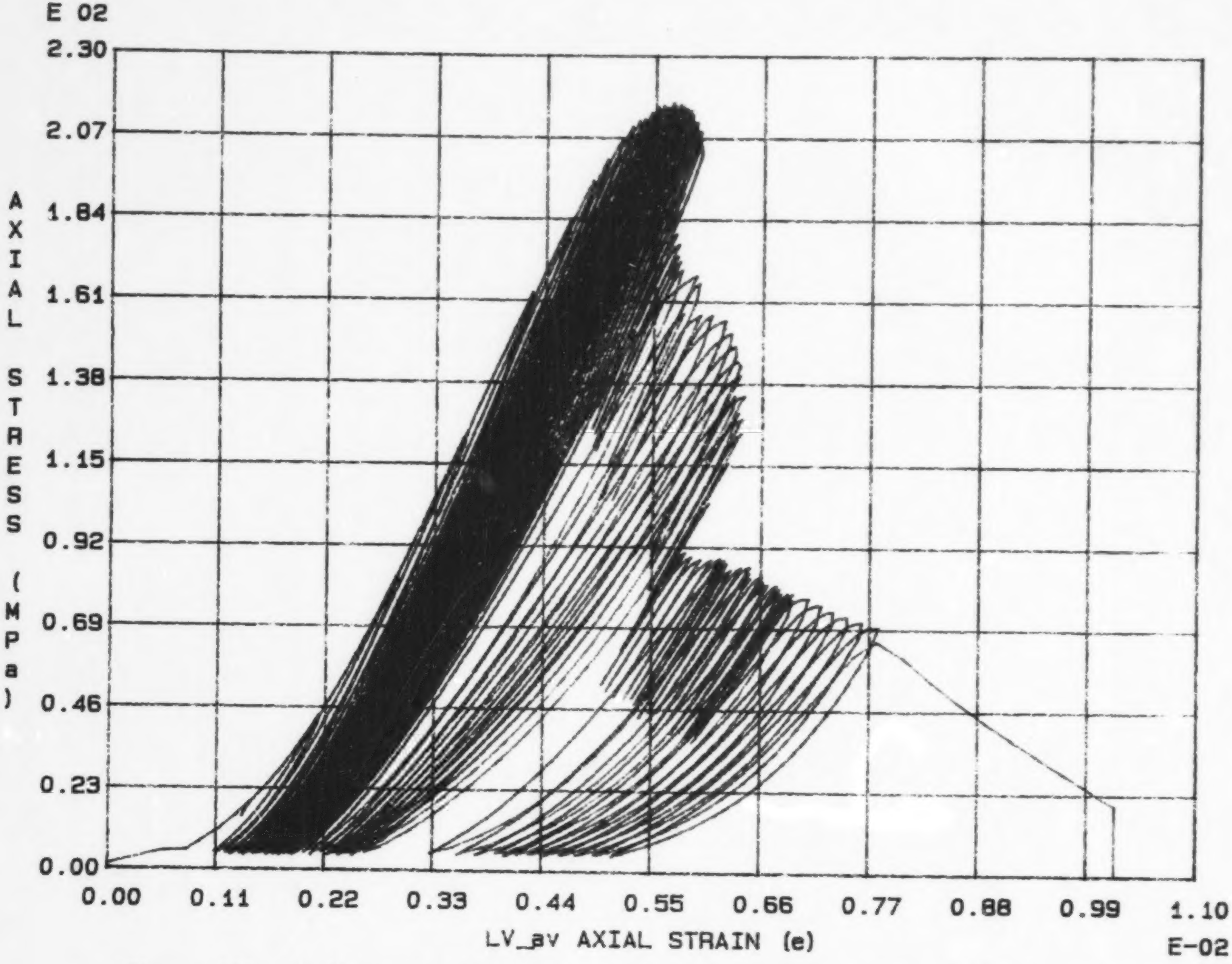

Figure A23. Loading and unloading curves (axial strain) for Specimen MB1-25.055.

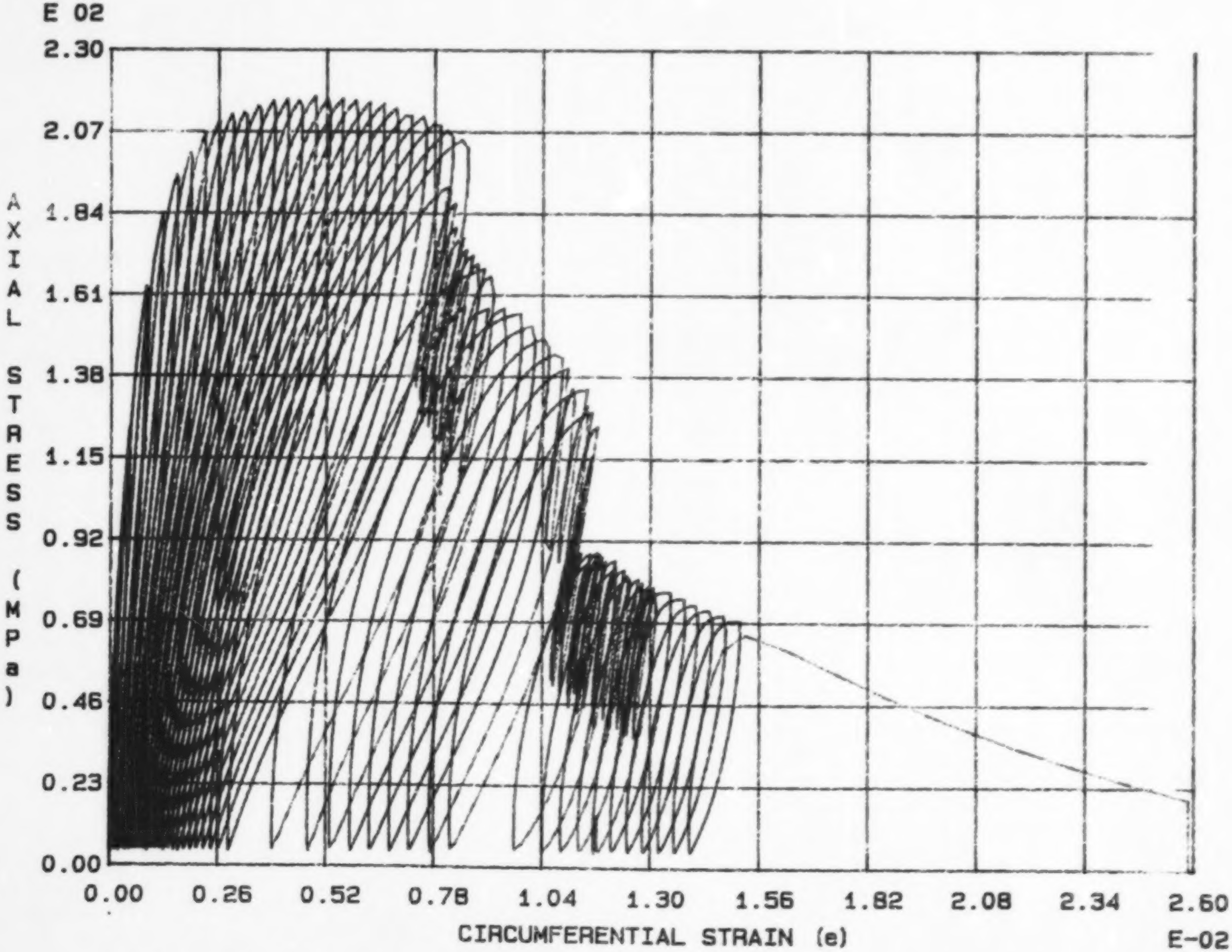

Figure A24. Loading and unloading curves (cir. strain) for Specimen MB1-25.055.

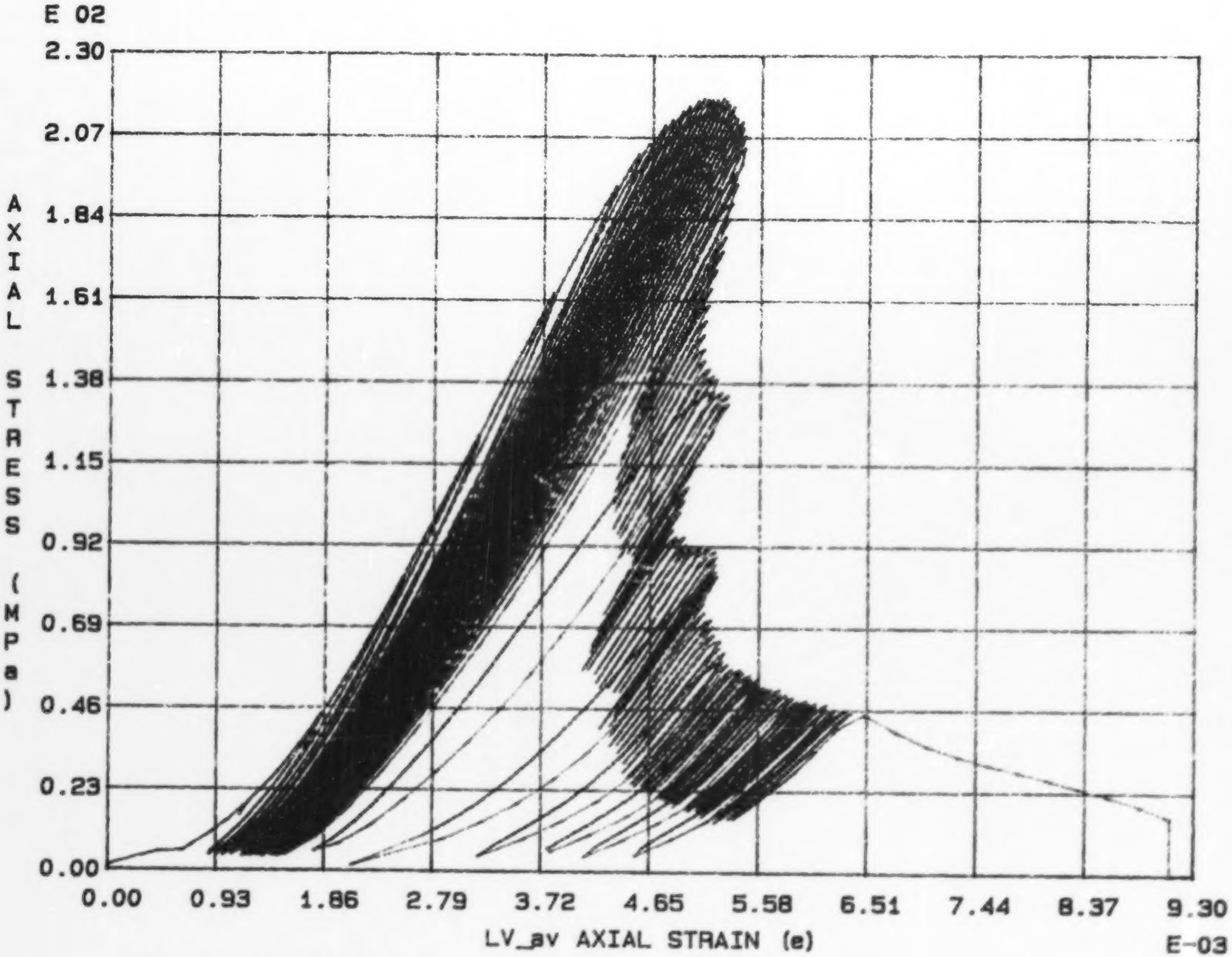

Figure A25. Loading and unloading curves (axial strain) for Specimen MB1-41.178.

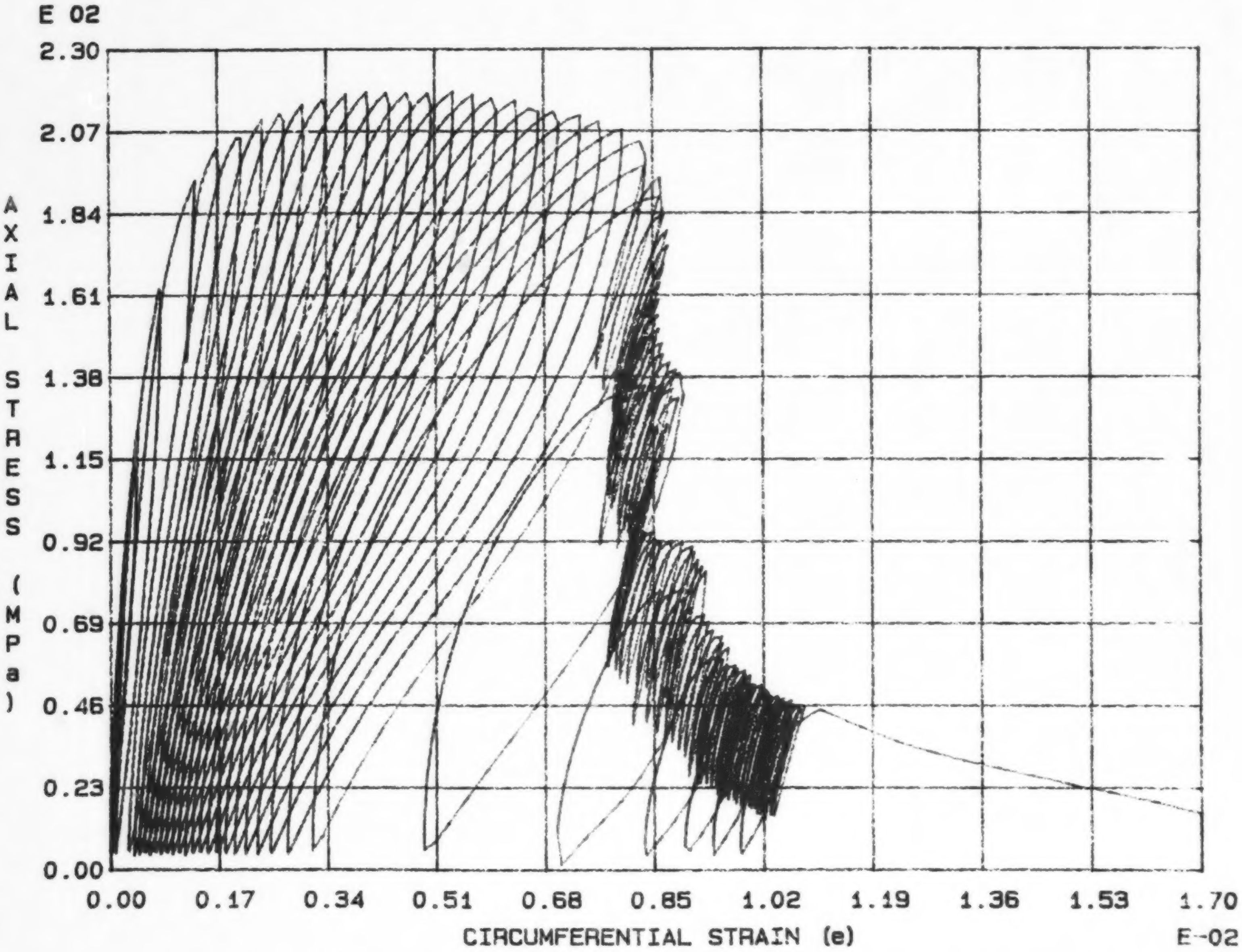

Figure A26. Loading and unloading curves (cir. strain) for Specimen MB1-41.178.

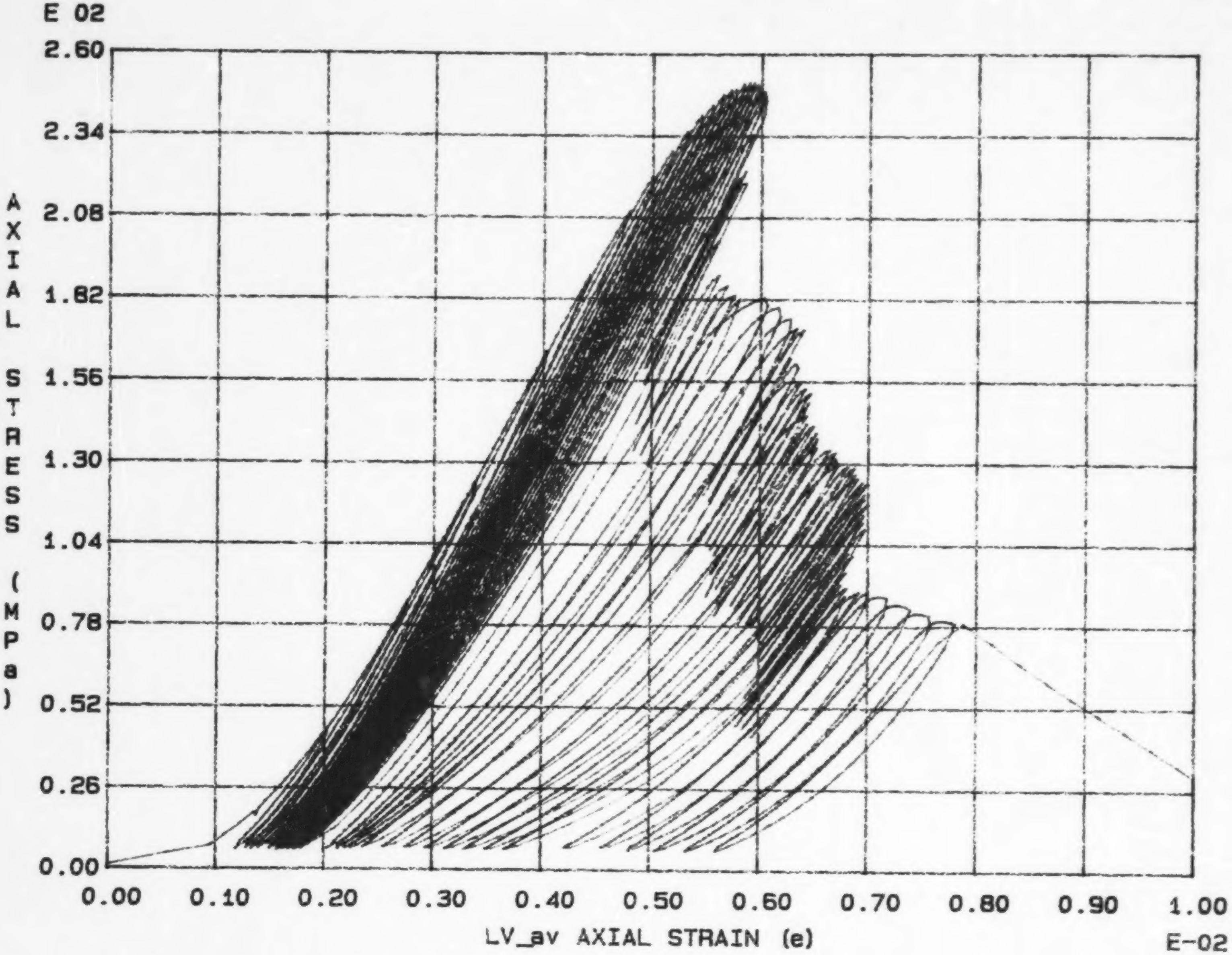

Figure A27. Loading and unloading curves (axial strain) for Specimen MB1-21.717.

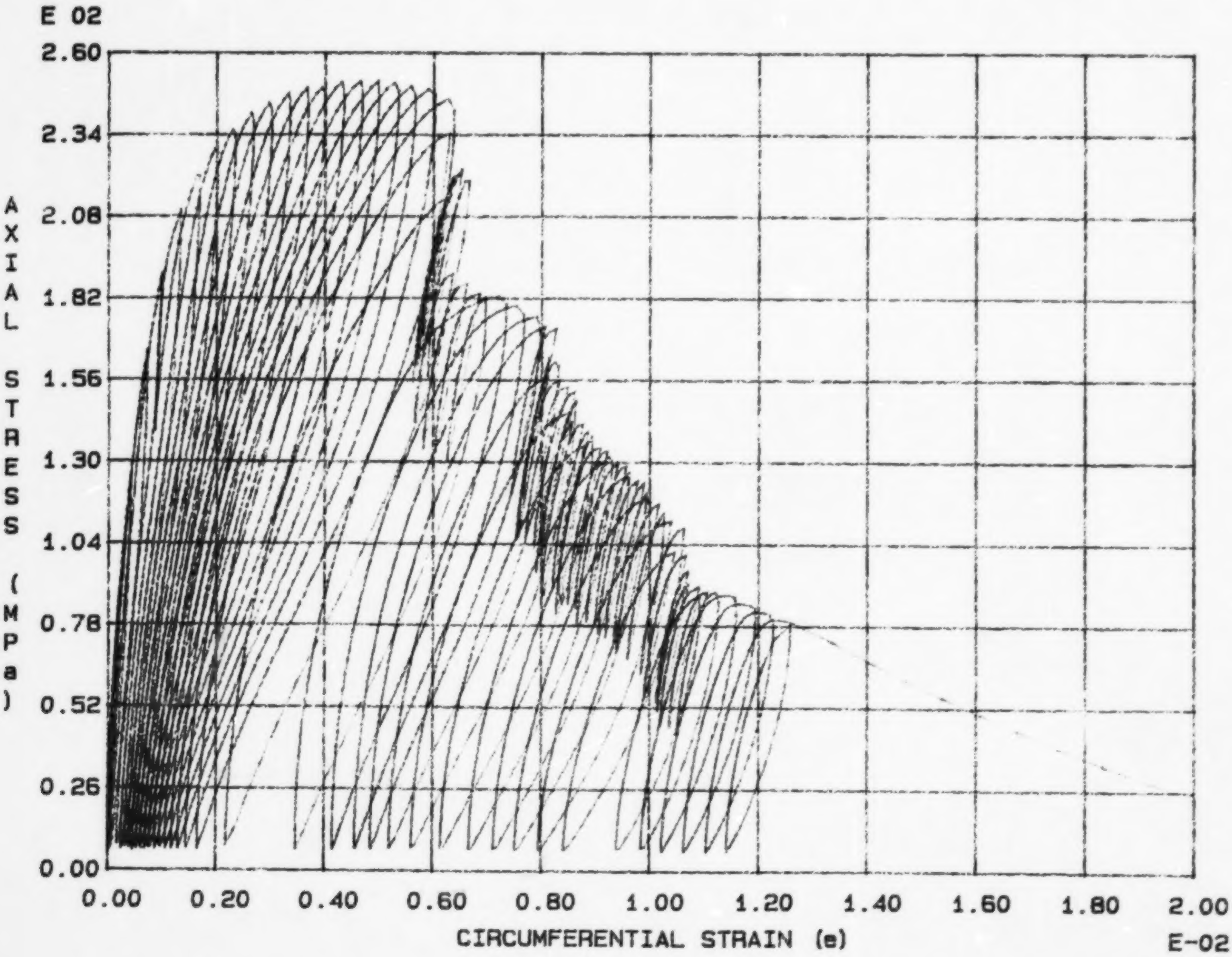

Figure A28. Loading and unloading curves (cir. strain) for Specimen MB1-21.717.

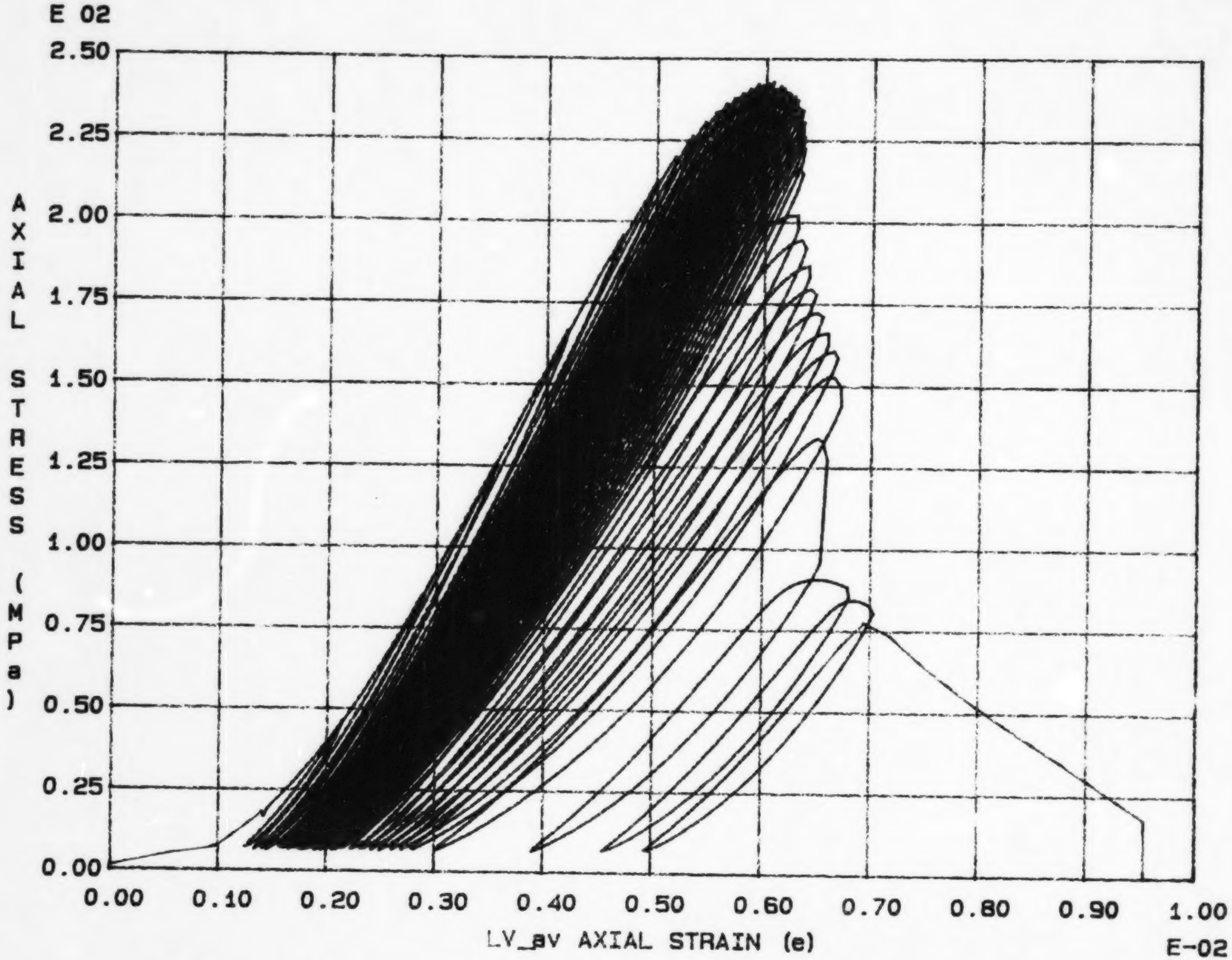

Figure A29. Loading and unloading curves (axial strain) for Specimen MB1-25.216.

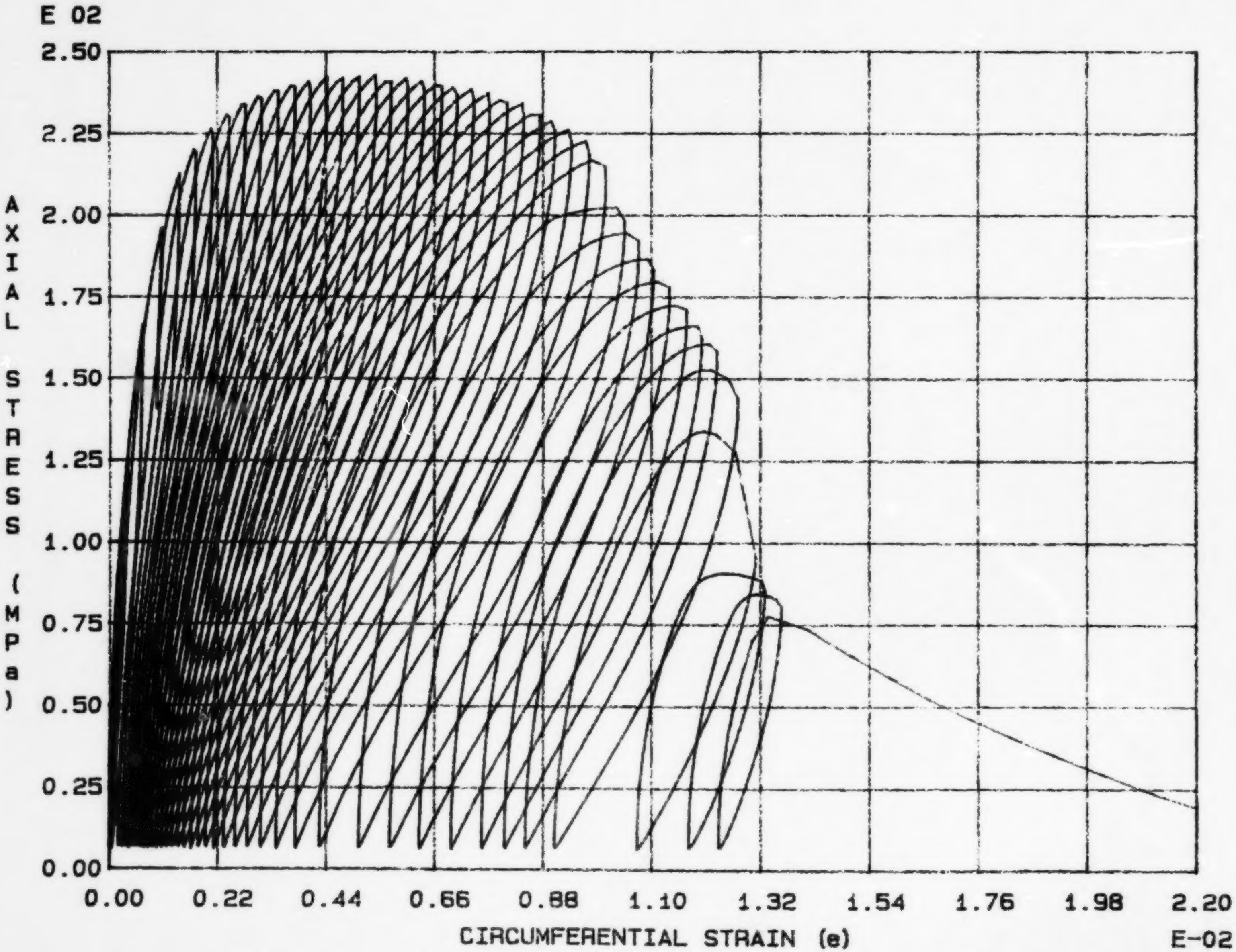

Figure A30. Loading and unloading curves (cir. strain) for Specimen MB1-25.216.

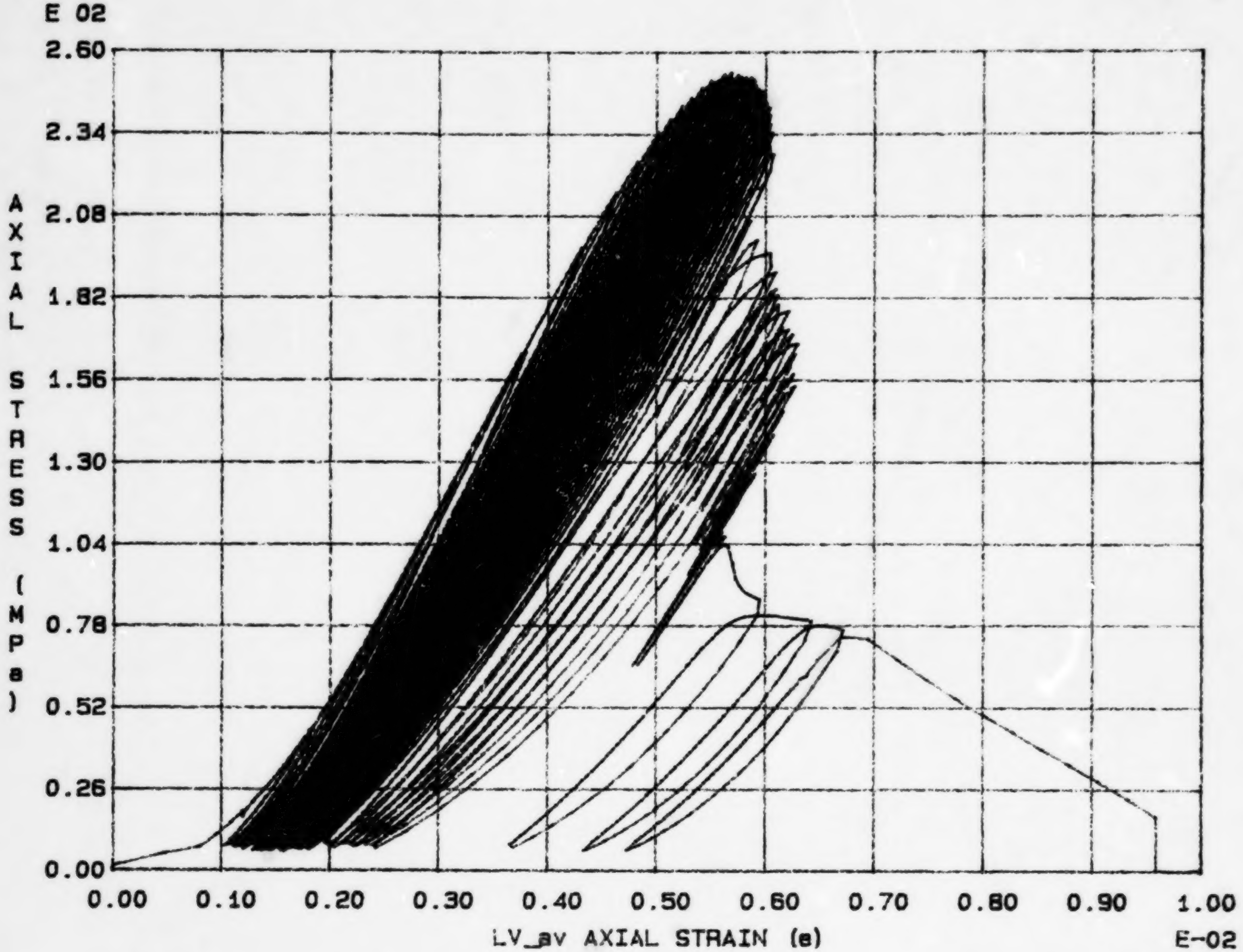

Figure A31. Loading and unloading curves (axial strain) for Specimen MB1-52.263.

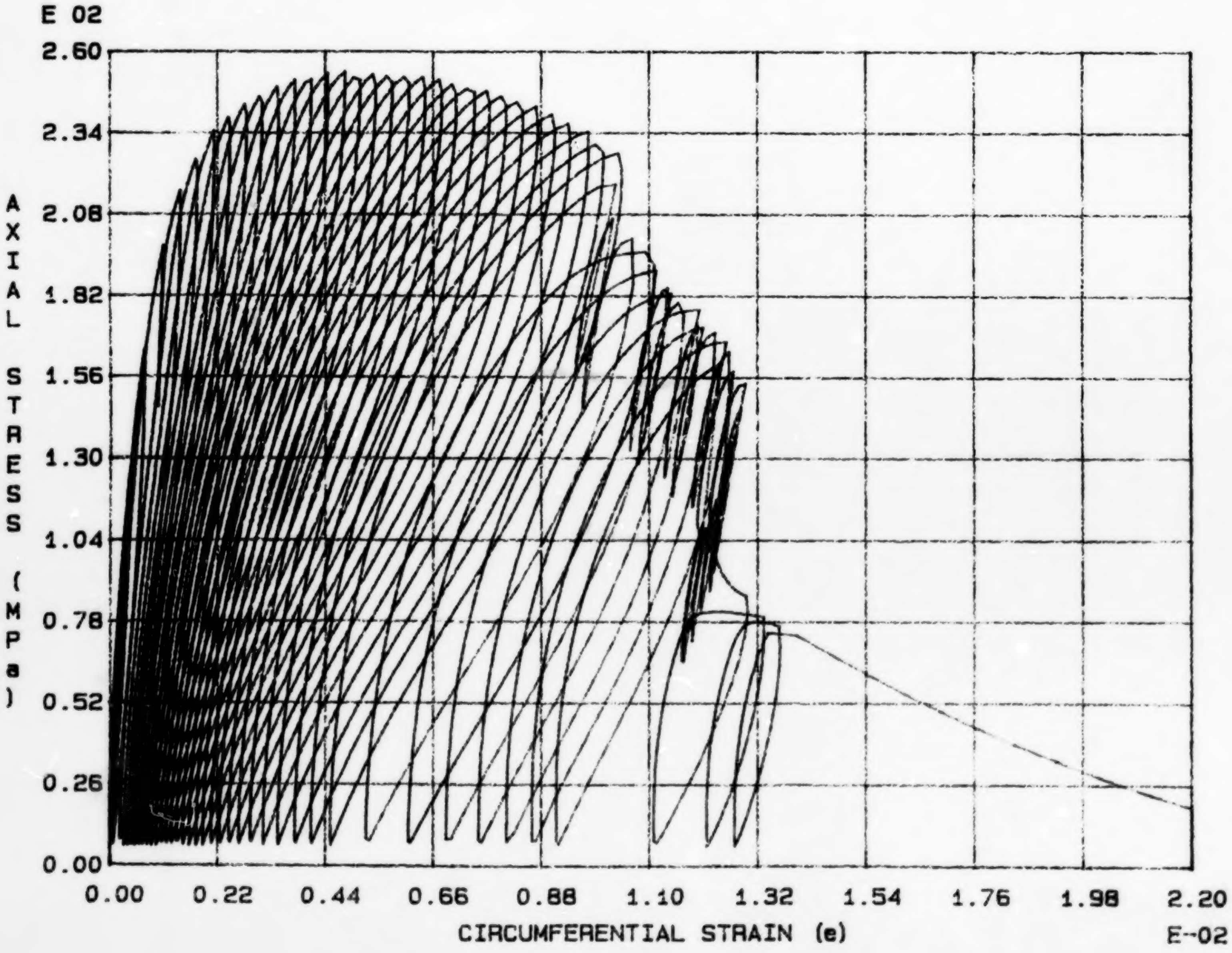

Figure A32. Loading and unloading curves (cir. strain) for Specimen MB1-52.263.

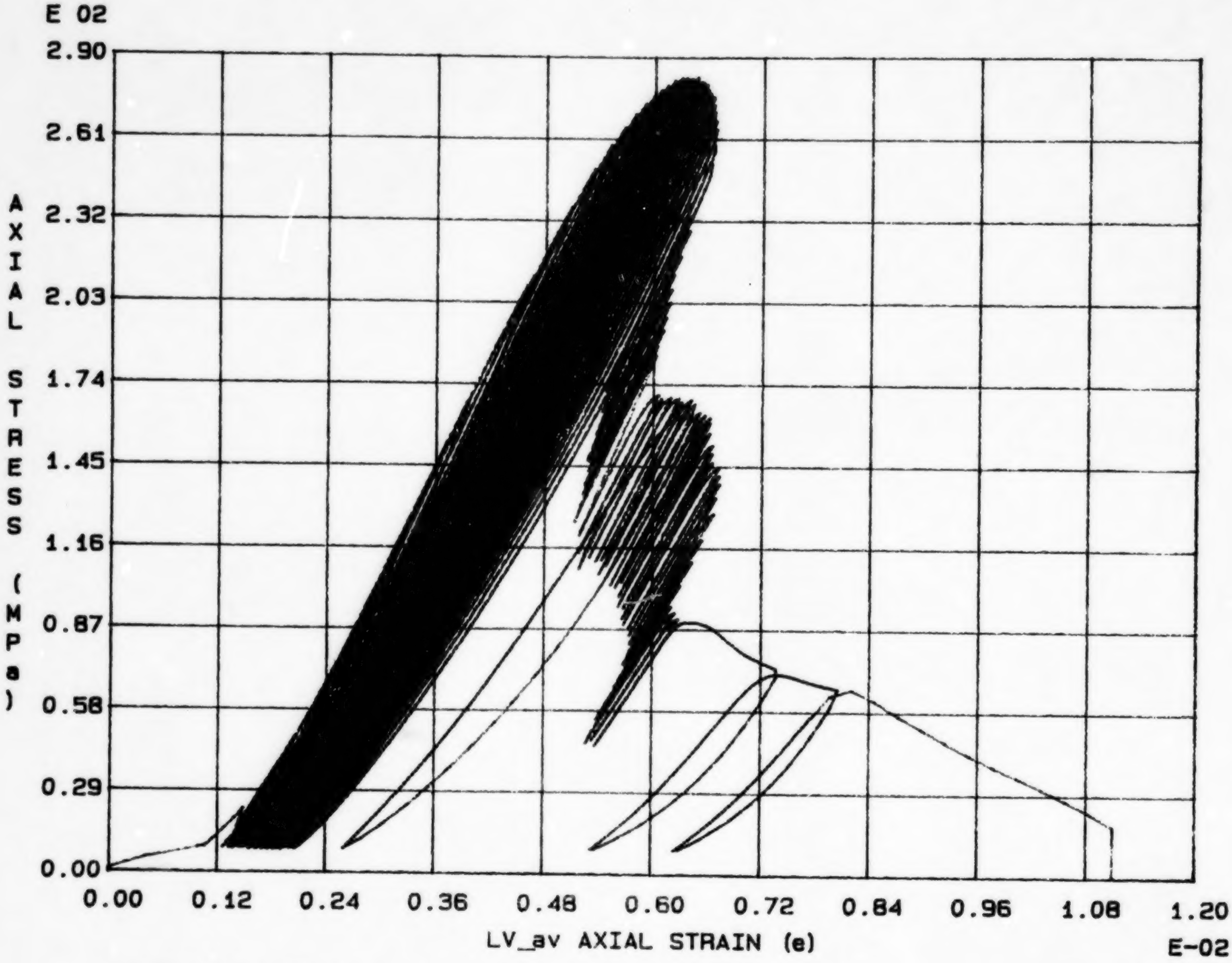

Figure A33. Loading and unloading curves (axial strain) for Specimen MB1-22.060.

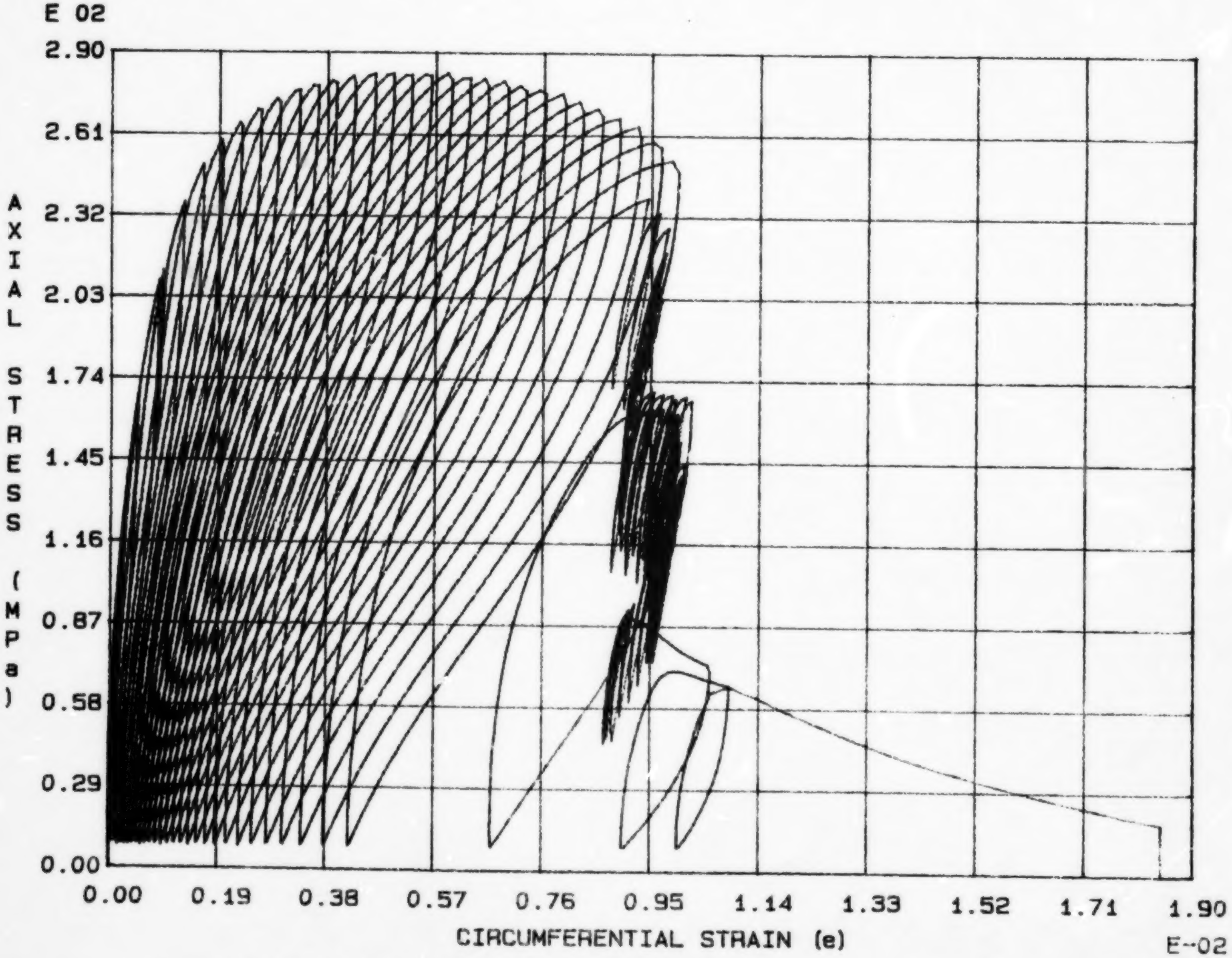

Figure A34. Loading and unloading curves (cir. strain) for Specimen MB1-22.060.

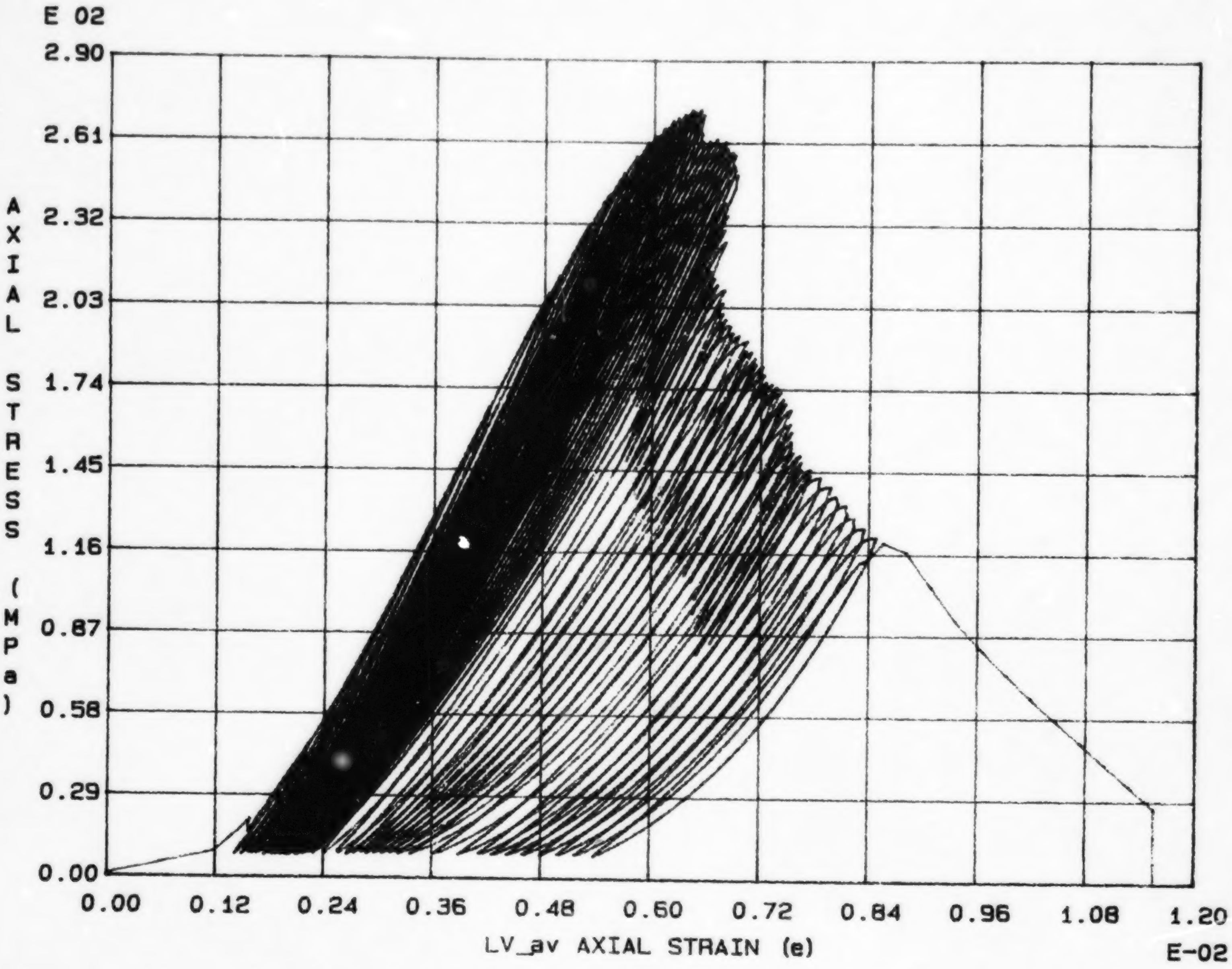

Figure A35. Loading and unloading curves (axial strain) for Specimen MB1-24.041.

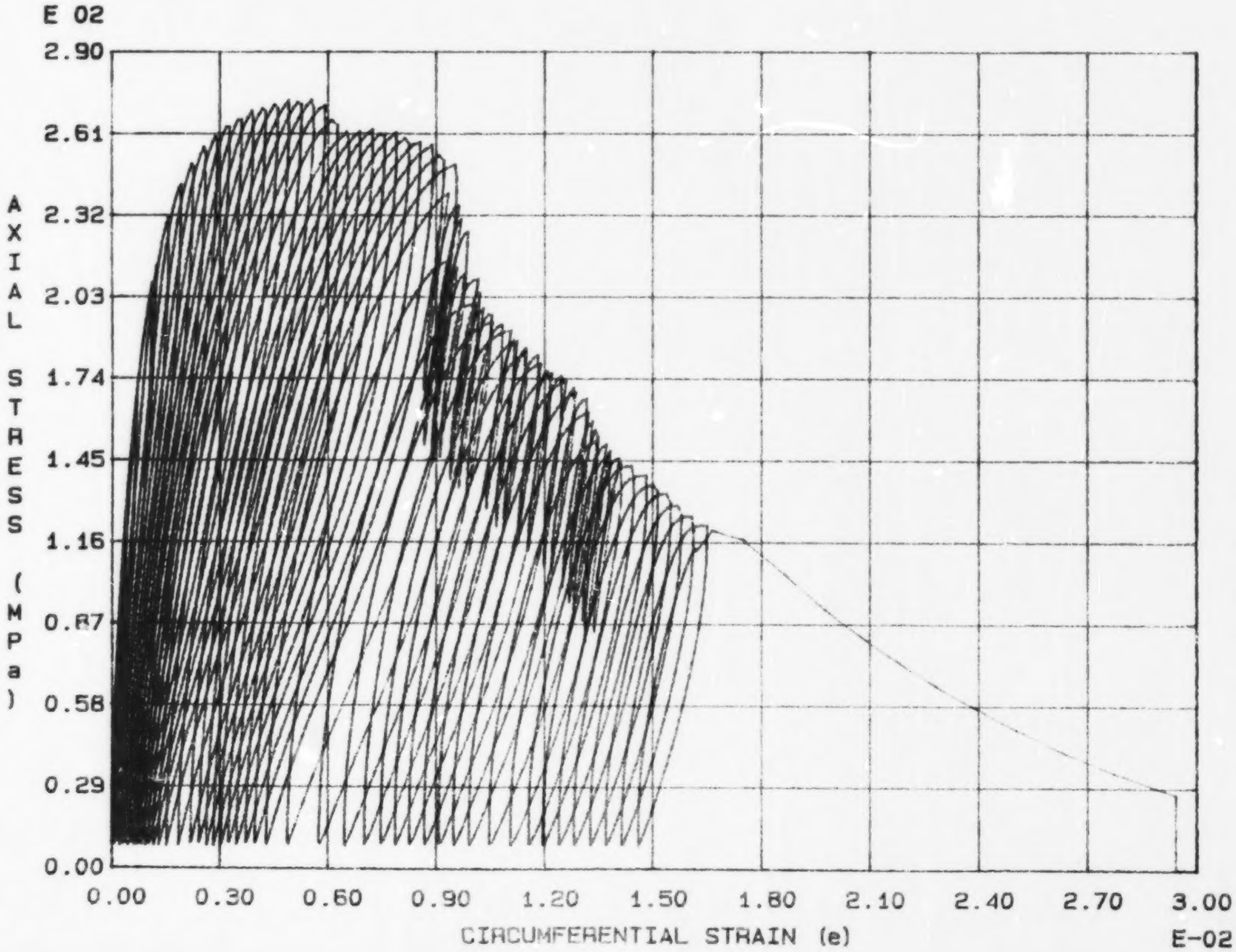

Figure A36. Loading and unloading curves (cir. strain) for Specimen MB1-24.041.

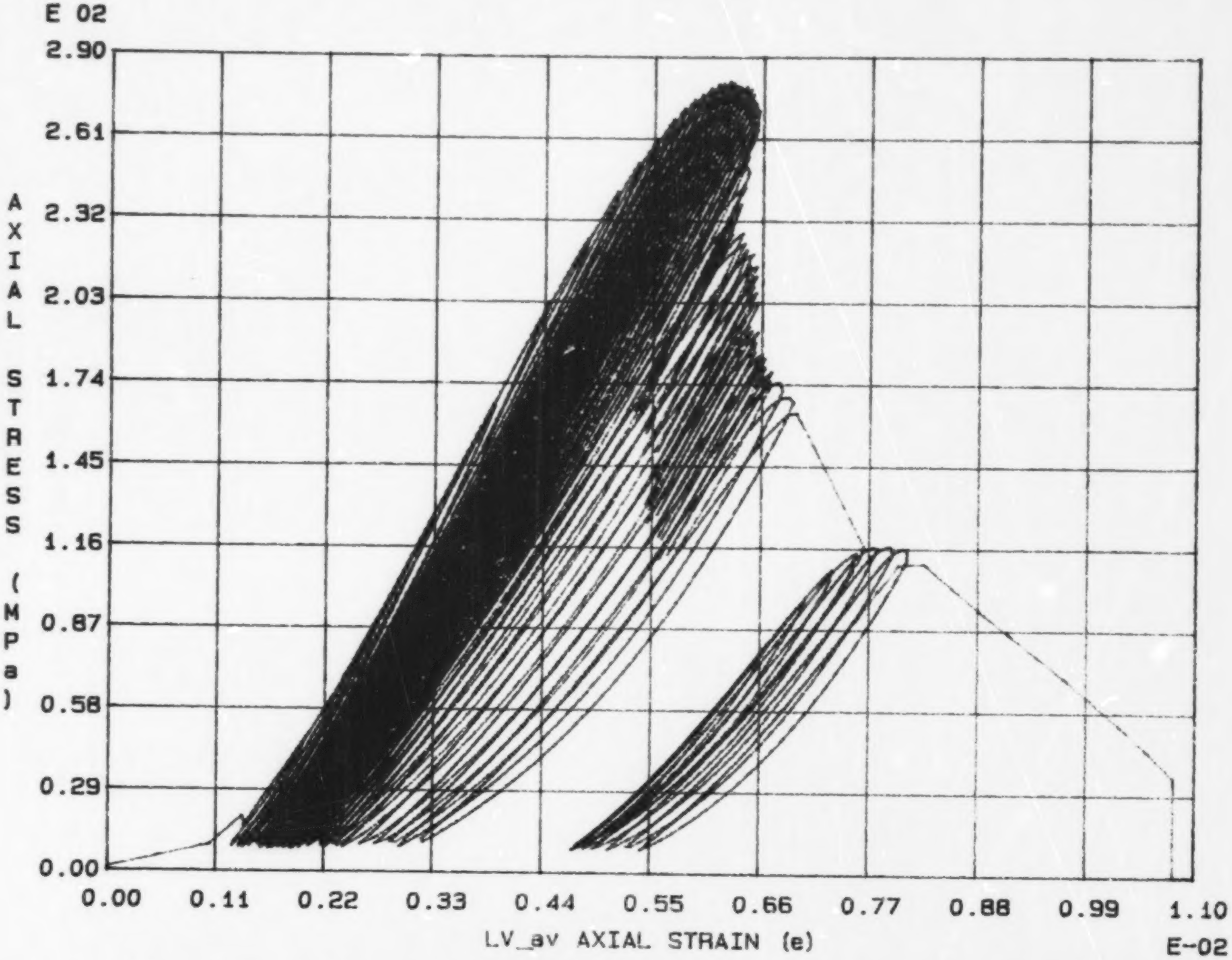

Figure A37. Loading and unloading curves (axial strain) for Specimen MB1-52.539.

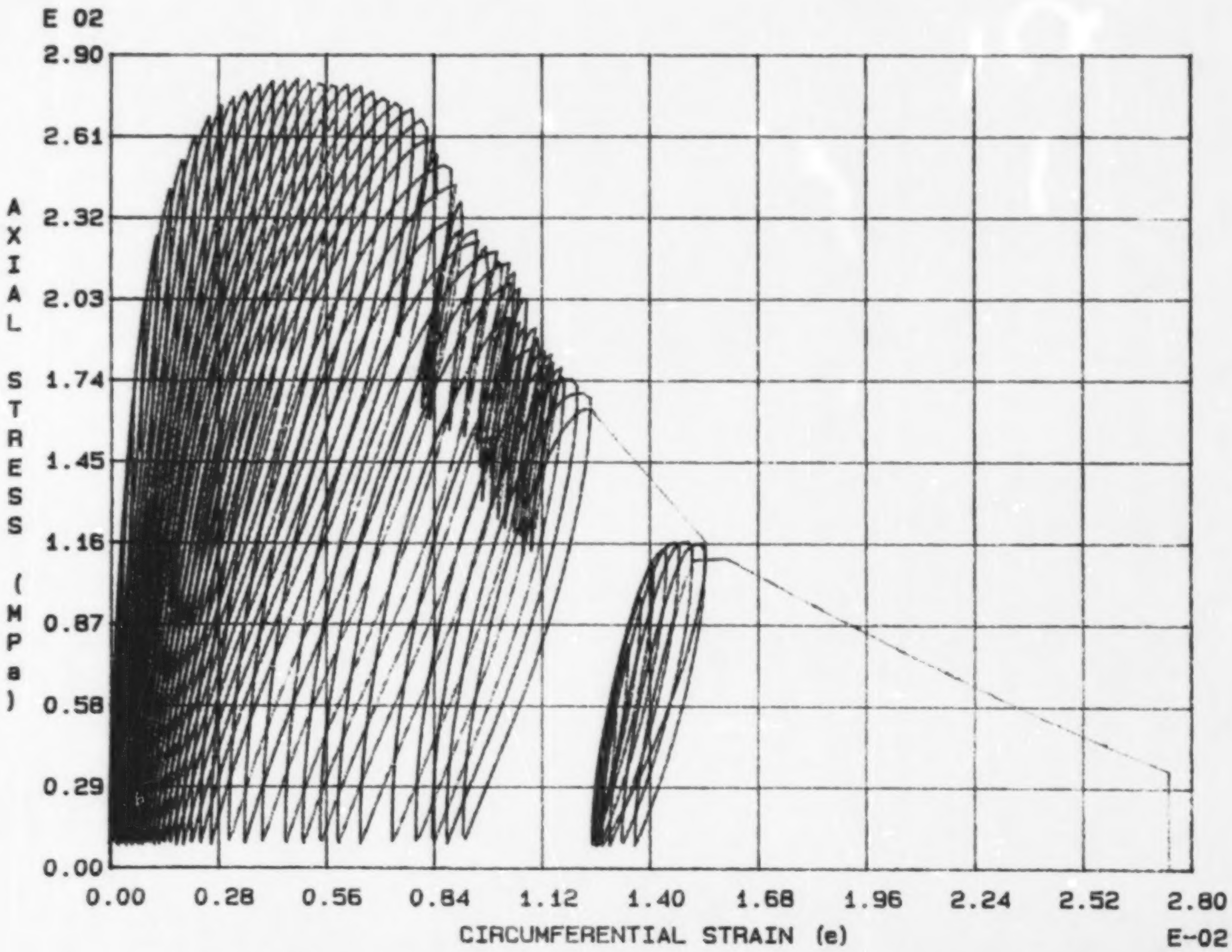

Figure A38. Loading and unloading curves (cir. strain) for Specimen MB1-52.539.

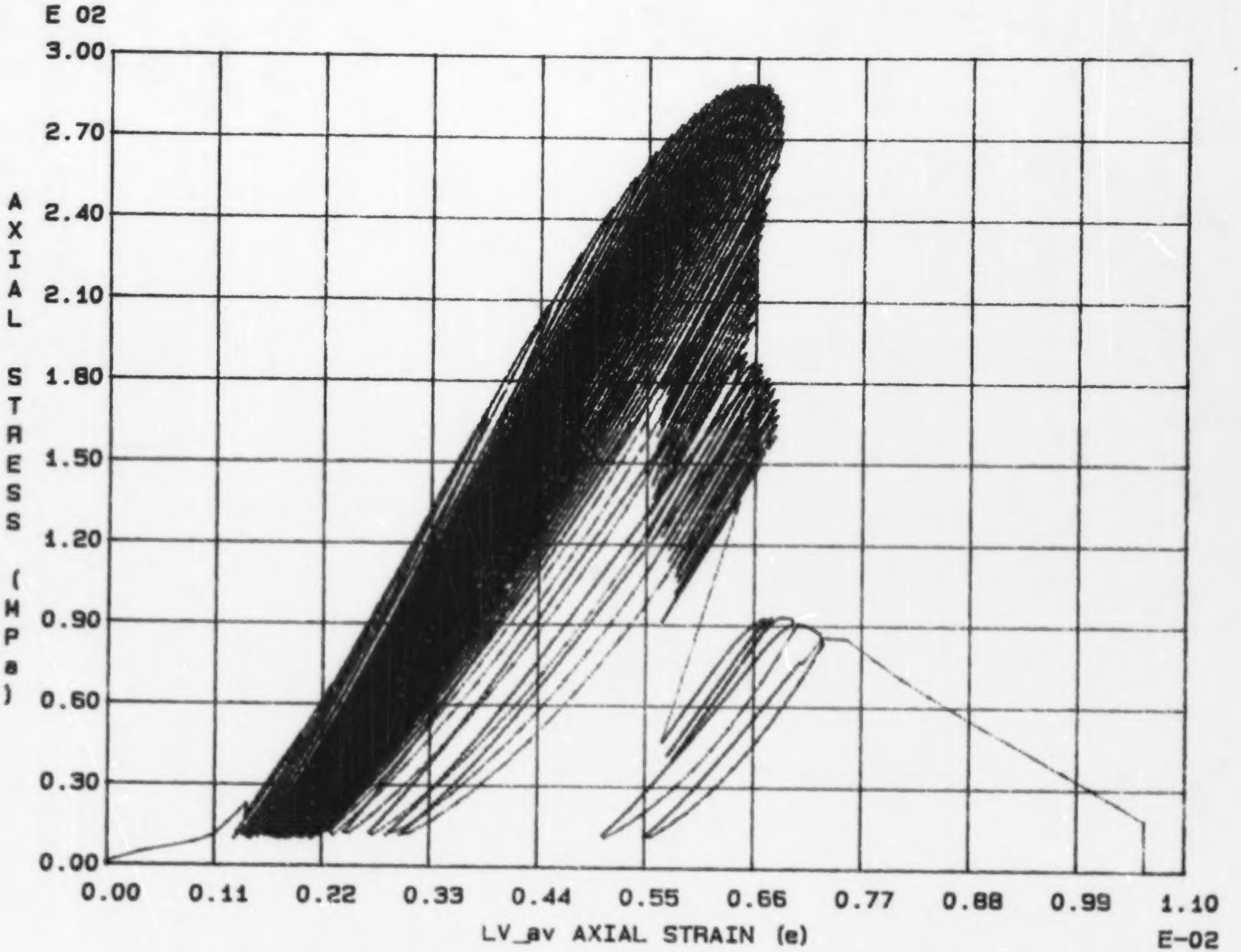

Figure A39. Loading and unloading curves (axial strain) for Specimen MB1-22.220.

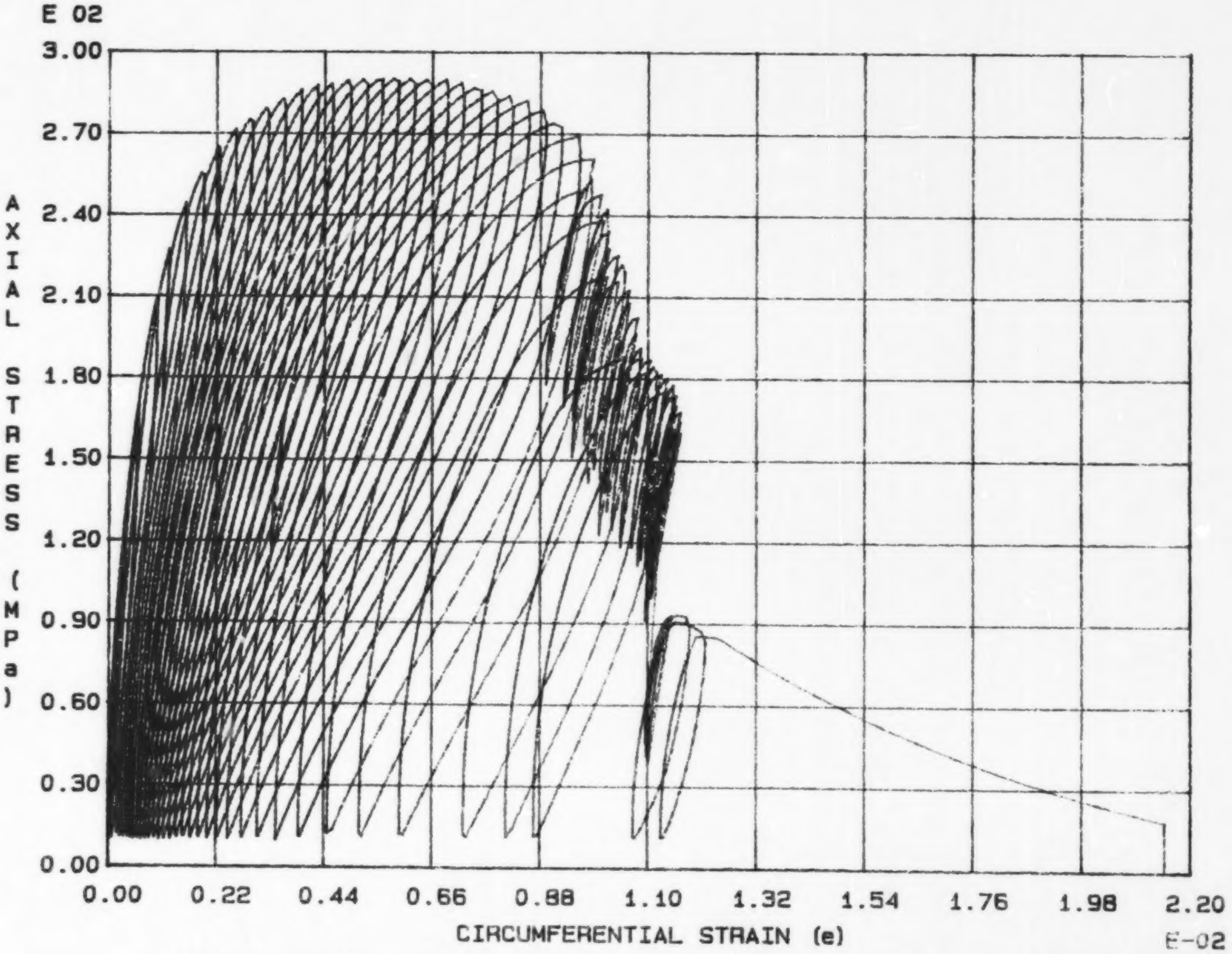

Figure A40. Loading and unloading curves (cir. strain) for Specimen MB1-22.220.

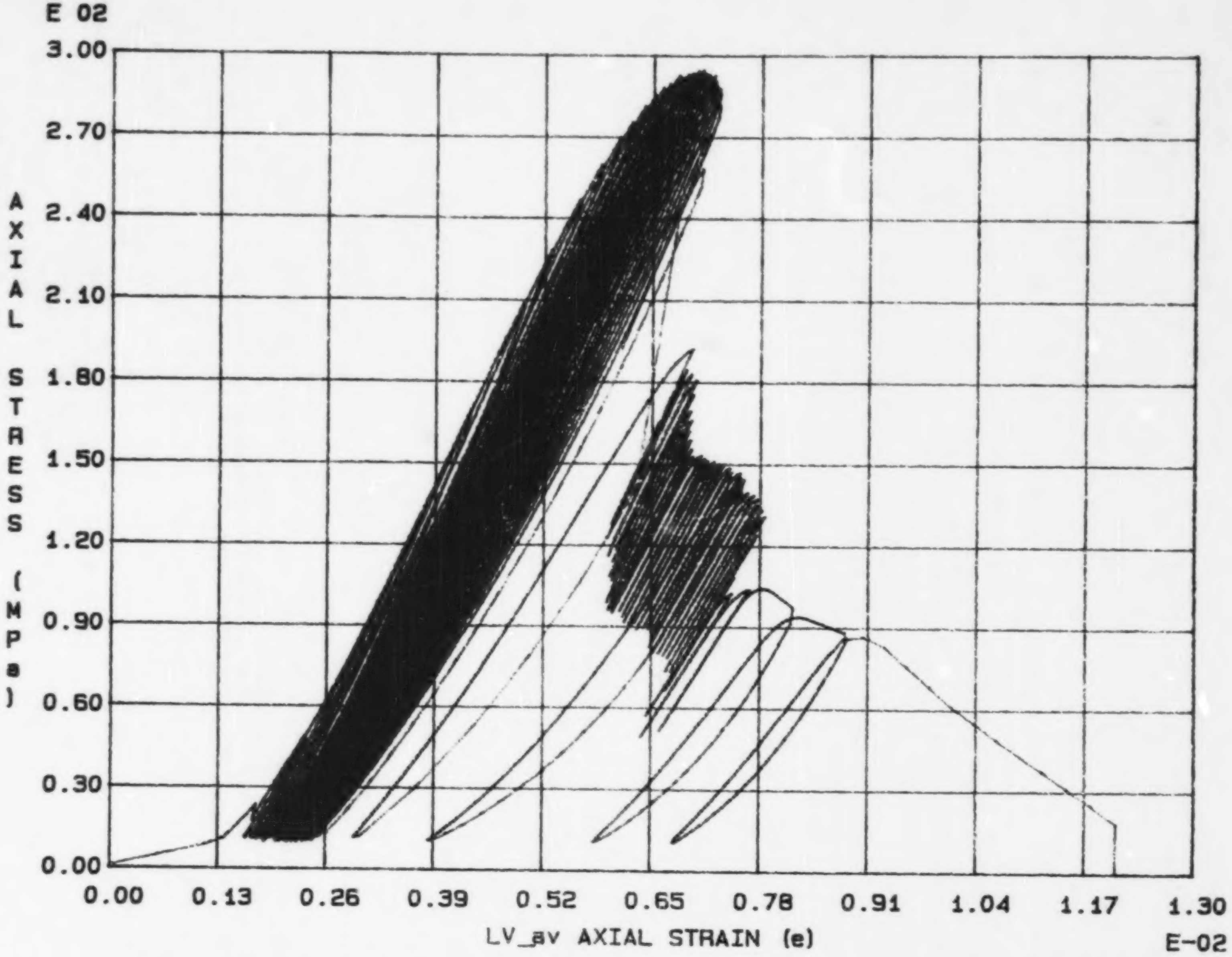

Figure A41. Loading and unloading curves (axial strain) for Specimen MB1-25.538.

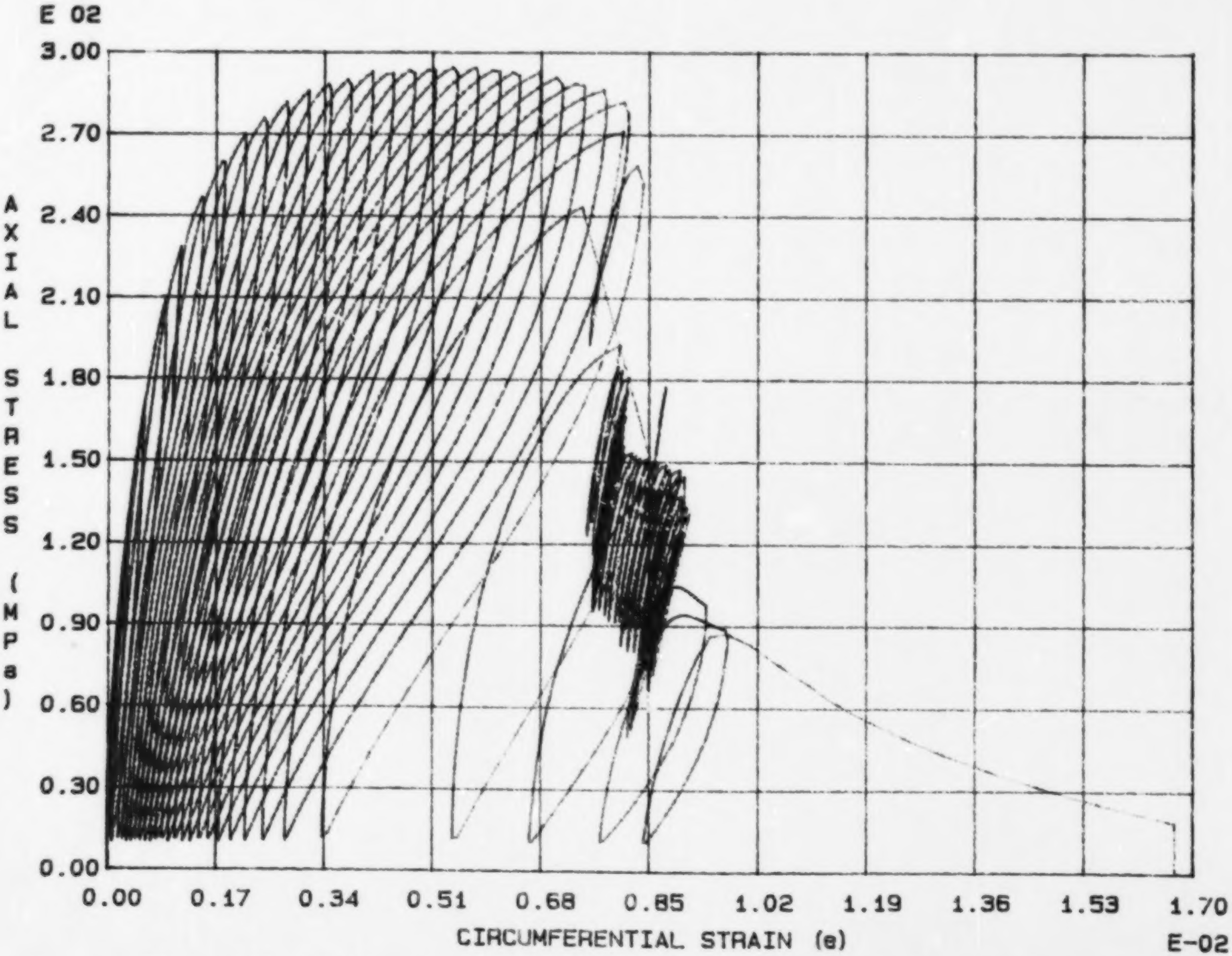

Figure A42. Loading and unloading curves (cir. strain) for Specimen MB1-25.538.

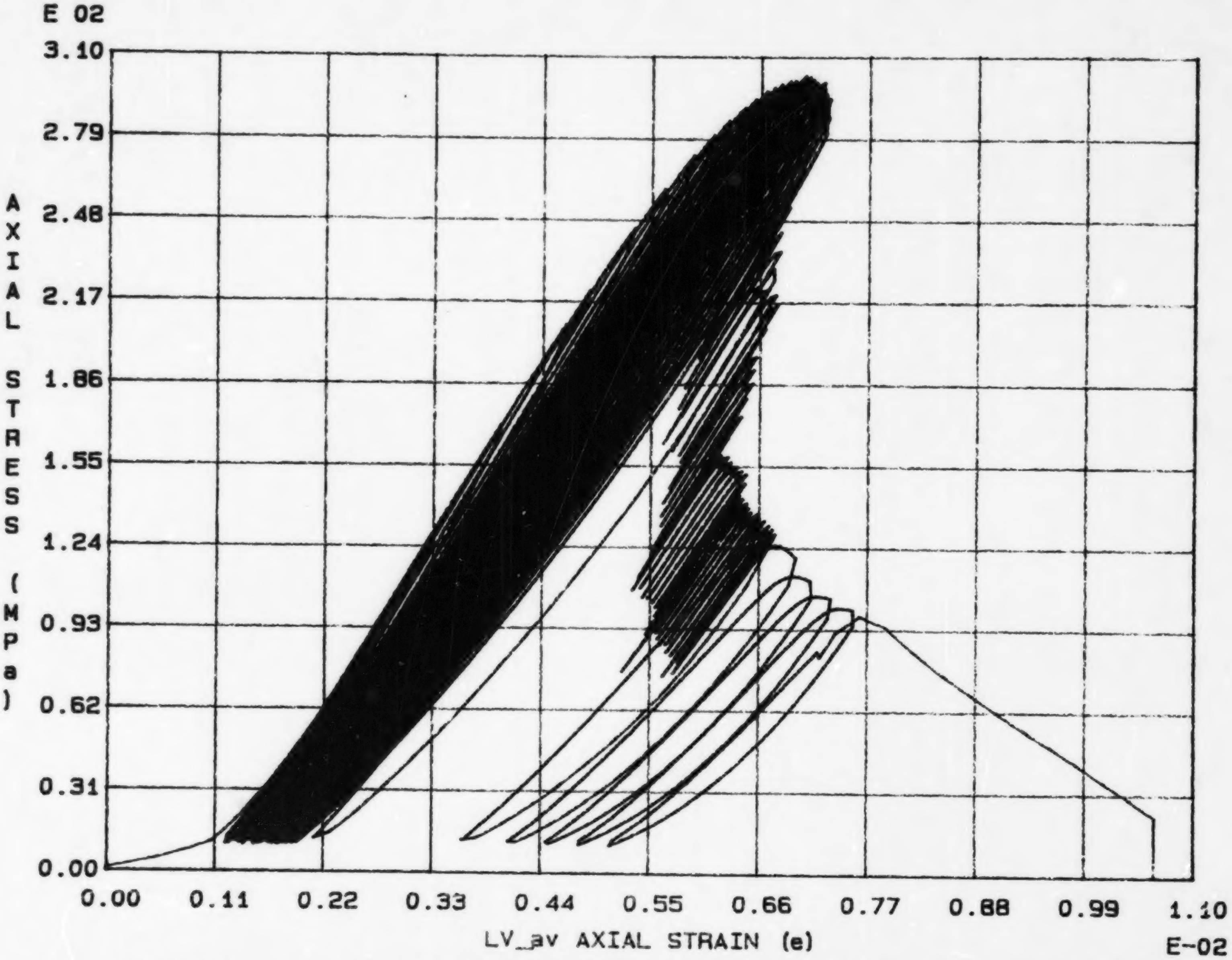

Figure A43. Loading and unloading curves (axial strain) for Specimen MB1-52.700.

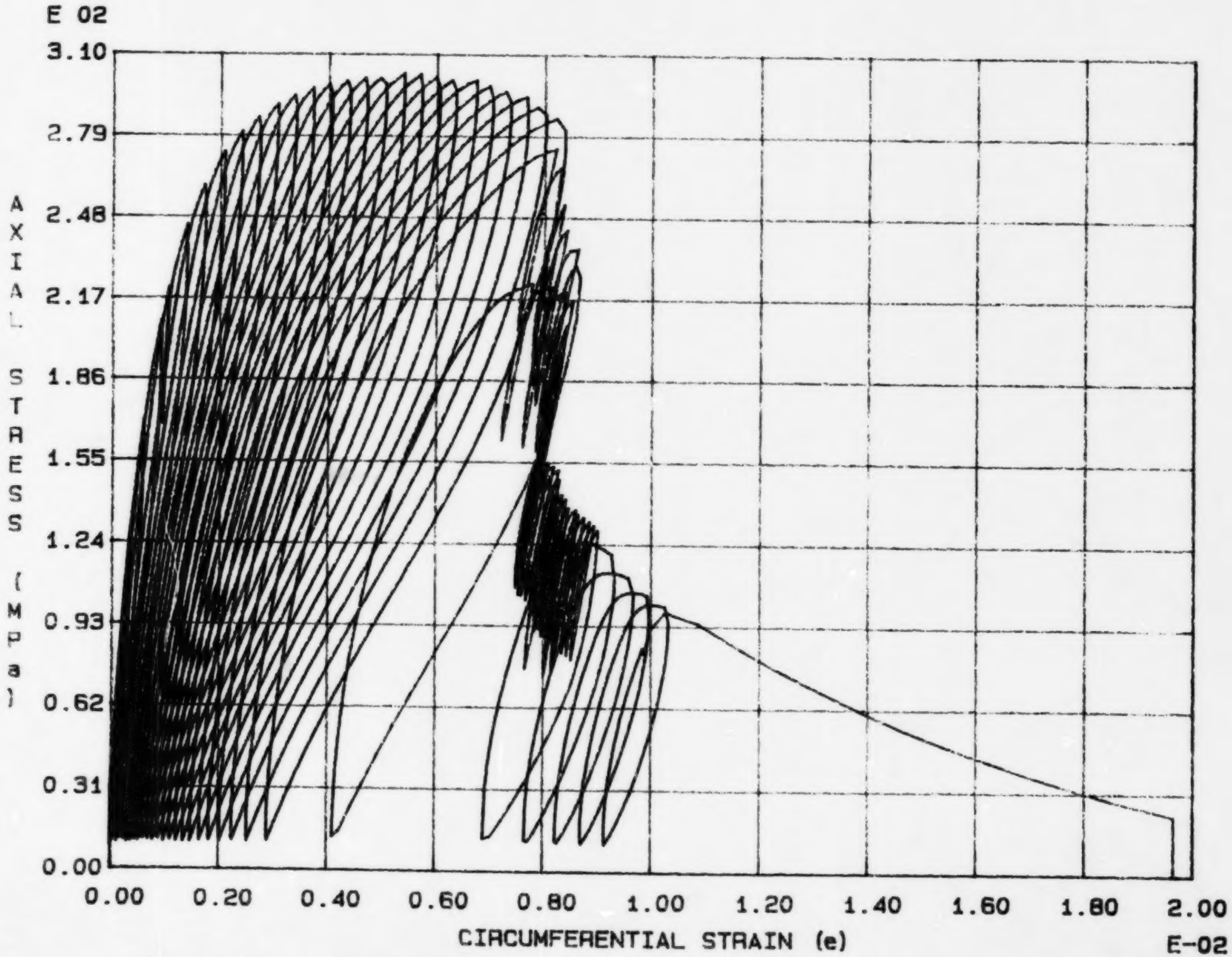

Figure A44. Loading and unloading curves (cir. strain) for Specimen MB1-52.700.

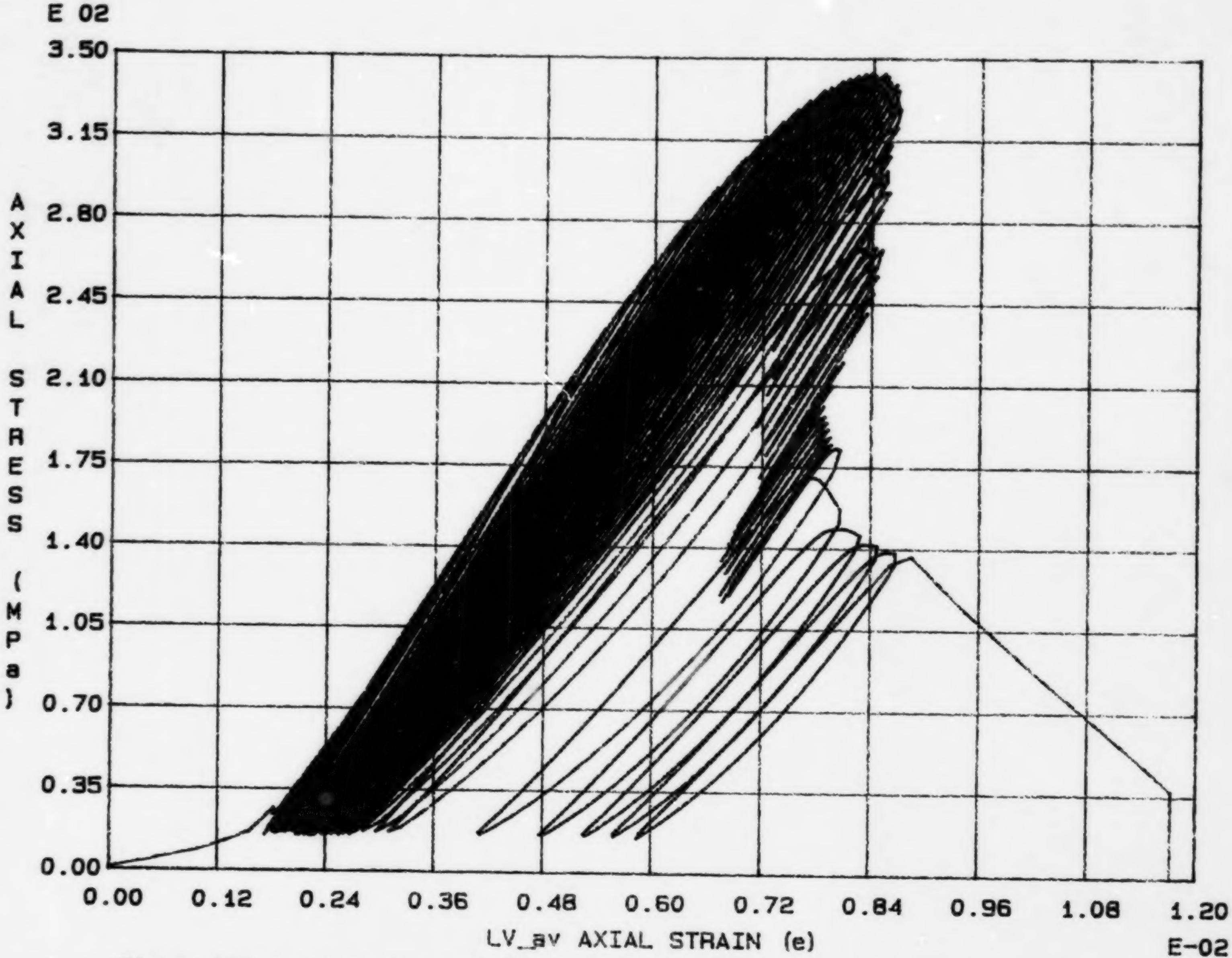

Figure A45. Loading and unloading curves (axial strain) for Specimen MB1-22.382.

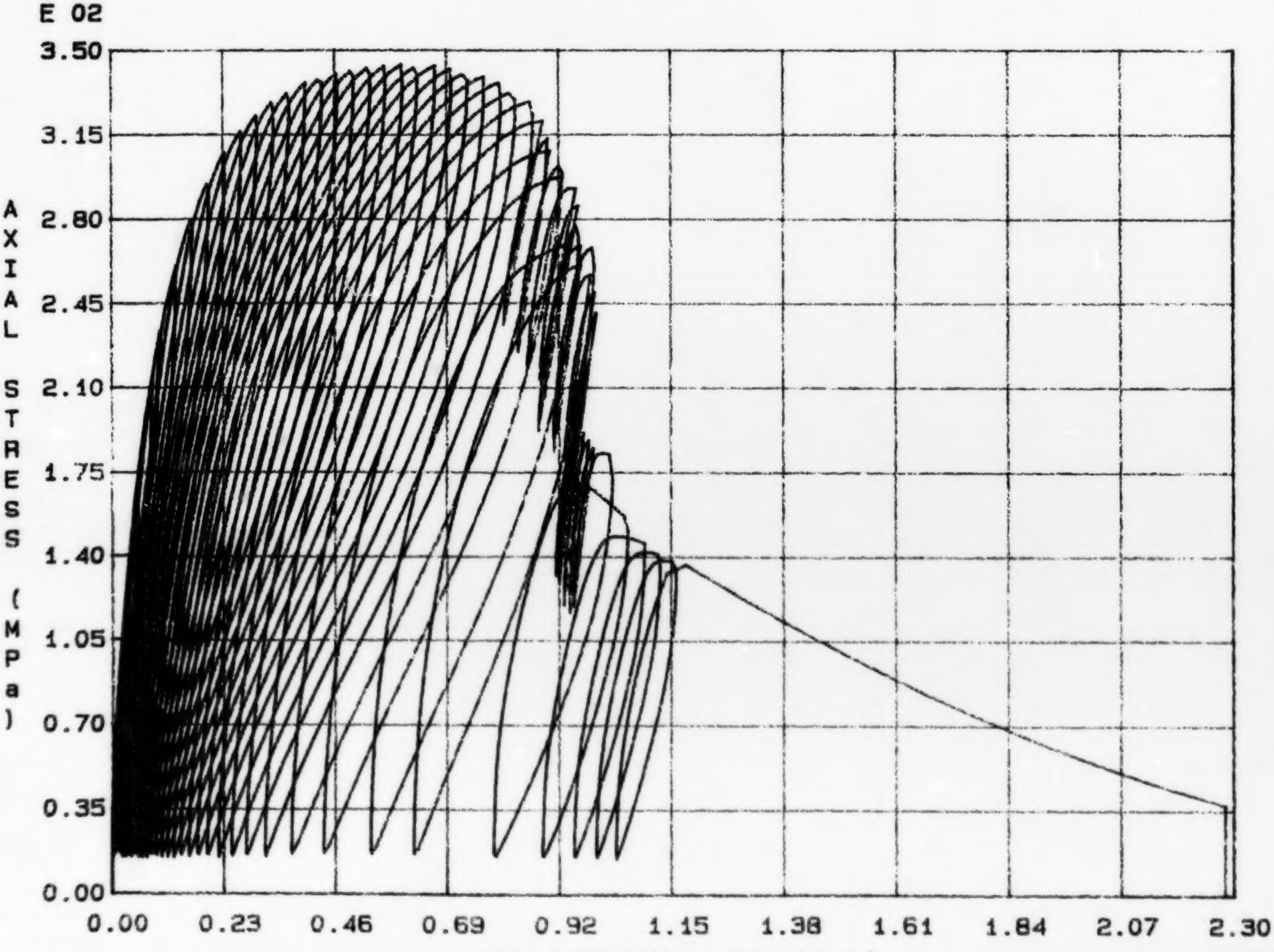

Figure A46. Loading and unloading curves (cir. strain) for Specimen MB1-22.382.

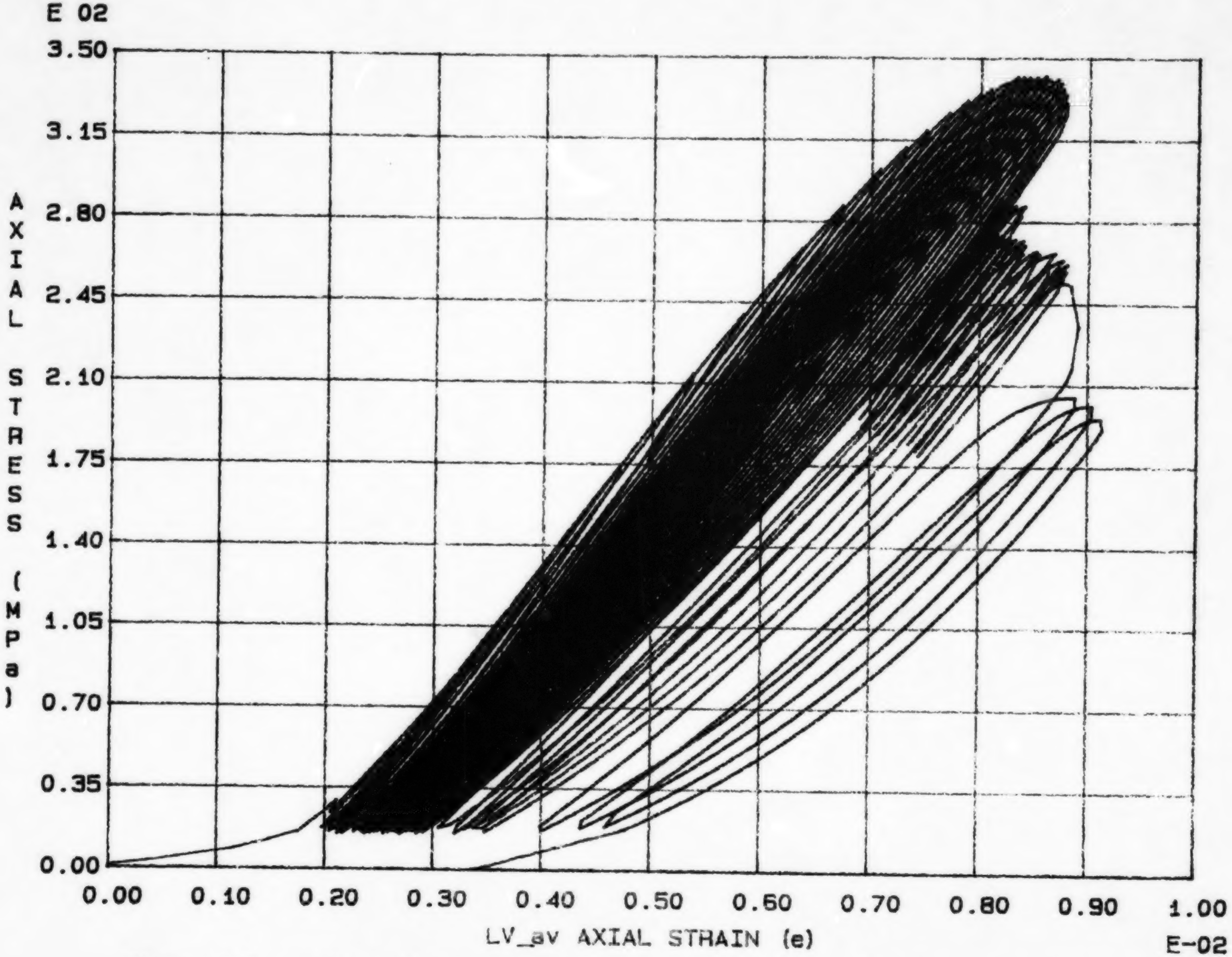

Figure A47. Loading and unloading curves (axial strain) for Specimen MB1-25.702.

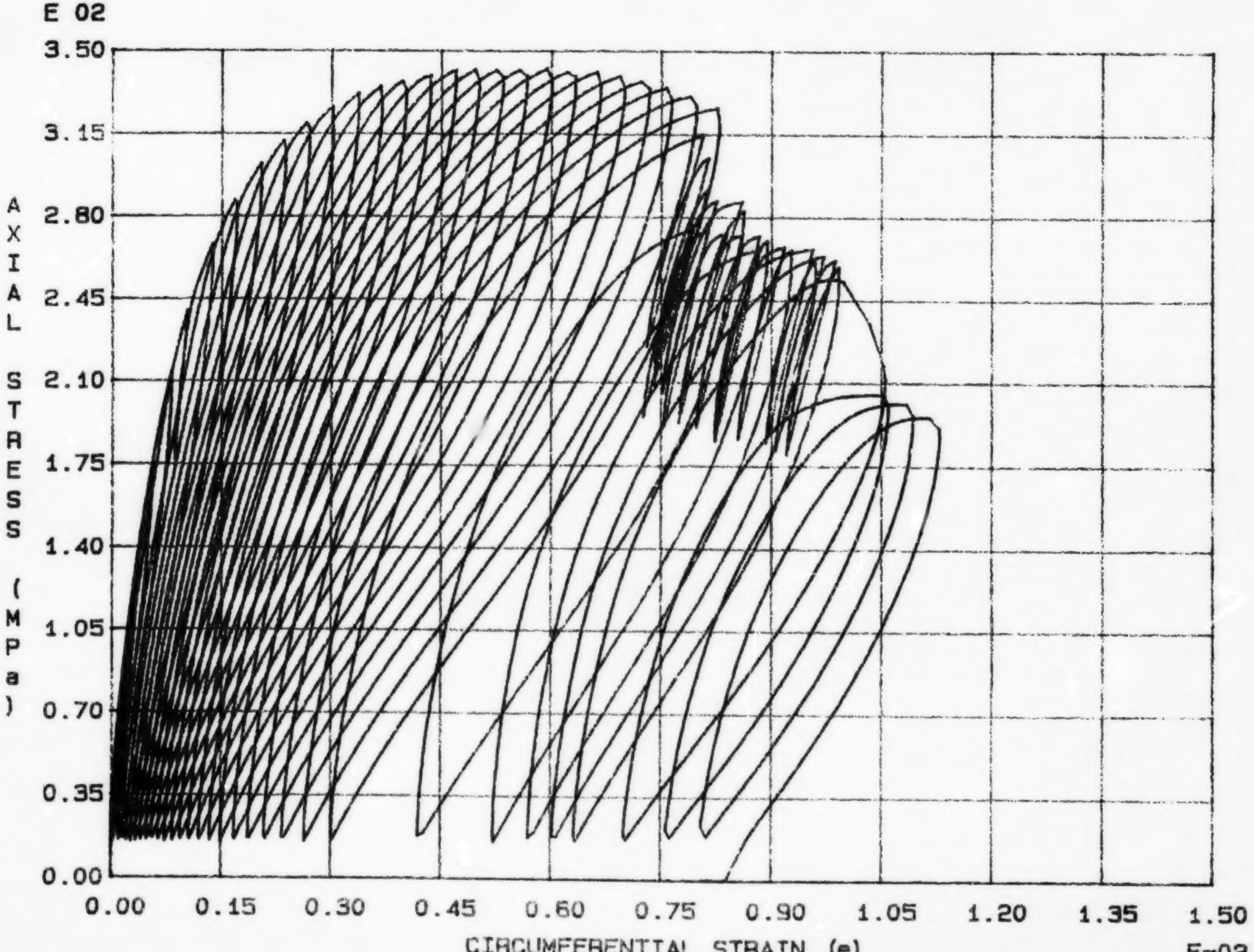

Figure A48. Loading and unloading curves (cir. strain) for Specimen MB1-25.702.

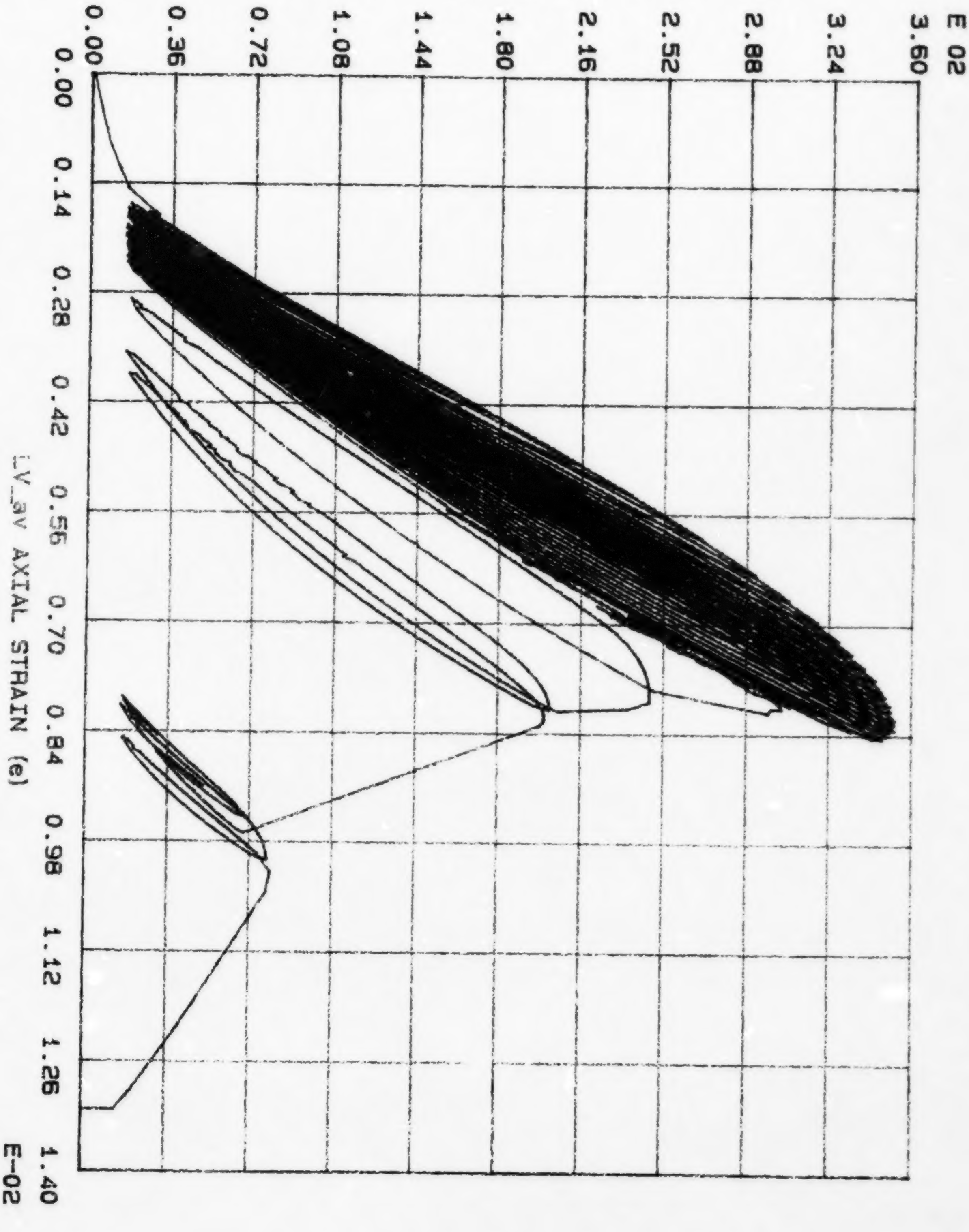

Figure A49. Loading and unloading curves (axial strain) for Specimen MB1-52.865.

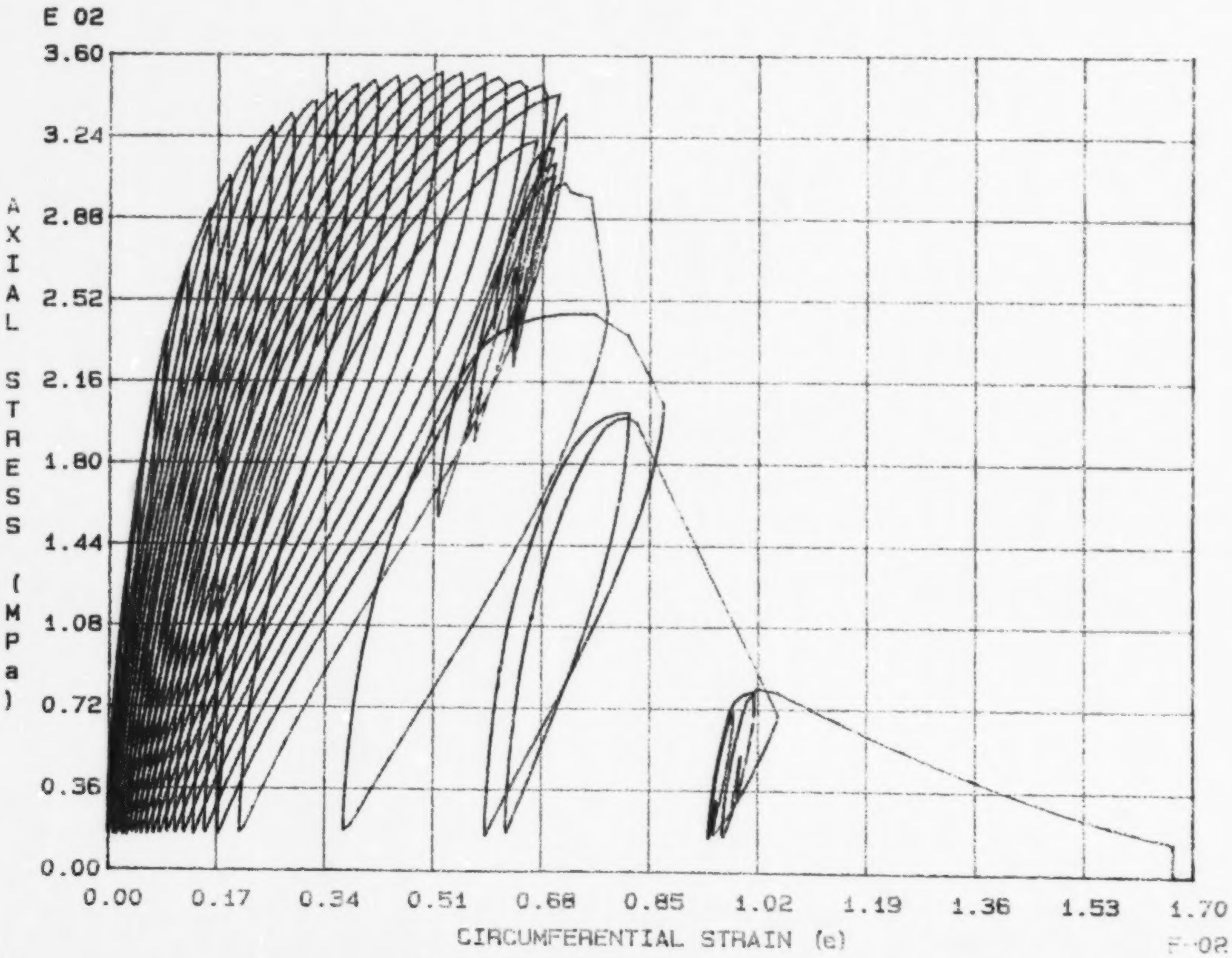

Figure A50. Loading and unloading curves (cir. strain) for Specimen MB1-52.865.

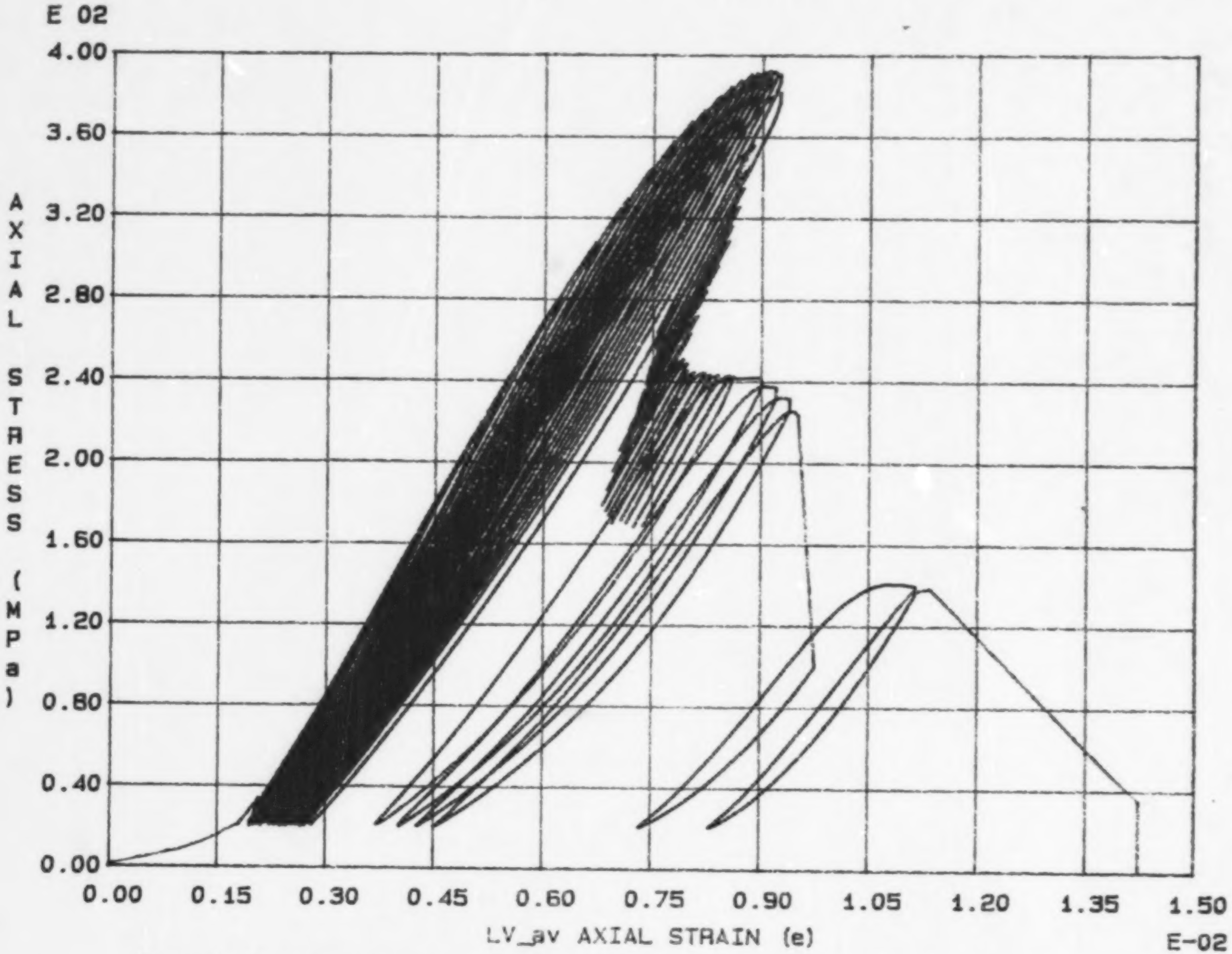

Figure A51. Loading and unloading curves (axial strain) for Specimen MB1-22.547.

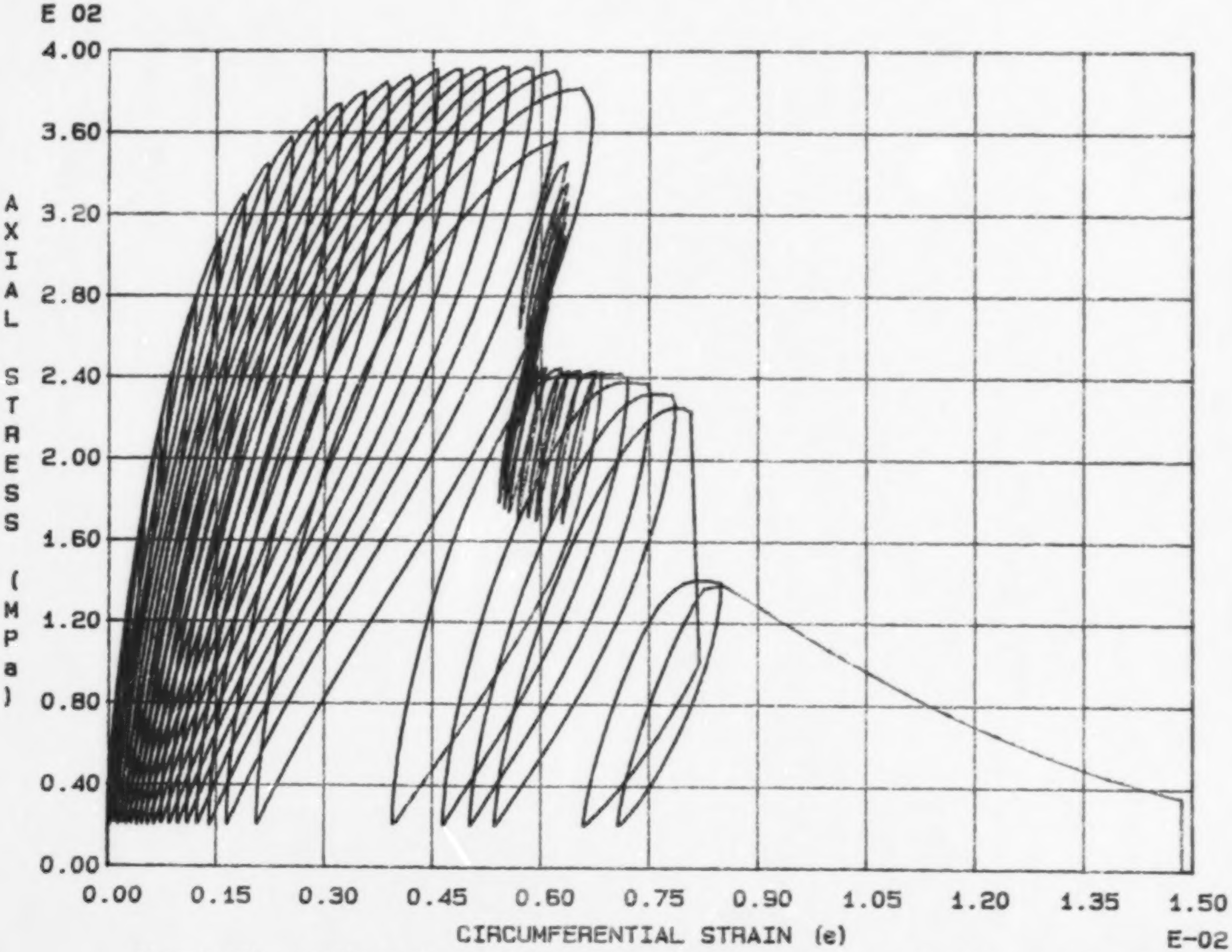

Figure A52. Loading and unloading curves (cir. strain) for Specimen MB1-22.547.

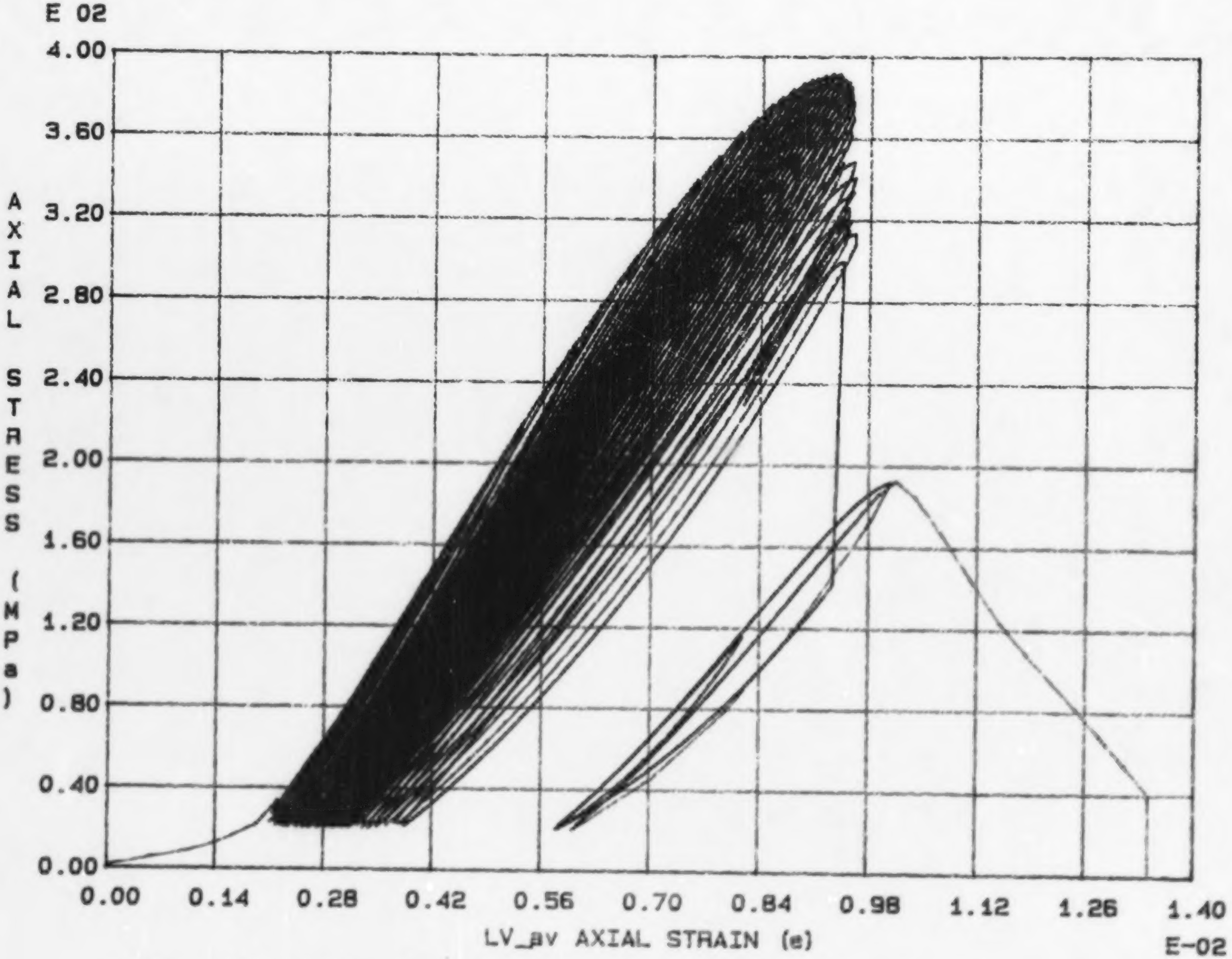

Figure A53. Loading and unloading curves (axial strain) for Specimen MB1-25.864.

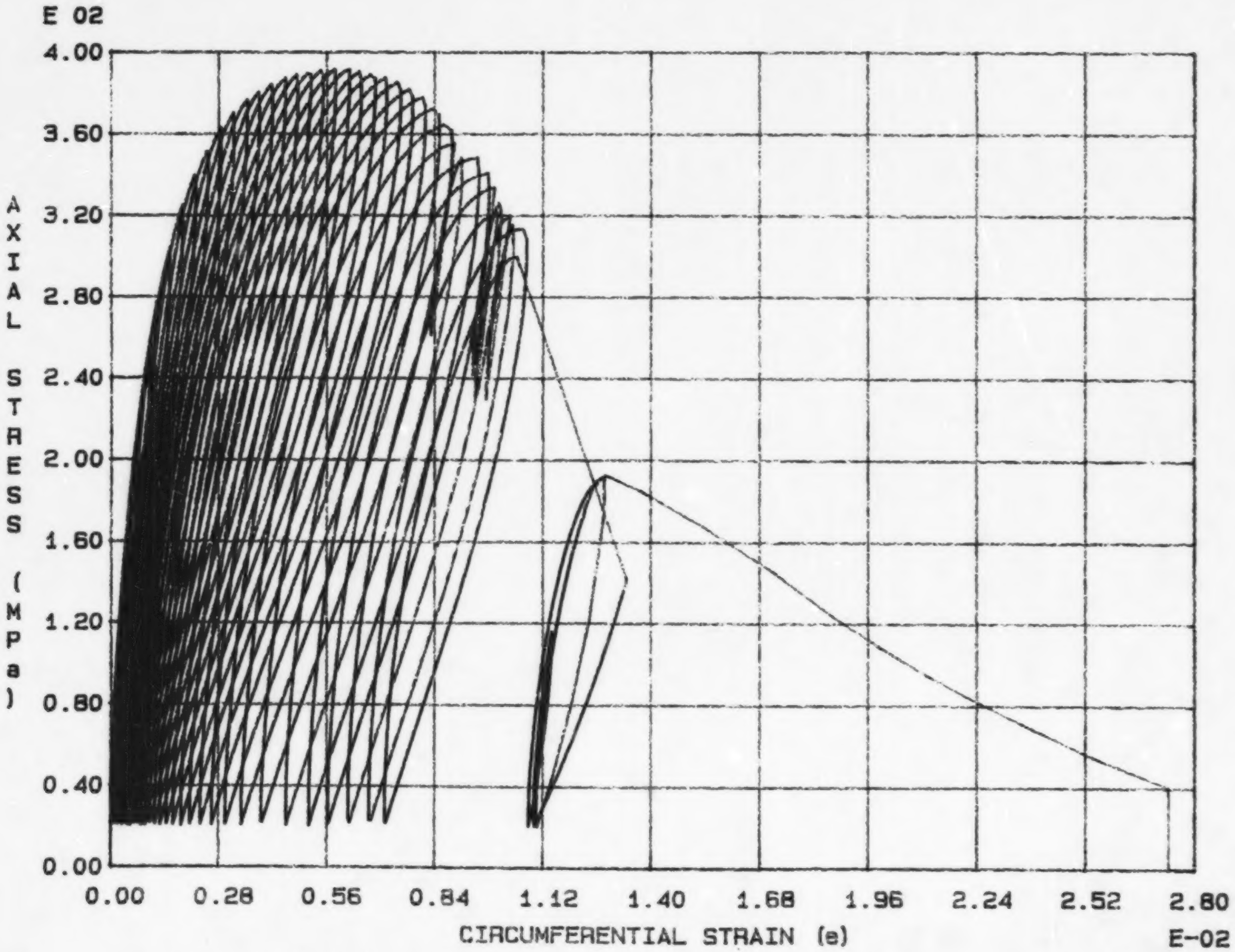

Figure A54. Loading and unloading curves (cir. strain) for Specimen MB1-25.864.

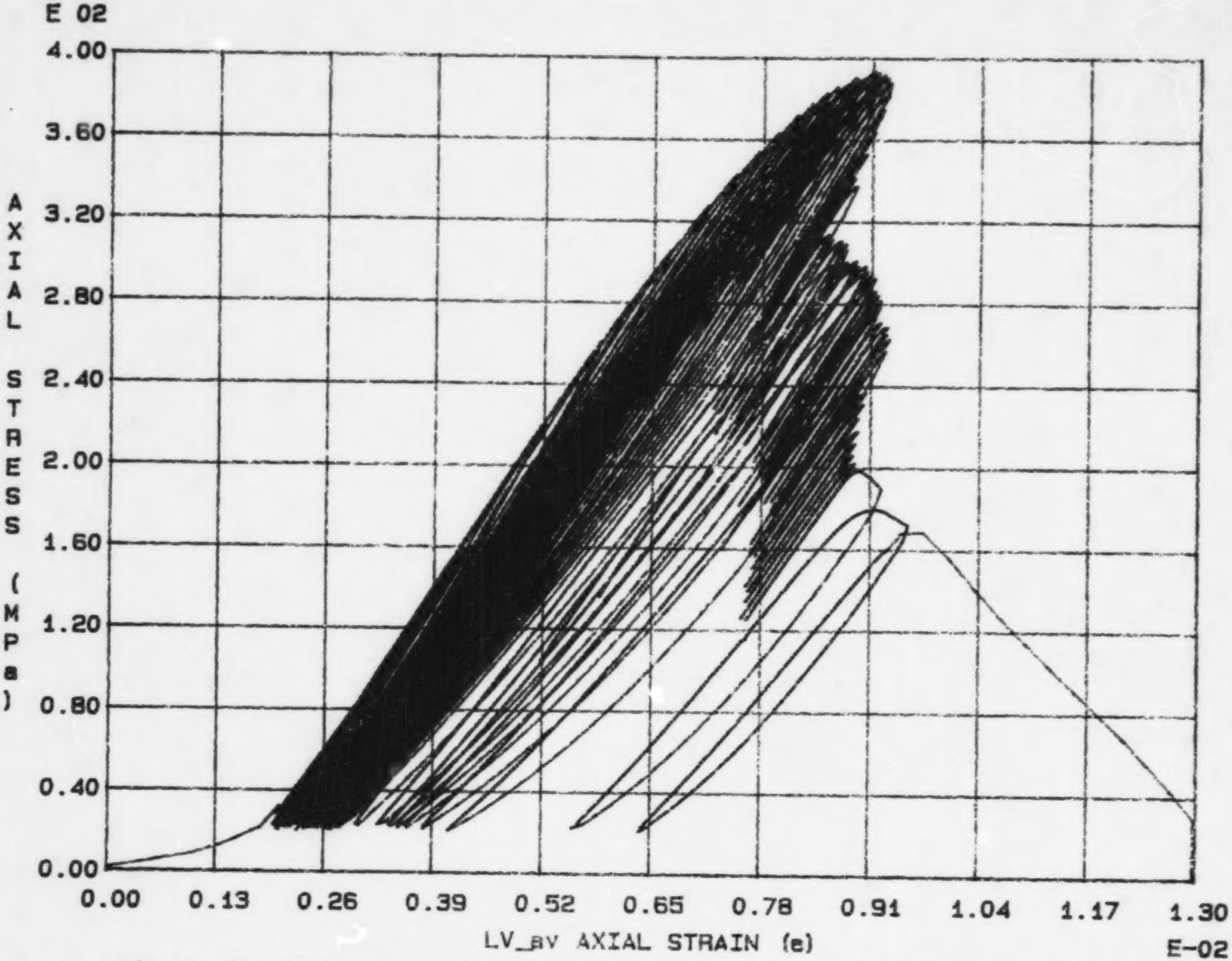

Figure A55. Loading and unloading curves (axial strain) for Specimen MB1-60.069.

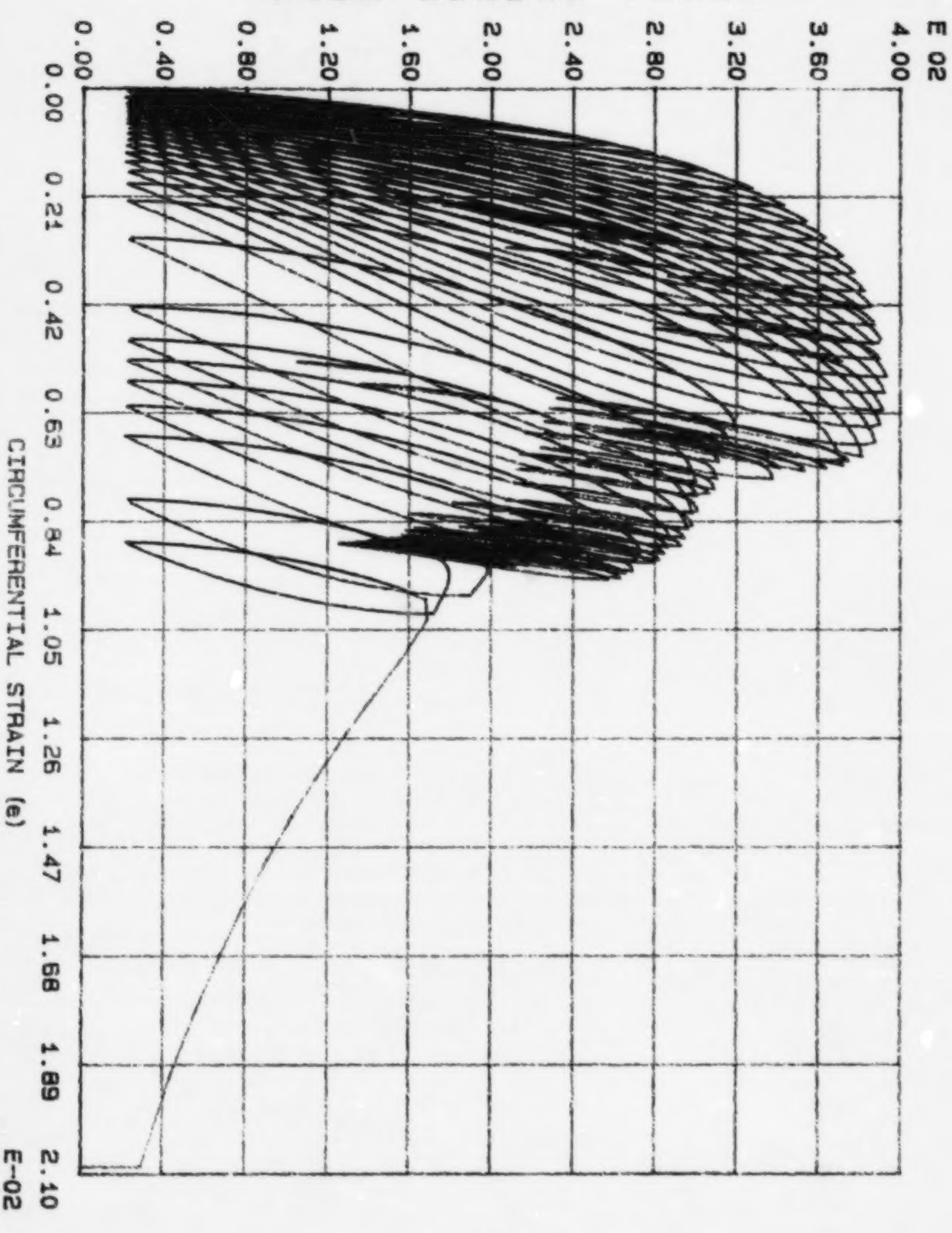

Figure A56. Loading and unloading curves (cir. strain) for Specimen MB1-60.069.

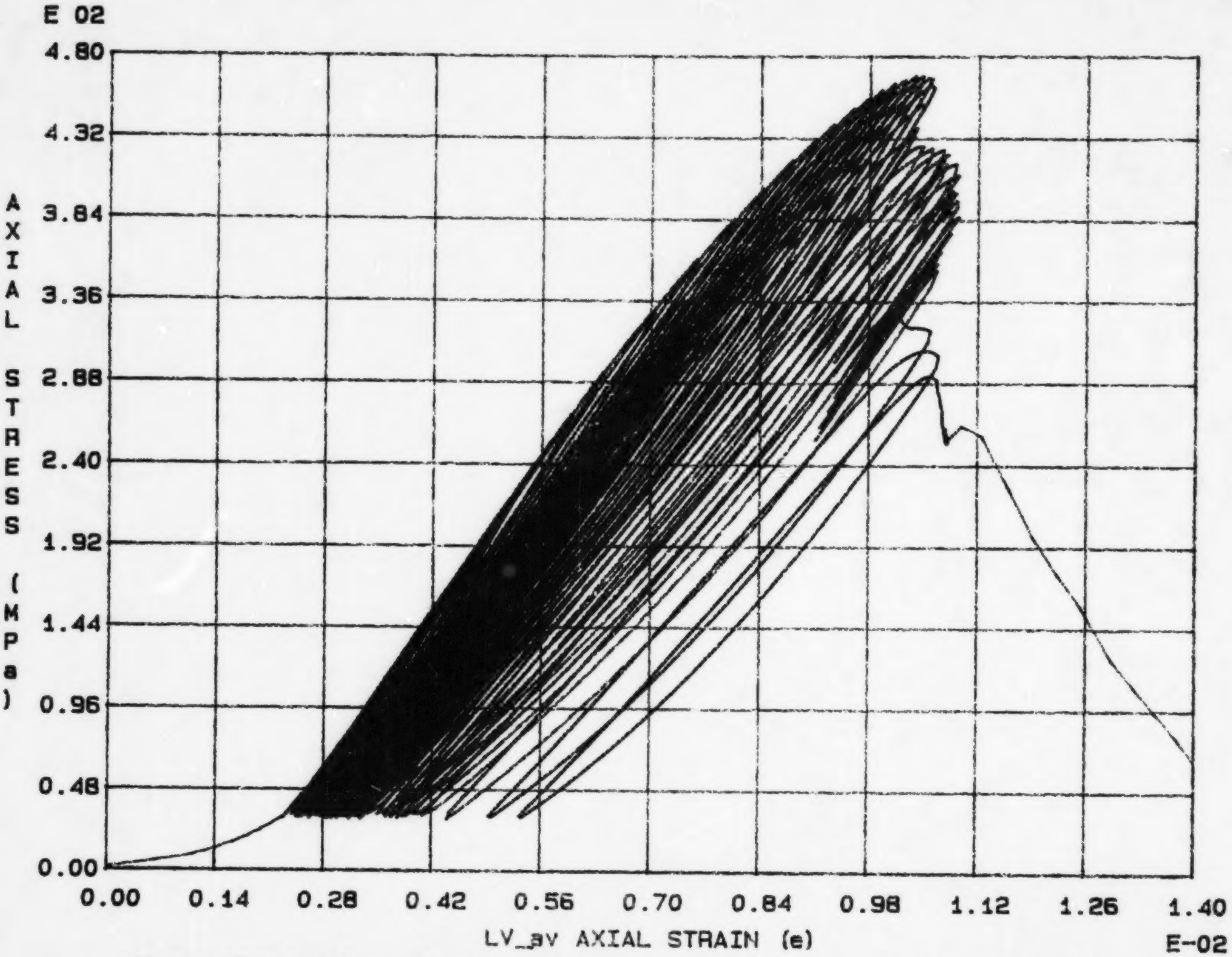

Figure A57. Loading and unloading curves (axial strain) for Specimen MB1-23.045.

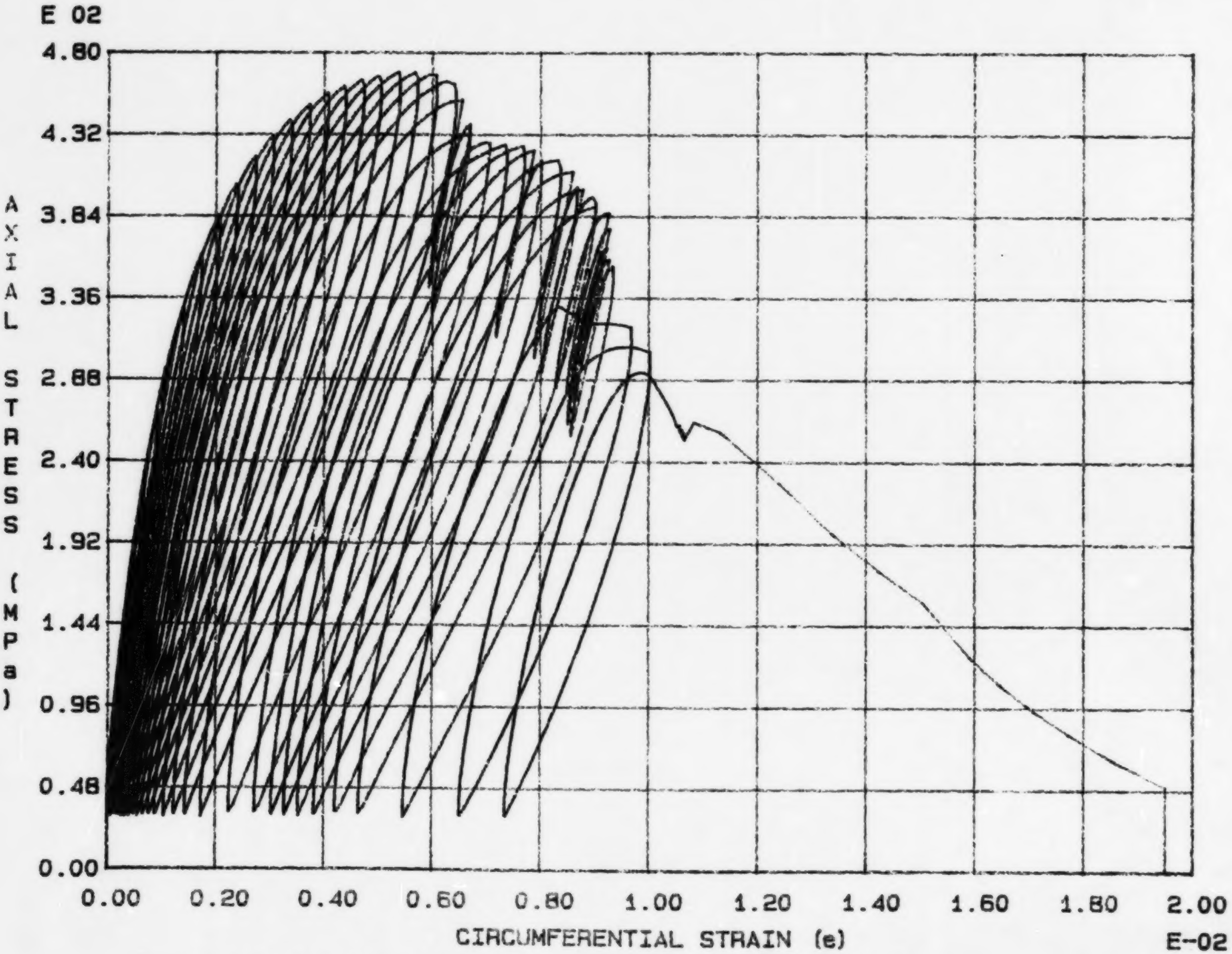

Figure A58. Loading and unloading curves (cir. strain) for Specimen MB1-23.045.

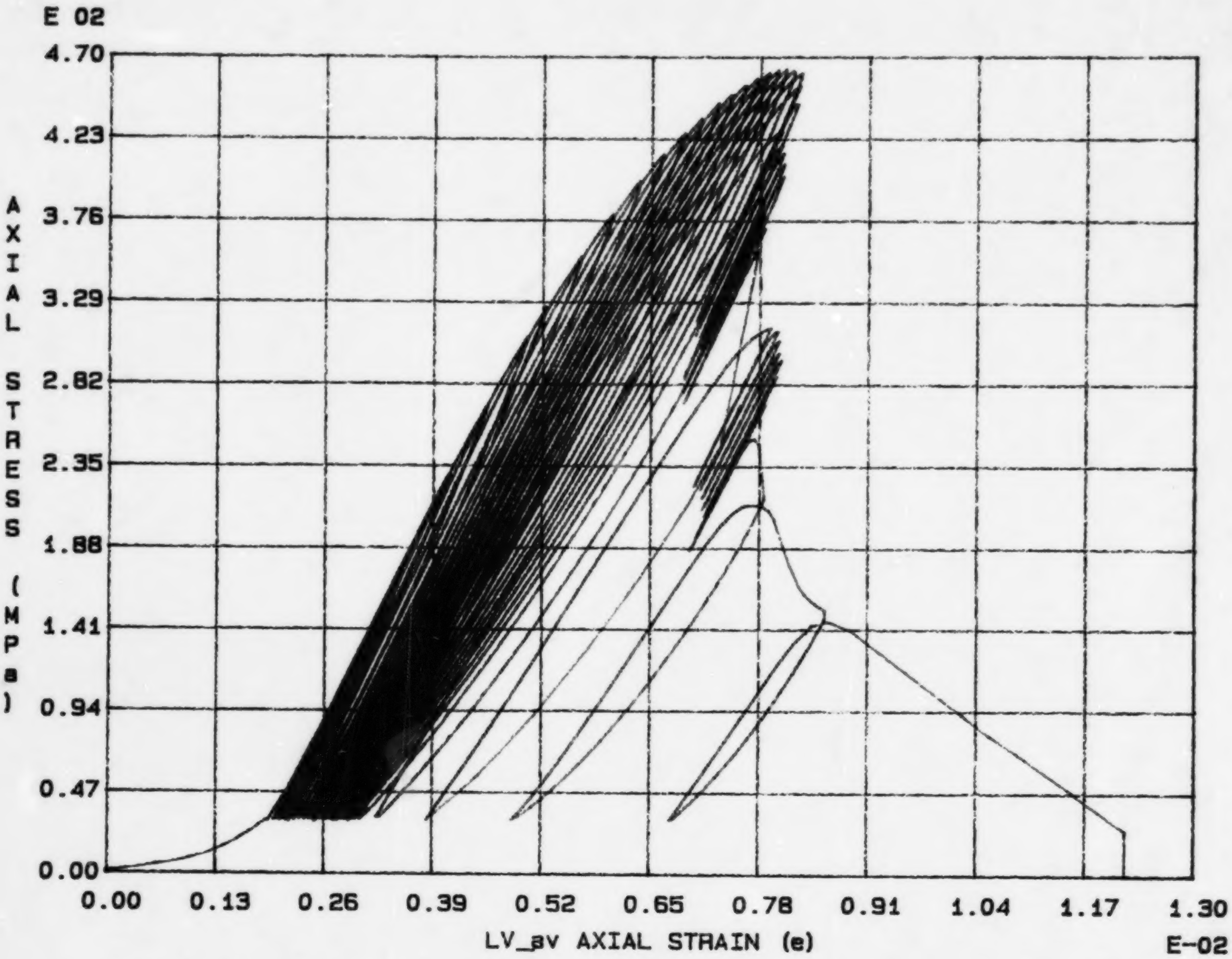

Figure A59. Loading and unloading curves (axial strain) for Specimen MB1-27.065.

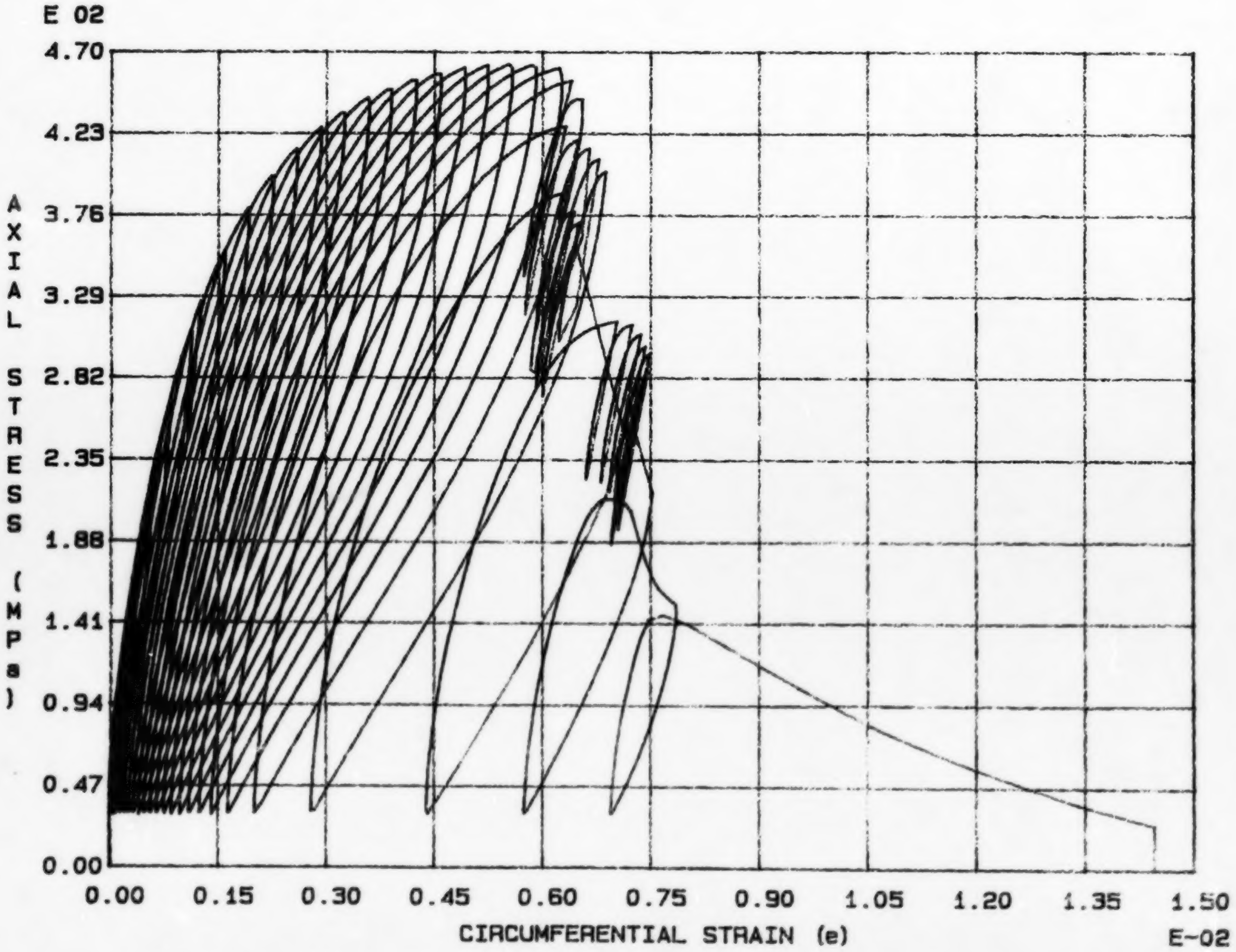

Figure A60. Loading and unloading curves (cir. strain) for Specimen MB1-27.065.

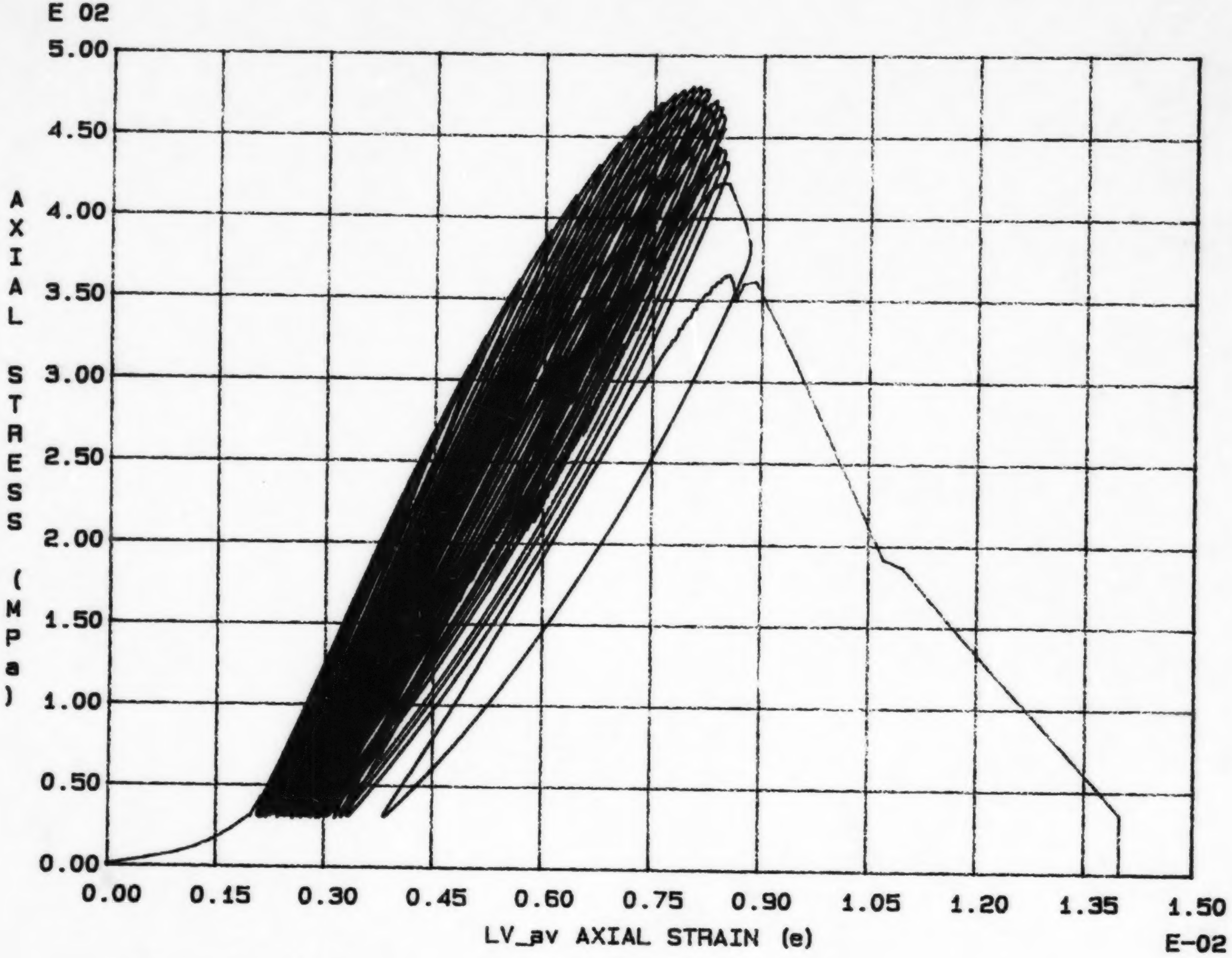

Figure A61. Loading and unloading curves (axial strain) for Specimen MB1-60.227.

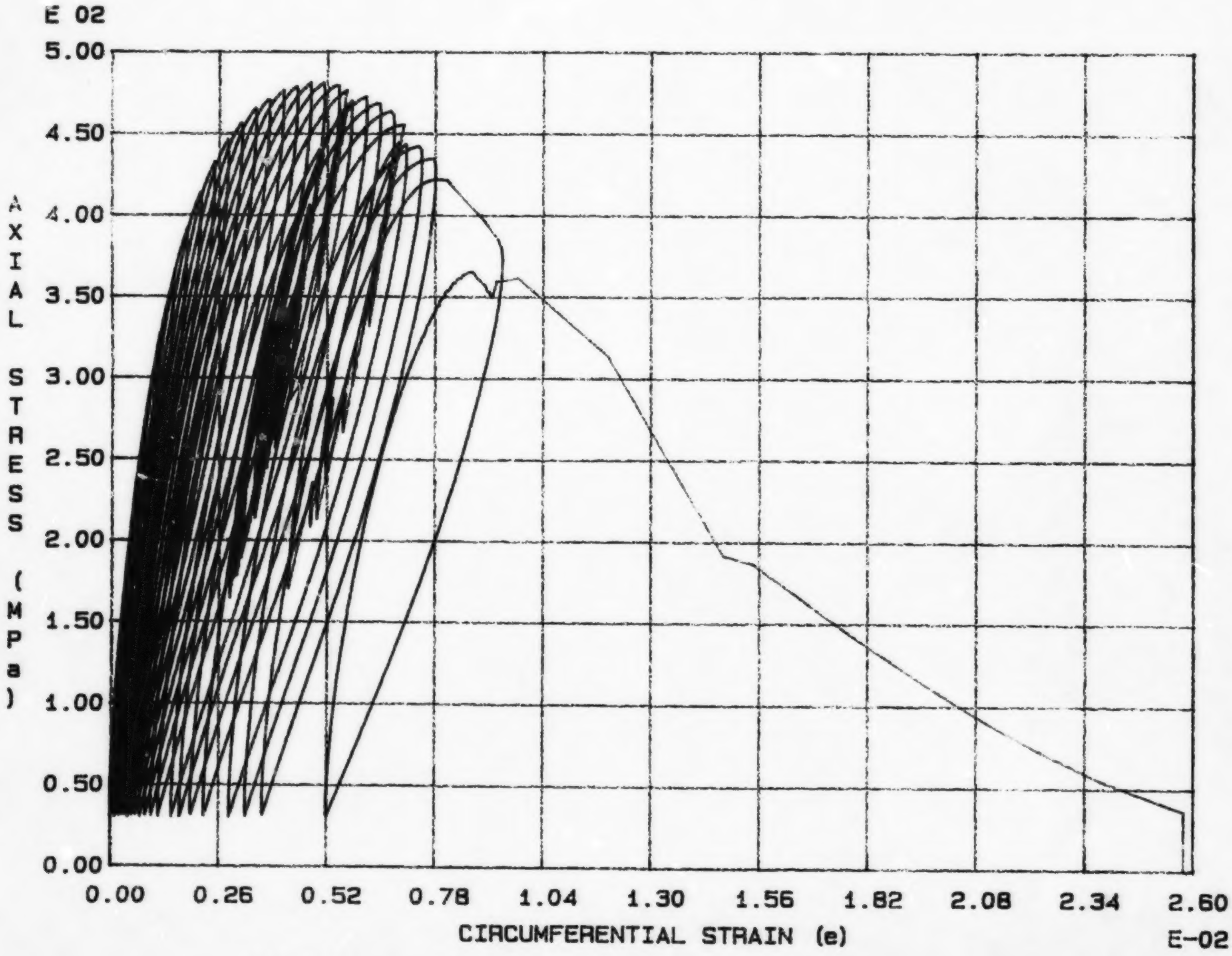

Figure A62. Loading and unloading curves (cir. strain) for Specimen MB1-60.227.

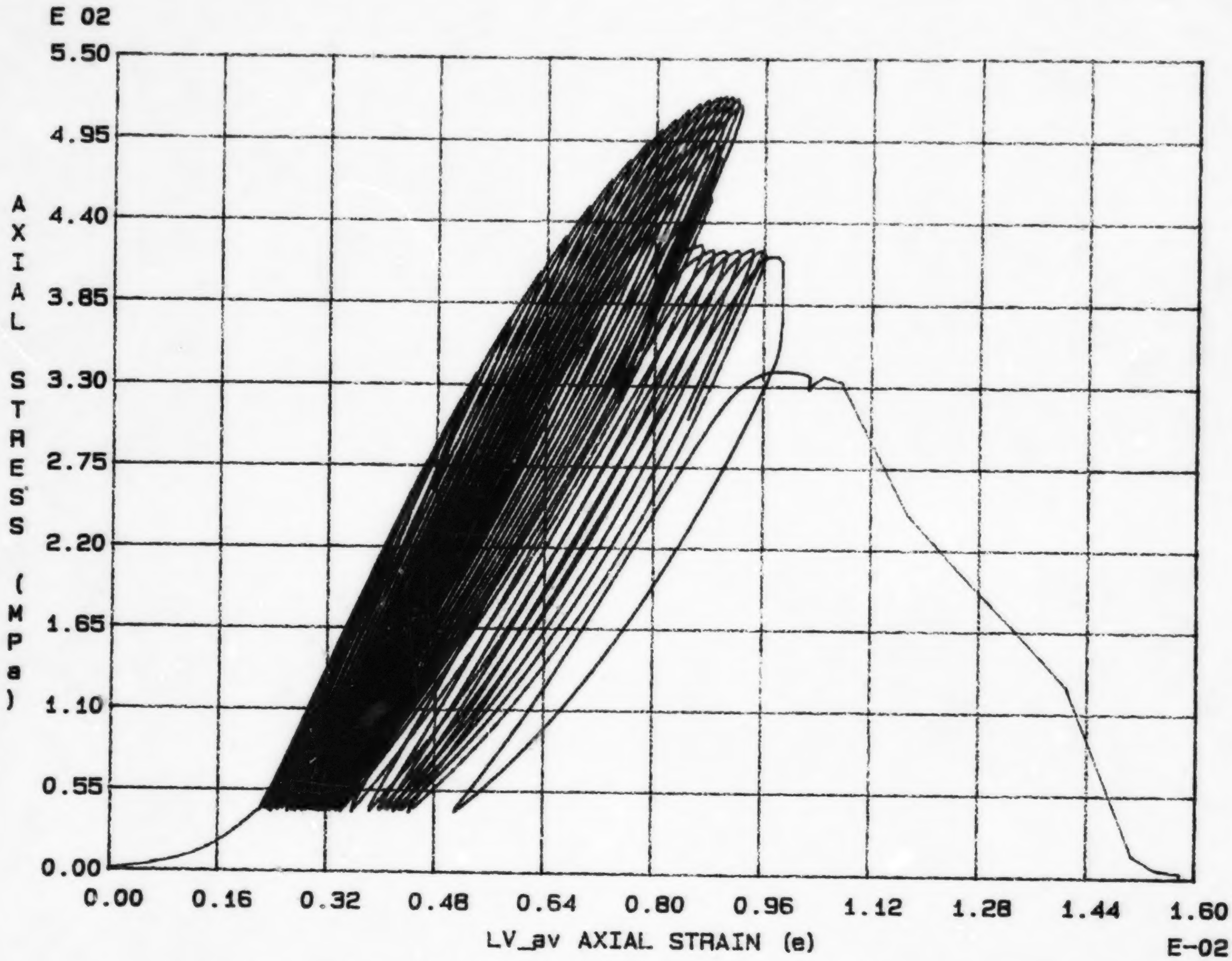

Figure A63. Loading and unloading curves (axial strain) for Specimen MB1-23.205.

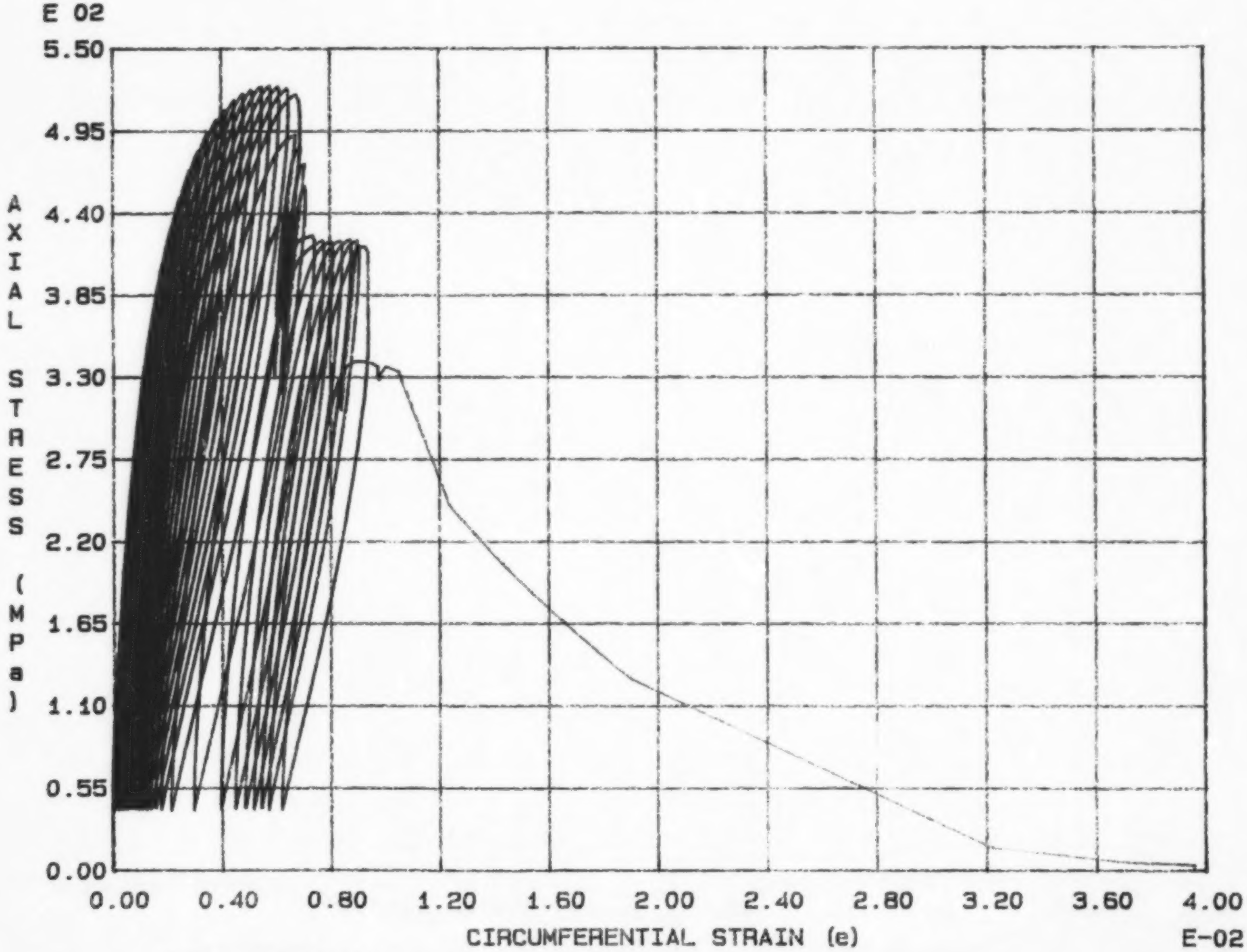

Figure A64. Loading and unloading curves (cir. strain) for Specimen MB1-23.205.

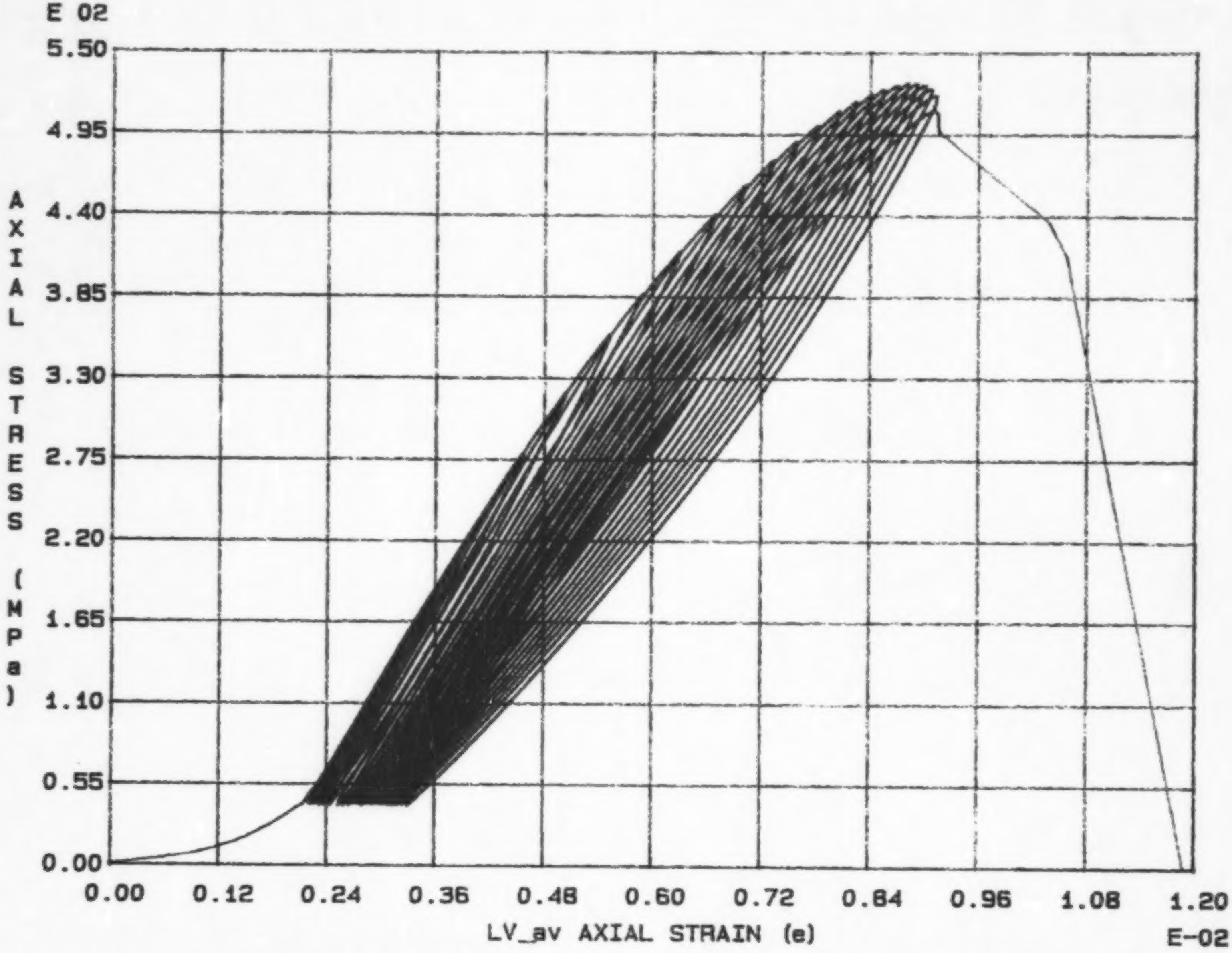

Figure A65. Loading and unloading curves (axial strain) for Specimen MB1-27.225.

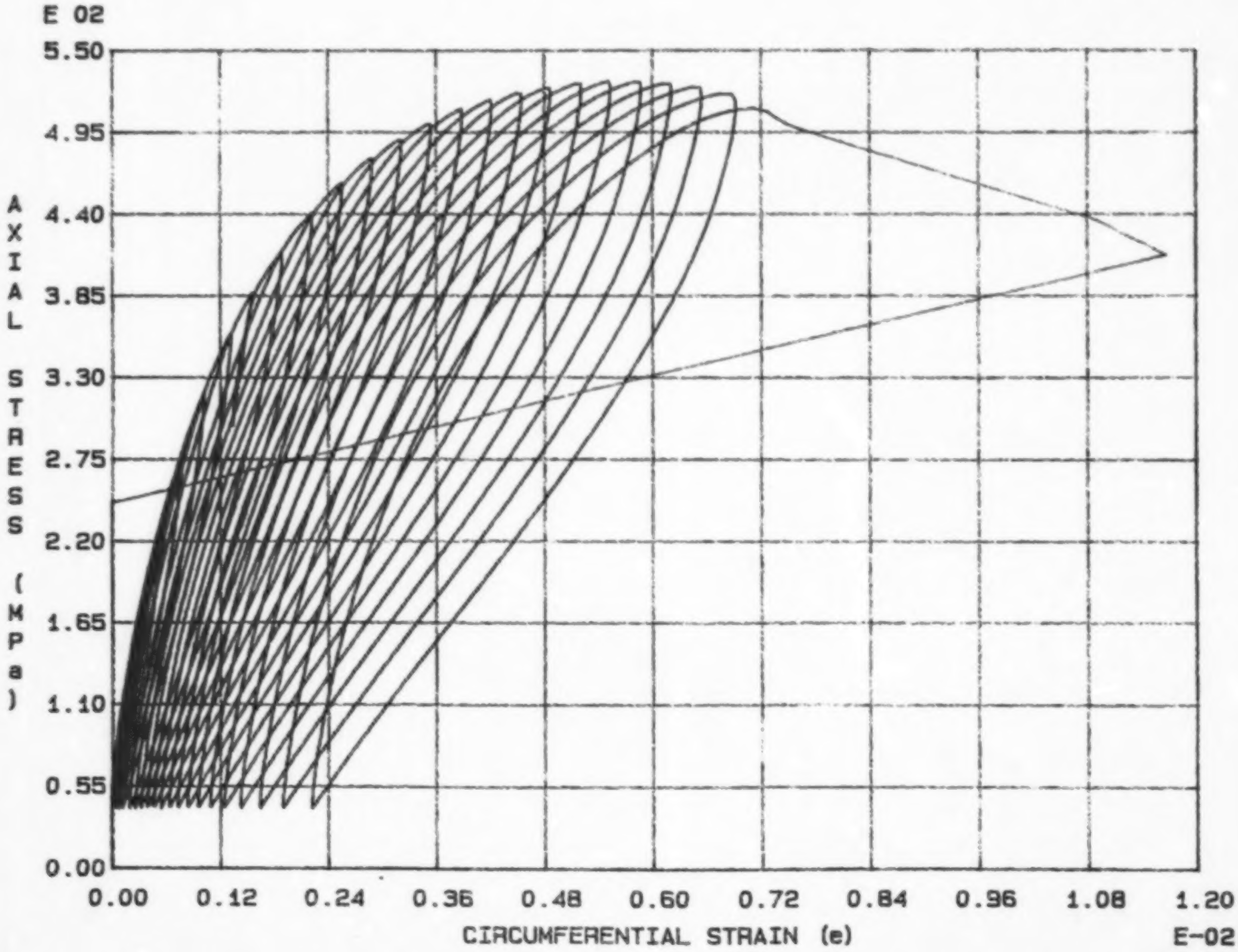

Figure A66. Loading and unloading curves (cir. strain) for Specimen MB1-27.225.

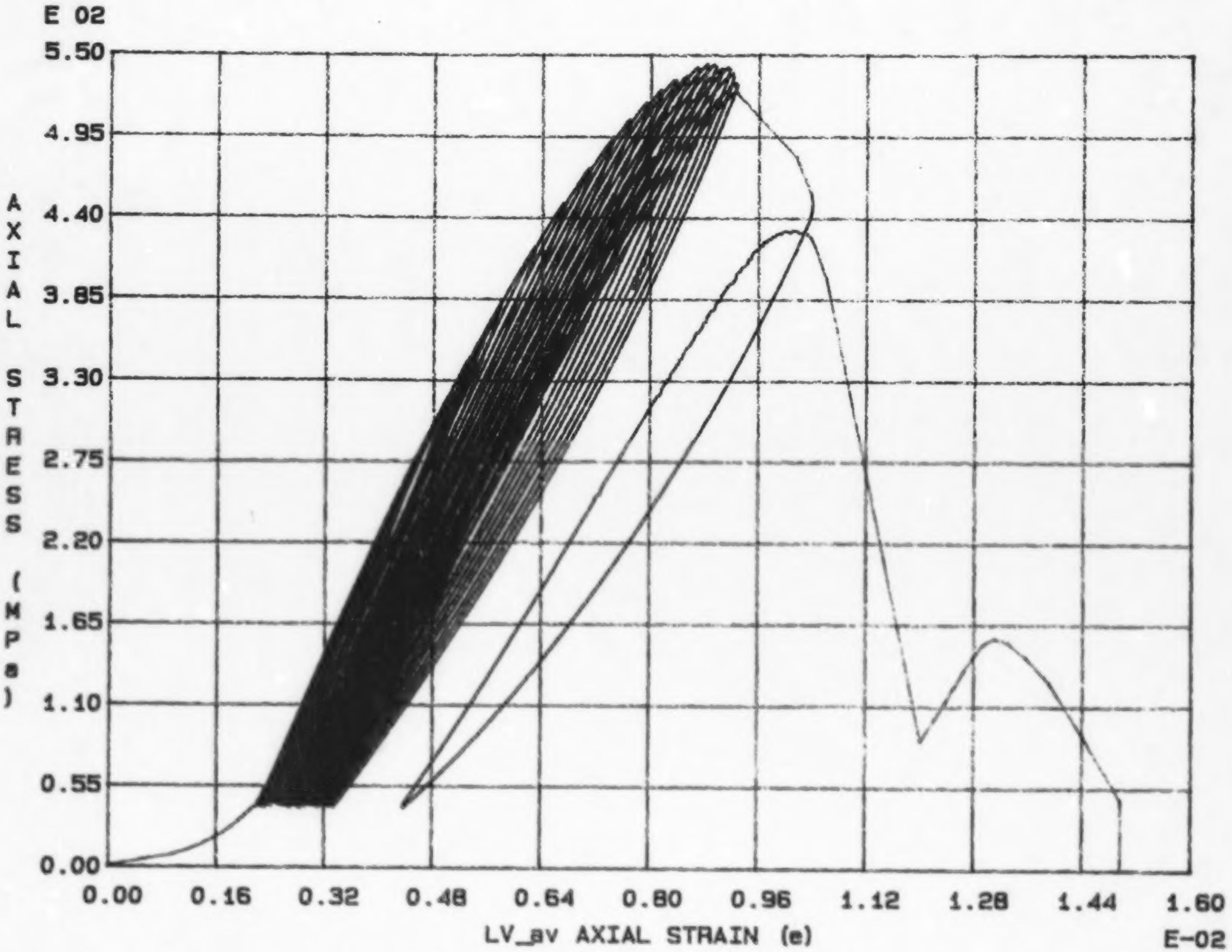

Figure A67. Loading and unloading curves (axial strain) for Specimen MB1-60.622.

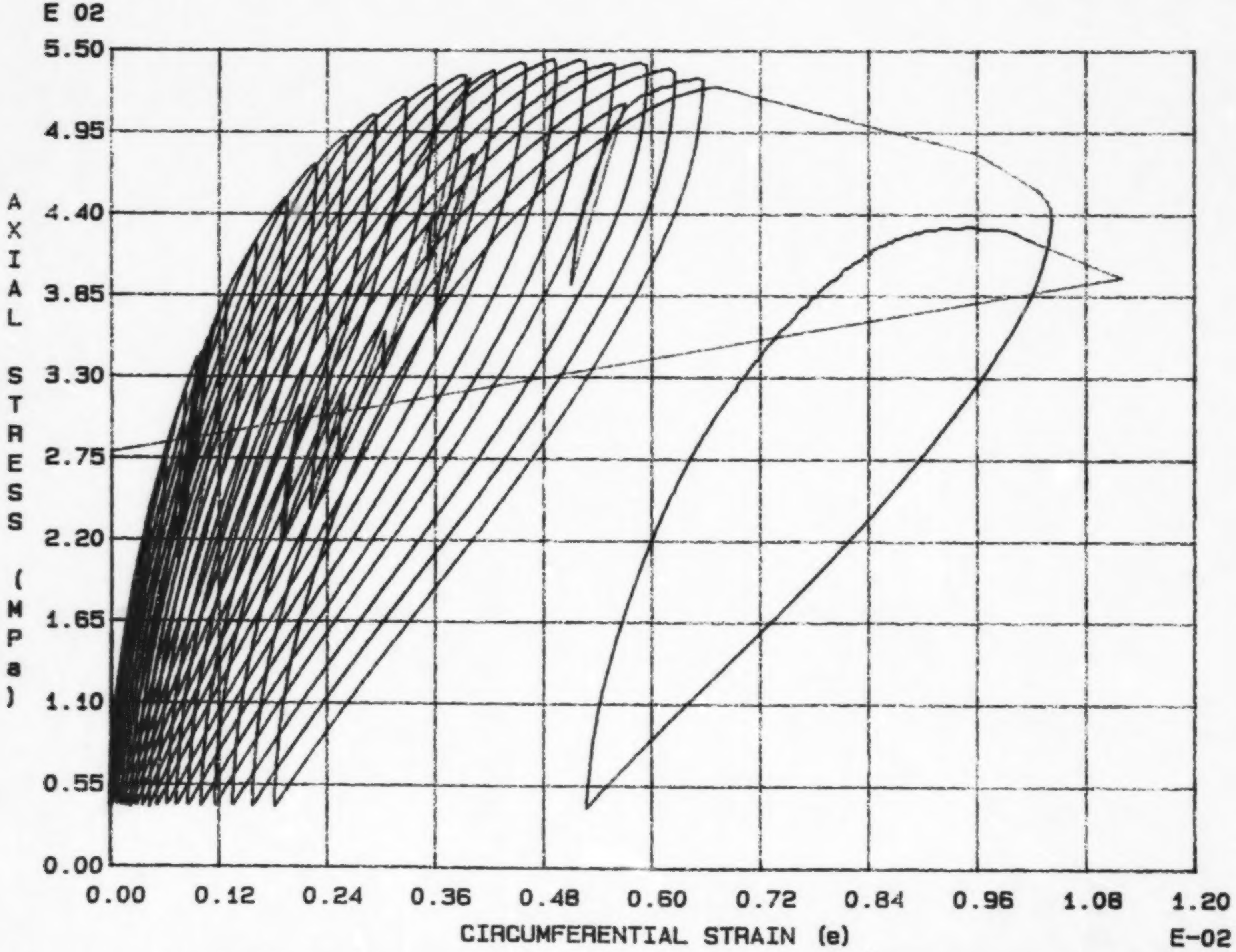

Figure A68. Loading and unloading curves (cir. strain) for Specimen MB1-60.622.

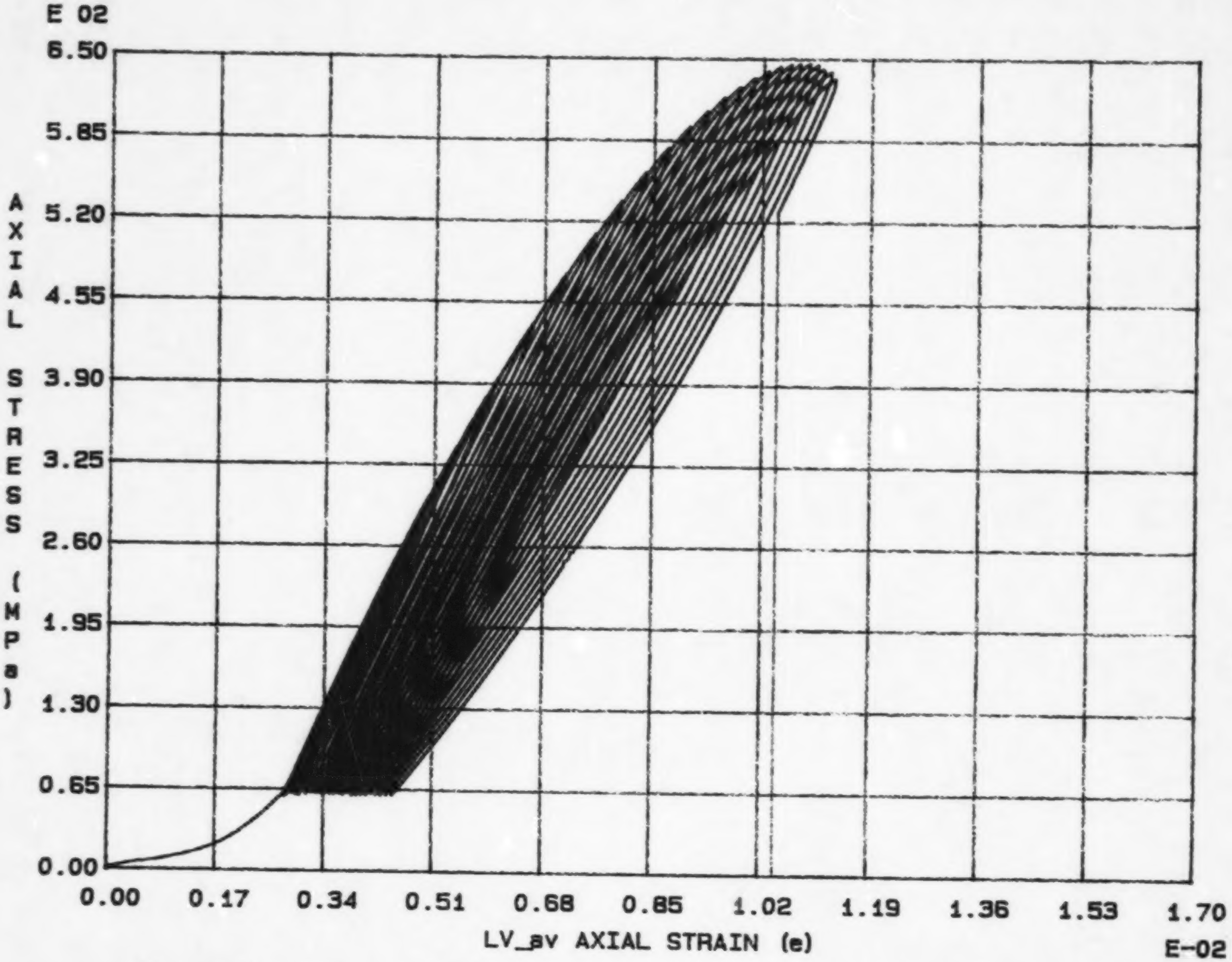

Figure A69. Loading and unloading curves (axial strain) for Specimen MB1-23.364

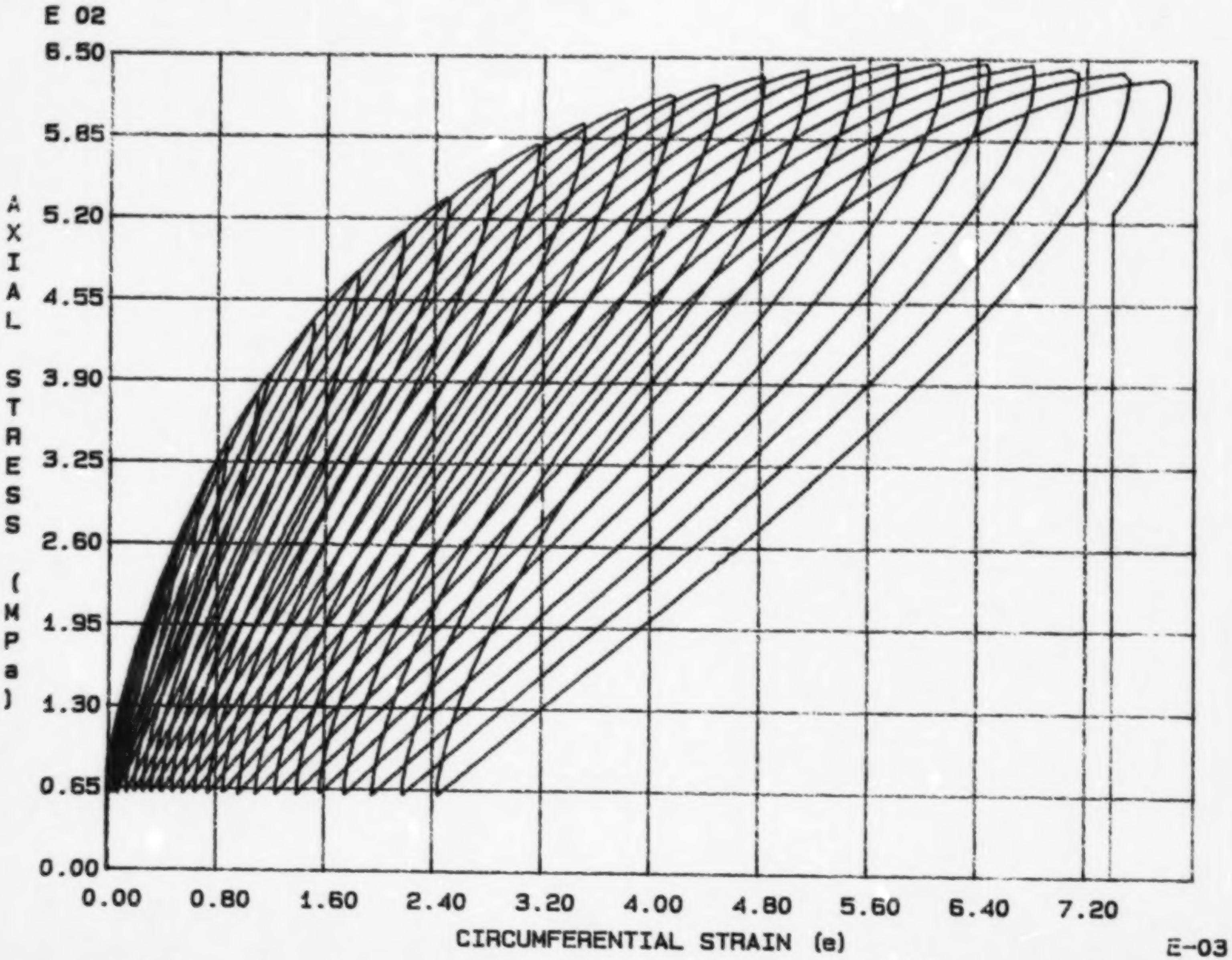

Figure A70. Loading and unloading curves (cir. strain) for Specimen MB1-23.364.

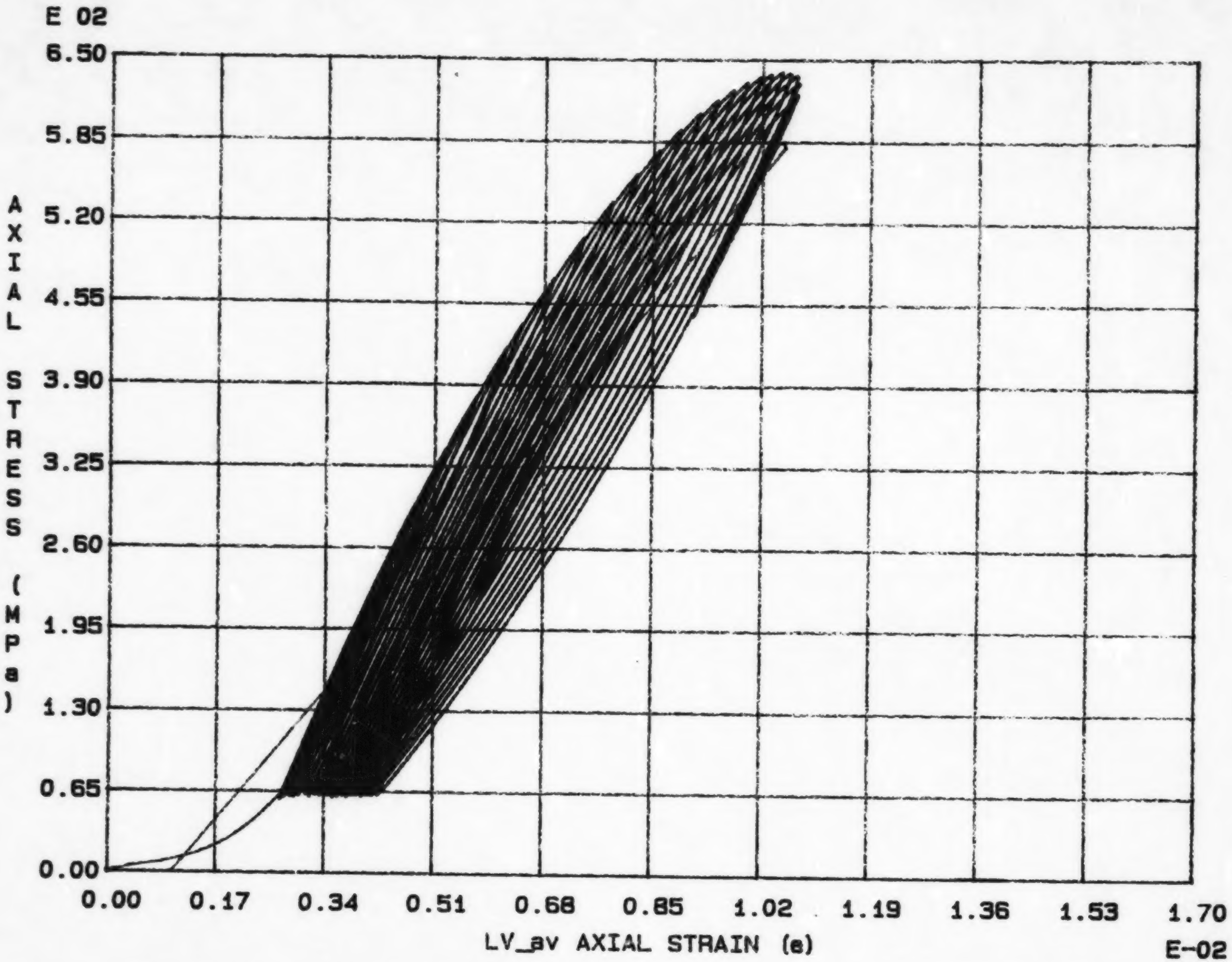

Figure A71. Loading and unloading curves (axial strain) for Specimen MB1-27.387.

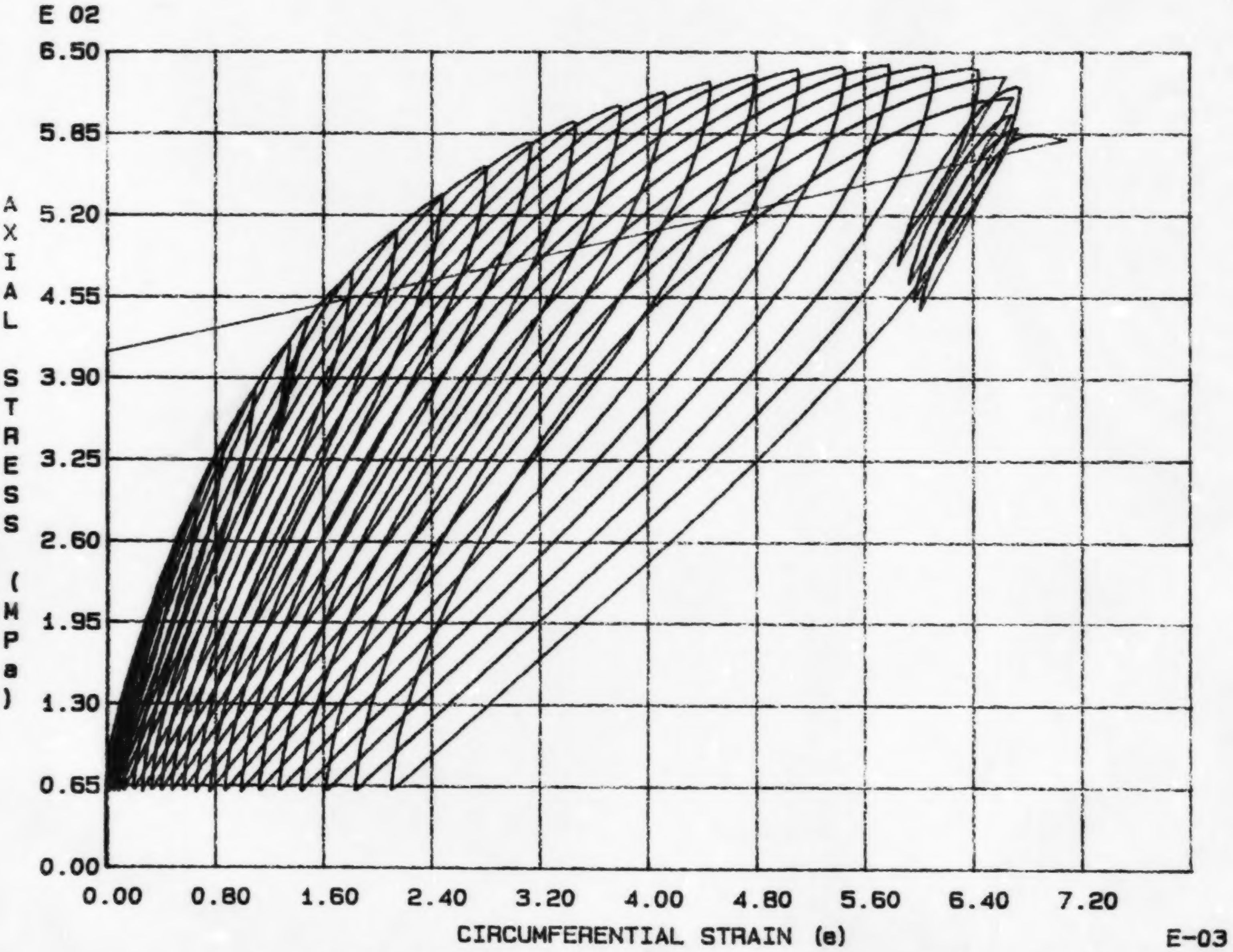

Figure A72. Loading and unloading curves (cir. strain) for Specimen MB1-27.387.

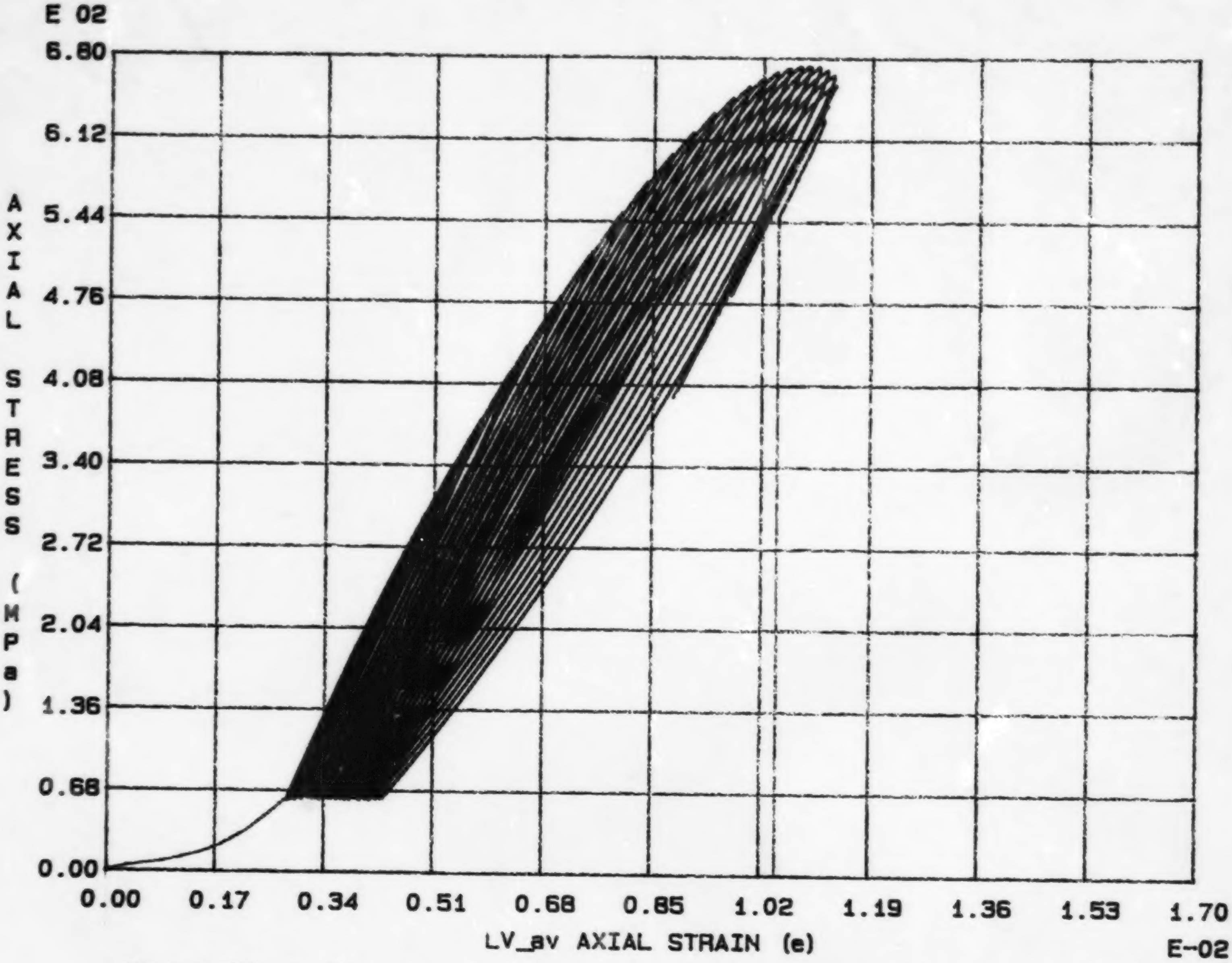

Figure A73. Loading and unloading curves (axial strain) for Specimen MB1-62.050.

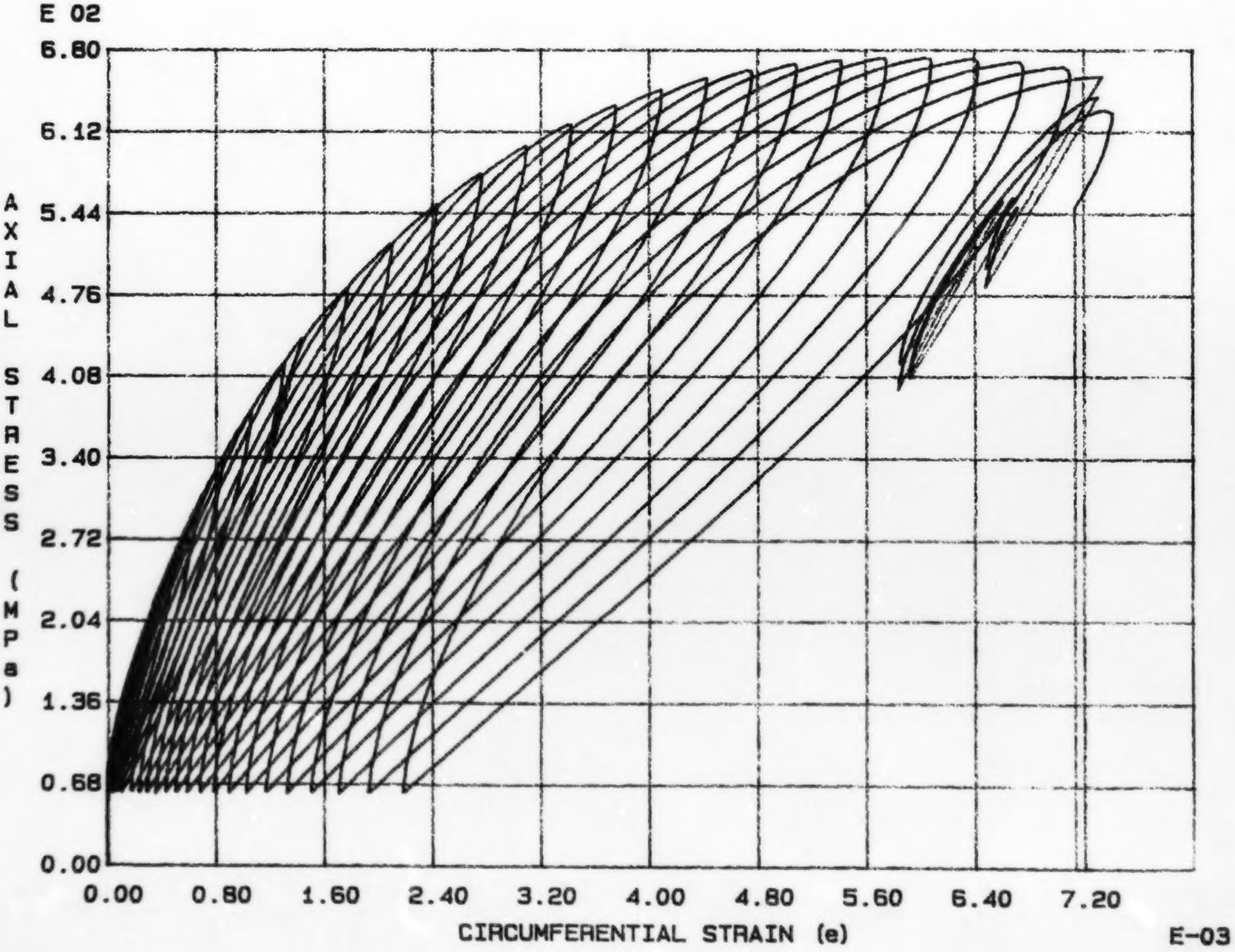

Figure A74. Loading and unloading curves (cir. strain) for Specimen MB1-62.050.